Bulletin 53
(Part 4 of 4 Parts)

THE SHOCK AND VIBRATION BULLETIN

Part 4
Damping and Machinery Dynamics

MAY 1983

A Publication of
THE SHOCK AND VIBRATION
INFORMATION CENTER
Naval Research Laboratory, Washington, D.C.

Office of
The Under Secretary of Defense
for Research and Engineering

SYMPOSIUM MANAGEMENT

THE SHOCK AND VIBRATION INFORMATION CENTER

Henry C. Pusey, Director
Rudolph H. Volin
J. Gordan Showalter
Jessica Hileman
Elizabeth A. McLaughlin
Mary K. Gobbett

Bulletin Production

Publications Branch, Technical Information Division,
Naval Research Laboratory

Bulletin 53
(Part 4 of 4 Parts)

THE SHOCK AND VIBRATION BULLETIN

MAY 1983

A Publication of
THE SHOCK AND VIBRATION
INFORMATION CENTER
Naval Research Laboratory, Washington, D.C.

The 53rd Symposium on Shock and Vibration was held at the Radisson Ferncroft Hotel, Danvers, MA on October 26-28, 1982. The U.S. Army Materials and Mechanics Research Center, Watertown, MA, was the host.

Office of
The Under Secretary of Defense
for Research and Engineering

CONTENTS

PAPERS APPEARING IN PART 4

Damping

Machinery Dynamics

PAPERS APPEARING IN PART 1

PAPERS APPEARING IN PART 2

Fluid Structure Dynamics

Dynamic Analysis

PAPERS APPEARING IN PART 3

Vehicle Dynamics

Vibration: Test and Criteria

TITLES AND AUTHORS OF PAPERS PRESENTED IN THE SHORT DISCUSSION TOPICS SESSION

NOTE: These papers were only presented at the Symposium. They are not published in the Bulletin and are only listed here as a convenience.

THE DEVELOPMENT OF A VISCOELASTIC AEROSPACE STRUCTURES TECHNOLOGY DAMPING DESIGN GUIDE
J. Soovere, Lockheed-California Co., Burbank, CA, M. Drake, University of Dayton Research Institute, Dayton, OH, L. Rogers and V. Miller, Air Force Wright Aeronautical Laboratories, Wright Patterson AFB, OH

APPROXIMATE RELAXATION MODULUS FROM THE FRACTIONAL REPRESENTATION OF COMPLEX MODULUS
L. Rogers, Air Force Wright Aeronautical Laboratories, Wright Patterson AFB, OH

DEVELOPMENT OF HIGH FREQUENCY ISOLATION SYSTEM
F. J. Andrews, Barry Controls, Watertown, MA

A RECENT APPLICATION EMPLOYING ELASTOMERIC TECHNOLOGY TO ISOLATE A HIGH RESOLUTION AERIAL RECONNAISSANCE CAMERA
D. F. Reynolds, Barry Controls, Watertown, MA

MERCURY ISOLATION SYSTEM/DESIGN, DEVELOPMENT MANUFACTURE AND TEST
M. Peretti, Barry Controls, Watertown, MA

LOOSENING OF BOLTED JOINTS DURING VIBRATION TESTING
J. J. Kerley, Jr., Goddard Space Flight Center, Greenbelt, MD

BOLTS AND FASTENER TIGHTENING TO BROCHURE IDEALNESS THROUGH VIBRATION SIGNATURES
A. S. R. Murty, Indian Institute of Technology, Kharagpur, India

DEVELOPMENT OF A MATERIAL TESTING MACHINE CAPABLE OF HIGH CYCLE LOADINGS SUPERIMPOSED ONTO LOW CYCLE LOADINGS
R. C. Goodman, University of Dayton Research Institute, Dayton, OH

PREDICTION OF STRUCTURAL RELIABILITY FROM VIBRATION MEASUREMENTS
P. Miakar, U.S. Army Engineer Waterways Experiment Station, Vicksburg, MS

PROGRESS REPORT ON U.S. STATE OF THE ART ASSESSMENT OF MOBILITY MEASUREMENTS PROGRAM
D. J. Ewins, Imperial College of Science and Technology, London, England

UNDERWATER SHOCK ANALYSIS OF A MISSILE LAUNCH TUBE
K. C. Kiddy, Naval Surface Weapons Center, Silver Spring, MD

THE VIBRATION OF SLIGHTLY CURVED RECTANGULAR PLATES UNDER COMPRESSION
S. M. Dickinson and S. Ilanko, University of Western Ontario, London, Ontario, Canada and S. C. Tillman, University of Manchester, Manchester, England

SHOCK ANALYSIS OF DICED DISK TRANSDUCER USING ANSYS
A. Haecker and H. Mitson, Gould, Inc., Cleveland, OH

SESSION CHAIRMEN AND COCHAIRMEN

Date	Session Title	Chairmen	Cochairmen
Tuesday, 26 Oct. A.M.	Opening Session	Mr. Richard Shea, U.S. Army Materials and Mechanics Research Center, Watertown, MA	Mr. Henry C. Pusey, Shock and Vibration Information Center, Naval Research Laboratory, Washington, DC
Tuesday, 26 Oct. P.M.	Elias Klein Memorial Lecture Plenary A	Mr. Henry C. Pusey, Shock and Vibration Information Center, Naval Research Laboratory, Washington, DC	
Tuesday, 26 Oct. P.M.	Machinery Dynamics	Dr. Ronald L. Eshleman, The Vibration Institute, Clarendon Hills, IL	Mr. Samuel Feldman, NKF Engineering Associates, Inc., Vienna, VA
Tuesday, 26 Oct. P.M.	Pyrotechnic Shock-Measurement/ Simulation	Mr. C. Douglas Hinckley, TRW Systems, Ogden, UT	Mr. Peter Bouelin, Naval Weapons Center, China Lake, CA
Tuesday, 26 Oct. P.M.	MIL-STD-810D Panel Session	Mr. Preston Scott Hall, Air Force Wright Aeronautical Laboratories, Wright Patterson Air Force Base, OH	Mr. Rudolph H. Volin, Shock and Vibration Information Center, Naval Research Laboratory, Washington, DC
Wednesday, 27 Oct. A.M.	Maurice Biot 50th Anniversary Lecture Plenary B	Mr. George J. O'Hara, Naval Research Laboratory, Washington, DC	
Wednesday, 27 Oct. A.M.	Vibration: Test and Criteria	Mr. John Wafford, Aeronautical Systems Division, Wright Patterson Air Force Base, OH	Mr. Howard D. Camp, Jr., U.S. Army Electronic Research and Development Command, Ft. Monmouth, NJ
Wednesday, 27 Oct. A.M.	Shock Testing and Analysis	Mr. Edwin Rzepka, Naval Surface Weapons Center, Silver Spring, MD	Mr. Ami Frydman, Harry Diamond Laboratories, Adelphi, MD
Wednesday, 27 Oct. P.M.	Damping	Dr. Frederick C. Nelson, Tufts University, Medford, MA	Dr. Lynn Rogers, Air Force Wright Aeronautical Laboratories, Wright Patterson Air Force Base, OH
Wednesday, 27 Oct. P.M.	Fluid-Structure Dynamics	Dr. Anthony J. Kalinowski, Naval Underwater Systems Center, New London, CT	Dr. Martin W. Wambsganss, Argonne National Laboratory, Argonne, IL
Thursday, 28 Oct. A.M.	Plenary C	Mr. Richard Shea, U.S. Army Materials and Mechanics Research Center, Watertown, MA	
Thursday, 28 Oct. A.M.	Dynamic Analysis I	Lt. Col. John J. Allen, Air Force Office of Scientific Research, Washington, DC	Dr. Robert L. Sierakowski, University of Florida, Gainesville, FL
Thursday, 28 Oct. A.M.	Vehicle Dynamics	Dr. Richard A. Lee, U.S. Army Tank-Automotive Command, Warren, MI	Dr. Grant R. Gerhart, U.S. Army Tank-Automotive Command, Warren, MI
Thursday, 28 Oct. P.M.	Dynamic Analysis II	Dr. James J. Richardson, U.S. Army Missile Command, Redstone Arsenal, AL	Mr. Brantley R. Hanks, NASA Langley Research Center, Hampton, VA
Thursday, 28 Oct. P.M.	Short Discussion Topics	Mr. R. E. Seely, Naval Weapons Handling Center, Earle, Colts Neck, NJ	Mr. L. Kenneth Stewart, U.S. Army Armament Research and Development Command, Dover, NJ

DAMPING

EXPERIMENTAL INVESTIGATION OF CONTROLLING VIBRATIONS USING MULTI-UNIT IMPACT DAMPERS

C.N. Bapat and S. Sankar
Department of Mechanical Engineering
Concordia University
Montreal, Quebec, Canada
and
N. Popplewell
Department of Mechanical Engineering
University of Manitoba
Winnipeg, Manitoba, Canada

Free and forced vibrations of multi-unit impact damper were investigated experimentally. In free vibrations, the time rate of decrease of maximum displacement increased with number of units and was nearly constant, only when initial deflection was greater than gap. In steady state motion, with identical gaps, under sinusoidal load, impacts generally occurred only over a fraction of a cycle. Performance, defined as a ratio of displacement amplitude with damper to displacement amplitude without damper, improved with number of units only when excitation frequency was equal to or greater than resonant frequency of damperless system. Maximum amplitude reduction occurred at resonance and otherwise, it decreased at a faster rate below resonance than above it. Hence, similar to a single-unit, even multi-unit impact damper should be used with caution when excitation frequency is below resonant frequency, as displacement amplification can occur in this range.

NOMENCLATURE

- A = displacement amplitude in absence of the impact damper, in.
- C = damping inclination, in/sec.
- Gap = Gap between mass m and M, in.
- K = equivalent spring constant of primary system, lb_f/in.
- M = equivalent mass of primary system, lb_f.
- m = mass of single particle, lb_f.
- N = number of particles.
- Nu = number of particles in action.
- r = frequency ratio, Ω/w_n.
- X_b = base acceleration in g's.
- X_{max} = displacement amplitude in presence of the impact damper, in.
- X_o = initial deflection of M, in.
- ξ = ratio of critical damping.
- w_n = natural frequency.
- Ω = forcing frequency.

INTRODUCTION

Free and forced vibrations of resonant mechanical systems can be controlled using properly designed single unit impact damper [5-8]. The requirement of large gap, in an optimally designed single unit damper, especially for lightly damped resonant system with high coefficient of restitution, may produce a problem if available space is limited. Also the loud noise and large acceleration level produced at impact, in case of single unit damper, can be reduced by using many units having the same total mass [1-4]. Thus, the vibration control system using multi-unit impact damper essentially consists of many solid particles, each of which moves freely and uniaxially within a clearance in its container.

Free vibrations of single unit damper were studied experimentally [5-7,10], however very little data is available for free vibrations of multi-unit damper.

The analytical studies for forced vibration, using simulation of motion on digital computer or solving coupled nonlinear algebraic equations can be very time consuming for multi-unit dampers [1,2]. The approximate method based on replacing impact forces by equivalent continuous force can simplify the analysis of the system [3,4]. However, this method is based on the

assumption that impacts are evenly distributed in time and hence occur one after another. On the contrary, actual experimental investigation with 2 to 3 units suggests that in steady state motion, impacts generally occur over a fraction of a cycle [2,9]. This requires investigation.

The purpose of this experimental investigation is to study the behaviour of multi-unit impact damper as a means of controlling free and forced vibrations. First, the effect of system parameters such as number of units, gap sizes and initial deflection on free vibration are considered. In the second part the effect of two additional parameters, viz. frequency and amplitude of external sinusoidal excitation on forced vibration are investigated.

FREE VIBRATION OF MULTI-UNIT IMPACT DAMPER

A schematic diagram of the experimental model and measuring equipment are shown in Fig. 1. Multi-unit impact damper consists of nine tubes gripped firmly between two countersunked plates in which it is possible to insert steel balls. This unit was rigidly fixed to the tip of a cantilevered plate spring. The gaps through which balls move can be adjusted using screws, item 4. The initial displacement, X_o, was set to a certain value by using screw, item 7, and the system was allowed to vibrate freely by using a release mechanism, item 6. The strain was recorded on strip chart recorder and using a calibration was converted to displacement. For the experiment a single ball with a mass, m, of 7.158×10^{-5} slug was selected. The equivalent viscous damping and natural frequency were determined using standard method of free decay and then equivalent mass and stiffness were calculated [11]. These were found to be

$$w_n = 83.57 \text{ rad/sec } (13.36 \text{ Hz}) \quad \xi = 0.0053$$

$$K = 1.8088 \text{ lbf/ft}, \quad M = 0.259 \times 10^{-1} \text{ slug}$$

The waveforms of free decay for various values of number of units, N, and equal gaps are given in Fig. 2. Comparison of Fig. 2(a) with the rest of the figures indicates that the effective damping seems to be the combination of inherent viscous damping, ξ, and damping due to impacts. From Fig. 2(b) - 2(f) it is seen that the decay of maximum displacement is not linear in time only initially when damping is predominantly due to impacts. Hence, this can be represented by a term, damping inclination, C, defined as [5]

$$C = \frac{X_1 - X_2}{t_2 - t_1} \qquad (1)$$

where t_1 and t_2 are times of maximum positive displacements X_1 and X_2 as shown in Fig. 2(c). The other important property of damper is the residual amplitude, b, defined as the amplitude at the time where extended linear portion cuts the time axis (See Fig. 2(c)). The residual amplitude, b, represents the amplitude of oscillation of the system at the point where impacts due to balls have very little effect on motion.

Figure 3 indicates that C increases linearly as N increases for all combinations of X_o and gap size. It should be noted that the gaps specified in these figures are equal. The variation of C with gap, shown in Fig. 4, indicates that there is an optimum gap size at which C is a maximum. The value of C increases with gap and reaches a maximum at a critical value of gap size; any increase beyond this critical gap size, C starts to decrease. The reason for this phenomenon is the fact that for small ratios of gap/X_o many impacts of small strength occur, hence energy loss is small; but as the gap increases to certain value (critical value), the number of impacts decrease but strength increases resulting in increased C. But for large ratios of gap/X_o, very few impacts occur and hence C remains small.

In Fig. 5(a),(b),(c) the variation of C with X_o for various gap sizes and N are presented. These figures indicate that for a given gap, C increases with X_o initially and then reaches a constant value. This particular behaviour of C, being independent of X_o for large values, is similar to a single unit damper [5-7].

The variation of residual amplitude, b, with X_o for various values of gaps and N, shown in Fig. 6, indicates that residual amplitude generally increases with gap and X_o.

From a designer's point of view, one would like to have a maximum C value and a minimum residual amplitude, b. Referring to Figs. 5(a) and 6(a) for a case when N = 3, it can be seen that at X_o = 0.1 in., Gap size = 0.25 gives the best result for both max. C and min. b. For X_o = 0.2, Gap size = 0.65 gives max. C. However, for minimum value of b, Gap size should be 0.25. For X_o = 0.6, Gap size = 0.75 should be selected for max. C and Gap size = 0.25 for min. C. From the results presented above, it is obvious that there must be a compromise in the selection of gap size for achieving max. C and min. b. To select the gap size an optimization method can be resorted to.

Another possible way to reach a compromise in the selection of the gap size is to arrange a multi-unit impact damper with different gap sizes. For example, in the case of N=9, the gap sizes could be selected between 0.25 in. to 0.75 in. in steps of 0.0625 in. Experiments were conducted with these different gap sizes and it was found that the value of C obtained was very close to the value of C for the case when an identical gap size equal to the average gap size was used. However, the residual amplitude was governed by the lowest gap size, i.e. 0.25 in. and produced a minimum value of b. Hence it can be concluded that a multi-unit damper with a variable gap size is a good compromise which will be superior in providing minimum b and an average value of C.

FORCED VIBRATION OF MULTI-UNIT IMPACT DAMPER

A schematic diagram of the experimental model and measuring equipment are shown in Fig. 7. The multi-unit impact damper discussed in the previous section was fixed to an electrodynamic shaker at the base. Sinusoidal acceleration at the base was produced using a feedback from the acceleration of the base using a control unit 6. The impact patterns were monitored measuring acceleration at the tip of the cantilever beam. The acceleration of the tip and strain at the base were monitored on a double beam oscilloscope.

Two of the typical records are shown in Fig. 8, where top and bottom trace represents tip displacement and acceleration (not to scale) respectively at two different excitation frequencies. Figure 8(a) is the steady state motion with nine secondary masses in action hitting one side of damper approximately within 1/6 of the cycle and then hitting the other side with no impacts in between. It is worth noting that time durations between these three consecutive sets are not identical. These two experimental observations differ significantly from the assumption used in Ref. 3 which states that impacts are evenly distributed in time. Motion shown in Fig. 8(b) is not exactly periodic, because from the experimental observation only six out of nine masses were in intense action while other three moved irregularly. Such motions are generally found when all masses are not in intense action.

The impact dampers are basically used to suppress resonant displacement amplitudes. The variation of displacement amplitude reduction, calculated as a ratio of maximum displacement with impact damper, X_{max}, to maximum displacement without it, A; and number of active units, Nu, is shown in Figs. 9 to 14 for three values of gaps of 0.24, 0.375, 0.5 and for rms base accelerations of 0.1g and 0.15g. Examinations of these figures indicates that the value of X_{max}/A is less than one for $r > 0.985$ and decreases with increasing number of units with a minimum at $r = 1$. Below $r = 0.985$, X_{max}/A is greater than one. This indicated that amplification occurring in this range are detrimental. The rate of increase of X_{max}/A is greater for $r < 1$ than for $r > 1$ and X_{max}/A increases beyond 1 as r decreases further and is near but not above 1 as r increases.

The variation of Nu indicates that for small gaps, large base acceleration and r near one , Nu approaches N. In the range of r between 0.94 to 1.04, Nu initially increases with r, then reaches N and remains constant for certain band width and any further increase in r results in decrease in Nu. This frequency bandwidth over which all units are in action widens with increase in excitation level but narrows with increase in N and gap size. In general for value $r < 1$, the active number of units are more than for $r > 1$.

CONCLUSIONS

In this paper an experimental investigation of controlling vibration using multi-unit impact dampers was presented. In case of free vibration, the damping inclination increased with number of units for all combinations of initial deflections and gap size. A good compromise may be achieved by properly selecting different gap sizes of a multi-unit damper. Damping inclination of such a unit approximately equals the sum total of damping inclinations of the individual units and the multi-unit damper produces a small residual amplitude. In case of forced vibration, damping effect increased with number of units when excitation frequency was equal to or above resonant frequency. Similar to a single-unit, even multi-unit damper could not eliminate the amplitude amplifications when forcing frequency was below the resonant frequency. In steady state motion, impacts occurred only over a fraction of a cycle.

REFERENCES

1. S.F. Masri, "Analytical and Experimental Studies of Multiple-Unit Impact Dampers", The Journal of the Acoustical Society of America, Vol. 45, pp. 1111-1117, 1969.

2. S.F. Masri, "Periodic Excitation of Multi-Unit Impact Dampers", Journal of the Engineering Mechanics Division, Proceedings of the American Society of Civil Engineers., Vol. 96, pp. 1195-1207, 1970.

3. C.Z. Cempel, "The Multi-Unit Impact Damper: Equivalent Continuous Force Approach", Journal of Sound and Vibration , Vol. 34, pp. 199-209, 1974.

4. C.Z. Cempel, "Receptance Model of the Multi-Unit Vibration Impact Neutralizer","MUVIN", Journal of Sound and Vibration , Vol. 40, pp. 249-266, 1975.

5. K. Yesuda and M. Tayoda, "The Damping Effect of an Impact Damper", Bulletin of the ASME, Vol. 21, pp. 424-430, 1978.

6. W.M. Mansour and D.R.T. Filho, "Impact Dampers with Coulomb Friction", Journal of Sound and Vibration , Vol. 33, pp. 247-265, 1974.

7. A. Ye. Kobrinsky, Mechanism with Elastic Couplings, Dynamics and Stability-NASA Technical Translation TTF-534.

8. N. Popplewell, C.N. Bapat and K. Mclachlan, "Stable Periodic Vibroimpacts of an Oscillator", to be published in Journal of Sound and Vibration, March 1983.

9. Y. Muzyka, "An Experimental Investigation of Multiple-Unit Impact Dampers", B.Sc. (Engineering) Thesis, Dept. of Mech. Engr., University of Manitoba, Winnipeg, 1981.

10. E. Skipur and L.J. Bain, "Applications of Impact-Damping to Rotary Priniting Equipment", Trans. of ASME, Journal of Mechanical Design, Vol. 102, pp. 338-343, April 1980.

11. C.N. Bapat, "A Study of Vibro-impact Systems", Ph.D. Thesis, University of Manitoba, Winnipeg, 1981.

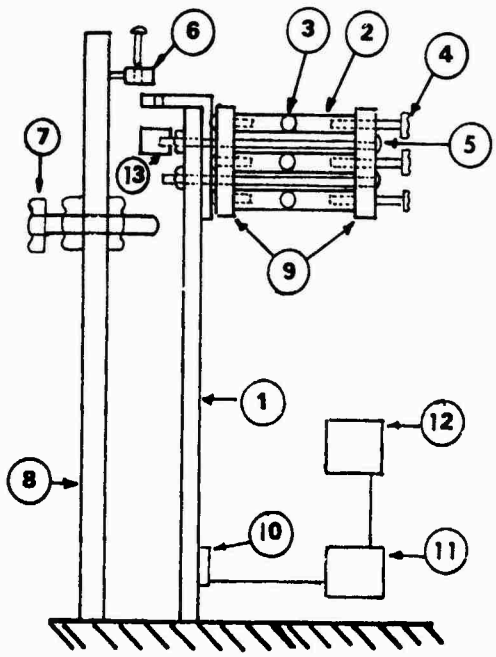

Figure 1. Details of the experimental apparatus and instrumentation.

Key:

1. Plate spring
2. Plastic tubes
3. Spherical balls (dia 0.25 in.)
4. Gap adjusting screws
5. Screws to fix damper
6. Release mechanism
7. Screw
8. Heavy beam
9. Side plates
10. Strain gauge
11. Strain indicator
12. Stripchart recorder
13. Accelerometer

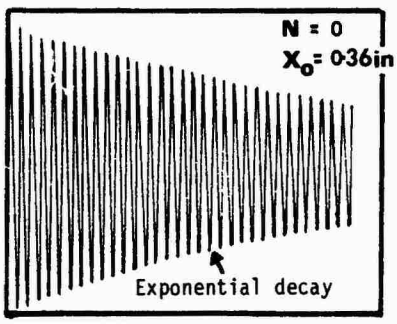

(a) Without any mass.

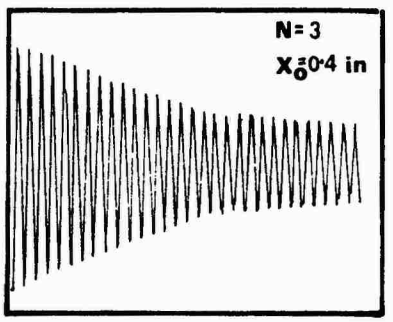

(b) Three masses. Gap = 0.55

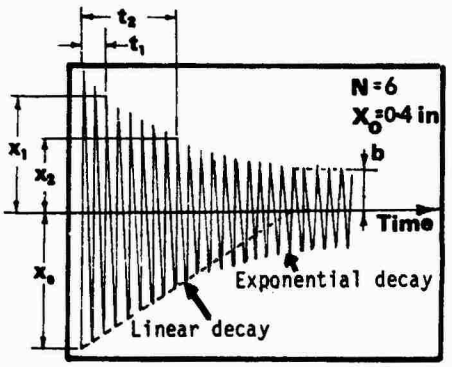

(c) Six masses. Gap = 0.55 in.

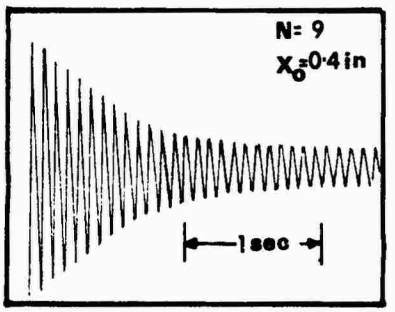

(d) Nine masses. Gap = 0.55 in.

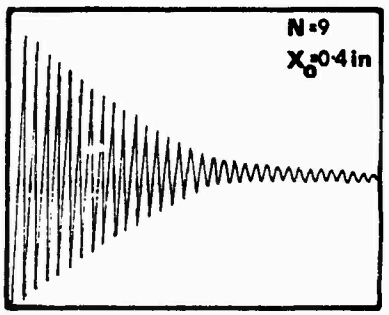

(e) Nine masses.
Gap = 0.25 to 0.75 in. in steps of 0.0625 in.

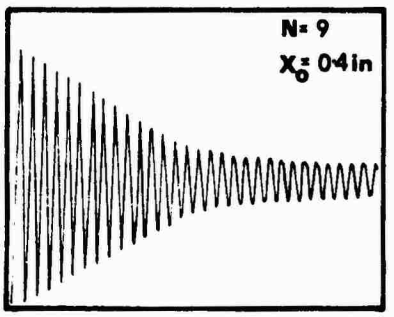

(f) Nine masses.
Gap = 0.5.

Figure 2. Waveforms of free decay of multi-unit impact-damper.

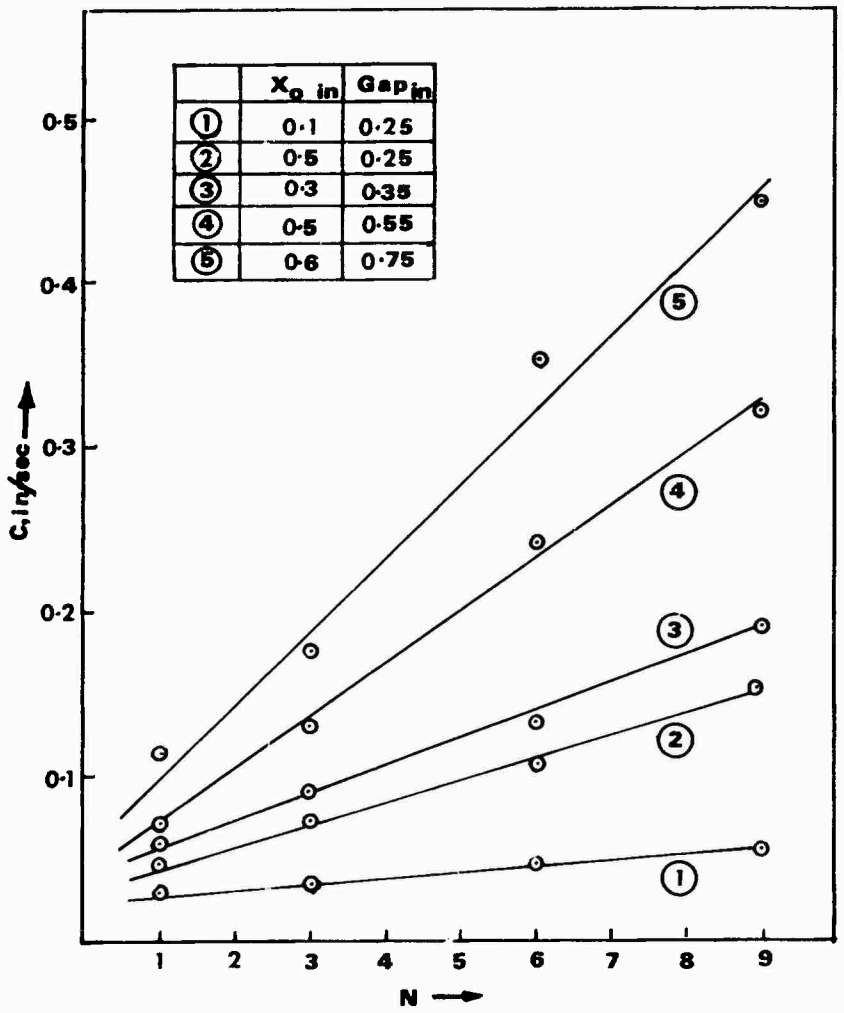

Figure 3. Variation of C with N.

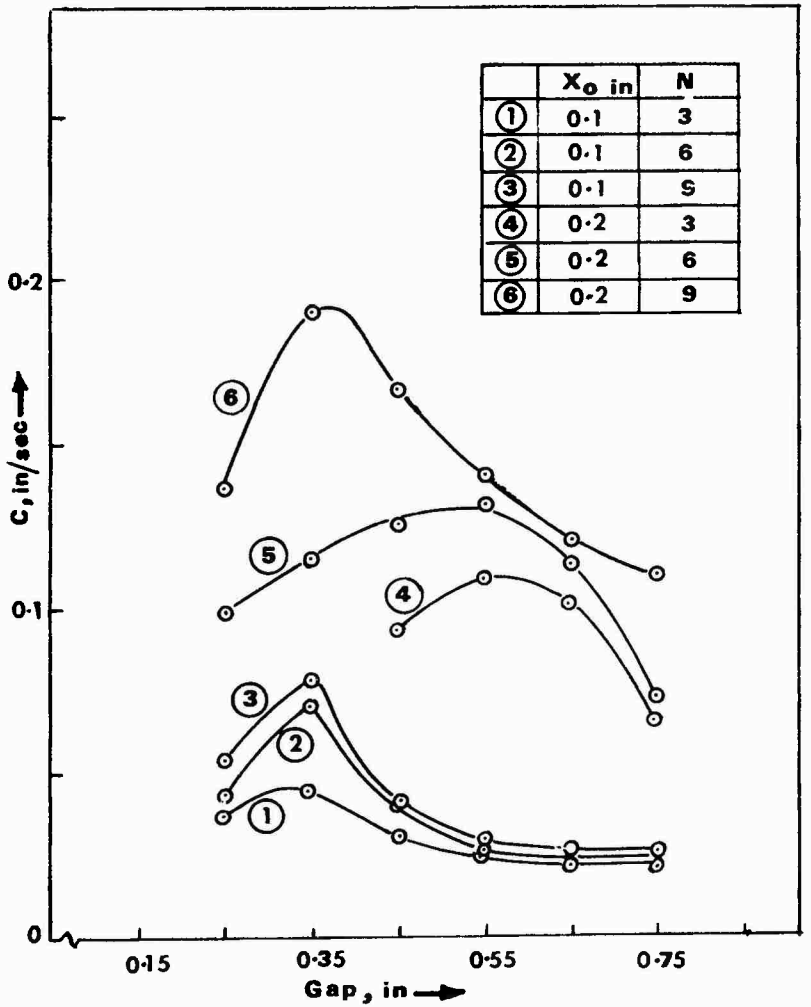

Figure 4. Variation of C with gap.

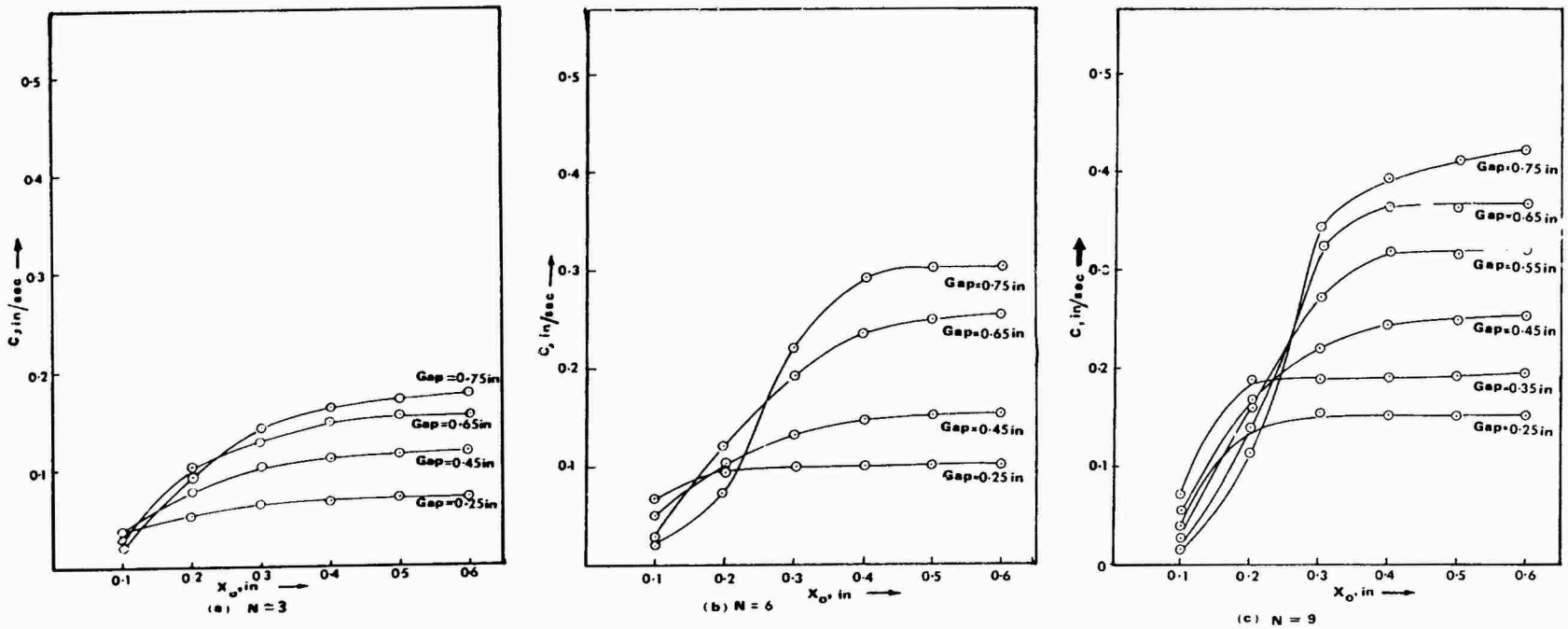

Figure 5. Variation of C with X_o.

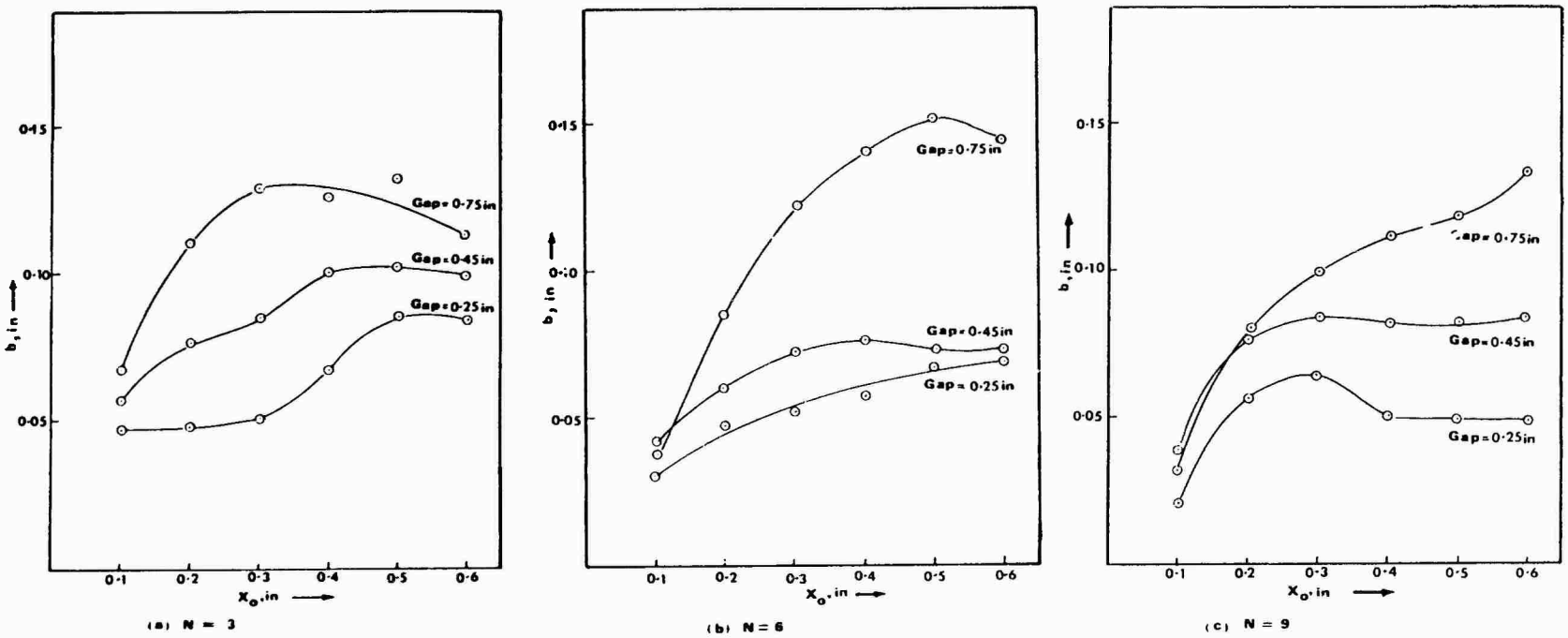

Figure 6. Variation of residual amplitude.

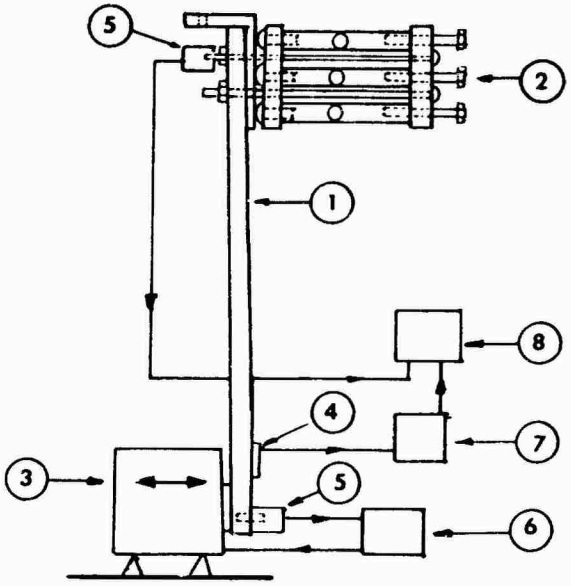

Figure 7. Experimental apparatus.

Key:

(1) Plate spring
(2) Multi-unit damper
(3) Shaker
(4) Strain gauge
(5) Accelerometer
(6) Control unit
(7) Strain indicator
(8) Double beam oscilloscope

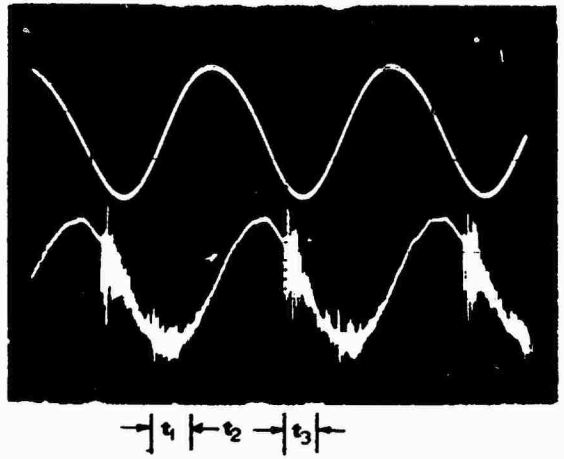

(a) Forcing frequency = 13.4 Hz.

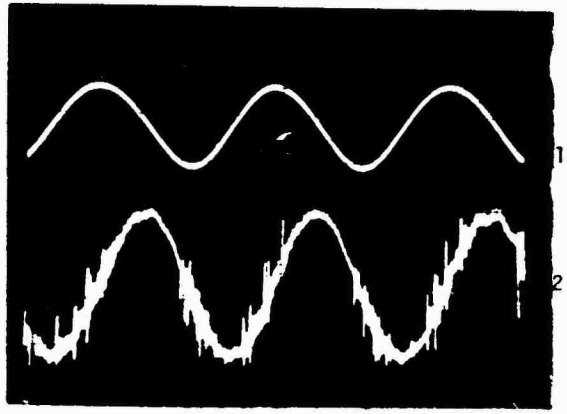

(b) Forcing frequency = 13.9 Hz.

Figure 8. Waveforms of forced motion with $\ddot{X}_b$=0.15 g (rms), N=9 and Gap = 0.25.

t_1 = duration in which impacts occur at one end.
t_2 = duration without impacts.
t_3 = duration in which impacts occur at other end.

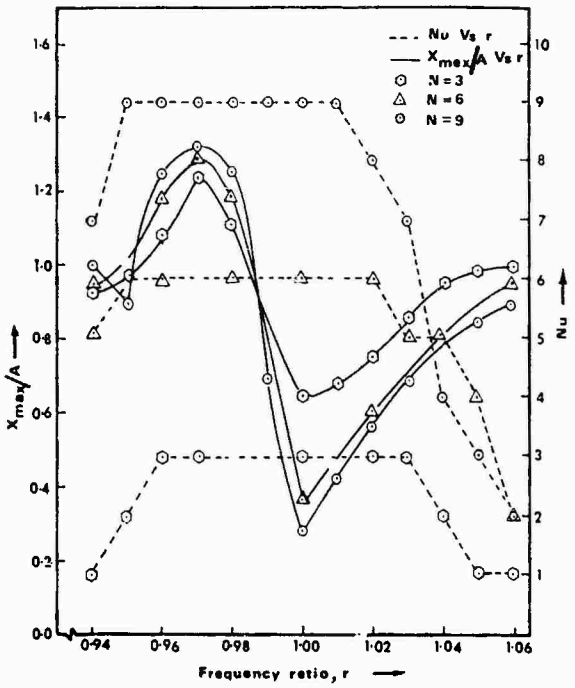

Figure 9. Variation of X_{max}/A and Nu with r
Gap = 0.25 in., $\ddot{X}_b$ = 0.1g (rms)

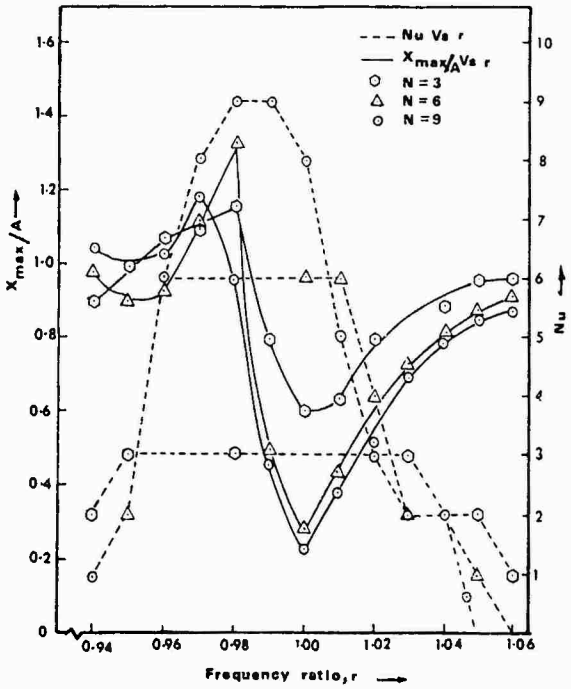

Figure 10. Variation of X_{max}/A and Nu with r
Gap = 0.375m, $\ddot{X}_b$ = 0.1g (rms)

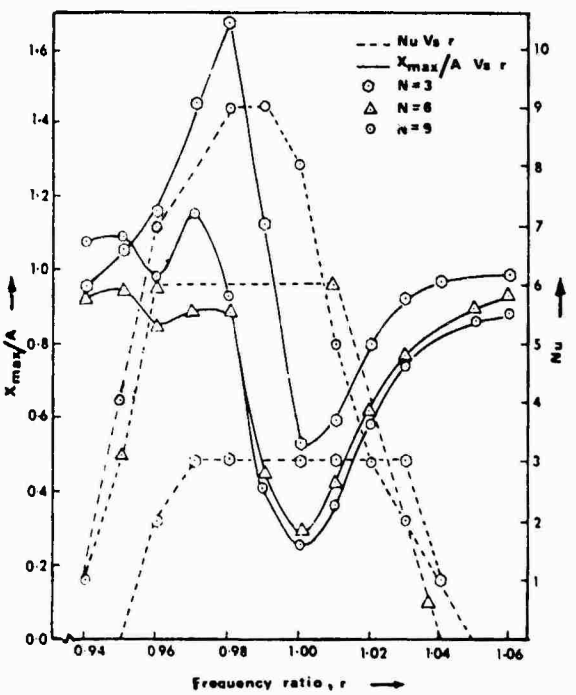

Figure 11. Variation of X_{max}/A and Nu with r.
Gap = 0.5 in, $\ddot{X}_b$ = 0.1g (rms)

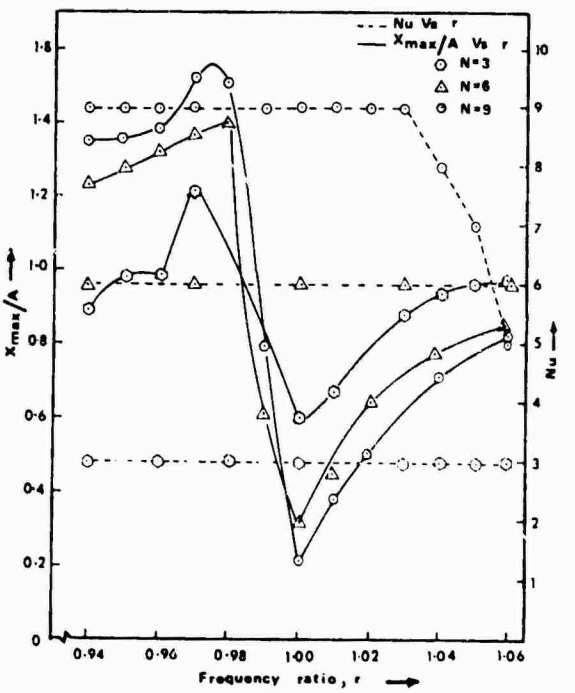

Figure 12. Variation of X_{max}/A and Nu with r.
Gap = 0.25, $\ddot{X}_b$ = 0.15g (rms)

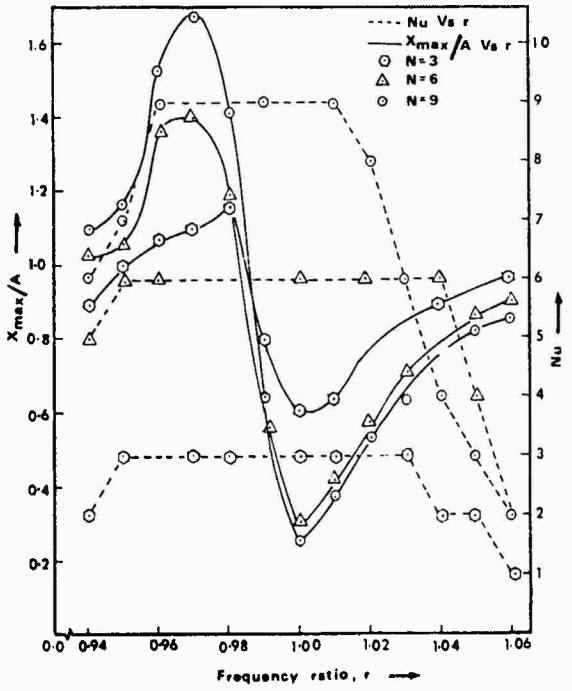

Figure 13. Variation of X_{max}/A and Nu with r.
Gap = 0.375 in., $\ddot{X}_b$ = 0.15g (rms)

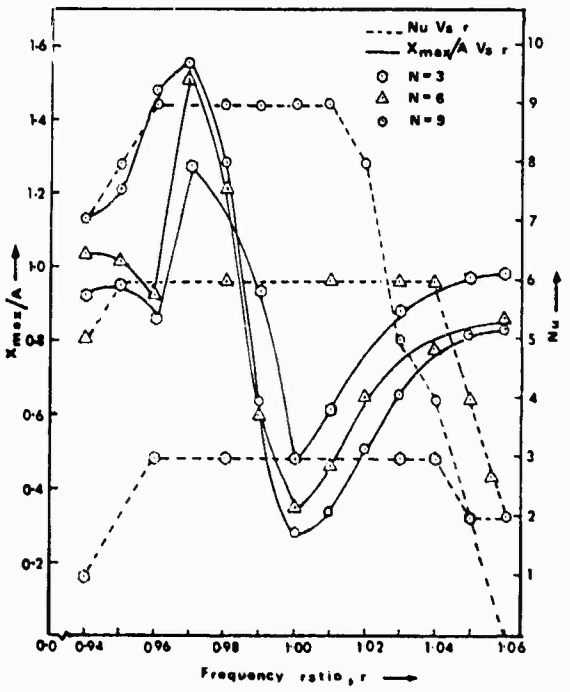

Figure 14. Variation of X_{max}/A and Nu with r.
Gap = 0.5 in., $\ddot{X}_b$ = 0.15g (rms)

DISCUSSION

Mr. Forward (Hughes Research Laboratory): I notice you have a model. Can we see it?

Dr. Bapat: Yes. I have here a plastic model, and it is like a child's rattle. When the system vibrates, we can see these balls moving to different sides. We use plastic so that we can monitor the actual motion of the balls. When they vibrate like this, we measure how many units move in that one direction. If they move in that direction, they will be moving like this. If they do not move in that direction, then they will be moving slowly.

Mr. Forward: What made you think of this? Did you really think it would be a damper?

Dr. Bapat: It is a damper. It is comparable to dynamic neutralizer.

Mr Nelson (Tufts University): Will it ever replace the Rubik's Cube?

Dr. Bapat: No.

AN EXPERIMENTAL HYBRID MODEL FOR A BILINEAR HYSTERETIC SYSTEM

K.R. McLachlan
Department of Civil Engineering

N. Popplewell, W.J. McAllister
Department of Mechanical Engineering
University of Manitoba, Winnipeg, Canada

and

C.S. Chang
Institute of Mechanics
Peking, People's Republic of China

An experimental model has been developed to simulate the non-linear behavior of a complex hysteretic system. Experimental data from the simplest form of this electro-mechanical model, the single degree-of-freedom system, is helpful in reconciling previously disparate theoretical results. It is believed that more general forms of such models will provide valuable physical insight into realistic situations.

INTRODUCTION

A bilinear hysteretic system is a simple but fairly general representation of practical structures like the piping in a nuclear power plant[1], stranded cable isolators[2], hysteretic dampers[3,4] and buildings with dry friction joints[5]. Nearly all publications pertaining to the dynamics of a bilinear hysteretic system are analytical or digital computer orientated[6-8]. The analysis has been limited primarily to a single degree-of-freedom system, excited sinusoidally. Yet the comparison in Fig. 1 of previous theoretical results indicates that an unexplained discrepancy occurs in the practically important region of the peak steady state displacement.

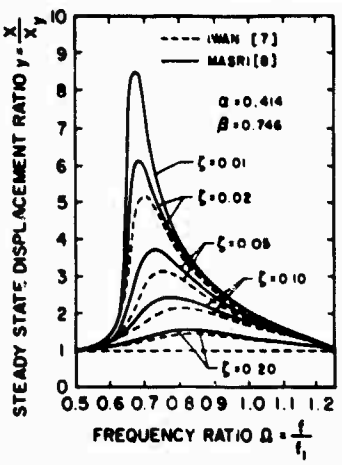

Fig. 1 - Previous theoretical results

Only a few analog computer experiments have been reported[6,7]. However, an electrical analog leaves doubt concerning the exactness of its similitude with the mechanical prototype, becomes quite complex to control if a model of more than one degree-of-freedom is required and gives less adequate insight into the physical relationships involved. It does permit, conversely, the generation of a more easily controlled, consistent and precisely known hysteresis loop. Therefore, a hybrid system in which a hysteretic restoring force is applied to a mechanical mass by electromechanical means is attractive. The hysteretic force could be provided by a current-carrying coil in a magnetic field. The magnets, when suitably supported, could form the discrete masses of the mechanical system. An appropriate first goal for such a hybrid model was felt to be the complementing and possible clarification of those theoretical results which yield the discrepancy shown in Fig. 1.

THE EXPERIMENTAL MODEL

There are a number of basic ideas which can be developed into a circuit. They range in complexity from real time digital computation to a simple analog circuit using biased diodes and a storage capacitor. The latter circuit was chosen to prove the validity of the hybrid model.

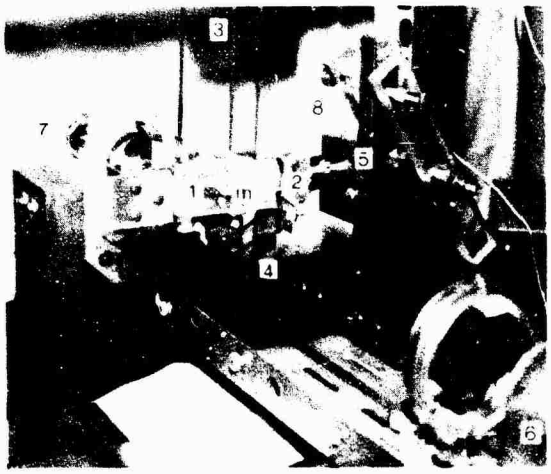

e) The hybrid model end photoelectric displecement trensducer

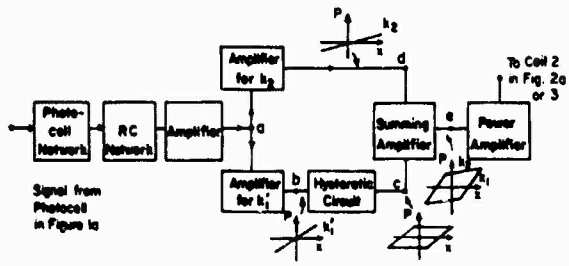

(b) Block diagram of circuit to generete hysteresis loop

Fig. 2 - The model end experimentel set-up

The hybrid model of e single degree-of-freedom system is shown in Fig. 2a. The mass is suspended virtually frictionless in eir by the three flexible end lineer ligaments of totel stiffness k_L in Fig. 3. These ligements, numbered 3 in Fig. 2e, ere errenged to reduce laterel swey of mass m. The hysteretic element consists of e current-cerrying coil, 2, fixed to e force gauge, 5, end e peir of rere-eerth magnets which eleo form pert of m. When m is excited by e sinusoidel force, F_I, its displecement will elter the width of slit 4 end, thereby change proportionately the intensity of light felling on photocell 6. The resulting signal from the photocell is amplified end processed by the circuit shown schematicelly in Fig. 2b. It should be noted thet the output of this circuit ceuses a current to flow in coil 2 which, depending on the processing chosen, may apply a restoring force to the mass. If the processing is linear and of non-zero transconductance, a force proportional to displacement, i.e. a spring, will be generated. If, however, the current in coil 2 is the result of processing in the bilinear hysteresis circuit, then the restoring force will be hysteretic. Obviously it is a simple matter to control the electrical circuits to give a wide range of yield points and to mix the linear and hysteretic signals to any extent required. A change in amplifier gains in the linear and hysteretic circuits of the system will alter the stiffness of the respective restoring forces. Typical input/output diagrams for a sinusoidal motion are shown in Fig. 2b.

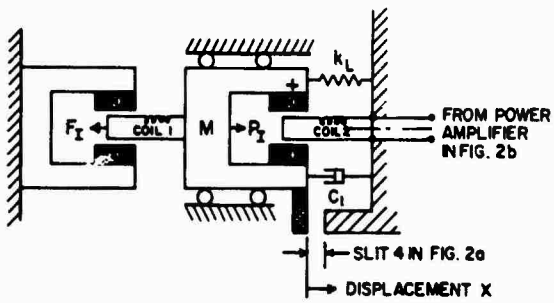

Fig. 3 - Schematic of hybrid model
+ N, S ere magnets

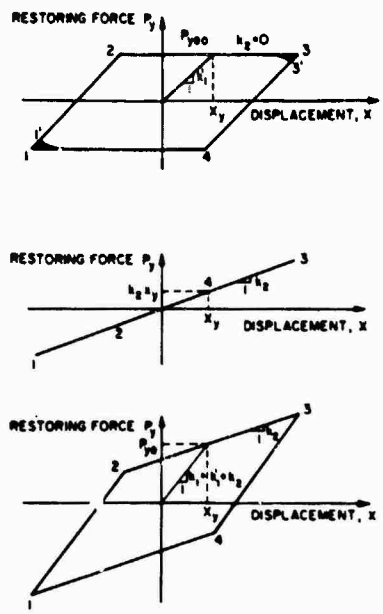

Fig. 4 - Formation of bilineer hysteresis loop

The simple circuit chosen has a number of limitations which must be recognized. Firstly, the lower limit of frequency is governed by the phase shift in the storage capacitor. Secondly, the real characteristics of the diodes result in imperfections in the shape of the bilinear hysteresis loop. These imperfections are caused primarily by (a) non-zero forward resistance and (b) a non-discrete "turn-on" voltage. The behavior of the circuit and the effects of non-discrete turn-on voltage for an assumed sinusoidal motion of mass m are shown in Fig. 4.

The ideal form for the hysteresis loop is illustrated in Fig. 4a (loop 1 2 3 4) while the actual hysteresis loop, due to the deficiency in the diode turn-on voltage, is indicated by loop 1' 2 3' 4. The yield load, P_{yeo}, in this figure depends upon the bias voltage applied to the diodes in the hysteresis circuit. The corresponding yield displacement, X_y, is given by

$$X_y = \frac{P_{yeo}}{k_1'} \qquad (1)$$

where k_1' is the analogous stiffness produced solely by the electrical signal at point c in Fig. 2b (i.e. when the signal from point d is set to zero). The signal at point d will provide an analogous stiffness k_2 as shown in Fig. 4b. When this signal is added to the hysteretic signal at the summing amplifier of Fig. 2b, a typical bilinear hysteresis loop is obtained as in Fig. 4c. The bilinear hysteretic signal is fed next to a power amplifier to generate a current in coil 2 of Fig. 3. As this coil is in a magnetic field, the current will induce, by Maxwell's principle, an electro-magnetic force, P_I, acting on m. The terminals of coil 2 are so connected to the power amplifier that P_I will always oppose the motion of the mass. Hence, a restoring force is produced which is analogous to a mechanical hysteretic spring. Details of the circuits corresponding to the block diagram of Fig. 2b are reported elsewhere[9,10].

Thus far, only the hysteretic effect has been discussed. The stiffness ratio, α_e, of the typical hysteretic loop shown in Fig. 4c is

$$\alpha_e = \frac{k_2}{k_1} \qquad (2)$$

where k_1 is the analogous stiffness produced by the resultant of the signals from point c and point d in Fig. 2b, i.e.

$$k_1 = k_1' + k_2 \qquad (3)$$

as shown in Fig. 4c. The yield load of this loop is given by

$$P_{ye} = P_{yeo} + k_2 X_y = \frac{P_{yeo}}{1 - \alpha_e} \quad . \qquad (4)$$

EQUATION OF MOTION

The forces acting on the mass of the hybrid model are shown in Fig. 3. The resulting equation of motion is

$$m\ddot{X} + C_1\dot{X} + k_L X + P_I = F_I \qquad (5)$$

where F_I or $B_1L_1I_1$ and P_I or $B_2L_2I_2$ are the instantaneous forces generated by the currents, I_1 and I_2, flowing in coil 1 of length L_1 and in coil 2 of length L_2 in a magnetic field of flux density B_1 and B_2, respectively. The currents I_1 and I_2 are given by[9],

$$I_1 = I_{1s} - \left(\frac{B_1L_1\dot{X}}{Z_{e1}}\right) \qquad (6)$$

$$I_2 = I_{2s} - \left(\frac{B_2L_2\dot{X}}{Z_{e2}}\right) \qquad (7)$$

where I_{1s} and I_{2s} are the currents in coil 1 and 2, respectively, with m blocked. The $B_1L_1\dot{X}$ and $B_2L_2\dot{X}$ are motion induced emfs and Z_{e1} and Z_{e2} are the total circuit impedances for coil 1 and 2, respectively.

Substituting equation (6) and (7) into equation (5) gives

$$m\ddot{X} + C_1\dot{X} + \frac{(B_1L_1)^2}{Z_{e1}}\dot{X} + \frac{(B_2L_2)^2}{Z_{e2}}\dot{X} + k_L X + B_2L_2I_{2s} = B_1L_1I_{1s} \qquad (8)$$

in which the terms

$$\frac{(B_1L_1)^2}{Z_{e1}}\dot{X} + \frac{(B_2L_2)^2}{Z_{e2}}\dot{X} \qquad (9)$$

are viscous damping forces[9,11]. The total damping coefficient, C, of the hybrid model, where

$$C = C_1 + \frac{(B_1L_1)^2}{Z_{e1}} + \frac{(B_2L_2)^2}{Z_{e2}}, \qquad (10)$$

was confirmed experimentally as viscous in nature by using a logarithmic decrement method. Eq. (8) can be written in a standard form for a bilinear hysteretic system as

$$\ddot{y} + 2\zeta\dot{y} + g(y) = \beta\cos\Omega t \qquad (11)$$

where $y = \frac{X}{X_y}$. $\qquad (12)$

The X_y is given by Eq. (1). Furthermore

$$\zeta = \frac{C}{C_c} = \frac{C}{2\sqrt{K_1 m}} \qquad (13)$$

and g(y) is the hysteretic restoring force described by a bilinear hysteresis loop of stiffness ratio $\alpha = \frac{K_2}{K_1}$ and a yield load P_y to be defined in the next section. Also,

$$\beta = \frac{\text{applied sinusoidal force}}{\text{yield load}} = \frac{B_1L_1I_{1s}}{P_y} \qquad (14)$$

and

$$\Omega = \frac{\omega}{\sqrt{(K_1/m)}} = \frac{f}{f_1} \qquad (15)$$

for $\omega = 2\pi f$ and $\sqrt{(K_1/m)} = \omega_1 = 2\pi f_1$. Eq. (11) was used to calculate the response of the hybrid model pertinent to Fig. 5.

DETERMINATION OF PARAMETERS α, β AND ζ FOR THE HYBRID MODEL

As can be seen from Fig. 3, the stiffness of the hybrid model is the resultant of the electromagnetic spring and the suspension ligaments. The stiffness ratio, α, of the model is ralated to the stiffness ratio, α_e, of the hysteretic element as follows

$$\alpha = \frac{K_2}{K_1} = \frac{k_2 + k_L}{k_1 + k_L} = \alpha_e \frac{\left(1 + \frac{k_L}{k_2}\right)}{\left(1 + \frac{k_L}{k_1}\right)} . \qquad (16)$$

Similarly, the yield load P_y of the hybrid model is the sum of the yield load of the hysteretic elament and $k_L X_y$ due to the ligaments, i.e.

$$P_y = P_{ya} + k_L X_y . \qquad (17)$$

By using Eqs. (1), (2) and (3), the yield load P_y can be expressed as

$$P_y = P_{yao} \frac{\left(1 + \frac{k_L}{k_1}\right)}{1 - \alpha_a} \qquad (18)$$

where P_{yao} can be measured from the loop shown in Fig. 4a. Then P_y and the force ratio, β, can be calculated straightforwardly. The remaining overall viscous damping ratio, ζ, may be determined by free-decay tests and the theoretical response curve can be then computed conventionally.

EXPERIMENTAL DETERMINATION OF THE RESPONSE OF THE HYBRID MODEL

The hybrid modal may be resonant at either the frequency equal to that of the applied force, F_I, or a rational fraction of the forcing frequency. These latter, sub-harmonic resonances[12] arise essentially from the stiffness non-linearity of the hysteretic system. When the hybrid modal is excited at its major resonant frequency, the amplitude of steady state response is controlled by the equivalent damping term[6] which depends on the area and shape of the hysteresis loop. Hence, the hysteresis loop reflects the system's capacity to reduce the large resonant vibration.

The clipping action of the diode circuit is not sharp but rounded as shown by point 3' in Fig. 2a instead of point 3 for the ideal case. Therefore, the area of the actual hysteresis loop will be smaller than the ideal one, by the shaded area in Fig. 2a. Hence less vibrational energy will be dissipated so that the experimental response curves should be slightly higher than the computed ones. Another extraneous effect is the lowering of the clipping voltage at small input signals to the hysteretic circuit. The clipping voltage had to be readjusted to the specified yield value to obtain the correct yield displacement, X_y. This shortcoming makes the experimental determination of the sub-harmonic resonances difficult because they are associated usually with small amplitudes. Consequently, a model is under development in which the diodes and storage capacitor will be replaced by a digital circuit.

The response curves of the present experimental model are in close agreement with those computed by using Iwan's method. Typical curves are plotted in Fig. 5. Peak values of the experimental curve have been checked separately six times, the scatter of this data, or scatterband in Fig. 5, is within ± 1.5% of the average value. It was found from the computations that a 2% decrease in P_y, analogous to that produced by diode deficiencies, would increase the peak displacement by about 7%. This resulting increase, of course, would produce an even better correlation with experiment than that shown in Fig. 5.

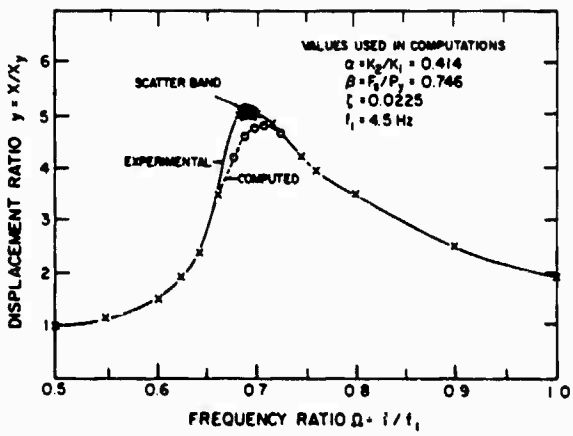

Fig. 5 - Experimental and computed responses

The agreement between Iwan's predictions and experimental data led to a re-examination of Ref.[8]. It was found that Masri[8] had inadvertently used a lower viscous damping coefficient than Iwan for the K_2 region of the bilinear hysteresis loop[9]. Based on identical damping coefficients for the K_1 and K_2 regions, the conditions of continuity of displacement, velocity and acceleration corresponding to each corner of the hysteresis loop should constrain the choice of ζ_2 in Ref.[8] to [9]

$$\zeta_2 = \sqrt{\frac{K_1}{K_2}} \; \zeta_1 . \qquad (19)$$

A lower value of ζ_2 than that required to satisfy Eq. (19) would increase, of course, Iwan's peak displacements to values given by Masri.

CONCLUSIONS

The principle of an experimental hybrid model haa been validated. The model has been helpful in reconciling a significant discrepancy in previously published results. Expansions are envisaged to aid, for example, in the design of optimal hysteretic attenuators to reduce the transmission of seismic induced vibrations from building to mechanical components.

REFERENCES

1. Stott, S.J. and Masri, S.F. Dynamic Excitation of A Single Degree of Freedom System, Rept. CE 78-09, University Southern California, May, 1978.
2. Aeroflex Laboratories Inc., Helicals Ride the Space Shuttle, Isolation News Vol. 7, No. 1, 1977.
3. Chang, C.S. and Tian, Q. An Experimental Study of the Non-Linear Behaviour of A Stranded Cable and Dry Friction Damper, The Shock & Vibration Bulletin No. 52, Part 4, pp. 155-160, May, 1982.
4. Skinner, R.I., Kelly, J.M. and Heine, A.J. Hysteretic Dampers for Earthquake-Resistant Structures, Earthquake Engineering & Structural Dynamics, Vol. 3, pp. 287-296, 1975.
5. Pall, A.V., Marah, C. and Fazio, P. Friction Joints for Seismic Control of Large Panel Structures, J. Prestressed Concrete Institute, Nov./Dec., pp. 38-61, 1980.
6. Caughey, T.K. Sinusoidal Excitation of A System with Bilinear Hysteresis, J. App. Mechanics, Vol. 27, pp. 640-643, 1960.
7. Iwan, W.D. The Dynamic Response of Bilinear Hysteretic Systems, Ph.D. Thesis, Earthquake Eng. Lab., California Inst. of Tech. 1961.
8. Masri, S.F. Forced Vibration of the Damped Bilinear Hysteretic Oscillation, J. Acoust. Soc. Am., Vol. 57, pp. 106-112, 1975.
9. Chang, C.S. An Experimental Hybrid Model for a Bilinear Hysteretic System, Rept. of Dept. of Mech. Eng., University of Manitoba, 1982.
10. Ma, P. Power Methods of Investigating Bilinear Hysteresis, Ph.D. Thesis, Dept. of Civil Eng., University of Manitoba, 1980.
11. Ma, P., McLachlan, K.R. and Shah, A. On the Provision of Viscous Damping in Structural Models, Proc. Canadian Soc. for Civil Engineering, Paper No. S/37.5, 1980.
12. Caughey, T.K. The Existence and Stability of Ultraharmonics and Subharmonics in Forced Non-Linear Oscillations, J. Applied Mechanics Vol. 21, pp. 327-335, 1954.

ACKNOWLEDGEMENTS

The financial support from the Manitoba Development Grant and the Natural Sciences and Engineering Research Council of Canada is acknowledged gratefully.

NOMENCLATURE FOR FIG. 2a

(1) Coil 1 for exciting force (only its edge can be seen). (2) Coil 2 for hysteretic element. (3) Three flexible ligaments for suspending mass m. They are also used as leads for coil 1. (4) Slit for the passage of light for the photoelectric displacement transducer. (5) Force gauge. (6) Photocell. (7) Light source. (8) Leads for coil 2.

MEASUREMENT AND ANALYSIS OF PLATFORM DAMPING IN ADVANCED TURBINE BLADE RESPONSE

Capt. Thomas J. Lagnese and Dr. D.I.G. Jones
Air Force Wright Aeronautical Laboratories
AFWAL/MLLN, Wright Patterson AFB, Ohio 45433

(U) The measurement of dry friction damping is experimentally investigated by means of a digital signal data processing technique. The experimental technique identifies narrow frequency bandwidth linearity of the non-linear response of a single turbine blade with dry friction damping. The non-linear response data is compared with analytical results for a two-degree of freedom model of the blade.

1. INTRODUCTION

In recent years the design of fan, compressor and turbine blades in jet engines have reached new levels of sophistication. It is no longer the exception to find engine manufacturers using turbine blades made of directionally solidified high strength nickel alloys, designed with a hollow core, or utilizing complex series of cooling patterns. The complexity of these new-generation blade geometries does not allow much variation in design without compromising advanced air flow characteristics. As a consequence, when resonant fatigue of blades becomes a problem, engineers are often faced with difficult and costly redesign. One alternative to redesign is to incorporate damping into the blade and/or disk system by friction and/or additive damping. With the implementation of damping into engine systems it becomes necessary to understand the non-linear phenomena involved from a fundamental point of view. This paper presents the results of an experimental investigation of the non-linear response of a broached blade specimen subjected to frictional damping. The experimental approach includes the measurement of the response of the component, in the form of a series of point to point receptances, with the data being acquired and processed using a digital signal spectrum analyzer. The experimental program involved the initial determination of the modal response of the undamped component and then measurement of the effect of gradually increasing frictional loads applied by means of a loading rod thrust against the platform of the blade. The effect of the increased frictional load was measured for several modes in terms of point to point receptances. The data, acquired through impact testing, was processed by Zoom Fourier analysis, which allowed for processing of the test data over narrow frequency bandwidths.

2. ANALYSIS

2.1 Discrete Model of Blade

The analytical direction taken in this paper addresses a need to accurately describe the non-linear phenomena associated with dry-friction damping using a simple, straight forward, model and yet maintain a capability to apply this technique to a wide variety of more complex structures. The approach taken was to use a mechanical receptance representation of the measured single blade response, with no external damping loads, and identify the dynamic characteristics of interest, particularly the modal damping and modal mass. The method involved measuring the blade structural response at several points of interest including the tip of the airfoil and the edge of the platform, as shown in figure 1. This information was then used to identify the corresponding discrete elements needed for defining the blade's receptance.

The turbine blade test specimen was represented as a discrete model having two degrees of freedom as in Figure I. An obvious advantage of the discrete model is the ease with which a continuous system can be described by a small number of mass and stiffness elements which represent identifiable terms in an ordinary second order differential equation. It is accepted that, since the frictionally-damped blade system has non-linear response characteristics, great care must be taken to accurately reproduce the experimental receptance data for the first two modes.

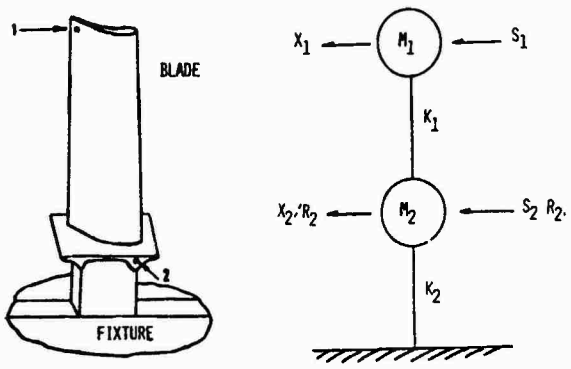

Figure 1 Turbine blade and corresponding discrete model with measurement points 1 and 2 indicated.

The damped two degree of freedom system response behavior allows one to look at the resonant frequency distribution of the model, identify the appropriate mass and stiffness elements, and give some indication of how well the model simulates the continuous nature of the broached blade specimen. The equations of motion which describe the displacement at points 1 and 2 include a parameter R_2 which is identified as a modal correction coefficient. The coefficient is a necessary part of the discrete model and corrects for the continuous nature of the specimen. Parametrically, R_2 controls the absolute amplitude of the point receptance at location 2, and the transfer receptances between locations 1 and 2. The equations of motion for the discrete model are:

$$m_1 \ddot{X}_1 + k_1 (X_1 - X_2/R_2) = S_1 e^{i\omega t} \quad (1)$$

$$m_2 \ddot{X}_2/R_2 + k_1 (X_2/R_2 - X_1) + k_2 X_2/R_2 = S_2 R_2 e^{i\omega t} \quad (2)$$

These equations can be solved for the steady-state response with S_1 and S_2 having harmonic time dependence, to give displacements at points 1 and 2:

$$X_1 = [S_1(k_1 + k_2 - m_2\omega^2) + S_2 R_2 k_1] / \Delta \quad (3)$$

$$X_2 = [S_2 R_2^2(k_1 - m_1\omega^2) + k_1 R_2 S_1] / \Delta \quad (4)$$

where

$$\Delta = (k_1 - m_1\omega^2)(k_1 + k_2 - m_2\omega^2) - (k_1)^2 \quad (5)$$

The solutions, X_1 and X_2, can be used to determine the system receptances:

$$\alpha_{11} = \partial X_1/\partial S_1 = (k_1 + k_2 - m_2\omega^2)/\Delta \quad (6)$$

$$\alpha_{12} = \partial X_2/\partial S_1 = \partial X_1/\partial S_2 = k_1 R_2/\Delta \quad (7)$$

$$\alpha_{22} = \partial X_2/\partial S_2 = (k_1 - m_1\omega^2) R_2^2 /\Delta \quad (8)$$

Once the receptances have been defined in terms of the elements of the discrete, lumped mass, model it is then necessary to numerically identify the elements to replicate experimentally observed receptances.

Evaluation of the experimental data (in Section 3) yielded the following discrete element values.

$m_1 = 1.7\text{x}10^{-2}$ kg

$f_1 = 840$ Hz

$k_1 = 6.5\text{x}10^{5}$ N/M

$m_2 = 3.0\text{x}10^{-2}$ kg

$f_2 = 1500$ Hz

$R_2 = .35$

$k_2 = 2.0\text{x}10^{6}$ N/M

As will be seen in Section 3, the identified receptances reproduce the experimental data quite well, with system resonances being analytically determined to within 7% of actual values. A drawback of this simple analysis is that the hysteretic damping which is present in each mode of the blade has not been accounted for in the lumped mass model by fixed values of η_1 and η_2 in this particular paper. Consequently, the peak amplitudes exactly at resonance are not precisely duplicated, but the amplitudes of off-resonant frequencies are modeled quite well for all receptance calculations. The behavior of α_{22} indicates the necessity of the modal correction coefficient R_2 being chosen carefully.

2.2 Discrete Model of Blade With Coulomb Friction

The equations of motion for the discrete model can be re-written in terms of the derived receptances. For exciting forces S_1 and S_2 at points 1 and 2; we have:

$$X_1 = S_1 \alpha_{11} + S_2 \alpha_{12} \quad (9)$$

$$X_2 = S_2 \alpha_{22} + S_1 \alpha_{21} \quad (10)$$

Using this model to incorporate a dry friction joint at point 2, and then linking this joint to ground, the equations of motion become,

$$X_1 = S_1 \alpha_{11} + \mu N \, Sgn(\dot{X}_2) \alpha_{12} \quad (11)$$

$$X_2 = \mu N \, Sgn(\dot{X}_2) \alpha_{21} + S_2 \alpha_{22} \quad (12)$$

Here, the term $N\mu Sgn\dot{X}_2$ defines a Coulomb model for the frictional force applied at the blade platform, N is the force normal to the platform, and μ represents the coefficient of friction between the blade platform and the damping rod. The linear summing of receptances allows the inclusion of the nonlinear term $\mu NSgn\dot{X}_2$ since this nonlinearity is external to the blade system. These equations of motion are solved assuming a steady state harmonic response of the form:

$$S_1 = S_{11} Cos\,\omega t + S_{12} Sin\omega t \quad (13)$$

and with X_1 and X_2 being presented in the form,

$$X_1 = A_1 Cos\omega t + A_2 Sin\omega t = A Cos(\omega t + \gamma) \quad (14)$$

$$X_2 = B Cos\,\omega t \quad (15)$$

For purposes of quasi-linearizing the equations of motion, $Sgn\,\dot{X}_2 = Sgn[-\omega B]Sin(\omega t)$ is expanded as a Fourier Series, and only the first term is retained for a first order analysis.

$$Sgn\,\dot{X}_2 = -Sgn(\omega B)Sin\omega t = -\frac{4}{\pi}Sgn(B)Sin\omega t \quad (16)$$

Upon substitution into the equations of motion one gets:

$$A_1 Cos\omega t + A_2 Sin\omega t = \alpha_{11}(S_{11} Cos\omega t + (S_{12} Sin\omega t) \quad (17)$$

$$B Cos\omega t = (S_{11} Cos\omega t + S_{12} Sin\omega t)\alpha_{21}$$

$$-[(4/\pi)\mu N \, Sgn(B) \, Sin\omega t]\alpha_{22} \quad (18)$$

The harmonic balance method gives solutions for A_1, A_2, and B, of the form:

$$A_1 = \alpha_{11} S_{11} \quad (19)$$

$$A_2 = \alpha_{11} S_{12} - (4\omega N/\pi)Sgn(B)\alpha_{12} \quad (20)$$

$$B = S_{11} \alpha_{21} \quad (21)$$

$$S_{12}\alpha_{21} = (4\mu N/\pi) \, Sgn\,(B)\alpha_{22} \quad (22)$$

$$S_1 = S_{11} Cos\omega t + (4\mu N/\pi)Sgn(B)(\alpha_{22}/\alpha_{21})Sin\omega t \quad (23)$$

$$S_{11} = S_1^2 - (4\mu N/\pi)^2(\alpha_{22}/\alpha_{21})^2 \quad (24)$$

and

$$B = \alpha_{21}\sqrt{S_1^2 - (4\mu N/\pi)^2(\alpha_{22}/\alpha_{21})^2} \quad (25)$$

$$X_1 = \alpha_{11} S_{11} Cos\omega t + \frac{4\mu}{\pi} NSgn(B)(\alpha_{22}/\alpha_{21} - \alpha_{21}) \, Sin\omega t \quad (26)$$

substitution into the equation of motion for X_1 yields:

$$A^2 = \alpha_{11}^2 S_{11}^2 + (4\mu N/\pi)^2[(\alpha_{11}\alpha_{22} - \alpha_{12}\alpha_{21})/\alpha_{21}]^2 \quad (27)$$

$$A = \sqrt{\alpha_{11}^2 \, S_{11}^2 - (4\mu N/\pi)^2 \, [2\alpha_{11}\alpha_{22} - \alpha_{12})/\alpha_{12}]^2} \quad (28)$$

With A and B now known, the solution is complete. Note that B will be real and exist only when:

$$|S_1| > (4\mu N/\pi)\alpha_{22}/\alpha_{21} \quad (29)$$

This means that for a given value of N, motion of mass m_2 will take place only over a limited frequency range. Figure 2 shows the variation of A and B with frequency for various values of the friction parameter

$$\beta = \frac{4\mu N}{\pi S} \quad (30)$$

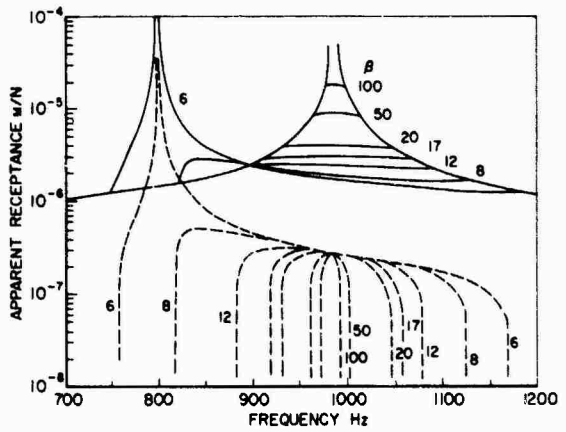

Figure 2 Predicted response of points 1 and 2 for frictionally damped system.

It is seen that, for large values of β, B exists only in a narrow frequency band around the resonance frequency, and that this band grows broader as β is reduced. The comparison

between these analytical results and the measured response will be discussed in section 3.

3. Experimental Investigations

3.1 Test System

The specimen chosen for this series of tests was a turbine blade made of a high temperature, high strength, nickel base alloy, and having design characteristics typical of the sophisticated blade geometries presently used in aircraft turbine engines. The blade was of hollow core construction to allow for cooling, and was structurally reinforced with an internal series of rod elements which give flexural stiffness. This turbine blade had no shroud, but did have a platform upon which the normal frictional load was applied for the tests, since this was the usual area for a frictional damping device to be applied in an operational environment. The root geometry of the turbine blade was a modified dovetail which was dynamically complex because the interface conditions between the dovetail and the broach block significantly affected blade response characteristics as a result of even slight changes in orientation. Consequently, after the blade was positioned in the broached fixture, it was fixed into place by a set screw which compressed the dovetail against the broaching block to keep orientation effects unchanged throughout the tests. The broached blade was attached to a massive clamping fixture which applied a constant pressure on both sides of the broach blocks by means of several high-strength bolts torqued to a fixed load. Once the blade was completely placed in the experimental fixture, the entire setup was placed on rubber pads which isolated the fixture from the surroundings. As illustrated in Figure 3.

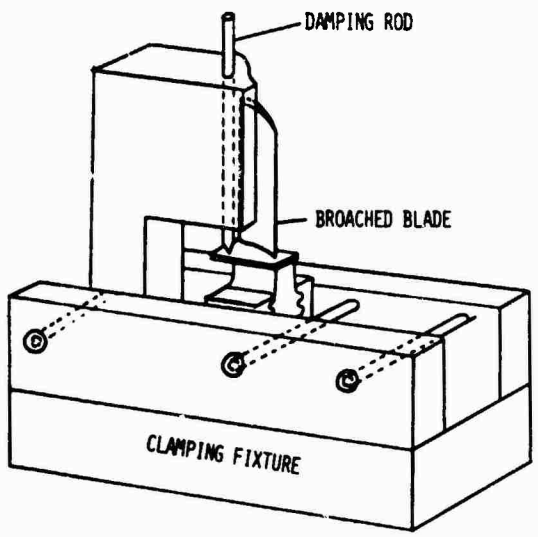

Figure 3 Sketch of turbine blade in experimental fixture.

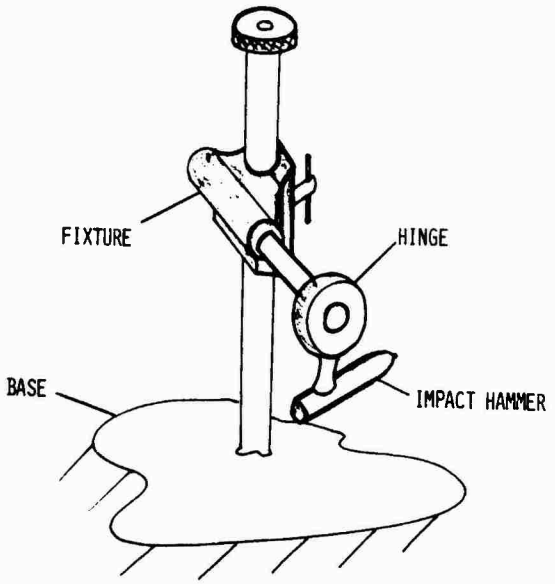

Figure 4 Sketch of impact hammer-pendulum.

The friction load on the blade platform was applied by means of a loading rod. Normal loads were applied by adding weights to a platform on top of the loading rod. Once a selected normal load was positioned a set screw was tighted to lock the rod in place and eliminate the possibility of the rod vibrating through the guide and hence disturbing the blade response.

The excitation to the blade system was provided by a miniature impact hammer. However, to gain more control of the input force and to obtain a constant force input throughout the test series, the impact hammer was modified as an impact pendulum as illustrated in Figure 4. Another major advantage of the impact pendulum design was the control which the operator had on impact location. The ability to control the impact is very important for effective mobility analysis of small complex structures. The response of the blade was measured by an Endevco type 22 miniature accelerometer which had very little mass loading effect on the blade response. The force gage impact pendulum and the accelerometer were calibrated as a system. The transfer function calibration was accomplished by attaching the accelerometer to a known mass and impacting this mass, the resulting "calibration transfer function" is then multiplied by the numerical value of the mass. The calibration transfer function, when divided into the measured transfer functions yields the actual frequency response of the structure.

A Hewlett Packard digital signal analyzer (5451 C) and HP 2100 computer were used to acquire and process the response data. Some

understanding of the Fourier analyzer algorithm is necessary so that non-linear phenomena can be identified and measured correctly. Simply stated, the Fast Fourier Transform is an algorithm which transforms response from the time domain to the frequency domain. The algorithm takes a data record in the time domain, which is digitized, and then transforms this data block into data corresponding to a discrete array of frequency lines. Using this block processing capability of the digital signal analyzer and applying it to data within very narrow frequency bands (Zoom Fourier Transform), one can investigate the nonlinear response associated with friction damping. A wide frequency band analysis is accomplished by analyzing the response on a narrow band basis, and then repeating the process as needed to cover the entire frequency range of interest. Typical resolution was a few hundredths of a percent of each mode center frequency, which allowed for very accurate determination of peak response and definition of mass and stiffness characteristics of the blade system.

3.2 Modal Analysis

The first tests were conducted on the undamped blade in order to obtain the basic receptance functions, the modal shapes and the natural frequencies. The tests were conducted by the impact technique, using the impact pendulum. The blade was impacted at a single point, and the response was measured at a large number of locations using a small accelerometer (Endeuco 22), moving it to each test location in sequence, according to the coverage illustrated in Figure 5. A typical plot of accelerance (acceleration/force) versus frequency is shown in Figure 6. From these plots, the mode shape and resonant frequencies were determined. Figure 7 identifies typical deformed mode shapes shown superimposed on the undeformed blade geometry for the four measured blade resonances. The discrete model was initially developed to simulate the undamped blade response. Further improvements to this model incorporated the proper values of the modal correction coefficient R_2 and normalized friction damping parameter to correctly simulate the blades resonant response to frictionally damped conditions (Figure 8) and undamped conditions (Figure 6). Figure 9 shows a comparison between response of the established discrete model and the candidate blade response using the indicated values of the discrete model parameters.

3.3 Measurement on Frictionally Damped Blade

Figure 4 shows the test configuration used to apply the frictional load to the platform. For various loads on the platform, the blade was impacted and the response measured at points 1 and 2 using the Zoom Fourier Transform with a center frequency of 860 Hz and a measured bandwidth of 128 Hz, with all 512 data points concentrated within this interval. Other frequency ranges were to be studied, but are not included in the report.

Figure 10 shows some typical plots of the apparent receptance (displacement/force) over the frequency range 850 to 950 Hz for the blade with 1.2, 1.59, 2.23 and 5.65 Kg load on the platform damper, for response points 1 and 2.

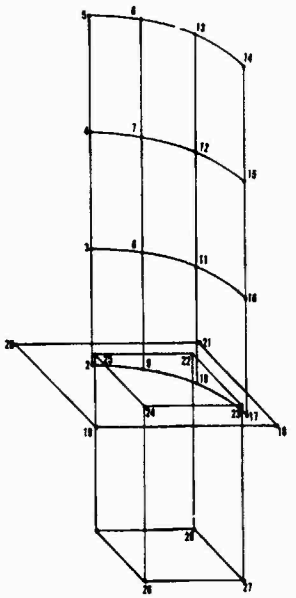

Figure 5 Modal blade geometry.

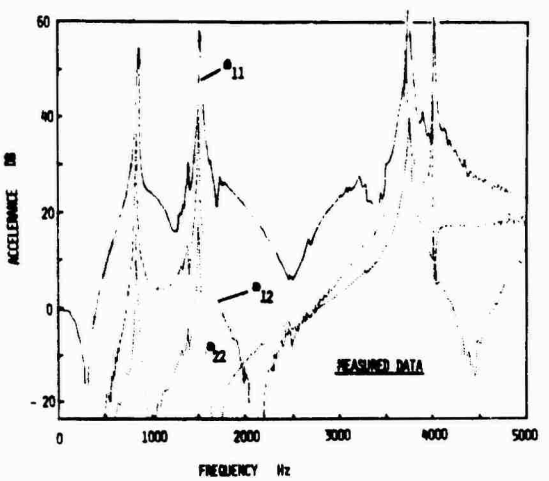

Figure 6 Experimental measured receptances for the undamped blade.

The data sets in Figure 10 are of first mode response at both tip and platform for three similar friction loading conditions. In both series of tests the amplitude of input force wasthe same, with amplifiers, signal

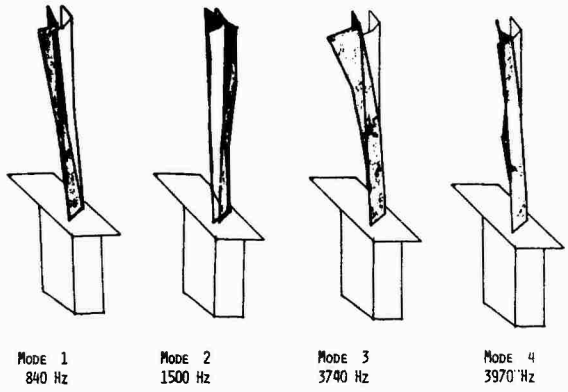

Figure 7 Typical modal deformation for the undamped blade.

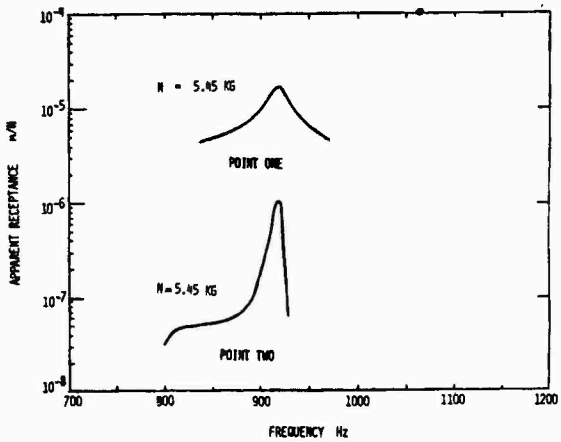

Figure 8 Experimentally measured receptance for frictionally damped blade.

conditioners and equipment unchanged, at all loading conditions. It is seen that for a loading of 1.2 Kg peak response at the platform occurs at a frequency of 890Hz, whereas peak tip response under identical loading occurs at a frequency of 910Hz. The 2% difference in frequencies is typical of the lower normal loading ranges, possibly indicating a control problem in normal loading of the blade specimen or a range of normal loading values where the response characteristics of the blade are most sensitive. For a load of 5.45Kg the effect of loading on response behavior is not as sensitive and peak amplitudes in both cases occur at frequencies within .2% of 920Hz. The tests at 18.8 kg normal loading tests were practically identical to the 5.45 kg test except for a slight increase in response amplitude, indicating that over the entire range of frictional loads tested no greater change in receptance was evident. Graphically, a plot of receptance ratio (i.e., the damped response divided by the undamped response) versus normal load, Figure 11, indicates that throughout the range of normal loads considered experimentally no significant change of peak receptance frequency of peak amplitude should be expected.

The plot of receptance ratio versus normal load indicates that even though a small change in the normal load should correspond to a small change in the peak receptance amplitude and frequency, any change in friction coefficient, impact force, normal loading eccentricity etc., could easily mask any effects which small incremental loading would have on non-linear structural response. This occurence was particularly evident for lower values of normal

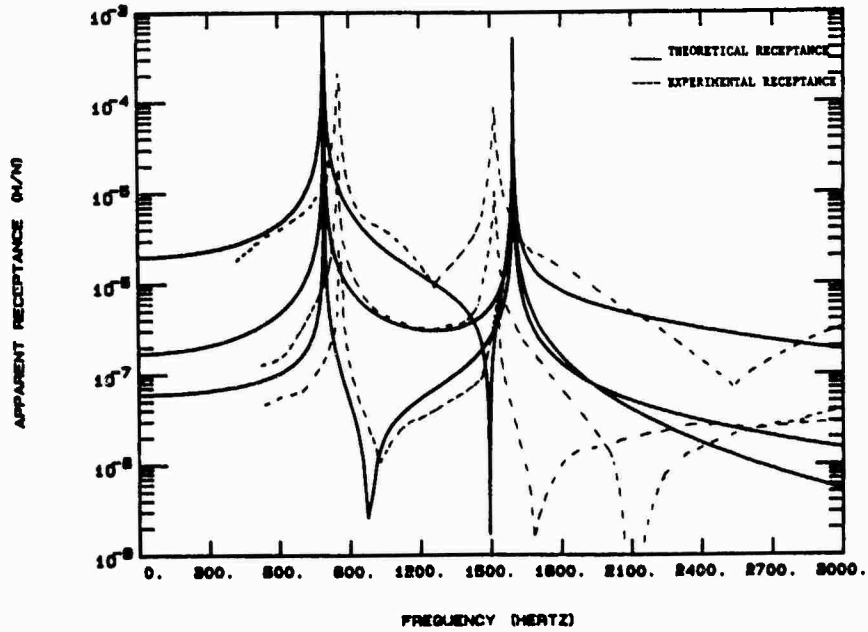

Figure 9 Comparison of experimental and analytically derived receptances for undamped blade

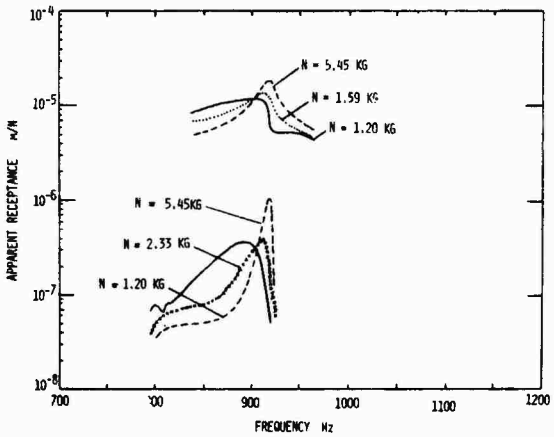

Figure 10 Comparison of experimental receptances at Point 1 (tip) and Point 2 (platform) for normal loads of 1.202 Kg, 1.59 Kg, 2.33 Kg and 5.45 Kg.

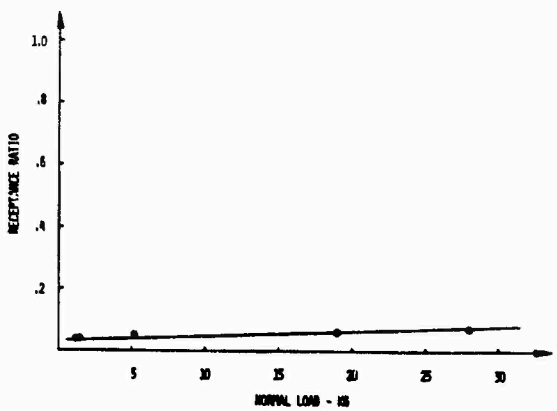

Figure 11 Effects of normal load on receptance ratio (relative to no-load receptance peak = 2.45×10^{-4} m/N.

load were one could expect to optimize the stress reduction due to friction. As smaller increments of normal loads were added, the corresponding amplitude and frequency effects become increasingly difficult to ascertain. On the other hand, higher loading increments changes in amplitudes and frequencies of response were identified easily.

Some generalities can be drawn regarding non-linear response phenomena of the turbine blade in light of the loading limitations of the experimental investigations. Qualitatively, there is an increase of frequency of the peak response with an increase in normal load for both tip and platform response. Quantitatively, the increase in peak response frequency with increase in load is not the same for the tip response and platform response. It is important ot note the experimental investigation of tip and platform resposne were completed as separate tests, i.e., tip and platform response were not measured simultaneously. Consequently, many variables that could be controlled or assumed constant for simultaneous measurements are, instead, masking the response characteristics which could otherwise be more easily quantified. One particular concern is the change between friction surfaces with time, since friction loads were applied with a tapered rod to the platform. The concentrated load could be high enough to cause some permanent deformation of the friction surfaces, which could lead to a varying friction coefficient throughout the series of testing.

A comparison of experimental results with analytical results (e.g.,Figures 12 and 13) shows that, qualitatively the frequency and amplitude effects of increasing the friction parameter in the discrete model will have the same effect as increasing the normal load in the experimental test system. A graphical representation of receptance ratio versus the friction parameter in Figure 14 indicates only slight increases of amplitude with increasing friction parameter after optimal receptance reduction is reached. The point of optimal receptance reduction, which corresponds to peak damping for the analytical model, occurs at a friction parameter = 10. A comparison of the two plots of receptance ratio indicate that if the experimental data were superimposed on the analytical data, the experimental data would fall between values 25 and 150 of the friction parameter. An estimate can be made of the input force by comparing the friction parameter to the normal load at the same value of receptance ratio. The result indicates an input force of 0.11 lb_f. Within this range of receptance ratio values, it is evident that we are well above the region of optimum dry friction damping, yet must increase the normal load greatly to reach the magnitude of the undamped receptance.

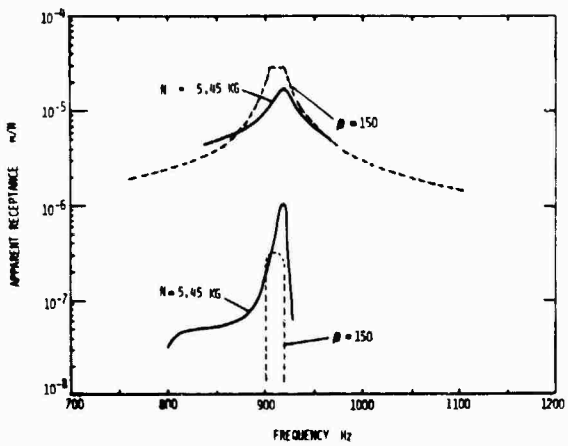

Figure 12 Comparison between experimental and analytical derived receptances for frictionally damped blade (β=30, N=1.2Kg).

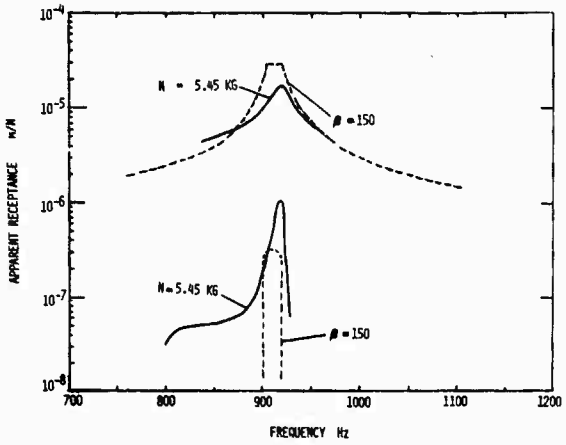

Figure 13 Comparison between experimental and analytical derived receptances for frictionally damped blade (β=150, N=5.45Kg).

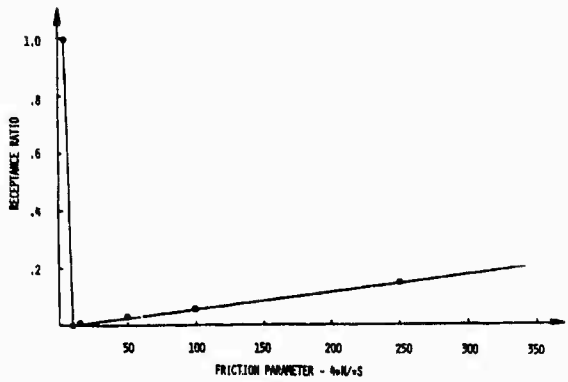

Figure 14 Effects of friction parameter on receptance ratio (relative to 1.0×10^{-3} m/N)

5. CONCLUSIONS AND RECOMMENDATIONS

1. A quick measurement of nonlinear response was accomplished through use of a Fourier digital signal analyzer and zoom data processing techniques. This measurement technique indicates that broadband nonlinear response to dry friction damping may be measured with reasonable certainty using narrow bandwidth response data.

2. Approximate solutions for the response of the blade subject to dry friction damping were achieved using a two degree of freedom lumped mass model The discrete model was successfully implemented to describe the turbine blade undamped receptances, which were then used to characterize the nonlinear response at the tip and platform of the blade. Possible refinements of the two degree of freedom model include incorporation of hysteretic damping so that derived point and transfer receptances would more closely model the actual blade response. The addition of hysteretic damping would also modify the damped response of the blade as modeled by receptances. A limitation of the discrete model is the inability of the model to accurately define the second mode of the blade.

3. A refinement to the experimental system would be to allow for a wider range of normal loading values to be applied to the blade platform. Therefore, determination of the normal loading effects on the blade non-linear response characteristics would be more readily identified.

4. Success of the digital signal processing technique to measure non-linear phenomena could be better established if experimental testing of the structure would be accomplished at several known levels of impact force as opposed to one constant impact force level as in the current series of tests. This testing would establish if the nonlinear response is quasi-linear over a small bandwidth, since each successive impact will yield a response somewhat different from the others due to the nonlinearity of the system. An additional improvement would be achieved if data acquisition of both tip and platform response could be accomplished simultaneouslv. Simultaneous data acquisition would eliminate any variation which could occur between tests due to changes in input force level, varying orientation of normal loads to the blade platform, or changes between the frictional surfaces of the platform and loading rod. Further insight into modal non-linear behavior could be achieved if successive zoom transfer functions were measured so as to resolve a larger percentage of the non-linear modal response.

ACKNOWLEDGEMENTS

The authors wish to acknowledge the efforts of Roxanne Lemaster and Joan Lowe of AFWAL/MLLN for the valuable assistance in preparing and compiling drafts and manuscripts.

Thanks are due to Mr. John Barnett of AFWAL, Ms. Elizabeth Dirkes and Mr. Dave Hopkins of UDRI for assistance in the data acquisition and reduction.

REFERENCES

1. Muszynska, A., Jones, D.I.G., Lagnese, T., Whitford, L., "On Non-Linear Response of Multiple Blade Response", Shock and Vibration Bulletin 51 (3), pp 89-110.

2. Griffin, J.H., "Friction Damping of Resonant Stresses in Gas Turbine Engine Airfoils", ASME Paper 79-GT-109.

3. Beards, C.F., "Some Effects of Interface Preparation on Frictional Damping of Joints", Int. J. Mach. Des. Res.,Vol. 15, pp 77-83.

4. Beards, C.F. and Imam, I.M.A., "The Damping of Plate Vibration by Interfacial Slip Between Layers", Int. J. Mach. Tool, Des. Res., Vol. 18, pp 131-137.

5. MacBain, J., Air Force Wright Aeronautical Laboratories, (AFWAL/POTA), Private Communication.

6. DenHartog, J.P., "Mechanical Vibrations", 4th Ed., McGraw-Hill, New York, 1956.

7. Bearden, J.L., "Bladed Disk Dynamic Response", Report AFAPL-TR-79-2002, WPAFB, OH 1978.

8. Ewins, D.J., "Whys and Wherefores of Modal Testing", SAE Journal, September 1979.

9. Jones, D.I.G., "Vibration of a Compressor Blade with Slip at the Root", AFWAL-TR-80-4003, Air Force Wright Aeronautical Laboratories, 1980.

10. Plunkett, R., "Friction Damping", Published in Proc. of ASME Symposium, Damping Application for Vibration Control (Ed. P.J. Torvik), Chicago, Illinois, November 1980.

11. Jones, D.I.G. and Muszynska, A., "Effect of Slip Damping on Response of a Vibrating Compressor Blade", ASME Paper 77-WA/GT-3, 1977.

12. Jones, D.I.G. and Muszynska, A., "Vibration of a Compressor Blade with Slip at the Root", Shock and Vibration Bulletin 48, 1978.

13. "The Fundamentals of Signal Analysis", Hewlett Packard, Applications Note 243.

14. Ewins, D.J., "Measurement and Application of Mechanical Mobility Data", Solartron.

15. Jones, D.I.G. and Muszynska, A., "On Modal Identification of Multiple Degree of Freedoms Systems from Experimental Data", to appear.

16. Dominic, B.J., "Analytical and Experimental Investigation of Turbine Blade Damping", UDRI-TR-82-39.

17. Tse, F.S., Morse, I.E., Hinkle, R.T., "Mechanical Vibrations Theory and Applications", 2nd Edition, Allyn and Bacon, Inc. 1978.

NOMENCLATURE

A	Amplitude of $X_1(t)$
B	Amplitude of $X_2(t)$
f_n	n-th Natural Frequency (Hz)
i	$\sqrt{-1}$
i,j	Points on Blade Surface (i,J=1,2)
k_1, k_2	Stiffnesses
m_n, m_2	Modal Mass (n=1,2,..,N.)
N	Normal Forces
R_2	Modal Correction Coefficient
S_1, S_2	Driving Force Amplitudes at points 1, 2
t	Time
$X_1(t)$	Response at Point 1
$X_2(t)$	Response at Point 2
α_{ij}	Transfer Receptance
α_{ii}, α_{jj}	Point Receptance
β	Friction Parameter
Δ	See Equation
ϕ, γ	Phase Angles
η_n	n-th Modal Loss Factor
μ	Coefficient of Friction
ω	Circular Frequency
ω_n	Natural Frequency of n-th Mode

DISCUSSION

Mr. LaLanne (National Institute of Applied Sciance): Is this blade in the fixture supposed to be a rotating blade? What is the use of this blade?

Mr. Lagnese: The blade in the fixture was simulated to have a pre-load on it.

Mr. LaLanne: Yes, I know. But is it a blade for a rotating stage or for a static stage?

Mr. Lagnese: It is for a rotating stage.

Mr. LaLanne: I do not think I understand. You were speaking about pre-load. Are you imposing some kind of force?

Mr. Lagnese: The pre-load simply puts a load on the root to lock it into position so that we could take the measurement.

Mr. LaLanne: How much pre-load was applied?

Mr. Lagnese: It waa about a 90 pound/inch torque into the root.

Mr. LaLanna: Waa it a very high atrength?

Mr. Lagnase: Yea. It has fairly high strength.

Mr. LaLanne: Is it very well clamped?

Mr. Lagneae: Yea.

Mr. LaLanna: Do you think there would be much highar equivalent force from clamping due to the cantrifugal effect when thia kind of blade is used?

Mr. Lagnase: Thera should be more clamping due to a centrifugal affect than what we could apply with tha fixture.

Mr. LaLanne: Will you be able to optimize the damping? If the force or torque ia so high when this kind of blada ia rotating in the fixture, can you do something to improve the damping or to fix soma kind of valua? If I am not mistakan, you are aaying I can manage something on torque, and I can assume I hava good damping. Ia that right?

Mr. Jones: There are so many queations in thia buaineas. What we tried to do in thia particular taat was to clamp tha dovetail complataly so it had no damping. We were looking only at damping from aliding friction betwean tha platform and the rod. This was an attempt to aimulate a clapper that one would use in a raal blade. It was an attempt to understand tha physical phanomena rather than to necessarily aimulate what happens in a real engina.

A VIBRATION DAMPING TREATMENT FOR HIGH TEMPERATURE GAS TURBINE APPLICATIONS

Ahid D. Nashif
Anatrol Corporation
Cincinnati, Ohio

and

William D. Brentnall
Solar Turbines, Inc.
San Diego, California

and

David I.G. Jones
Materials Laboratory, AFWAL/MLLN
Wright-Patterson AFB, Ohio

This paper describes an investigation of the behavior and properties of a family of vitreous enamels designed to give high damping properties when applied as coatings to high temperature static components in gas turbine engines. Complex modulus properties and effects of thermal aging are discussed.

INTRODUCTION

Damping materials are being widely used today to solve a variety of noise and vibration problems in structures ranging in type from automotive to aerospace [1-3]. This use of damping materials has been increasing rapidly in recent years, partly because many polymeric viscoelastic materials have been developed to work effectively for such applications. However, polymeric viscoelastic materials are usually limited to certain temperature ranges, typically well below 500°F. This has resulted in a gap as far as the application of damping materials to high temperature systems is concerned, especially in gas turbine engines. The Materials Laboratory at Wright Patterson Air Force Base has sponsored several research programs [4-11] aimed at investigating the dynamic behavior of vitreous enamels at high temperatures, for possible application in engines.

As a result of the research programs on the dynamic behavior of vitreous enamels, it was determined that such materials behave in much the same way as polymeric viscoelastic materials, but at higher temperatures. In other words, the enamel coatings undergo a reversible transition process, as temperature increases, where the modulus of the material decreases while the loss factor increases. Within such temperature ranges, each enamel coating exhibits high damping capabilities similar to those of polymeric viscoelastic materials. Much of the early research work has concentrated on the development of test methods [4-11] and understanding the effects of different glass compositions on the damping behavior as a function of temperature and frequency [12-15]. However, limited information has been available as far as practical application of such materials to engine structures is concerned [1-3], especially with respect to durability. Therefore, the present research program [16] was

initiated to identify a family of enamel coatings to work effectively over different temperature ranges, typical of those found in gas turbine engines, and to withstand service in the engine environment.

This paper describes a family of glass/enamel coatings designed to cover a temperature range from 400°C to 900°C (750°F to 1650°F) and a frequency range from 100 to 10,000 Hz. These materials were evaluated for use on different sheet alloys typical of those used in gas turbine engines. The linear viscoelastic damping properties of the enamel coatings were determined using a vibrating beam test apparatus in conjunction with a digital fast Fourier analyzer system and a control computer to determine the material damping properties from the frequency response data. The data are presented in the form of temperature-frequency spectrum maps and plots of storage modulus, loss factor, and loss modulus as a function of temperature and frequency. The effects of long term high temperature isothermal exposure, representative of service temperatures, on coating stability and coating-substrate interactions are discussed.

DAMPING PROPERTIES OF THE VARIOUS COATINGS

A number of enamel coatings were considered for this investigation in order to span a wide temperature range over which structures are likely to be subjected during service.

Approximately 30 enamel coatings were formulated and screened, based on firing characteristics, adherence, response to high temperature thermal exposure, structural stability, and initial damping characteristics. The enamels were mainly complex lead-boro silicate, alkali-boro silicate or barium-boro silicate glasses with various mill additions of metal oxides (Cr_2O_3, Al_2O_3, clay, etc.).

One of the main criteria sought was to ensure that the product of the material loss factor and Young's modulus (the loss modulus ηE) be as high as possible over as broad a range of temperatures and frequencies as possible. This is because such enamels will be used primarily in unconstrained layer treatments or coatings [1,5]. In order for such treatments to be competitive at high temperatures with similar polymeric treatments at lower temperatures it was necessary to establish minimum goals for the loss modulus (En). Such a value was set at 4×10^5 lb/in^2 (i.e. 2.76×10^9 Pa) in the contract [16].

On the basis of these screening tests, five enamel compositions were selected to cover the required temperature range. The selected compositions are identified as S-1B, S-2B (lead borosilircates), S-4B, S-6B (alkali borosilicates), and S-8B (barium borosilicates) as summarized in Table 1.

The enamel damping properties were determined using the techniques described in Appendix 1. The results of the measurements were characterized using the temperature-frequency superposition method and curve fitted with analytical functions as described in Appendix 2 [12-15].

The damping properties of these enamels are shown in Figures 1 through 5 in terms of temperature and frequency for glasses S1-B through S8-B. Note that the temperature of peak damping (peak En), at a fixed frequency of 1000 Hz varies from about 410°C for S1-B to 850°C for S8-B, so that these five enamels cover the entire temperature range from 375°C to 1000°C with significant overlap. Table 2 summarizes the effective damping range ($\eta E > 2.76 \times 10^9$ Pa) for these and other enamels studied.

EFFECTS OF AGING

The effect of long term thermal exposure on both enamel coatings and substrate alloys, with special emphasis on substrate-enamel interactions and the effects of such interactions on the enamel properties, were investigated. Both cyclic furnace exposures, and long term (1000 hour) isothermal furnace exposures (air atmosphere), were used to determine coating stability and to define undesirable coating-substrate interactions. Table 3 summarizes some of the weight change data observed after 200 hours of cyclic thermal testing. Weight changes were almost insignificant.

Exposure temperatures for the 1000-hour tests were arbitrarily chosen at 50°C above the peak damping temperatures at 1000 Hz. Examples of coating microstructure in the as-coated condition, and after thermal exposure, are shown in Figures 6 through 9 for glass S2-B. For this particular coating/substrate combination there was no significant coating/matrix interaction or reduction in cross section. Figures 10 through 12 represent preliminary results showing the thermal exposure effects on damping properties of some of the enamel coatings.

It is seen that, for glasses S-2B and S-48, no significant changes in damping behavior occurred, but for glass S-18 considerable shift, to a higher temperature range, took place. Modification of this glass is clearly needed before it can be used in service and further work to stabilize it is in progress and will be reported separately.

Figures 13 and 14 show dispersive x-ray spectra of the glass S-28 before and after 1000 hours isothermal exposure, respectively.

CONCLUSIONS AND RECOMMENDATIONS

A family of enamel coatings has been developed to work effectively on different metal substrates, typical of those used in gas turbine applications, over a wide temperature range. Preliminary results showing the effects of aging and thermal exposure on the damping properties of these coatings are encouraging. Further research in this area is continuing to overcome the practical problems of applying such materials to structures for the purpose of vibration control.

REFERENCES

1. J.J. DeFelice and A.D. Nashif, "Damping of an engine exhaust stack", Shock and Vibration Bulletin 48, Part 2, 1pp 75-84, 1975.

2. D.I.G. Jones, "High temperature of dynamic systems", Shock and Vibration Digest, October 1976.

3. D.I.G. Jones, "High temperature damping of dynamic systems", Shock and Vibration Digest, 1981.

4. P. Sridharan and R. Plunkett, "Damping in porcelain enamel coatings", AFML-TR-71-193, Air Force Materials Lab., 1971.

5. A.D. Nashif, "Enamel coatings for high temperature damping materials", Ceramics Bulletin, 53(12), 1974.

6. R. Plunkett, "High temperature damping", SAE Paper 720809, SAE National Aerospace Meeting, San Diego, 1972.

7. D.I.G. Jones and C.M. Cannon, "Control of gas turbine stator blade vibrations by means of enamel coatings", J. Aircraft, 12(4), pp 226-230, 1975.

8. G. Graves et al, "On tailoring a family of enamels for high temperature vibration control", Proc. 15th Annual S.E.E. Meeting, Gainesville, 1978.

9. G.A. Graves, C.M. Cannon and 8. Kumar, "A study to determine the effect of glass compositional variations on vibration damping properties", AFWAL-TR-80-4061, Air Force Wright Aero. Labs., 1980. [See also Glass Tech., 22(2), 99-104, 1981].

10. P. Sridharan, "Damping in porcelain enamel coatings", AFML-TR-74-191, Air Force Materials Labs., 1976.

11. D.M. Hopkins and M.L. Drake, "Porcelain enamel material testing procedures to determine the damping properties and the results of selected materials", AFWAL-TR-80-4116, Air Force Wright Aero. Labs., 1980.

12. J.D. Ferry, Viscoelastic properties of polymers, John Wiley and Sons Inc., New York, 1961.

13. L.C. Rogers, "On modeling viscoelastic behavior", Shock and Vibration Bulletin 51, Part 1, pp 55-69, 1981.

14. D.I.G. Jones, "An attractive method for displaying material damping data", J. Aircraft, 18(8), pp 644-649, 1981.

15. D.I.G. Jones, "Temperature-frequency equivalence of dynamic properties of damping materials", J. Sound Vib., 33(4), pp 451-470, 1974.

16. Solar Turbines Inc., San Diego; Air Force Contract No. F33615-79-C-5108.

17. A.D. Nashif, "A new method for determining damping properties of viscoelastic materials", Shock and Vibration Bulletin 36, pp 37-47, 1967.

18. D.I.G. Jones and A. Muszynska, A., "On the modal identification of multiple degree of freedom systems from experimental data", Shock and Vibration Bulletin 53, 1983.

19. Schwarzl, F., Physica 17, 830, 923 (1951).

20. Heyboer, J., Dekking, P., and Staverman, A.J., Proc. 2nd Int. Cong. on Rheology, Oxford 1953, page 123.

APPENDIX 1

MEASUREMENT AND DATA ANALYSIS METHODS

The vibrating beam test technique was used to measure and evaluate the damping properties of the enamel coatings [5,9,10,17]. By this technique the measured frequency response of the coated and uncoated beams are used to compute the properties of the enamel coating by itself. The measurements are obtained at different frequencies corresponding to different modes of vibration of the beam and at different temperatures. Using the results of these measurements, the temperature-frequency superposition principle [12-15] is then used to collapse all the data on one master graph. The data is then curve-fitted with analytical expressions so that the properties of the material can be easily stored on the computer for later analysis.

Beam Specimens

The dimensions of the beam specimens used in this investigation are given in Figure 15. Three different alloys, typical of those used in gas turbine engines, were selected, namely alloys are Hastelloy-X, 347 stainless steel, and Haynes 188. Massive roots were welded on the beam to better simulate the required fixed boundary condition of a cantilever beam.

Experimental Setup

A high temperature bending beam apparatus based on that described in References [9,11] was used to test all beam specimens. An important change was made in the system to change the excitation method. This change was made in order to obtain good signal to noise ratios during the measurements and thereby eliminate some of the experimental obstacles to automating the setup. The earlier setup utilized a noncontacting magnetic transducer to excite the beam, and was found to be adequate as long as careful alignment between the beam and transducer was maintained, as was possible in manually controlled tests. However, at high temperatures excessive bending was noted in the beam and it was not possible to maintain high excitation force levels to the beam at all temperatures. The setup described here utilizes an impact technique to apply the force to the beam through a solenoid operated with a frequency generator to control the impact rate. A schematic of the automated setup is shown in Figure 16.

Figure 17 represents the instrumentation used with the setup. The computer is used to (a) automatically control and change the temperature of the furnace to maintain a uniform temperature along the length of the beam to within ±5°F, (b) initiate the analyzer, at the point when the desired temperature is reached, to generate the frequency response of the beam and then (c) perform zoom transform analysis on each desired mode of vibration, (d) compute the frequency and damping loss factor of each mode and (e) store the measured data on tape for later analysis.

Procedure

The general procedure used to measure the variation of the modal frequency and damping values of both the coated and uncoated beams with temperature was as follows. An initial temperature such as 204°C (400°F), was specified and sufficient time was allowed for the initial temperature

stabilization. The computer then triggered the analyzer to generate the averaged first frequency response data, measured by the force transducer, for a chosen number of impacts on the beam. The frequency response data was then stored digitally in the computer and a zoom Fourier transform was applied for each resonant mode in turn to provide the necessary resolution for measuring the frequency and damping loss factor. The damping loss factor was determined for each mode using either the familiar 3 dB or a 10 dB bandwidth method [18], depending on the level of damping values, and stored in the computer in a recording sequence along with the mode number, the natural frequency, and the temperature at which the measurements were taken. For most beams, the second, third, fourth, and in some cases the fifth mode of vibration were evaluated. After completing these measurements, the computer incremented the furnace temperature setting by a pre-selected amount, such as 25°F, and the entire process was repeated until the selected maximum temperature was reached. A typical zoom Fourier transform plot and a temperature spectrum map are shown in Figures 18 and 19.

Data Reduction

Since the enamel was coated equally on both sides of the metal beam, the well known equations for the symmetric beam technique [17] were used to compute the damping properties. These properties, which include the storage Young's modulus E, and the loss factor η, are given by the following equations [17]:

$$E = \frac{[(\omega_n/\omega_{1n})^2 (1 + 2h_r\rho_r) - 1] E_1}{8h_r^3 + 12h_r^2 + 6h_r}$$

$$\eta/\eta_n = 1 + \frac{E_1}{(8h_r^3 + 12h_r^2 + 6h_r) E}$$

where E_1 = Young's modulus of metal beam

$h_r = H_2/H_1$

$h_r = H_2/H_1$

H_2 = thickness of damping material

H_1 = thickness of metal beam

$\rho_r = \rho_2/\rho_1$

ρ_2 = density of damping material

ρ_1 = density of metal beam

η_n = loss factor of composite beam in nth mode

ω_{1n} = nth circular frequency of metal beam

ω_n = nth circular frequency of composite beam

APPENDIX 2

CHARACTERIZATION OF THE DAMPING PROPERTIES

The damping properties of each enamel coating were characterized and displayed using the temperature-frequency superposition principle [12-15]. By this means, measurements of the damping properties with frequency, made at different temperatures, can be collapsed on one master graph by using the appropriate temperature shift factor. Considerable effort [13] has been expended to establish functional forms for such a shift factor, along with the necessary graphical and analytical representations. Both types of representations will be used to describe the damping properties of the various enamel coatings here.

To illustrate the principle, consider the damping properties measured for one of the enamel coatings, labeled S-8B. Two separate batches of this composition were processed and applied to Hastelloy-X beams in two basic thickness ranges (a) 0.005 to 0.006 in. and (b) 0.008 to 0.01 in., for each side. Table 4 gives some of the specimen dimensions and data, along with others investigated. Figure 19 shows a typical temperature spectrum map for one of the four coated beams, and Figures 20 and 21 illustrate the variation of modal frequency and damping with temperature for the same beam. Using these values, along with the beam geometries, and the frequencies of the uncoated beam in the equations given earlier the damping properties for each temperature and frequency were calculated and plotted in the temperature nomogram format as in Figures 22 and 23. The results for beams 1019, 1036, and 1039 are also plotted in these two figures. The temperature-frequency shift factor,

a_T, used to collapse all the data in these figures is given by the following equation [15]:

$$\log a_T = -C_1(T - T_0)/(T - T_\infty)$$

where C_1, T_0, and T_∞ are material constants determined experimentally for each composition.

It is evident from the above figures that, considering the relatively low scatter of the results, the technique used for this investigation is an effective tool for determining the damping properties of enamel coatings. Similar plots are shown for glasses S-1B, S-2B, S-4B, and S-6B in Figures 24 to 27, respectively.

Curve Fitting the Data

With damping properties of each enamel coating measured and plotted in terms of reduced frequency and temperature analytical expressions were then used to curve fit the data. For this purpose the following expressions [19,20] were used for the storage modulus, E, and loss factor, η, of each coating.

$$E = \check{E} + \hat{E}\left[1 - \frac{1}{1+(\beta\omega a_T)^n}\right]$$

and

$$\eta = \frac{n\pi\hat{E}(\beta\omega a_T)^n}{2E\,[1+(\beta\omega a_T)^n]^2}$$

where $\check{E}$, $\hat{E}$, β, n and are constants to be determined. $\check{E}$ is the value of E as $\omega a_T \to \infty$, $\hat{E}$ is the value of E at $\omega a_T = 0$ and β and n are related to the value of ωa_T at which ηE is a maximum and the maximum value of η.

Using the above equations, it was possible to curvefit the data with analytical expressions which are superimposed on the averaged results in the figures.

TABLE 1
Test Specimens

Specimen Number	Average Thickness (mils)	Density (g/cc)
1002/S1A	9.4	4.38
1004/S1B	9.1	4.80
1005/S2A	11.7	4.34
1007/S2B	10.5	4.22
1008/S3A	11.8	3.63
1010/S3B	11.7	3.61
1011/S4A	12.7	2.59
1012/S4B	10.6	2.58
1022/S4C	10.9	2.47
1013/S5A	10.5	2.51
1014/S5B	11.7	2.46
1015/S6A	11.6	3.31
1016/S6B	10.5	3.01
1023/S6C	11.3	3.15
1017/S7A	13.3	3.02
1018/S7B	11.9	2.79
1019/S8A	11.5	3.25
1020/S8B	11.9	3.29
1024/S8C	10.5	3.33
1021/S9A	11.6	2.80
1025/S11A	10.9	3.22
1026/S11B	10.4	3.44
1027/S12A	12.5	3.27
1028/S12B	12.0	3.28
1029/S13C	11.4	3.08
1030/S13B	11.4	3.07
347 Stainless Steel		
3004/S2B	11.6	4.07
3005/S3A	11.8	3.63
3006/S4B	12.2	2.44
3002/S5B	11.7	2.46
3001/S6A	11.6	3.31
3007/S7B	11.9	2.79
Haynes 188		
2005/S2A	12.3	4.16
2006/S3B	12.7	3.62
2007/S4A	13.1	2.33
2001/S5A	13.9	2.41
2002/S6A	10.89	3.07
2011/S7A	13.9	2.89
2012/S7B	11.9	2.96
2013/S9A	11.6	2.91

TABLE 2
Temperature Range of Effective Damping (ηE 2.75x10^6 KPa) for Program Enamels Coatings

Specimen Number	Enamel Coating	Effective Damping Range (°C)	
		10^2 Hz	10^4 Hz
1002	S-1A	535 - 625	625 - >900
1004	S-1B	550 - 630	630 - 900
1005	S-2A	580 - 660	660 - 870
1007	S-2B	610 - 680	680 - >900
1008	S-3A	670 - 720	715 - 860
1010	S-3B	680 - 730	730 - 840
1011	S-4A	680 - 730	730 - 840
1012	S-4B	670 - 690	690 - >900
1022	S-4C	670 - 690	670 - 680
1013	S-5A	660 - 680	650 - >900
1014	S-5B	680 - 690	690 - >900
1015	S-6A	640 - 770	730 - >900
1016	S-6B	670 - 700	710 - >900
1023	S-6C	690 - 740	700 - >900
1017	S-7A	660 - 810	750 - >900
1018	S-7B	690 - 750	710 - 890
1019	S-8A	720 - 802	780 - >900
1020	S-8B	700 - 850	800 - >900
1024	S-8C	730 - 870	780 - >900
1021	S-9A	790 - 880	870 - >900
1025	S-11A	800 - 860	850 - 880
1026	S-11B	800 - 880	860 - 880
1027	S-12A	800 - 880	880 - 890
1028	S-12B	820 - 880	870 - 1000
1029	S-13C	780 - 820	860 - 1000
1030	S-13B	770 - 830	820 - 1000

TABLE 3
Weight Change Data After 200-Hour Cyclic Tests
(Coated Hastelloy X)

Coating	Weight Change (mg/cm²) After Exposure at Indicated Temperature (°C/°F)								
	427/ 800	482/ 900	538/ 1000	593/ 1100	649/ 1200	704/ 1300	760/ 1400	815/ 1500	871/ 1600
S-1A	-0.046	-0.092	+0.36	-	-	-	-	-	-
S-1B	-0.038	-0.078	+0.66	-	-	-	-	-	-
S-2A	-0.089	-0.096	+0.007	-	-	-	-	-	-
S-2B	-0.067	-0.078	-0.026	-	-	-	-	-	-
S-3A	-	-	-0.037	-0.23	-0.129	-	-	-	-
S-3B	-	-	-0.041	-0.21	-0.085	-	-	-	-
S-4A	-	-	-0.018	-0.037	+0.092	-	-	-	-
S-4B	-	-	-0.015	-0.10	+0.018	-	-	-	-
S-4C	-	-	-	-	-	-	-2.21	-0.37	-
S-5A	-	-	-0.007	-0.067	-0.011	-	-	-	-
S-5B	-	-	-	-0.081	+0.003	-	-	-	-
S-6A	-	-	-	+0.003	+0.041	-0.174	-	-	-
S-6B	-	-	-	+0.025	-0.137	+0.066	-	-	-
S-6C	-	-	-	-	-	-	-	-0.20	-0.875
S-7A	-	-	-	-0.225	-0.007	+0.018	-	-	-
S-7B	-	-	-	-0.100	-0.174	+0.0296	-	-	-
S-8A	-	-	-	-	-	-0.06	-0.029	-4.5	-
S-8B	-	-	-	-	-	+0.003	+0.048	-0.425	
S-8C	-	-	-	-	-	-	-	-0.194	-
S-9A	-	-	-	-	-	-0.0148	-0.055	+0.077	-0.0001
S-9B	-	-	-	-	-	+0.040	+0.092	+0.360	-
S-10A	-	-	-	-	-	-	-	-	-
S-10B	-	-	-	-	-	-	-	-	-
S-11A	-	-	-	-	-	-	+0.17	+0.45	-0.046
S-11B	-	-	-	-	-	-	+0.13	+0.18	+0.069
S-12A	-	-	-	-	-	-	+0.085	+0.132	-1.28
S-12B	-	-	-	-	-	-	+0.09	+0.155	+0.064
S-13B	-	-	-	-	-	-	+0.005	+0.14	-0.039
S-13C	-	-	-	-	-	-	+0.06	-0.30	+0.170

+ = Weight Gain
- = Weight Loss

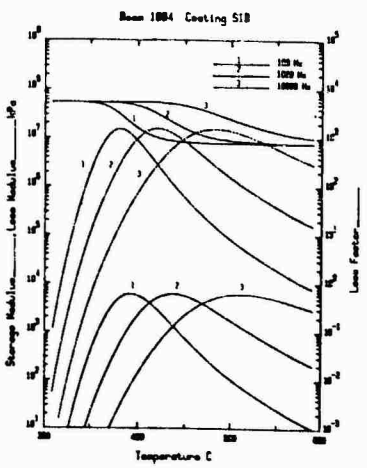

Figure 1: Complex Modulus Properties of Enamel S1-B vs. Temp.

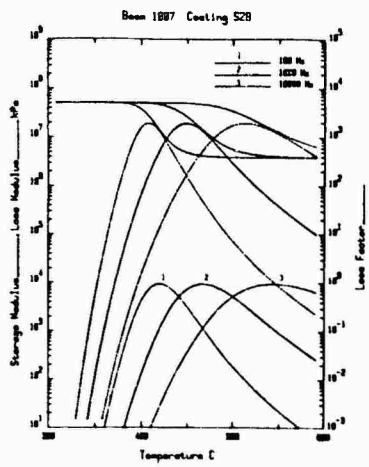

Figure 2: Complex Modulus Properties of Enamel S2-B vs. Temp.

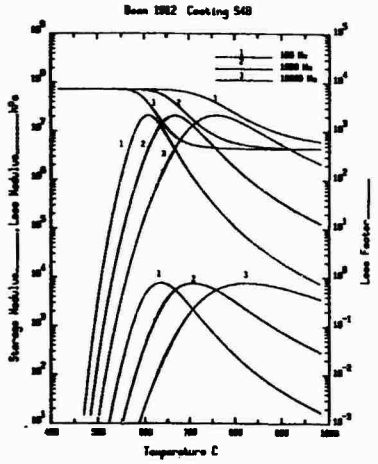

Figure 3: Complex Modulus Properties of Enamel S4-B vs. Temp.

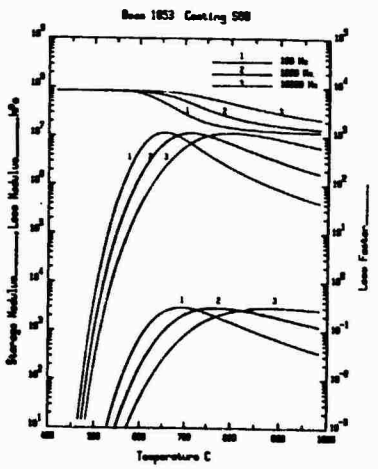

Figure 4: Complex Modulus Properties of Enamel S6-B vs. Temp.

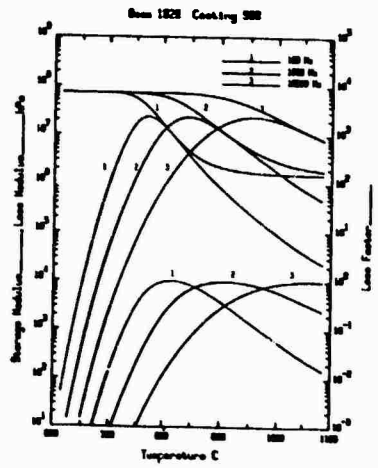

Figure 5: Complex Modulus Properties of Enamel S8-B vs. Temp.

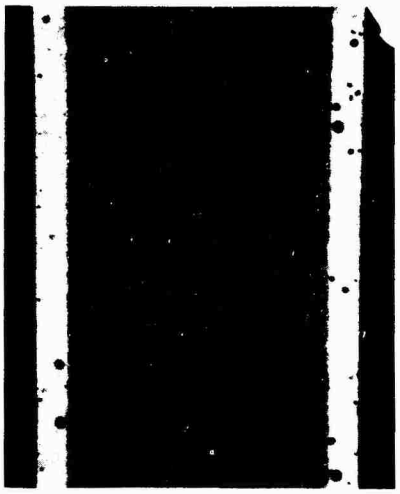

Figure 6: S2-B Enamel Coating on Hastelloy-X Substrate-as Coated

Figure 7: S-2B Enamel Coating on Hastelloy-X Substrate-as Coated

Figure 8: S2-B Enamel Coating on Hastelloy-X Substrate-Furnace Exposed 1000 Hours at 970°F

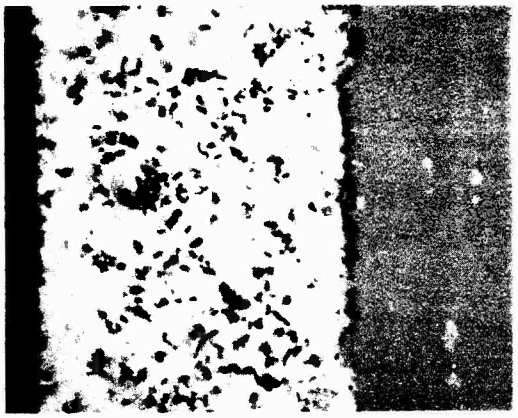

Figure 9: S2-B Enamel Coating on Hastelloy-X Substrate-Furnace Exposed 1000 Hours at 970°F

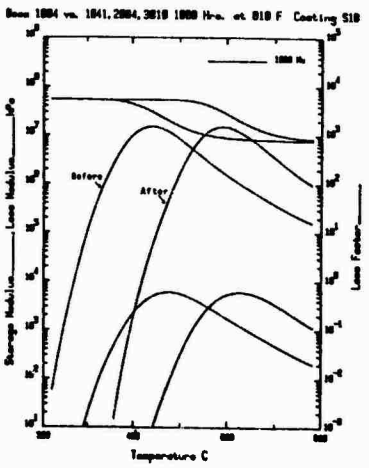

Figure 10: Complex Modulus Properties of Enamel S-1B Vs. Temperature after 1000 Hours at 810°F

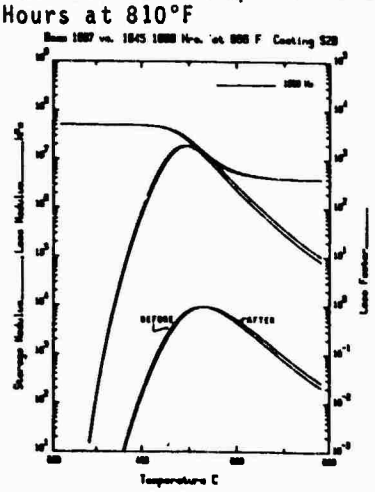

Figure 11: Complex Modulus Properties of Enamel S2-B Vs. Temperature after 1000 Hours at 966°F

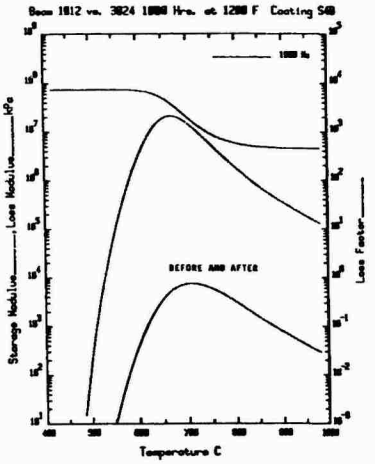

Figure 12: Complex Modulus Properties of Enamel S4-B Vs. Temp. after 1000 Hours at 1200°F

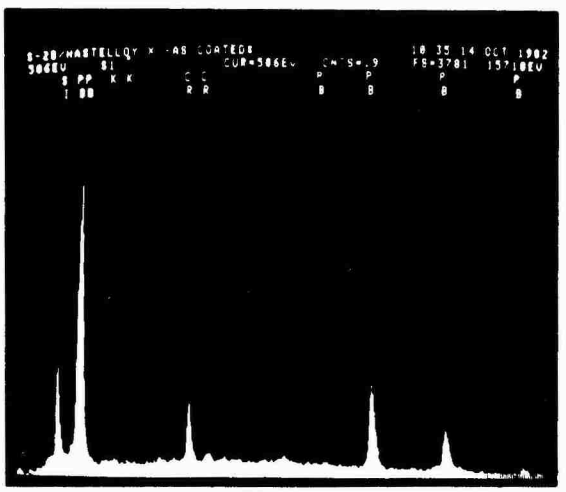

Figure 13: S-2B Enamel Coating on Hastelloy-X Substrate-As Coated

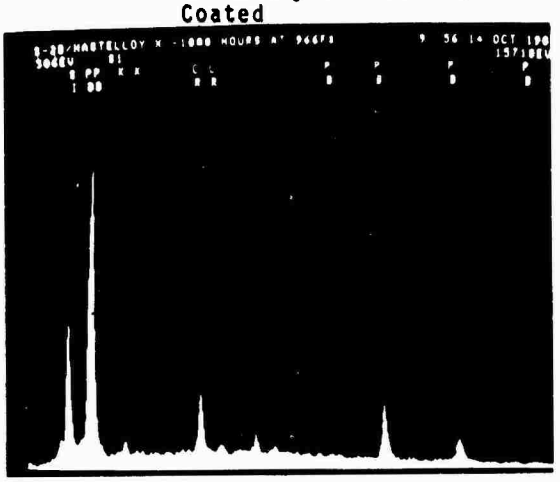

Figure 14: S-2B Enamel Coating on Hastelloy-X Substrate Furnace Exposed 1000 Hours at 970°F

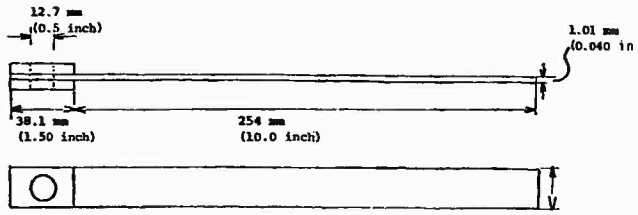

Figure 15: Schematic of Vibrating Beam Specimen

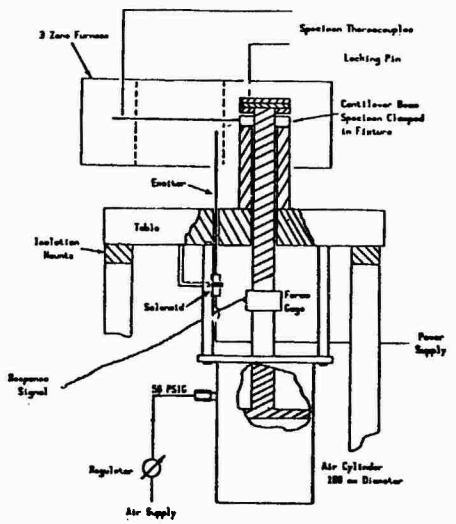

Figure 16: High Temperature Damping Test System

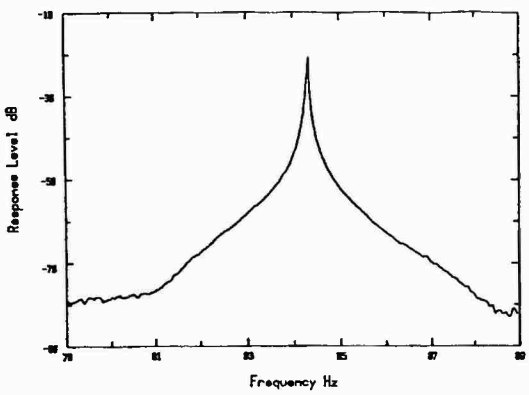

Figure 18: Typical Zoom Transform Response

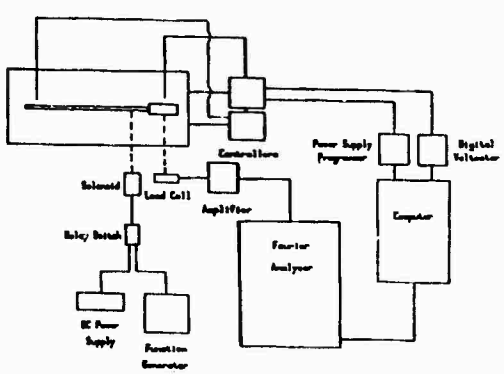

Figure 17: Schematic of Instrumentation

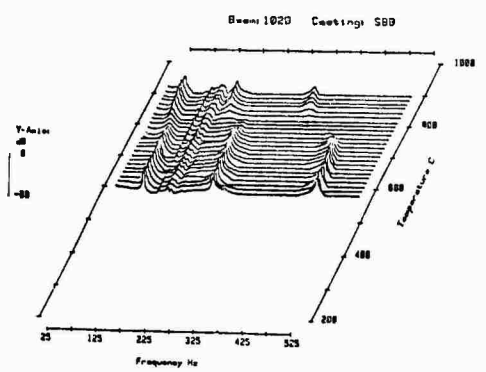

Figure 19: Typical Temperature Spectrum Map for Beam Specimen

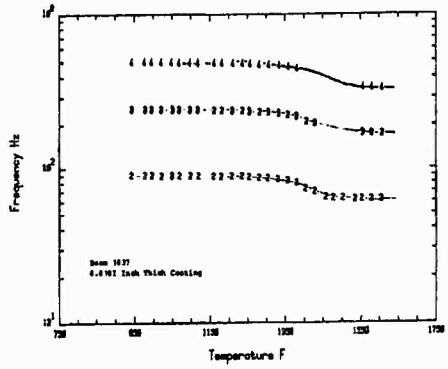

Figure 20: Resonant Frequency Vs. Temperature for Beam 1037 With Coating S8-B (Modes 2,3,4)

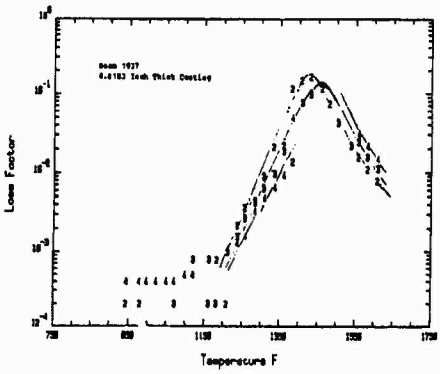

Figure 21: Loss Factor Vs. Temp. for Beam 1037 With Coating S8-B (Modes 2,3,4)

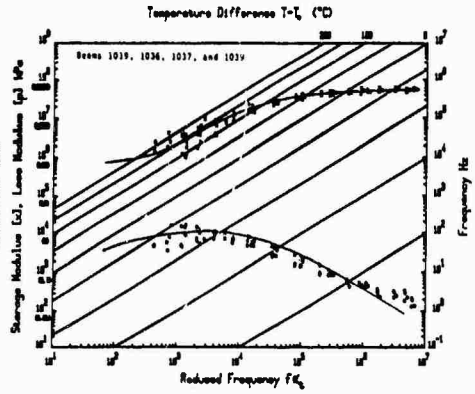

Figure 22: Reduced Temperature/Freq. Nomogram for Coating S8-B (Summary of Beams 1019, 1036, 1037, 1038, 1039)

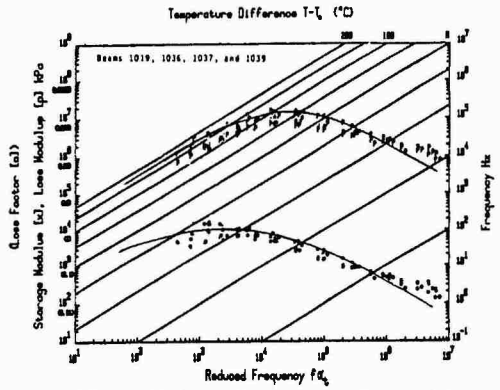

Figure 23: Reduced Temperature/Freq. Nomogram for Coating S8-B (Summary of Beams 1019, 1036, 1037, 1038, 1039)

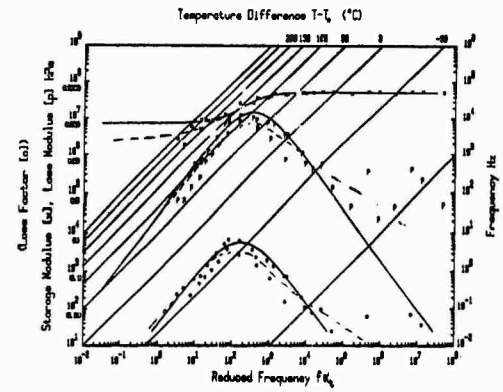

Figure 24: Reduced Temperature/Freq. Nomogram for Coating S1-B (Beam 1004)

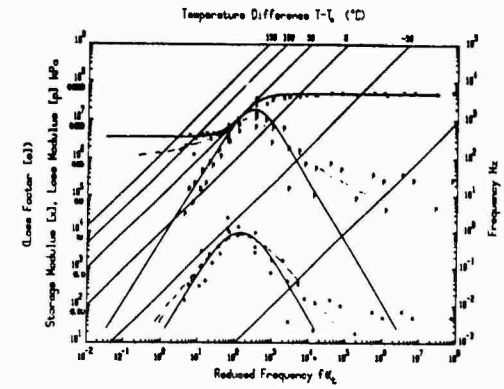

Figure 25: Reduced Temperature/Freq. Nomogram for Coating S2-B (Beam 1007)

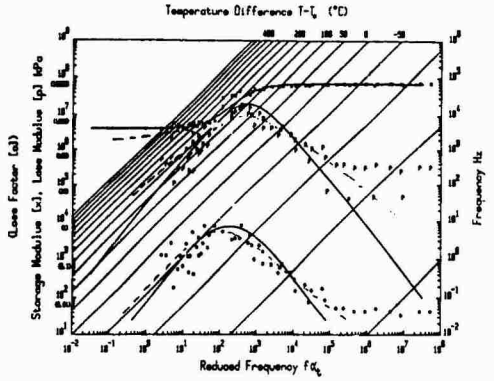

Figure 26: Reduced Temperature/Freq. Nomogram for Coating S4-B (Beam 1012)

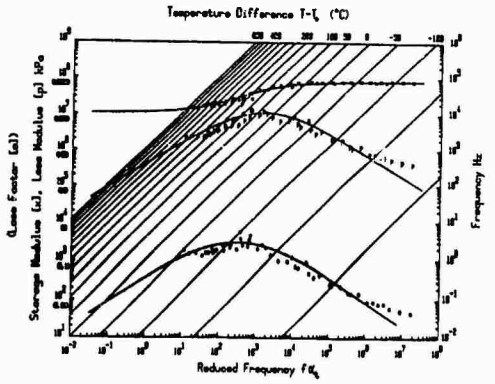

Figure 27: Reduced Temperature/Freq. Nomogram for Coating S6-B (Beam 1053)

DISCUSSION

Dr. Eshleman (The Vibration Institute): You said that the properties are good. In layman's terms, what do you consider good with respect to elastomer and normal temperatures? How do they compare?

Mr. Nashif: Vitreous enamels have a much higher loss modulus than viscoelastic materials. They usually have a loss modulus about ten times higher than the best free-layer damping material, so their effectiveness will be considerably better. Another thing about the temperature range is that it is fairly wide where they provide that high peak with temperature for the loss modulus; you can use vitreous enamel between 150 and 200 degrees C and it still provides good damping. But damping really is all relative, and I can't tell you how good it is unless you tell me what kind of problem you want to use it on.

Mr. Drake (University of Dayton Research Institute): In your aging studies, at what temperature, relative to peak g or peak damping, did you age your specimens?

Mr. Nashif: That was one of the things we discussed many times, and then eventually decided that people are likely to use those materials at the place where they provide peak damping. So we selected the place of peak damping with temperature as the temperature to which we would expose the material for 1,000 hours. And since material properties vary with frequency, we had to select another parameter. So we fixed the peak damping with temperature at 1,000 Hz.

EXPERIMENTAL MEASUREMENT OF MATERIAL DAMPING USING DIGITAL TEST EQUIPMENT

P. W. Whaley
Associate Professor of Engineering Mechanics
University of Nebraska-Lincoln
Lincoln, Nebraska

and

P. S. Chen
Graduate Research Assistant
University of Nebraska-Lincoln
Lincoln, Nebraska

A procedure for measuring loss factor under random vibration using two digital spectrum analyzers is described. For sinusoidal testing, errors of several orders of magnitude can result from slightly missing the specimen resonant frequency. This means that the processing bandwidth in digital spectrum analysis procedures must be very small, typically requiring a high resolution FFT. A weighting function is introduced to eliminate this bandwidth constraint by calculating the exact transfer function from the measured RMS transfer function. This provides a rapid, accurate procedure for calculating loss factor.

NOMENCLATURE

English:

A	beam specimen cross sectional area
E	Young's modulus
e	measured loss factor error
F_o	amplitude of the force supplied by the shaker
F	viscoelastic damping constant
h	thickness of the beam specimen
H_m	measured RMS transfer function
H_e	exact transfer function
I	beam specimen moment of area
m	mass of the shaker head
q_i	generalized coordinate
$S_{\ddot{z}}$	power spectral density (PSD) of the base acceleration
S_ϵ	PSD of the strain
W	weighting function
x_o	location of the strain gauge
y	beam transverse displacement
$\ddot{z}$	base acceleration

Greek:

Δ	deviation of the excitation frequency
ϵ	strain
η_s	exact specimen loss factor
$\bar{\eta}_s$	measured loss factor
ρ	density
ϕ_i	mode shape function
$\phi_i''(x_o)$	second derivative of mode shape evaluated at $x=x_o$
ω	frequency
ω_i	specimen natural frequency
ω_s	unloaded natural frequency of the shaker
ξ_i	modal damping factor

INTRODUCTION

The dissipation of energy during structural vibration continues to be the subject of considerable research. Although discrete multi-degree of freedom structural models are possible, appropriate models for damping mechanisms are not always available. That is because energy dissipation during structural vibration is a complicated phenomenon, arising from friction in joints, viscosity in fluids, and relative motion between the molecules of solids. Appropriate models for damping mechanisms usually depend on the particular application and involve

engineering judgement. In this paper, a forced vibration material damping measurement technique is described which utilizes modern digital test equipment.

Material damping is important since resonant amplitudes are typically several orders of magnitude greater than static deflections. Therefore, the maximum response under broad-band excitation typical of aerospace applications would be the resonant condition. There are three common damping mechanisms: fluid viscosity, friction, and material damping. Although it is at least an order of magnitude smaller than the other two, material damping is important in space applications where there would be no air resistance. In addition, a recent study has related material damping to the process of fatigue [1]. Finally, an understanding of material damping leads to better damping models and better designs.

Any damping measurement procedure must be independent of the particular damping model. In Reference [2], it is demonstrated that the loss factor is a material property and that any of the three principal damping models can be expressed in terms of the loss factor. The loss factor is a material property and is independent of boundary conditions. By definition, the loss factor is twice the modal damping factor. Reference [3] describes a forced vibration technique for measuring loss factor using a base excited cantilever beam vibrating at resonance. This paper is based on that procedure except that digital Fast Fourier Transform (FFT) processors were used to collect and process the data. This results in a much faster procedure for measuring material damping.

ANALYSIS

The loss factor is taken to be the material property defining energy dissipation when the strain is below the yield point. In that case, the loss factor is constant with strain amplitude, giving rise to linear damping models. The double cantilever beam is a convenient test specimen since it enables the loss factor to be calculated from forced vibration measurements of the base acceleration and the strain somewhere in the beam.

Consider the double cantilever beam indicated in Figure 1. Using the viscoelastic damping model, the differential equation of motion is:

$$EI\frac{\partial^4 y}{\partial x^4} + FI\frac{\partial^5 y}{\partial x^4 \partial t} + \rho A\frac{\partial^2 y}{\partial t^2} = \rho A\ddot{Z}. \qquad (1)$$

The solution to equation (1) is known to be:

$$y(x,t) = \sum_{i=1}^{\infty} \phi_i(x) q_i(t). \qquad (2)$$

In the vicinity of resonance, only one mode dominates for lightly damped systems, so

$$y(x,t) = \phi_1(x) q_1(t).$$

Combining equations (1) and (2) and invoking orthogonality of the normal modes, the ordinary differential equation for the generalized coordinate results.

$$\ddot{q}_1 + 2\xi_1\omega_1\dot{q}_1 + \omega_1^2 q_1 = \frac{1}{\ell}\int_0^{\ell} \ddot{Z}\phi_1(x)dx \qquad (3)$$

Equation (3) may be solved for q_1, then using the relationship between bending strain and transverse deflection, the result is:

$$\frac{\frac{h}{2}}{|\varepsilon(x_0)|} = \frac{\sqrt{(\omega_1^2-\omega^2)^2 + (2\xi_1\omega_1\omega)^2}}{\frac{h}{2\ell}\phi_1''(x_0)\int_0^{\ell}\phi_1(x)dx} \qquad (4)$$

At resonance, $\omega=\omega_1$ and the loss factor can be solved using equation (4):

$$\eta_s = 2\xi_1 = \frac{h}{2\ell}\frac{\phi_1''(x_0)\int_0^{\ell}\phi_1(x)dx}{\omega_1^2}\frac{|\frac{h}{2}|}{|\varepsilon(x_0)|} \qquad (5)$$

Equation (5) is equivalent to Gibson and Plunkett's equation for loss factor which they derived using the shear force at the base [3].

Equation (5) is based on the assumption that the excitation frequency is exactly at resonance. Gibson and Plunkett [3] assured this condition by using a resonant-dwell test with a fine-tune on the oscillator allowing precise location of resonance. With digital test equipment this is not possible since only discrete frequencies result from the FFT processor. Therefore, in order to provide useful results it is necessary to investigate the possible error incurred by exciting at frequencies slightly off resonance.

Consider that the excitation frequency is $\omega=\omega_1+\Delta$. Then from equation (4),

$$\frac{|\frac{h}{2}|}{|\varepsilon(x_0)|} = \frac{\sqrt{\eta_s^2(\omega_1^2+\omega_1\Delta)^2 + (2\omega_1\Delta+\Delta^2)^2}}{\frac{h}{2\ell}\phi_1''(x_0)\int_0^{\ell}\phi_1(x)dx} \qquad (6)$$

The error in loss factor measurements will be:

$$e = \frac{\eta_s - \bar{\eta}_s}{\eta_s}$$

Combining equations (5) and (6), the result is:

$$e = \sqrt{[1 + (\frac{\Delta}{\omega_1})^2]^2 + [(\frac{\Delta}{\omega_1})^2 + 2(\frac{\Delta}{\omega_1})]^2/\eta_s^2} - 1 \quad (7)$$

Figure 2 is a plot of equation (7) versus (Δ/ω_1) for various loss factors. Figure 2 shows that order of magnitude errors can result for very small errors in the resonant frequency. The processing bandwidth must be below about 0.05 percent of the resonant frequency in order to assure errors less than 5 percent with loss factors of around 4×10^{-3}. Figure 2 also shows that the measurement error is highly dependent on the loss factor to be measured. This means that in order to assure acceptable results, a preliminary estimate of the material loss factor must be available.

Although digital test techniques allow for rapid data collection and processing, equation (7) shows that there is a constraint on the allowable processing bandwidth in order to assure acceptable results. The next section is a discussion of loss factor measurements made using FFT processors.

EXPERIMENTAL PROCEDURE

In the previous section, the theory of loss factor measurement using base excited cantilever beams was outlined. Reference [4] contains detailed descriptions of loss factor measurements under random excitation. Narrow band random excitation is a convenient test method for digital test equipment since averaging capability can be used to avoid precise continuous adjustment of excitation frequency. However, in order to apply random excitation it is necessary to carefully select the processing bandwidth of the FFT spectrum analyzer in order to avoid the serious errors possible in lightly damped structures. This section gives the instrumentation details for loss factor measurements on aluminum and composite double-cantilever beam specimens.

Figure 3 is an instrumentation diagram for the digital processing of data in the frequency domain. This represents a typical two-channel data acquisition system commonly used in experimental modal analysis. Reference [5] contains details of that theory, and for measuring mode shapes and natural frequencies the accuracy would typically be within the accuracy of the calibration of the equipment. Damping measurements, however, have typically not been very reliable. Figure 4 demonstrates the reason that digital test equipment does not provide a faithful measurement of damping. Even with sinusoidal excitation, the FFT processor only gives the frequency response at discrete frequencies. Those discrete frequencies can be thought of as a series of constant bandwidth filters which give the Root-Mean-Square (RMS) of the response spectrum which lies within each bandwidth. Therefore larger processing bandwidths naturally yield lower amplitudes for sinusoidal signals. This is why the processing bandwidth should be made as small as possible.

Two different materials were investigated in this experiment: Aluminum 6061 alloy and E-glass epoxy crossply composite. In order to minimize the external energy loss such as slip damping, air damping and the undesired rocking mode on the beam-shaker system, double cantilever beams were used. The Aluminum specimen is 0.254 m long with the cross section of 0.03 m by 0.011 m as shown in Fig. 5. A center block was made thicker than the other part so that it can be treated as the base of the cantilever beam, then the slip damping can be avoided. The composite specimen is 0.254 m long with the cross section of .032 m by 0.0016 m and a thickened center block was shown in Fig. 5. The geometric center of these double cantilever beams were carefully tuned so that they will coincide with the center of the shaker system. To decrease the dynamic unbalance, a further step of tuning the natural frequencies of the two sides of these specimens were taken. This step was done using accelerometers on both sides of the specimen excited at resonance. While measuring the natural frequencies by either the oscilloscope or the spectrum analyzers, the length of the test beams can then be adjusted to match natural frequencies.

The physical properties of the two types of specimens are summarized in Table 1. Using Figure 2, the FFT processor bandwidth was 0.05 Hz for the aluminum specimen and 0.025 Hz for

TABLE 1
Properties of the Specimens

Specimen	Young's Modulus Gpa	Density kg/m^3	Area Moment of Inertia m^4	length m	Fundamental Frequency Hz
Aluminum	69.0	2630	3.33×10^{-9}	0.254	136.2
Composite	22.1	1993	1.09×10^{-11}	0.254	50.4

the composite. The tip amplitude of the beams was kept low so that air damping is negligible according to Gibson and Plunkett [3]. The high resolution mode of the spectrum analyzers was used to provide the required narrow bandwidth processing. A Hanning window was used in collecting all random data. Table 2 indicates the loss factor measurements under random excitation for the aluminum and composite specimens along with an exponential decay and sinusoidal

TABLE 2
Experimental results of material loss factor

	Aluminum 6061 alloy	E-glass epoxy crossply composite
Random Excitation	1.871×10^{-3}	2.623×10^{-3}
Resonant-Dwell	2.06×10^{-3}	2.729×10^{-3}
Exponential Decay	2.335×10^{-3}	3.357×10^{-3}

measurement for comparison purposes. (See Reference [4] for further details.) As shown in Table 2, the composite specimen loss factor is 40% higher than Aluminum specimen loss factor. Gibson [6] has pointed out that a crossply composite specimen which has the natural frequency at 47.8 Hz has the loss factor of 2.7×10^{-3} at small amplitudes. Loss factor of 2.623×10^{-3} for the specimen which has natural frequency at 50.425Hz is consistent. When the viscoelastic damping model was employed, a specimen of higher natural frequency may be expected to have higher loss factor, since the damping coefficient is proportional to the frequency by this damping model. Plunkett and Max [7] tested an Aluminum 6064 alloy specimen which has its natural frequency at 29 Hz and measured its loss factor as 1.2×10^{-3}. Therefore, loss factor of 1.871×10^{-3} for an Aluminum 6061 alloy specimen with the natural frequency at 136.2 Hz is reasonable since the loss factor for Aluminum 6064 alloy and Aluminum 6061 alloy may be different.

This shows that accurate measurement of material damping using digital test equipment is possible, provided that the processing bandwidth is sufficiently small to provide accurate results. This means that an alternative to the sinusoidal testing used in Reference [3] may be possible which provides experimental data much more quickly. The advantage of random excitation is that fine-tuning the specimen resonant frequency is not necessary, but the FFT processors must have a high resolution capability. One of the primary uses of such a rapid data reduction procedure using a microcomputer is in measuring the loss factor at several modes to get the frequency dependence of damping. Although random vibration can excite several modes at once, the bandwidth constraint becomes more serious at higher modes. Therefore, an additional procedure is required for random vibration loss factor measurements.

Since a microcomputer already exists in the instrumentation, it is a simple matter to include equation (7) directly in the data processing procedure. It is required to define a weighting function defined by:

$$W = \sqrt{[1 + (\frac{\Delta}{\omega_i})^2]^2 + [(\frac{\Delta}{\omega_i})^2 + 2(\frac{\Delta}{\omega_i})]^2/\eta_s^2} \qquad (8)$$

Equation (8) represents the actual measurement of $\ddot{z}$ and $\epsilon(x_o)$ under arbitrary processing bandwidth. Then it is a simple matter to modify that measurement using equation (8) to give a corrected loss factor measurement:

$$\eta_s = \frac{h}{2\ell} \frac{\phi_i''(x_o) \int_0^\ell \phi_i(x)dx}{\omega_i^2 \; W} \frac{|\ddot{z}|}{|\epsilon(x_o)|} . \qquad (9)$$

Although simple in principle, the precise definition of the weighting function in equation (8) will be different when the excitation is random.

USE OF A WEIGHTING FUNCTION

Equation (9) is suggested as an approach to loss factor measurement under random excitation which is independent of processing bandwidth. The function, W, is defined to be a function of processing bandwidth and the relative mass and stiffness of the shaker head and specimen. Most FFT processors provide an RMS transfer function, and for two-channel operations, the transfer function is:

$$H_m(x_o,\omega) = [<\epsilon(x_o,t)^2>/<\ddot{z}^2>]^{1/2} . \qquad (10)$$

In equation (10), both the measured strain and acceleration must have the same processing bandwidth. Equation (10) is fundamentally different from most interpretations of the transfer function since it represents the ratio of averaged values within some processing bandwidth. The weighting function can be defined as the quantity multiplying equation (10) to give the exact transfer function at resonance.

The exact transfer function at resonance can be calculated from equation (4) and represents the zero-bandwidth case:

$$H_e(x_o,\omega_i) = \frac{\frac{h}{2\ell}\phi_i''(x_o)\int_0^{\ell}\phi_i(x)dx}{2\xi_i\omega_i^2} \qquad (11)$$

The RMS transfer function must be calculated by taking the Power Spectral Density (PSD) of strain and acceleration within the processing bandwidth. The square root of the ratio is the RMS transfer function.

First consider the PSD of the base acceleration. Since all frequencies within the processing bandwidth are excited, the dynamics of the shaker core must be included. Reference [8] has evaluated that by considering the beam resonance and the shaker dynamics as a two-degree of freedom lumped parameter system. With the damping in the shaker neglected, the PSD of the shaker head acceleration is.

$$S_{\ddot{z}}(\omega) = \frac{[(\omega_i^2-\omega^2)^2+(2\xi_i\omega_i\omega)^2]F_o/m}{[(\omega_s^2-\omega^2)(\omega_i^2-\omega^2)-\omega_i^4]^2+[(\omega_s^2-\omega^2)(2\xi_i\omega_i\omega)]^2} \qquad (12)$$

In equation (12), ω_s is the unloaded natural frequency of the shaker head, normally supplied by the manufacturer. The PSD of the strain may be calculated using equation (4):

$$S_\varepsilon(x_o,\omega) = \frac{[\frac{h}{2\ell}\phi_i''(x_o)\int_0^{\ell}\phi_i(x)dx]^2 S_{\ddot{z}}(\omega)}{(\omega_i^2-\omega^2)^2+(2\xi_i\omega_i\omega)^2} \qquad (13)$$

Now since the mean square is the integral of the PSD - frequency curve, equations (12) and (13) may be combined to give the RMS transfer function. Figure 4 demonstrates the integral within a single processing bandwidth centered at resonance. The weighting function, which is a function of processing bandwidth and loss factor, is calculated using equations (10) and (11):

$$W(\Delta,\eta_s) = H_e(x_o,\omega)/H_m(x_o,\omega). \qquad (14)$$

Figure 6 is a plot of the weighting function, W, versus processing bandwidth compared to data. The RMS transfer function was calculated by numerically integrating the PSD curves using trapezoidal rule. This can be done routinely even on micro-computers and the result stored for later use in calculating the exact transfer function. This procedure results in loss factor measurements under random vibration which can be made rapidly independent of processing bandwidth.

SUMMARY AND CONCLUSIONS

A forced-vibration loss factor measurement technique using digital test equipment is described. The base-excited double cantilever beam is used as a test specimen where the excitation frequency is set at resonance, giving a material loss factor measurement. When the excitation frequency is slightly off resonance, errors of several orders of magnitude are possible. Since digital spectrum analyzers inherently provide only discrete frequencies, it is impossible for FFT processors to provide the measured transfer function exactly at resonance. In order to provide useful results, the processing bandwidth must be made as small as possible, typically requiring a high resolution mode.

Under random excitation, there are two practical advantages over traditional sine-dwell test procedures: First, there is no need to precisely control the excitation frequency at resonance since all frequencies are present. Second, more than one mode can be excited during a single test. However, in order to conveniently apply random excitation, it is necessary to consider the severe bandwidth limitations. By introducing a weighting function, the exact transfer function may be calculated from the measured RMS transfer function. The weighting function is calculated by numerically integrating the PSD functions of the base acceleration and strain. The result is a weighting function which is independent of loss factor for lightly damped structures. This provides a general material damping measurement procedure for use with digital test equipment.

REFERENCES

1. Whaley, P. W., "A Thermodynamic Approach to Material Fatigue," to be presented to the Advances in Life Prediction Methods Conference, Albany, NY, 18-20 April 1983.

2. Smith, G. M., Y. C. Pao, and J. D. Fickes, "Determination of a Dynamic Model for Urethane Prosthetic Compound," Experimental Mechanics, Oct 1978.

3. Gibson, R. F., and R. Plunkett, "A Forced-Vibration Technique for Measurement of Material Damping," Experimental Mechanics, Aug 1977.

4. Chen, P. S., "Experimental Measurement of Loss Factor by Random Excitation," Unpublished M.S. Thesis, University of Nebraska, 1982.

5. Halvorson, W. G., and D. L. Brown, "Impulse Technique for Structural Frequency Response Testing," Sound and Vibration, Nov 1977, pp 8-21.

6. Gibson, R. F., "Elastic and Dissipative Properties of Fiber-Reinforced Composite Material in Flexural Vibration," Ph.D. Thesis, University of Minnesota, Applied Mechanics, 1975.

7. Plunkett, R. and Sax, M., "Nonlinear Material

Damping for Nonsinusoidal Strain," Journal of Applied Mechanics, Dec 1978, Vol. 45.

8. Granick, N., and J. E. Stern, "Material Damping of Aluminum by a Resonant-Dwell Technique." NASA TN D-2893, Aug 1965.

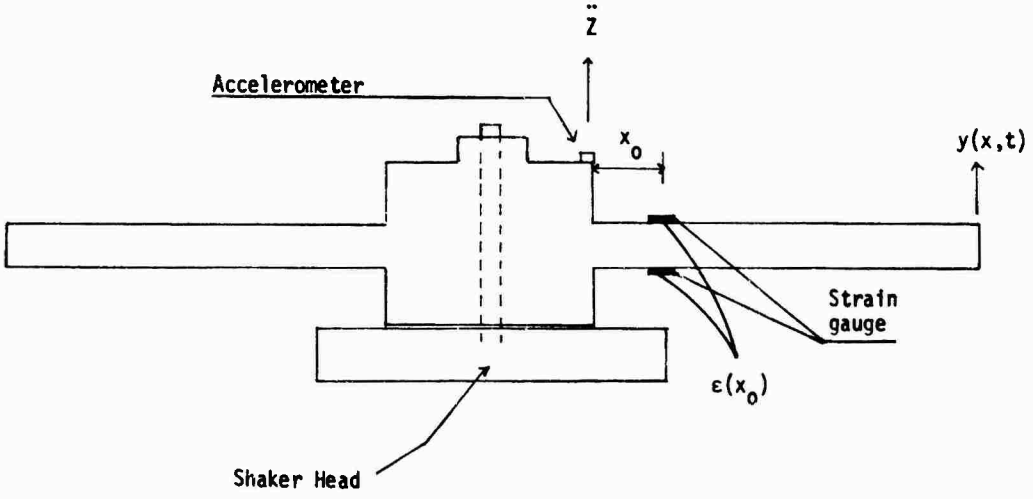

Figure 1. Schematic Diagram of the Base-Excited Double Cantilever Beam

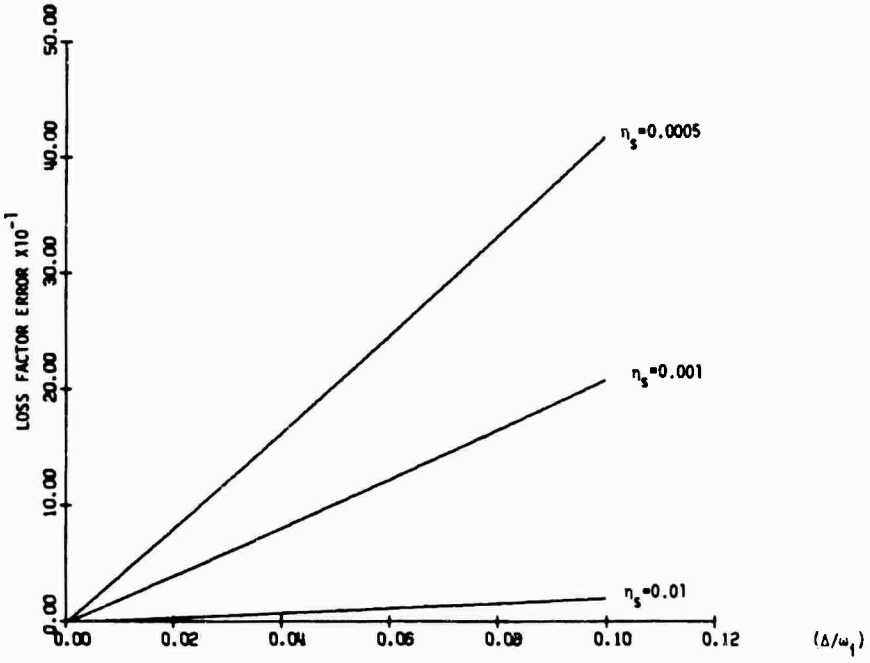

Figure 2. Error in Damping Measurements Caused by Missing the Specimen Natural Frequency

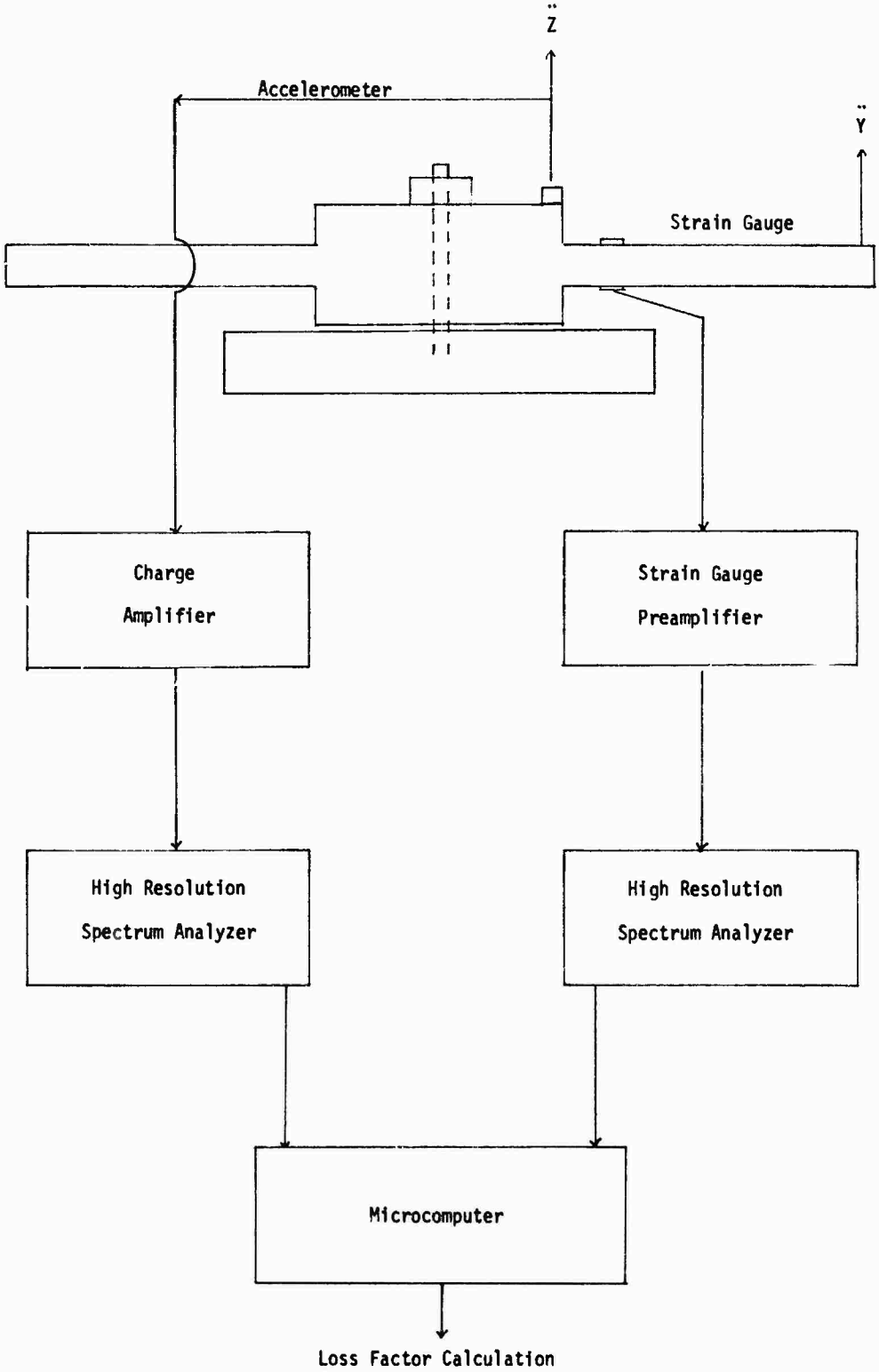

Figure 3. Instrumentation Diagram for Loss Factor Measurements Using Digital Test Equipment

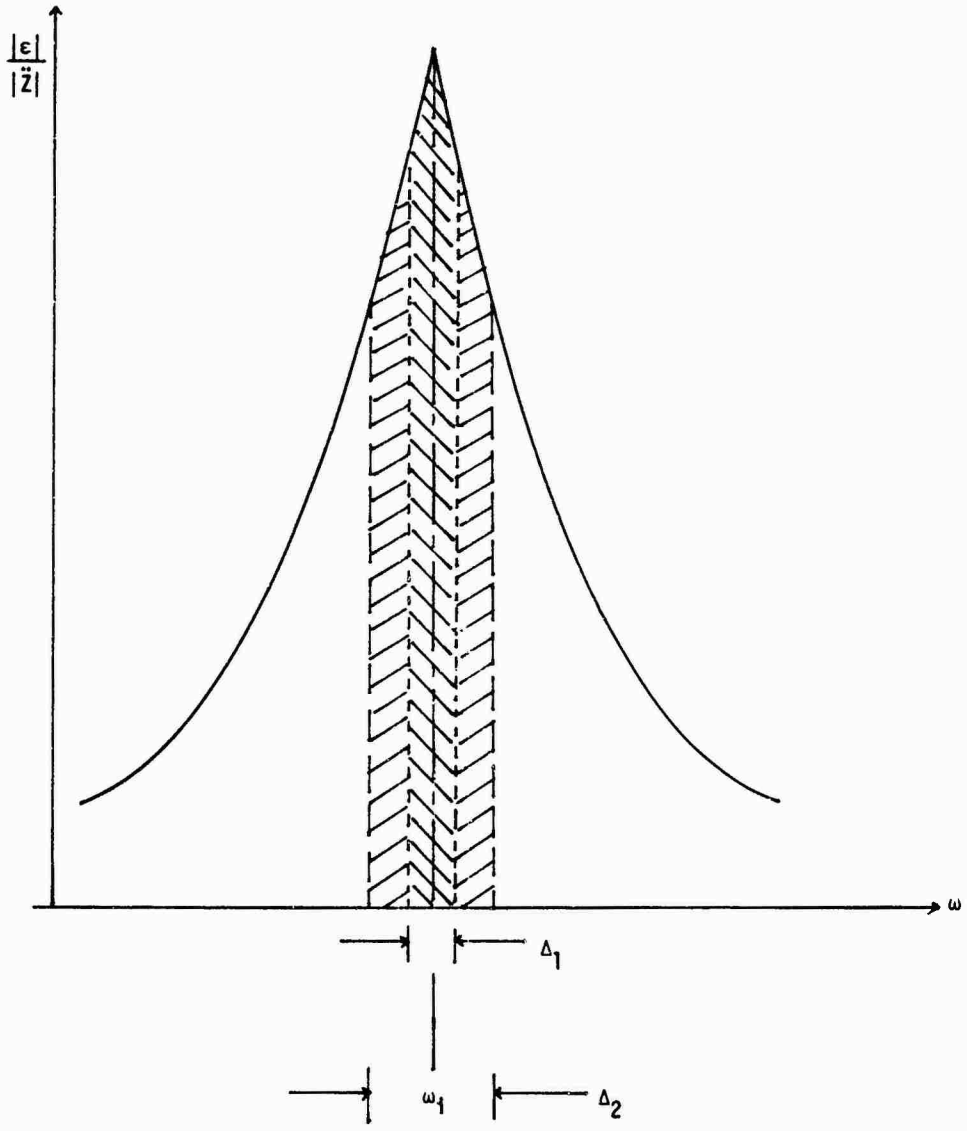

Figure 4. Resonant Amplitude with Two Different FFT Processor Bandwidths.

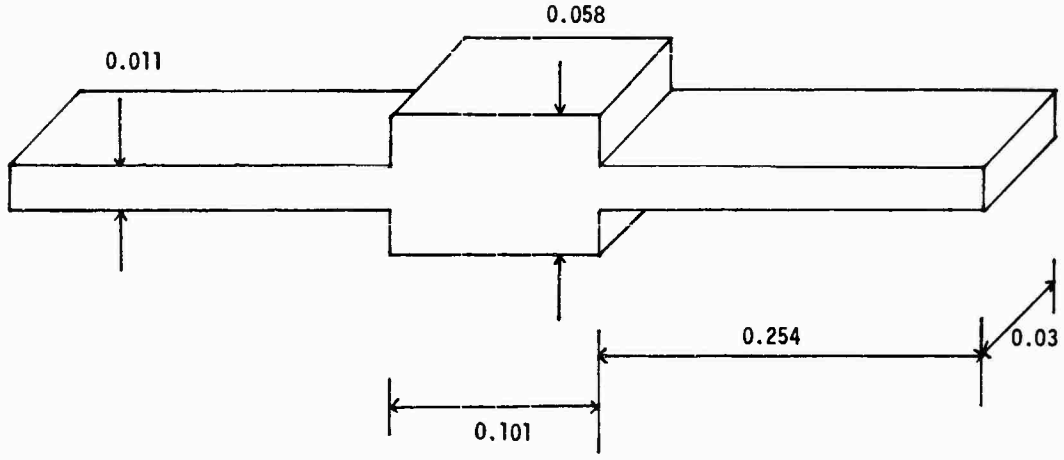

a. Dimensions of Aluminum Specimen in Meters.

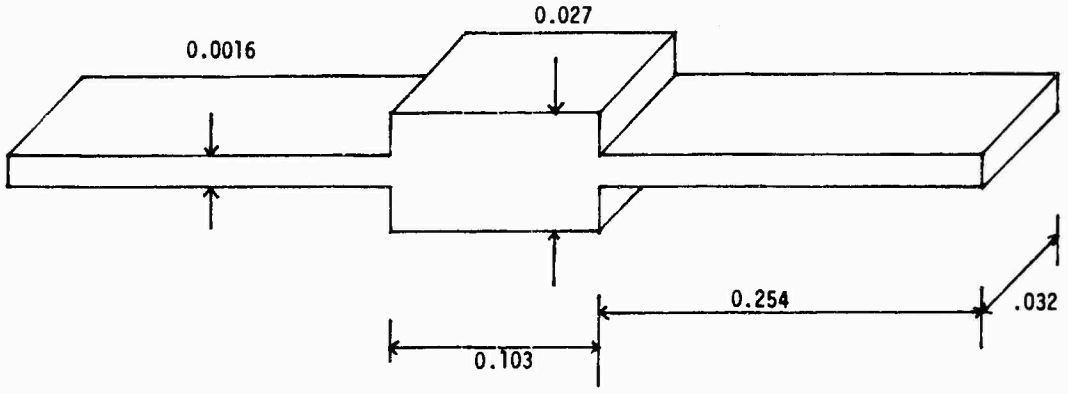

b. Dimensions of Composite Specimen in Meters.

Figure 5. Schematic of the Base Excited Double Cantilever Beam Specimens.

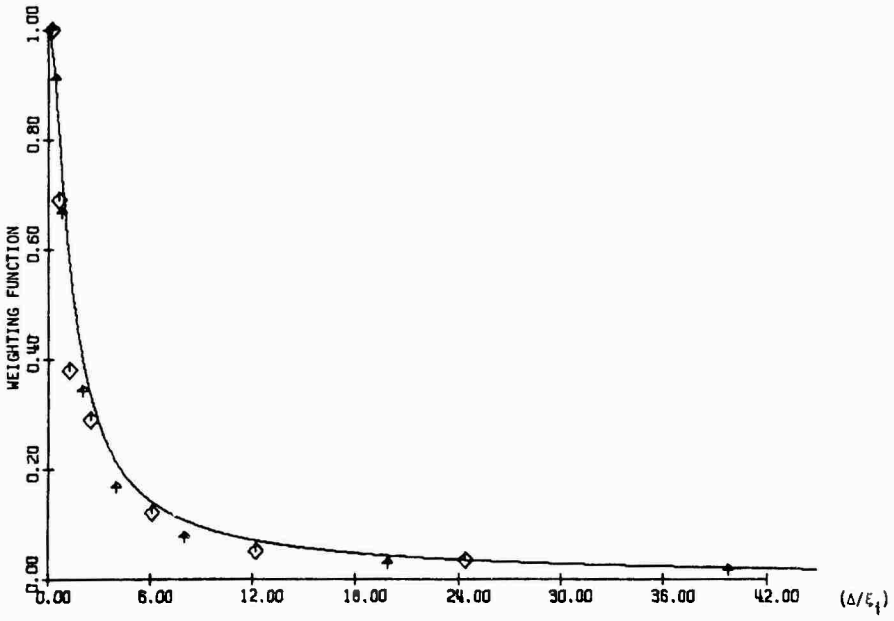

Figure 6. Weighting Function for Measuring Loss Factor Under Random Vibration Compared with Data.

ELECTRONIC DAMPING OF A LARGE OPTICAL BENCH

Dr. Robert L. Forward
Hughes Research Laboratories
Malibu, California 90265

and

Dr. Charles J. Swigert
Hughes Aircraft Company
Culver City, CA 90230

and

Capt. Michael Obal
Air Force Weapons Laboratory
Kirtland AFB, NM 87117

Electronic damping was used to reduce the amplitude of response of two problem vibrational resonances in a large optical bench. A small (76.2 x 15.88 x 1.52 mm) 14-g piezoelectric ceramic strain transducer was used as a sensor, and ten others in parallel were used as a combined driver in a velocity-feedback damping loop operating on the bench. The data taken during this study shows that electronic damping using a single damping loop is sufficient to control both modes even when excited at the high levels of acoustic and vibrational noise experienced by the bench in its operational environment.

INTRODUCTION

We have demonstrated active electronic damping techniques on a large optical bench used in the aerospace environment. The current configuration of this bench requires that stringent alignment be maintained among various optical control components for proper operation. These alignment constraints are difficult to achieve because of the sensitivity of the various optical components to vibration and acoustic noise.

The primary sources of the vibration environment are the environmentally induced noise levels and, to a lesser degree, vibrations in the mounting structure for the bench. To isolate the optical components from this noise environment, the optical bench is supported on four elastic isolators. Unfortunately, there are other paths of vibrational coupling to the bench, such as acoustic coupling, vibration coupling through pressure diaphragms around various optical components, and pressure coupling through coolant water supplies to bench optical components.

The normal modes of the optical bench were analyzed using the NASTRAN finite element structural analysis program. There are 185 modes below 700 Hz. Most of the vibrational mode responses of the optical bench at the lower frequency modes are compensated for by an active alignment system which uses two active mirrors. These move to keep the beam properly directed through the various optical components. The control servos for this active system start to fall off at 250 Hz, so that resonances above this frequency cannot be controlled properly and may, in fact, be amplified by the servo response characteristics.

Initial tests with the bench in its environment showed an unacceptable amount of angular jitter in the optical beam path. Analysis of the test data

*Work sponsored by Air Force Contract F29601-80-C-0056.

showed that a majority of the jitter in the optical path was caused by two resonances. The resonances were not only seen in the optical path, but also in accelerometers attached to the bench. The measured accelerations correlated well with the observed optical jitter. The forward acceleration at a point at the left rear end of the bench where a critical mirror is attached is shown in Figs. 1 and 2. Figure 1 is the power spectral density plot from 100 to 1,000 Hz, while Fig. 2 is the backward sum of rms acceleration obtained by integrating the power spectral density from 1,000 Hz down to 100 Hz. As can be seen by the two figures, one resonance at 267 Hz causes 60% of the response with an acceleration level of 0.50 g rms, while another 22% is contributed by a resonance at 302 Hz with an acceleration level of 0.18 g rms. The remaining 18% of the response comes from other resonances. As will be demonstrated later, these two resonances can be shown to be vibrational modes of the optical bench. The modes are well coupled to the system optics through their effect on the mirror box, and are outside the effective range of the bench active alignment servo bandwidth.

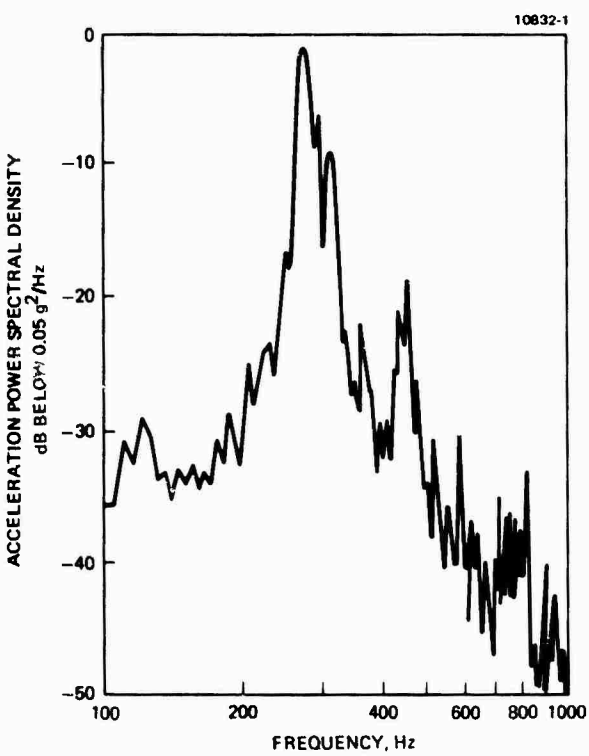

Fig. 1. Forward bench acceleration power spectral density on tab below left rear mirror box.

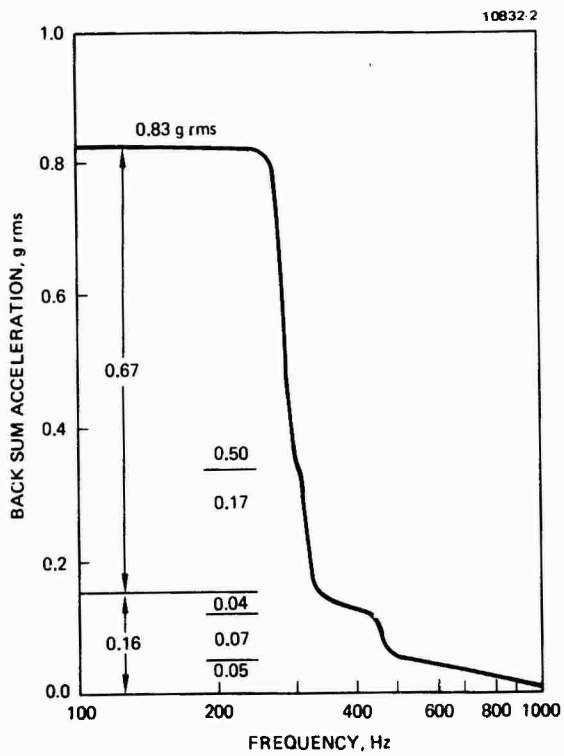

Fig. 2 Back sum of forward bench acceleration on tab below left rear mirror box.

Our task in this study was to determine if some form of electronic damping applied to the optical bench could control these modes.[1-5] The alternative to damping (either active or passive) would be a redesign of the optical bench to remove the resonances, or an upgrade of the active mirror alignment systems so they could cope with these high frequency modes.

There was initially some concern as to whether a simple application of electronic damping would suffice for the problem of damping the optical bench. First, the bench is massive and stiff, and the driver transducers might not be capable of handling such a large structure. The bench weighs about 1,400 kg and consists of a metal honeycomb structure 25 cm thick, with bonded top and bottom plates of reinforced carbon fiber composite varying from 1.25 to 3 cm thick. The modulus of elasticity of the composite is 100 GN/m^2. The effective mass of the modes, however, is probably much less than the total bench mass. The NASTRAN model, for example, predicts an effective mass of about 25 kg.

The second area of concern was that there was more than one vibrational mode to be damped. As we have shown before [3,4], if there is more than one

vibrational mode, then a single damping circuit may not be able to damp all the modes at the same time. For a single damping loop to control more than one mode, the sensor and driver transducers must have the same phase relationship to all the modes to be damped. This is usually accomplished by colocating the sensor and driver. Too close a placement, however, leads to problems with direct electrical and mechanical coupling of the driver transducer to the sensor transducer by channels other than those through the structure to be damped. Even then, at a sufficiently high level of damping, the modes will overlap in frequency space, and can reconfigure into new modes. One will be well coupled to the damping circuit and will be highly damped, while the others will become decoupled from the damping circuit and will return to their original low-damped state [3-4]. Our preliminary testing on the optical bench was to ascertain (1) that it was possible to find placements for the transducers that would permit both problem modes to be damped to an adequate level with a single, simple feedback circuit, (2) that there were not other modes that were 180 degrees out of phase and would oscillate, and (3) that a resonable level of damping would be achieved without the modes reconfiguring into a damped and an undamped mode.

A third area of concern was whether the electronic damping circuits and the driving transducers could supply the force and power levels needed to combat the vibrational excitation levels to be expected in the bench operational environment. To supply the power needed, we developed a high-voltage, high-power electronic circuit and used it to drive a number of forcing transducers in parallel. Test in the bench environment showed that the power level was adequate to produce significant amounts of electronic damping.

STUDY OF OPTICAL BENCH MODES

The primary problem mode of the optical bench, the 267 Hz mode, has a shape that is shown in Fig. 3. Notice that most of the motion in the mode is in the bending of the "tab" at the left rear portion of the bench. This tab holds one of the critical mirrors supported by its mirror box. Figure 3 was derived by Captain Steve Lamberson of AFWL from his NASTRAN model. The NASTRAN model gives the frequencies and shapes of the modes accurately, but assumes a default structural damping of 2%, or a Q of 50, for all the modes.

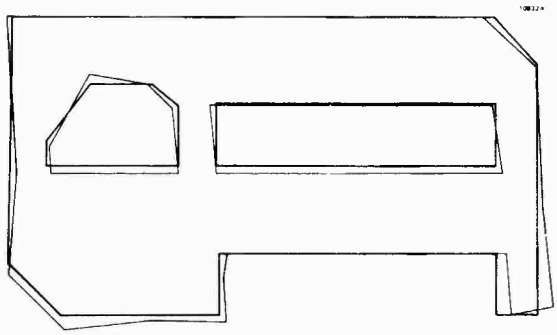

Fig. 3. NASTRAN model prediction of 267 Hz mode shape.

(The Q of a mode is defined as the ratio of the center frequency of the mode to the half-power bandwidth. The Q is inversely proportional to the structural damping coefficient, which in turn is twice the fraction of critical damping. A Q of 10 is equivalent to a structural damping coefficient of 0.1, or 5% of critical damping.)

Numerous modes are predicted by the NASTRAN model for this region of the frequency spectrum, including those at 247, 262, 267, 275, 284, 288, 289, 293, 300, 309, and 316 Hz. To determine the frequency and response amplitude of the actual modes in the bench and their effect on the left rear mirror, the bench was analyzed using a shaker and accelerometers.

To insert a known level of vibration into the bench, a 34 N (150 lbf) shaker was attached between the floor and the front left side of the bench through a force gauge. The shaker was driven by a random noise source, and the force applied to the bench was read out by the force gauge. Accelerometers were then placed at various points on the bench, including the same point on the bench that the acceleration measurements were taken for Figs. 1 and 2. A General Radio Modal Analysis System then correlated the output of the accelerometers with the output of the force gauge. By placing accelerometers at many different points on the bench, it was possible not only to determine the frequency and amplitude of the modes, but also their shape. It was found that any mode that causes a forward directed acceleration of the bench at the tab holding the left rear mirror box caused both a linear motion and a tilt of the mirror. (See Fig. 4.) The tilt then produces a misdirection of the optical path, or optical beam jitter.

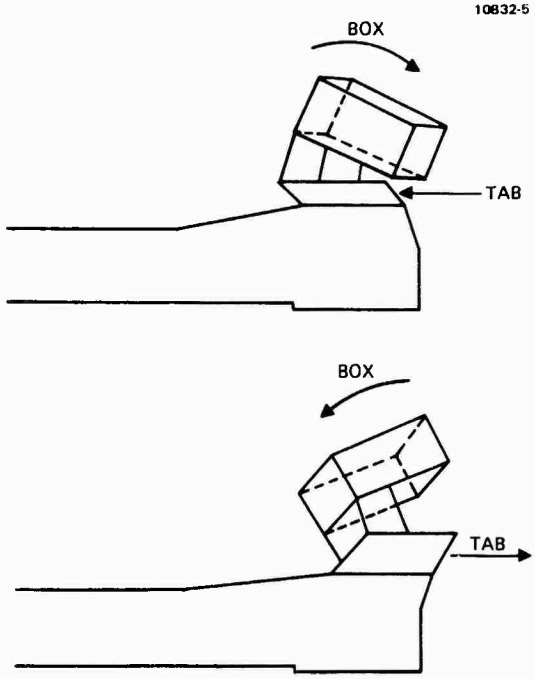

Fig. 4. Motion of left rear mirror box on top of horizontally vibrating tab.

The response of the forward accelerometer on the tab below the mirror box to the shaker excitation is shown in Fig. 5. This figure shows that many modes in the bench contribute to horizontal tab acceleration. The predominant modes, however, are at frequencies of 275, 318, and 345 Hz. Because of changes made to the bench between the data taken in Figs. 1 and Fig. 5, there were shifts in the modal

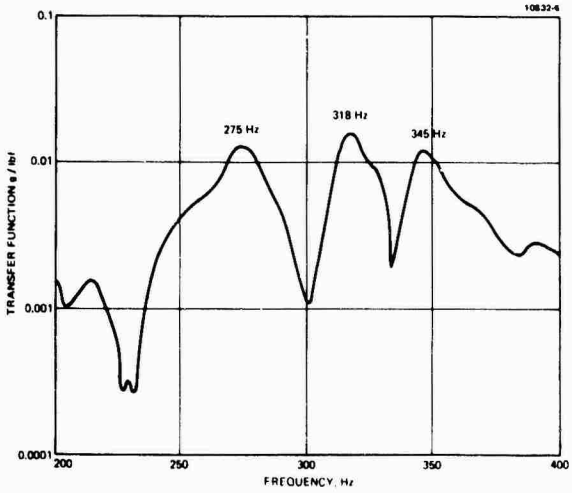

Fig. 5. Forward bench acceleration from shaker at point below left rear mirror box.

frequencies. We can identify the 275 Hz mode as being the previous 267 Hz mode, the 318 Hz as being the old 302 Hz mode, and the 345 Hz mode as being one of the modes in Fig. 1 that was many decibels down in its response to environmental excitation (as opposed to shaker excitation). These shaker tests showed that the two problem resonances seen during the test are bench modes, since they are excited by shaking the bench. The tests also showed that the two modes produce significant horizontal and vertical accelerations at the tab holding the left rear mirror box, and that these bench tab motions will in turn produce tilts in the mirror, which consequently causes jitter on the output beam.

ELECTRONIC DAMPING

The first task in applying electronic damping to a structure is to find some method to sense what the structure is doing. The second task is to find some way to drive the structure. Once the problem modes are detected by a sensor and excited by a driver, then the loop between the sensor and driver is closed using a feedback circuit that produces a drive that is proportional to the velocity of the structure motion. The effect of this electromechanical circuit will be to produce velocity feedback damping. In principle, electronic damping can use any type of sensor or driver. We have used accelerometers, velocity meters, and piezoelectric strain transducers as sensors; and shakers, torquers, mass loaded piezoelectrics, and piezoelectric strain transducers as drivers. Piezoelectric ceramic strain transducers have proved to be versatile, since they can be used either as a sensor or a driver, work directly on the structure without requiring a mechanical ground to work against, have good electrical-to-mechanical energy conversion efficiencies, and are very sensitive and powerful for their size [2]. Typically, the ratio of transducer mass to structure mass needed for electronic damping is less than one part in 1,000.

Based on the mode shape predictions, we noticed that most of the motion that would couple into the optical path would take place in the tab at the left rear portion of the bench holding the left rear mirror. Since our piezoelectric transducers are strain transducers, we chose places for attachment that would have high strain induced in the bench by the motions of the 275 Hz mode. The transducers that we had on hand for use in the feasi-

bility study were Gulton piezoelectric ceramic strain transducers that were 76.2 x 15.88 x 1.52 mm in size, and weighed 14.1 g without leads. The elastic modulus of the piezoelectric ceramic is similar to that of aluminum, i.e., 70 GN/m^2. The positions of the transducers and the accelerometer that we used in this study are shown in Fig. 6. (We were somewhat limited in placement choice because of the proximity of plumbing and the left rear mirror box.)

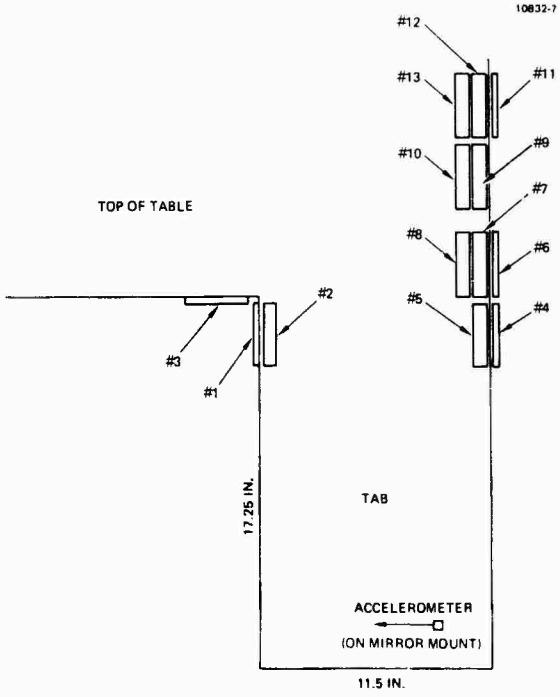

Fig. 6. Placement of transducers and forward accelerometer.

Our first task was to determine if these transducers were detecting the desired modes. Using the shaker to excite the bench, we obtained a transfer function between the force gauge on the shaker-bench interface and the voltage output of each of the transducers. Transducer 3 had relatively poor coupling to the modes, while transducer 1 and 2 had good coupling to the modes at 275 and 318 Hz. In addition, transducer 2 had little coupling to other modes (See Fig. 7.) All the transducers on the back edge of the table had approximately the same transfer function, although transducers 4 through 8 were slightly better coupled than transducers 9 through 13. Because of this similarity, it was decided to run transducers 4 through 13 in parallel as a driver, and to use transducer 2 as the sensor, since it would limit the response of the feedback loop to the two

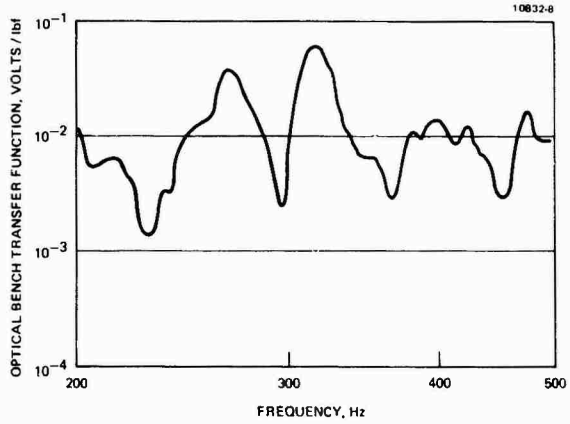

Fig. 7. Optical bench transfer function from shaker force gauge of piezoelectric transducer 2.

modes of interest. The voltage transfer function of the ten transducers in parallel is shown in Fig. 8. (Since the transducers are in parallel, the voltage amplitude is the mean of the individual transducers, while the current would be the sum.) The transfer function shows good coupling to the 275 and 318 Hz modes, plus a significant response at 345 Hz.

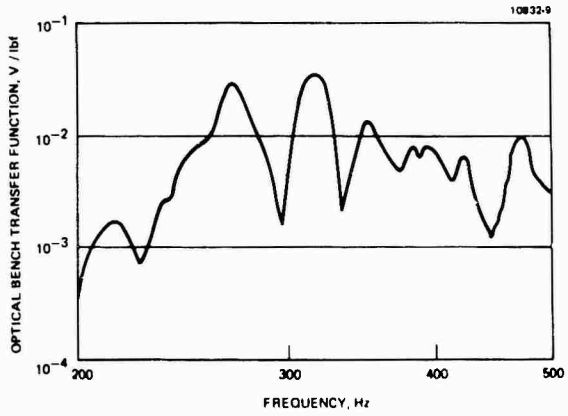

Fig. 8. Optical bench transfer function from shaker force gauge to piezoelectric transducers 4 through 13 in parallel.

We then set up a damping loop between transducer 2 and the ten driver transducers. (See Fig. 9.) The output from the sensor Transducer 2 was placed into the input of one of our special damping circuits that can independently vary gain, center frequency, bandwidth, and phase with minimum interaction. The circuit also has the advantage that the first stage is a current-to-voltage amplifier. This not only provides good coupling to the piezoelectric strain transducer, but also produces a 90 degree phase shift that is independent of frequency. This automatically gives

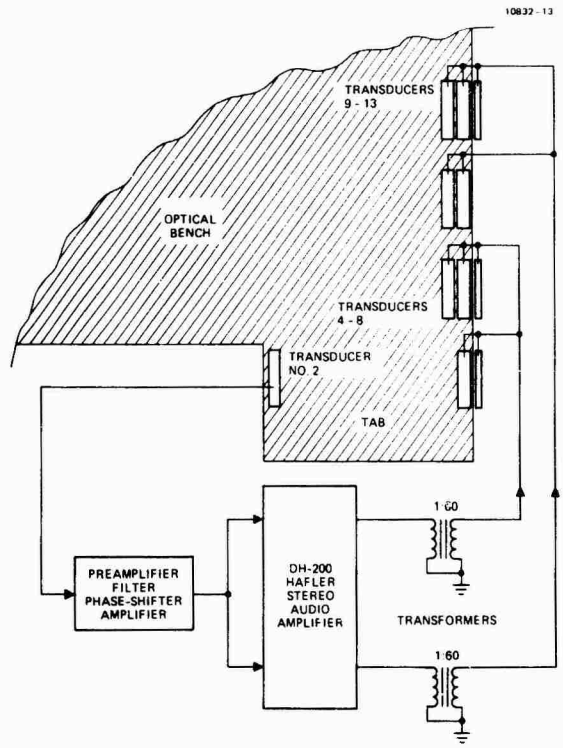

Fig. 9. Schematic of electronic damping feedback loop.

the 90 degree phase shift needed for velocity damping. The schematic is shown in the appendix. Once this circuit has been used to find the optimum circuit characteristics for a particular damping problem, it can be replaced by a much simpler circuit with fixed gain, frequency, bandwidth, and phase.

The frequency of the bandpass filter was set near 275 Hz and the Q of the filter was set at 3, giving a bandpass of about 90 Hz. The gain and phase were then adjusted to give high damping without oscillation.

To handle the power levels expected during bench operation in its environment, we modified the final power stages of the feedback circuit. The power stage was replaced with a 200 W stereo-audio amplifier, coupled into transformers that provided a 1:60 voltage amplification. Each half of the audio amplifier drove five of the transducers in parallel through one of the transformers. Diodes were used in the input to the final stages so that the maximum output drive voltages would be kept well below the voltage arc-over point for the transducers (about 2,000 V peak).

With the damping loop tuned and operational, we were able to drastically reduce the amplitude of the two problem modes at 275 and 318 Hz, as well as to significantly decrease the amplitude of the mode at 345 Hz. The response of the optical bench to the shaker excitation, with and without the electronic damping loop active, is shown in Fig. 10. The 275 Hz mode was decreased in amplitude by a factor of 3.2 or 10.2 dB, while the 318 Hz mode was reduced by a factor of 3.6 or 11.2 dB.

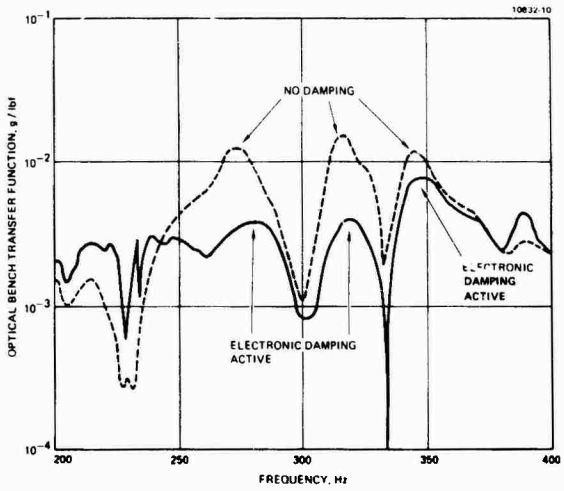

Fig. 10. Optical bench transfer function from shaker force gauge to forward accelerometer on tab with and without electronic damping active.

PASSIVE DAMPERS

While our electronic damping studies were in progress, other potential solutions to the bench vibration resonance problem were being brought along in parallel. The first technique used an untuned passive damper, consisting of two 20 cm long, 10 cm wide stiff plates. One plate was attached to the rear of the left rear mirror box, and the other to the back of the mirror box pedestal on the bench.

The plates overlapped about 5 cm, and a viscoelastic rubber was bonded between the two in the region of overlap, forming a damper. This damper was designed to work on the relative vertical motion of the mirror box with respect to the top of the table, with the rubber providing damping. The damping plates were attached to the table and a small decrease in amplitude (2 to 3 dB) of the vibrational resonance at 275 Hz was observed. Despite the small effect, it was decided to leave the damping plates on the bench.

The second technique used a passive tuned damper, consisting of two inertial weights (0.59 kg each), attached to a bench mounting fixture through a viscoelastic rubber. (See Fig. 11.) By

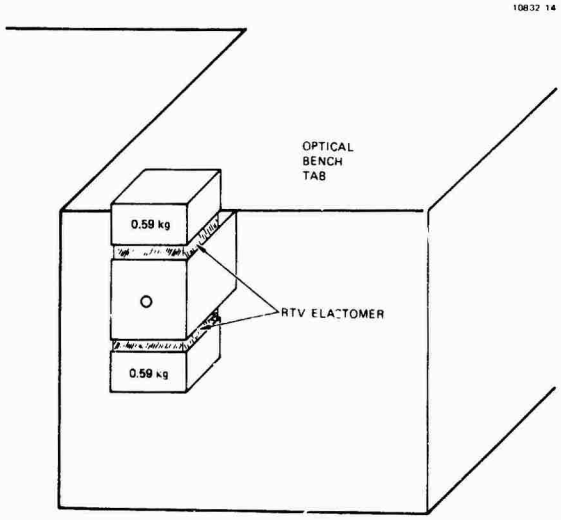

Fig. 11. Passive-tuned damper. Central block is bolted to bench tab.

proper choice of the rubber thickness and compound (typically 5 mm of solid silicone RTV rubber), the device could be "tuned" to resonate near the frequency of the bench mode at 275 Hz. When the passive tuned damper was attached to the end of the tab in the proper orientation, the vibrational energy in the bench would couple into the tuned damper, causing the tuned damper to vibrate at high amplitude. These high amplitude vibrations were then dissipated by the rubber compound.

MULTIPLE DAMPER TESTS AT LOW VIBRATORY LEVELS

Various damping techniques were tested on the optical bench under varying types of bench excitation. Figure 12 shows the transfer function from a force gauge in the head of a calibrated hammer to the forward-facing accelerometer on the mount for the left rear mirror box on the tab. The hammer was used to strike the back side of the tab in the forward direction. The dotted curve was the response when only the damping plates were used. A number of changes, in addition to the damping plates, were made to the optical bench, between the data shown in Figs. 10 and 12. Therefore, the dotted curve becomes our new baseline. (The differences in shape of the curves in Figs. 10 and 12 are caused by the difference in excitation. Fig. 10 is excited by a shaker and Fig. 12 by a calibrated hammer. The frequency of the resonant peaks are the same, but their amplitude and shape differ with the two means of excitation.)

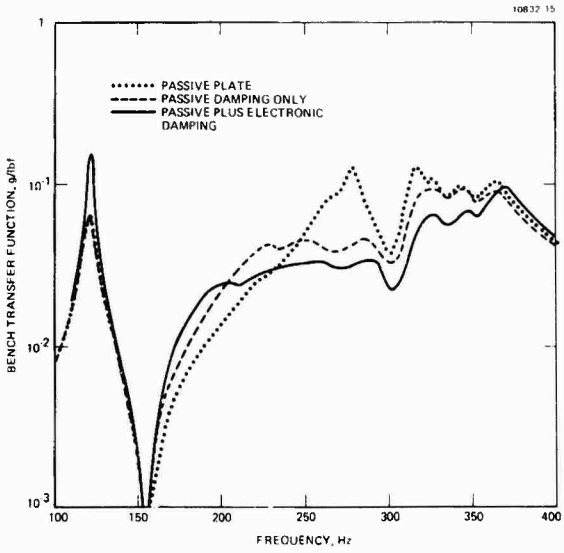

Fig. 12. Bench transfer function between hammer and forward-facing accelerometer on bench tab for three different damping conditions.

Next we attached the passive tuned damper and adjusted it to give maximum damping to the 275 Hz mode. The resulting response curve is given by the dashed line in Fig. 12. As can be seen, the passive tuned damper produced a reduction in the response at 275 Hz of 2.7 in amplitude or 8.6 dB in power. There was also a small reduction in the amplitude of the 318 Hz mode. Although the amount of damping was not as great as the 10.2 dB obtained from electronic damping alone (Fig. 10), it was significant, and we left both of the passive dampers on during the remainder of the tests.

With both passive damper systems on, the electronic damping circuit was turned on, and the bench was retested with the calibrated hammer. The resulting transer function, with all three damping systems active, is given by the solid line in Fig. 12. As can be seen, the 275 Hz mode amplitude was reduced a factor of 3.8 in amplitude or 11.6 dB in power and has been pushed so far into the background level that it no longer exists as a distinct mode. The electronic damping also had a significant effect on the 318 Hz and 345 Hz modes.

Note that the electronic damping circuit caused an increase in the vibrational mode at 122 Hz. This mode would oscillate if the gain of the electronic damping feedback circuit were further increased. This amplification

of a mode, other than the one being damped, is one type of problem that arises when trying to damp more than one mode with a single damping loop. Fortunately, the 122 Hz vibrational mode is well within the servo bandwidth of the active mirror alignment system. Thus, the effects of a vibration at this frequency on the optical path will be compensated by the active alignment system. If this were not the case, it would be necessary to construct another feedback loop to damp out the 122 Hz mode. This second damping loop can share the same sensor input with the 275 Hz mode, and its output can be summed with the output of the 275 Hz filter amplifier prior to the power amplifier stage. (An example of feedback loops sharing common sensors and drivers is given in Ref. 5, where five feedback damping circuits shared three sensors and two drivers in various combinations.)

MULTIPLE DAMPER TESTS AT HIGH VIBRATORY LEVELS

With the two passive tuned dampers and the electronic damping circuit operational, the optical bench was subjected to the high levels of vibrational and acoustic noise generated by its environment in two tests. The first test used both passive and electronic damping, while the second used passive damping only. Although the optical bench had gone through a number of modifications, and differences in the generated noise level from test to test were generally anticipated, it was felt that the noise conditions in the two tests were similar to the earlier tests that produced the data for Figs. 1 and 2. The results of all three tests are plotted together in Figs. 13 and 14. Figure 13 is the acceleration power spectral density of the response from the forward facing accelerometer mounted on the tab below the left rear mirror box. Figure 14 is the back sum acceleration in rms gravities from 1,000 Hz down to 100 Hz.

The tallest curve (dotted) in Fig. 13 is the result of the earlier test with no damping. It is a repeat of Fig. 1 with the data smoothed to take out the digitalization noise. The lowest curve (solid) in Fig. 13 is the result of the first test with both passive and electronic damping techniques operating. We can see from Fig. 13 that the peak of the 275 Hz mode has been decreased by 12.2 dB, and the 318 Hz mode has been decreased by 5.1 dB.

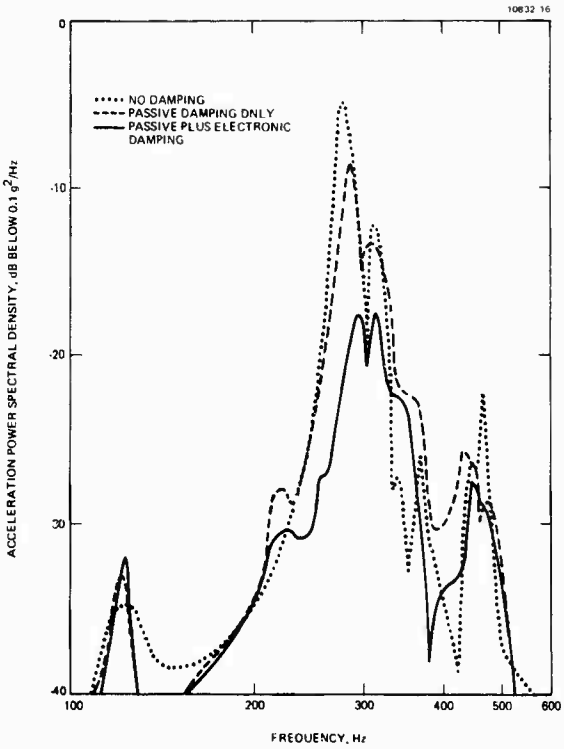

Fig. 13. Acceleration power spectral density from forward accelerometer on bench tab for three different damping conditions during high-level vibrational and acoustic tests.

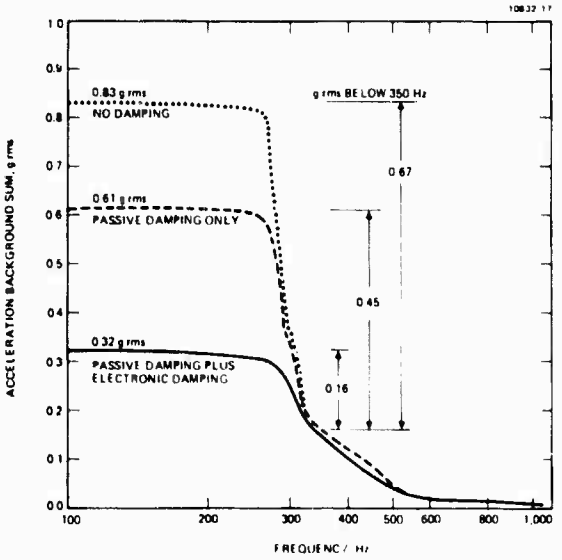

Fig. 14. Back sum of forward acceleration on bench tab for three different damping conditions during high-level vibrational and acoustic tests.

If we go to Fig. 14, which shows the backward sum of the total acceleration, we can see that the combined damping techniques significantly affect

the total rms acceleration. The level dropped from 0.83 g rms to 0.32 g rms, a factor of 2.6 in amplitude, or 8.3 dB in power. If we only consider the change in rms acceleration at frequencies below 350 Hz, where the level is 0.6 g rms, then the ratio between damped and undamped case is greater. The difference is 4.2 in amplitude and 12.6 dB in power.

This high vibration test, with all three damping solutions operating, was then followed on the same day by another high vibration test, with the electronic damping circuit turned off, leaving only the two passive dampers acting on the 275 Hz mode. These data are shown as the dashed lines in Figs. 14 and 15. As can be seen, the passive-tuned damper was not as effective as it had been previously in the low level tests. The 275 Hz peak was only reduced by 3.5 dB, and the total back sum acceleration only dropped from 0.83 g rms to 0.61 g rms, a factor of 1.3 in amplitude, or 2.6 dB in power. The decrease in rms acceleration below 350 Hz was also small, (3.5 dB) matching the decrease in peak response at 275 Hz.

There are two possible reasons for the degradation in performance of the passive-tuned damper between the low- and the high-level tests. One is that the tuning had drifted off and the damper became less effective; the other is that the passive tuned damper saturated at high power levels. An evaluation of the passive damper tuning variation with temperature was performed. This showed that dissipation of mechanical power in the mode heats the silicone elastomer thereby changing the shear modulus and, as a result, the tuning resonance.

Because the passive tuned damper was probably not operating properly in the high-level tests, most of the 12+ dB improvement between the earlier undamped test and the later multiple damped test probably can be attributed to the electronic damping circuit.

CONCLUSIONS

Shake tests have shown that there are two vibrational modes of significant concern in the large optical bench under study: a mode at 275 Hz, and a mode at 318 Hz. They produce significant horizontal accelerations at the tab holding the left rear mirror box, and these horizontal motions will in turn produce tilts in the left rear mirror, which produces the angular jitter seen on the optical beam path during tests in the bench operational environment.

During both low-level shake tests and high-level environmental tests, it was shown that a single sensor piezoelectric transducer and ten driver transducers can reduce the amplitude of these problem modes by up to 12 dB without saturating, and without causing oscillations in other bench modes.

ACKNOWLEDGMENTS

The authors wish to acknowledge the assistance of James P. Lauffer (Anamet Labs), Major John Russell, TSgt. Jack Vlk, Captain James Van Sickel, and Brian F. Hower, who spent many hot second-shift hours dressed in cleanroom suits helping us collect vibration data. Robert L. Forward also wishes to acknowledge the technical assistance of Cesar De Anda and the extremely cooperative Hughes team in Albuquerque. He also wishes to publicly praise the bravery and professional dedication of Gary D. Thurmond, who despite having his finger broken and his nail torn off in a late evening mishap with an air-lock door, showed up early the next morning with his finger in a splint to assist in the installation of the drive transducers.

REFERENCES

1. R.L. Forward, "Electronic Damping of Vibrations in Optical Structures," Appl. Opt. 18, 690-697 (March 1979).

2. R.L. Forward, "Picostrain Measurements with Piezoelectric Transducers," J. Appl. Phys. 51, 5601-5603 (November 1980).

3. C.J. Swigert and R.L. Forward, "Electronic Damping of Orthogonal Bending Modes in a Cylindrical Mast — Theory," J. Spacecraft and Rockets 18, 5-10 (January-February 1981).

4. R.L. Forward, "Electronic Damping of Orthogonal Bending Modes in a Cylindrical Mast — Experiment," J. Spacecraft and Rockets 18, 11-17 (January-February 1981).

5. C.P. Liu and R.L. Forward, "Electronic Damping of Resonance in Gimbal Structures," AIAA Paper No. 81 0556, Proceedings AIAA/ASME/ASCE/AIS 22nd Structures, Structural Dynamics, and Materials Conference, Atlanta, Georgia, 6-8 April 1981.

APPENDIX

SCHEMATIC FOR DAMPING LOOP PREAMPLIFIER/FILTER/PHASE SHIFTER/POWER AMPLIFIER

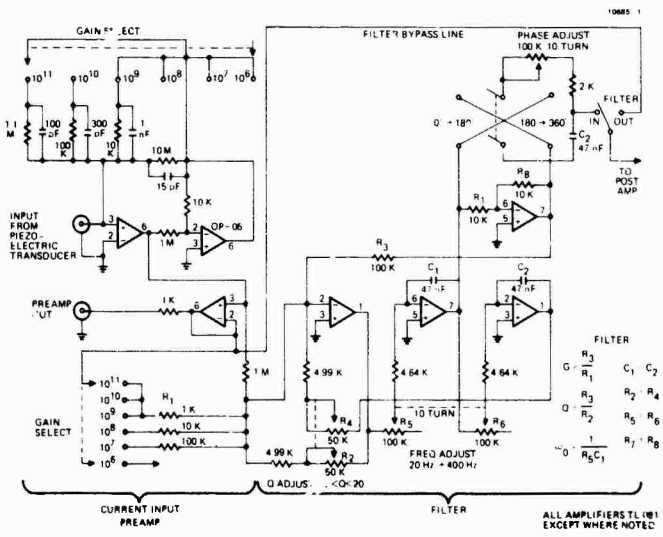

Fig. A-1. Schematic for preamplifier/filter/phase shifter.

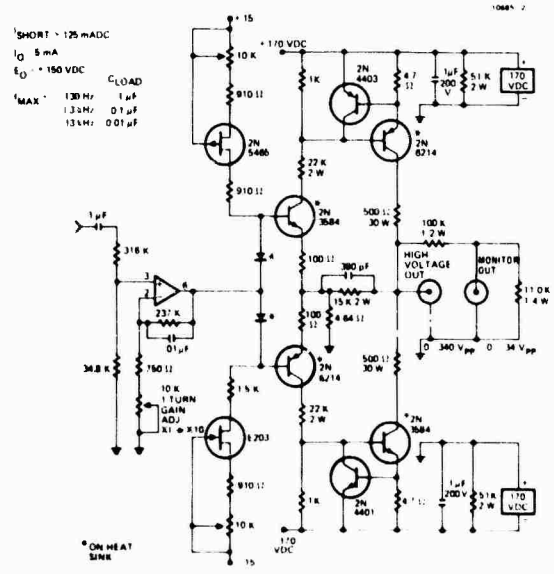

Fig. A-2. Schematic for power amplifier.

DISCUSSION

Voice: What was the bench material?

Mr. Forward: I think it was graphite epoxy with stainless steel honeycomb.

Mr. Jha (SPAR Aerospace) Can you use electronic damping for heavy space structures? Is it possible? Are there any programs?

Mr. Forward: I think the real problem is that it involves an active circuit. In space we have a weight problem, and you must count the electronics in, not just what you are packaging. One of the things I found about electronic damping is the amount of material I have to put on the struture is very small. Another thing is that in space the amount of

power, the noise power that is getting in, is very small. You would be surprised. If you take a very large, heavy bench, or a large space structure that moves at a couple of millimeters so that you can see it, you can calculate the frequency at a few tens of hundreds of Hertz. You can calculate the amount of energy in that structure, and quite typically it's less than the joule. Sometimes it is a few joules. But that is only Watts in terms of power. So I think the answer is, in space I would really try and find a passive system. But there are some situations where electronic damping is very powerful because all you do is increase the gain, and you have more damping. It is very powerful, and you should use it on any kind of ground-based structure.

Mr. Volin (Shock and Vibration Information Center): What was the source of the 267 Hz excitation?.

Mr. Forward: That was a natural mode of the bench, and the acoustic environment of the bench had plenty of excitation at that level. So that was a very sensitive mode of the bench, and more important, it happened to activate that tab which had an optical component on it.

Mr. Sankar (Concordia University): That term electronic damping, is it a force generator? There are ten piezo-electric transducers. Are they force generators?

Mr. Forward: They are strain generators.

Mr. Sankar: What is the maximum force that they can generate in terms of strain level?

Mr. Forward: It depends on the size of the transducer, but basically, the forces are quite high. We made that bench sing. We could actually hear it ringing when we drove it. If I put these things in the proper place, they will shake the structure as much as a shaker will. I think the main thing is that they have the strength for this; barium titanate has the strength of aluminum, and so it will bend other structures. If you put it on steel, it won't bend it as much. I really don't know how much force it will put into a structure because it depends on the structure. But the equations are just straight forward equations out of old handbooks. I think the important thing about barium titanate piezo-electric transducers like these is they are very good couplers; you get something like 35% electro-mechanical transfer of energy into a structure and back out again. They work both ways; you can use them as a driver or as a detector. As a detector they are 50,000 times more sensitive than a resistance strain gage, and I have published a paper which demonstrates that. If you go to the manufacturer, he finds they are only 50 times more sensitive than a resistance strain gage; the reason is, that they are high impedance, but the manufacturer probably used a low impedance scope when he made the measurements. But anyway, they are very sensitive since they can measure strains down to 10^{-13} and 10^{-16} inches per inch; they are also very powerful force drivers. And the other beauty about them is since they work on strain, they work between different parts of the structure. You don't need an inertial ground for them to push against, unlike a shaker. I have been able to damp out vibration in practically anything when I used them.

Mr. Sankar: Was the one that was used a commercial unit?

Mr. Forward: Yes, they are commercial units. There are certain ones you can buy that are very convenient to use. But this one is made by Gulton, and they make them for phonograph pickups, and they make them for the Navy sonar. It is the same kind of material used in sonar, and in ultrasonic cleaners. They will make them to your specifications. Basically, it is a piece of ceramic that is made just like a plate. You take a green clay, and you mold it to whatever shape you want. You can get hemispherical shapes, curved shapes, or you can get any shape you want. Before you bake them, you put on the electrodes and you apply a very high voltage, like 5,000 or 10,000 volts. This polarizes the material and as it is baked, it builds in an electric field. The piezo-electric effect varies as the square of the voltage, but when you build in the polarization field, you have a bias, therefore it becomes a linear response. The real problem with these is that they are temperature sensitive, but you can get mixtures that are not so bad. The other real problem, to be frank, is quality control. I have gotten two different batches, and when I looked at the ceramic underneath the plating, one was greenish; the other was yellow. The reason for that is, when they make them, they take a handful of this, a handful of barium titanate, a handful of lead zirconate, mix it up, and that is the starting material. So the quality control is bad on these, but if you want to use them, you will have to fight all of that.

Mr. Nelson (Tufts University): This sounds like visco-elastic material.

Mr. Forward: Yes. I have some other published papers in the Journal of Physics that go into some technical detail on exactly how to use them.

MEASUREMENT OF STRUCTURAL DAMPING USING THE RANDOM DECREMENT TECHNIQUE

J. C. S. Yang, N. G. Dagalakis
University of Maryland
College Park, Maryland

and

G. C. Everstine, Y. F. Wang
David Taylor Naval Ship R&D Center
Bethesda, Maryland

The use of the Random Decrement analysis technique was investigated for the determination of natural frequencies and damping ratios of different structural systems. The technique was applied to actual experimental response data recorded from transducers placed on off-shore platforms, bridges, and human bones.

To validate the technique, an analytical study was conducted with some simple systems as well as with a finite element model of a complex structural system. The excitation signal used was a random white noise signal. Damping values were preset for all the cases considered. The results of the analysis for the cases in which the structural modes were well separated showed excellent agreement. When the modal density was high, a curve fitting program was used. The results from the analysis of the response of a finite element model of the complex structural system subjected to a random input excitation showed reasonable agreement. This study has demonstrated that the technique can be used to determine damping of a complex structural system, and the technique is relatively independent of the input excitation. This technique can be used for the detection of cracks in structures and also has the potential of providing a more accurate estimate of the transfer functions of a structural system.

INTRODUCTION

A major experimental effort required in using various analytical techniques for prediction of dynamic response of complex structural systems is in evaluating the coupling loss and dissipation loss factors. These values are needed whether the analytical technique used is a deterministic technique, such as finite element analysis, a modal technique, or a statistical energy technique. These values have been obtained experimentally by measuring the decay rate for the system for various force input and acceleration output points. These measurements are usually very time-consuming, tedious, and complex, and extracting meaningful and useful information from them is inefficient and expensive. A power spectral density approach has been considered, with damping measured by the half-power point bandwidth method. However, this method was found to have a large measurement variance, especially when the bandwidth was small, and cannot be applied when two modes are close together. In addition, erroneous answers are obtained when assumed linear systems are actually nonlinear, a problem which cannot be detected unless the input is also measured. The autocorrelation function, wherein damping data are obtained from the logarithmic decrement, was investigated as an alternative, but the problem with the use of autocorrelation signatures is that the level of the curve depends on the intensity of the random input, which can seldom be measured or controlled in a natural environment. Consequently, a technique is used which can obtain the damping values of complex structures, on line, when only response data are available. In this paper we describe the use of the Random Decrement technique to obtain the damping values of an offshore platform model from random vibration response measurements taken at the University of Maryland. An analytical study was conducted using some simple systems as well as a finite element model of a complex structural system to validate the

This paper was presented at the 52nd Shock and Vibration Symposium.

technique.

RANDOM DECREMENT ANALYSIS

The Random Decrement (Randomdec) technique was originally developed by Mr. H. A. Cole for the measurement of damping and for the detection of structural deterioration of airplane wings subjected to wind flutter excitation[1,2]. Other applications have been studied by various other authors[3-5].

The Random Decrement technique is a fast-converging method for extracting meaningful information from random data. In this process segments of the random vibration response of a transducer placed on an object subjected to random excitation are ensemble averaged to form a signature which is representative of the free vibration decay curve of the structure. This signature can be used to measure damping or to detect incipient failures. The method is particularly useful in field measurements of structures and mechanical systems because excitation is provided naturally by such random inputs as acoustic noise, fluid flow, wind, etc.

In this section we present a brief, rather intuitive explanation of the principles of the Random Decrement technique. A more extensive mathematical derivation was developed by Reed[6].

The response $x(t)$ of a linear system is governed by the following basic equation:

$$m\ddot{x}(t) + c\dot{x}(t) + k\,x(t) = f(t) \qquad (1)$$

The solution of this differential equation depends on its initial conditions and the excitation $f(t)$. Since for linear systems the superposition law applies, the response can be decomposed into three parts: response due to initial displacement $x_d(t)$, response due to initial velocity $x_v(t)$, and finally response due to the forcing function $x_f(t)$.

The Random Decrement analysis consists of averaging N segments of the length τ_1 of the system response in the following manner: The starting time t_i of each segment is selected such that $x_i(t_i) = x_s$ = constant and the slope $\dot{x}_i(t_i)$ alternates between positive and negative. This process can be represented in mathematical form:

$$\delta(\tau) = \frac{1}{N}\sum_{i=1} x_i(t_i + \tau) \qquad (2)$$

where $x_i(t_i) = x_s \qquad i = 1, 2, 3 \ldots .$

$$\dot{x}_i(t_i) \geq 0 \qquad i = 1, 3, 5 \ldots .$$

$$\dot{x}_i(t_i) \leq 0 \qquad i = 2, 4, 6 \ldots .$$

The function $\delta(\tau)$ is called the Random Decrement signature and is defined only in the time interval $0 \leq \tau \leq \tau_1$. The meaning of the Random Decrement signature can now be determined. If the parts due to initial velocity are averaged, they cancel out because parts with positive and negative initial slopes are taken alternately and their distribution is random. Furthermore, if the parts due to the excitation are averaged, they also vanish because, by definition, the excitation is random. Finally, only the parts due to initial displacement are left and their average is the Random Decrement signature representing the free vibration decay curve of the system due to an initial displacement, which corresponds to the bias level x_s. (Fig. 1)

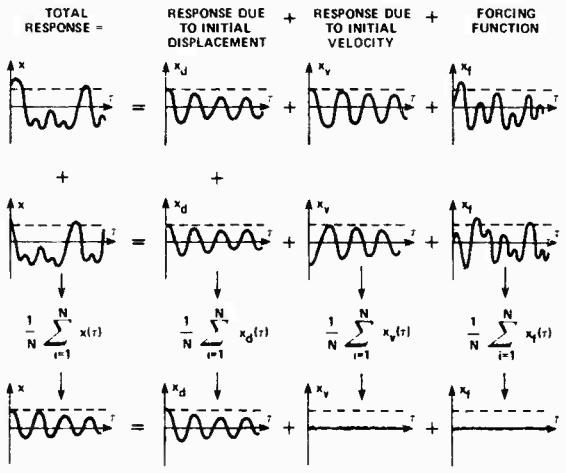

Fig. 1 - Principles of Randomdec technique

In practice, the technique is implemented with a Random Decrement computer which converts each segment into digital form and adds it to the previous segments (Fig. 2); the average is then stored in the memory and can be displayed on a screen. The number of segments to be averaged for the Random Decrement signature depends on the signal shape; usually 400 to 500 averages are sufficient to produce a repeatable signature.

One particularly interesting characteristic of the Random Decrement technique should be mentioned: it requires no knowledge of the excitation $f(t)$ as long as it is random. Neither the type nor the intensity of the input affect the signature.

For a single-degree-of-freedom system the natural frequency and damping ratio can be calculated directly from the Random Decrement signature by the logarithmic decrement measurement since the signature is a free vibration decay curve of the system. For multi-degree-of-freedom systems in which the modes are

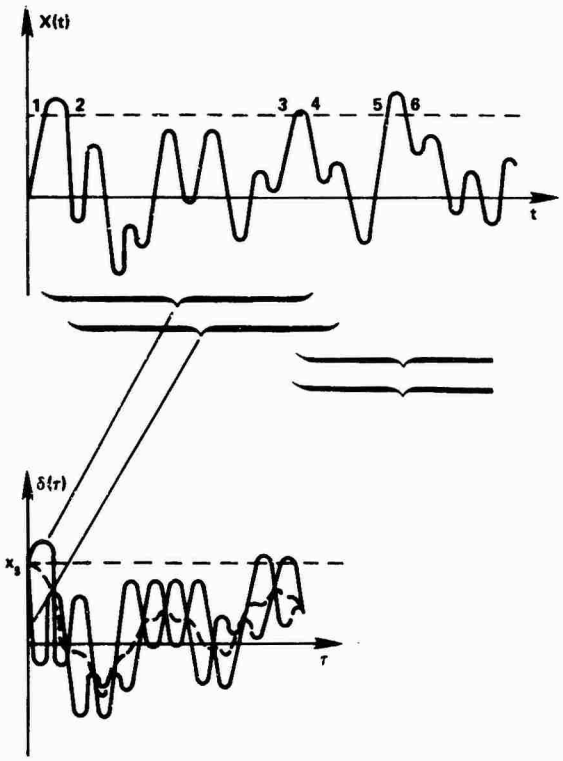

Fig. 2 - Extraction of the Randomdec signature

well separated, the natural frequency and damping ratio can be determined by bandpass filtering the response data about the natural frequency first to yield a single-mode Random Decrement signature of interest. However, if the principal modes of a multi-degree-of-freedom system are closely spaced, they cannot be separated by a filter without distorting the Random Decrement signature. In such a case curve fitting is introduced to solve this problem. The curve fitting program uses an optimization algorithm[7] which finds the best combination of natural frequencies and damping ratios that minimizes the mean square error between a mathematical function, which describes the response, and the Random Decrement data.

EXPERIMENTAL DETERMINATION OF DAMPING

The work performed included the collection and analysis of response data using 1/40 and 1/14 scale steel models of an existing offshore platform from the Gulf of Mexico as shown in Figure 3. These models were selected for ease of handling and testing in the laboratory. The 1/40 scale model is a welded steel frame having four primary legs braced with horizontal and diagonal members. The primary legs of the model have a diameter of 25 mm (.984 inch), and the horizontal and diagonal legs have a diameter of 15 mm (.591 inch).

The 1/14 scale platform model is mounted on piles embedded in 29 inches of sand (See

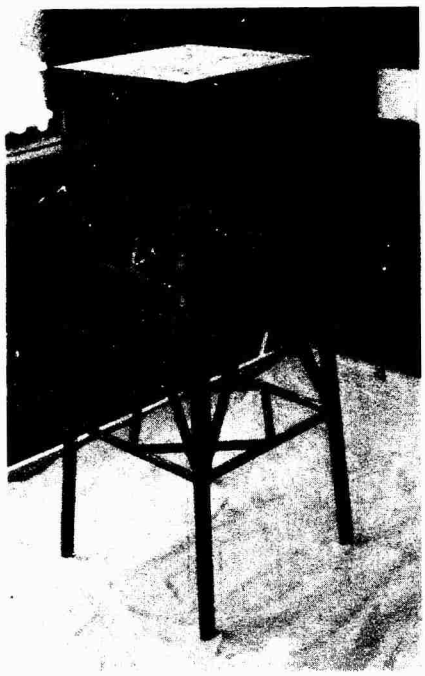

(a) 1/40 scale platform

(b) 1/14 scale platform

Fig. 3 - Platform models used in studies

Figure 4). The platform consists of five sub-levels with a catwalk on the periphery of the fifth level. The four main columns are two-inch diameter steel tubing, the central column is 9/16 inch diameter, and the cross members are 3/4 inch diameter steel tubes welded to the main columns. The material is ASTM A513-70 carbon steel with a minimum tensile strength of 80,000 psi.

Various types of foundations were investigated to examine the ability of the Random Decrement technique to determine damping over a wide range of frequencies and type of supports.

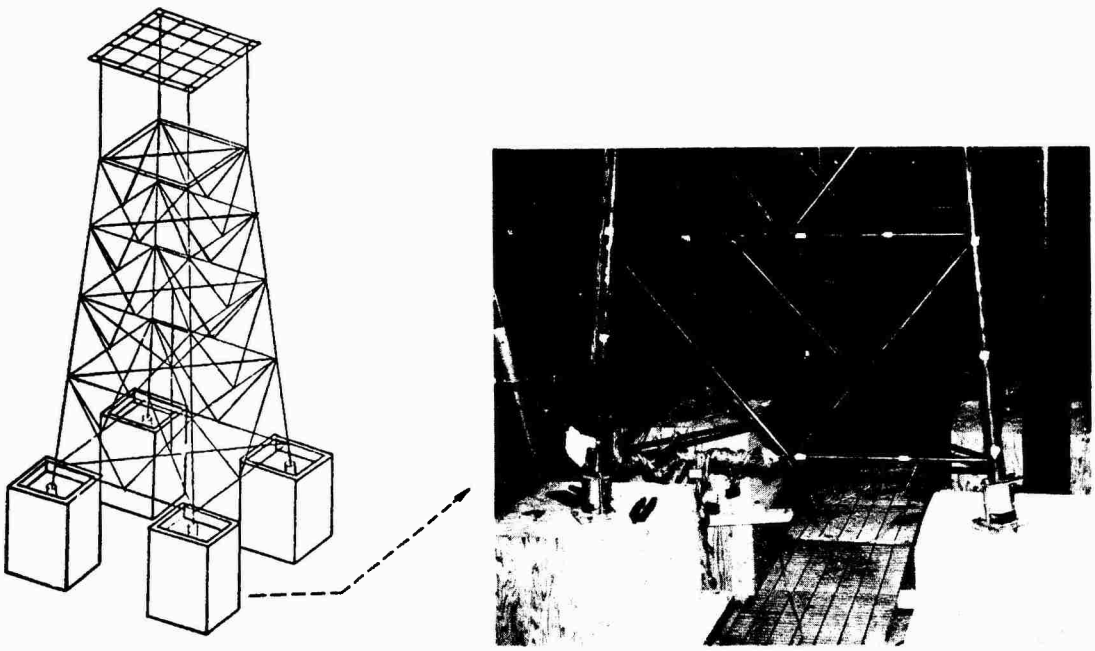

Fig. 4 - 1/14 Scale offshore platform mounted on wooden piles embedded in soil

DAMPING OF 1/40 SCALE PLATFORM FOR EXCITATION AT BASE

The first test series was made by exciting the base of the model in a horizontal plane by a Calidyne 5000 lb. shaker, or by an MB Electronic, PM 50, 30 lb. shaker. The shake table consisted of a 4' x 6' sheet of 3/4" plywood with 1" x 8" pine wood sides supported on a cast iron grating. The grating was resting on two rubber inner tubes. The two shakers were attached to the wooden sides of the table with their axes of motion in the longitudinal direction. An accelerometer was placed on the base of the platform in the direction of motion. A picture of the shake table with the test model is given in Figure 5.

Three types of foundations were simulated in this test series:

RIGID BASE: The four primary legs were attached to a rigid plate which was, in turn, rigidly mounted to the shake table.

FREE BASE: The four primary legs were attached to a rigid plate, but the plate was not rigidly attached to the shake table.

EMBEDDED IN SOIL: The four primary legs and the base plate were imbedded in two inches of soil.

Two conventional techniques, sine sweep and free response, and the Random Decrement technique were used to obtain the structural damping. A summary of the damping measurements from all three techniques is given in Table 1. More details of the study are given by Yang et al. [8].

DAMPING OF THE 1/14 SCALE PLATFORM

For these tests, the platform was mounted either on a fixed base or on piles. The excitation location was different from that of the 1/40 side platform, however. Sinusoidal and random excitation of the model in the fixed-base condition was located at about mid-height of the model on one support leg and at mid-span along one horizontal member. For the condition of the platform on piles the soil was placed in four plywood boxes each 30 inches

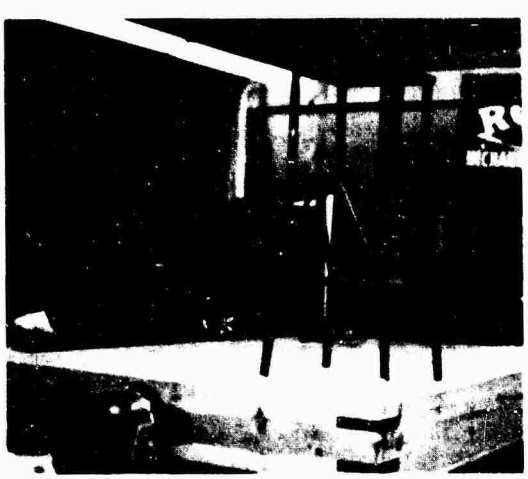

Fig. 5 - Shake table and test model

Table 1: Summary of Results

Test Condition	Conventional Techniques				Random Decrement	
	Sine Sweep		Free Response			
	Freq.	Damping	Freq.	Damping	Freq.	Damping
Fixed	15.1	.045-.060	15.1	.024	14.2	.015
	66.0	.0025-.0045	66.0	.0046	63.8	.1130
Free	64.9	.004-.006	64.9	.0045	62.8	.0030
Platform Embedded 2 inches in Sand	6.9	.065-.085	6.9	.070	8.1	.065
	59.5	.02 -.04	59.5	.029	60.5	.071

deep and 2 feet square. The soil was placed to a depth of 29 inches and vibrated to increase its stiffness. Each box was placed so that once piles had been located in the center, the large platform model could be lowered onto the piles and bolted in place. The piles were made of pinewood with a cross-sectional area of 2.625 square inches and approximately 29 inches long. Excitation location was six inches below the top plate along one of the primary supports. The response of the structure was monitored with accelerometers placed at various positions on the structure.

Figure 6 shows the free vibration decay for the first two modes. The damping coefficients were determined from the free vibration decay using the Logarithmic Decrement Technique. The corresponding damping ratios are

Frequency	Damping Ratio
9.2 Hz	.09
19 Hz	.049

Since the value of 9 percent for the first mode is typical of that of structures on soil foundation, it appears that the Random Decrement technique is accurately determining the damping ratio for structures mounted on soil foundations.

VALIDATION OF DAMPING MEASUREMENTS

An analytical model was used to validate damping measurement by the Random Decrement technique. This test offers the advantage that one knows and can control the value of the damping in advance.

Two different types of analytical system models were used: (1) low order lumped parameter spring, mass and dashpot systems, and (2) a relatively high order finite element model of a complex structural system.

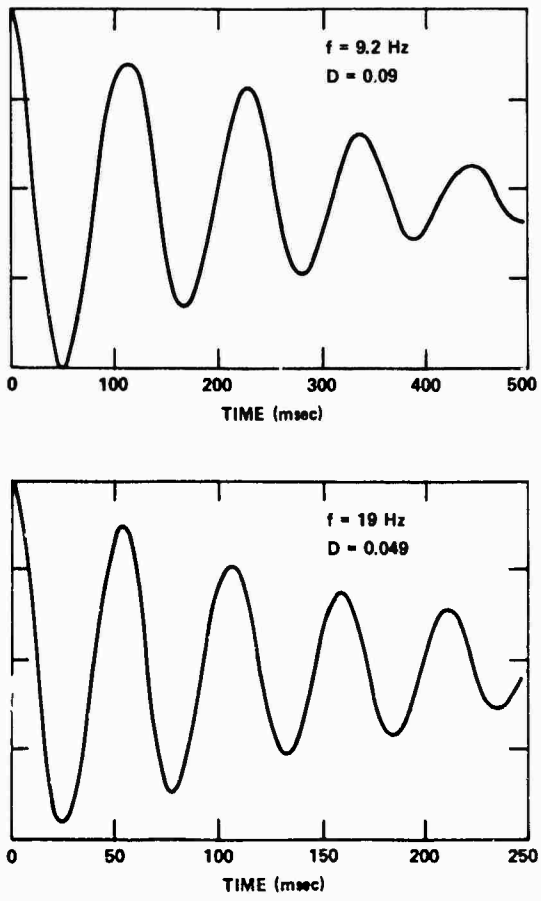

Fig. 6 - Free vibration decay of 1/14 scale model mounted on pile foundation using Random Decrement technique

The natural frequencies and damping coefficients of the models were set in advance by the proper selection of parameters. Then a computer model of the system was developed. For the lumped parameter model this model consists of a set of linear first order differential equations (state equations). In the case of the finite element model the NASTRAN computer program was used to generate the equations.

A numerical code which generates a random input force was then used to excite the structural models. The time response was simulated, and this response was then used in the Random Decrement analysis procedure.

The damping was obtained from the free response signature of the model, through the use of either the standard logarithmic decrement technique or a curve fitting algorithm.

LUMPED PARAMETER MODEL TEST

A two degree of freedom (fourth order system) lumped parameter system, shown in Fig. 7, was used for this test.

Two different cases were considered. In the first case the system had two oscillatory modes with damped frequencies well separated from each other. In the second case the system has two oscillatory modes with damped frequencies closely spaced.

A. TWO DEGREE OF FREEDOM LUMPED PARAMETER SYSTEM WITH WELL SEPARATED MODES

For the system of Fig. 7, the following parameters were selected:

$M_1 = 1$, $K_1 = 2256$, $C_1 = 1$

$M_2 = 2$, $K_2 = 250$, $C_2 = 0.1$

The excitation force F(t) was provided by a special computer program based on a random number generating subroutine, which generates a function F(t) by summing a large number of equal amplitude, random frequency and random phase sinusoids over the desired frequency range.

A standard fourth order Runge-Kutta integration routine was used to simulate the time response of the system. Figure 8 shows the power spectral density (PSD) curves of the input excitation and the output variable displacement $x_1(t)$, and indicates that the system has two well separated modes.

The output displacement signal was then filtered and processed to produce the Random Decrement Signatures of the two modes of the system. Two sets of filter bandpass cut-off frequencies were used based on the PSD of Figure 8. One, from 0 to 6 Hz, produced the Random Decrement signature of Figure 9; the other, from 6 to 10 Hz, produced the Random Decrement signature of Figure 10.

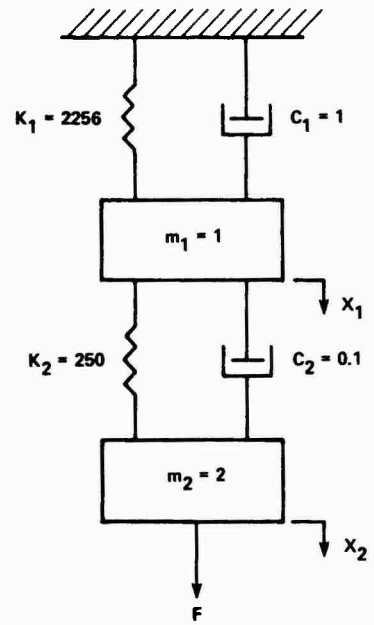

Fig. 7 - Two-degree-of-freedom system with well-separated modes

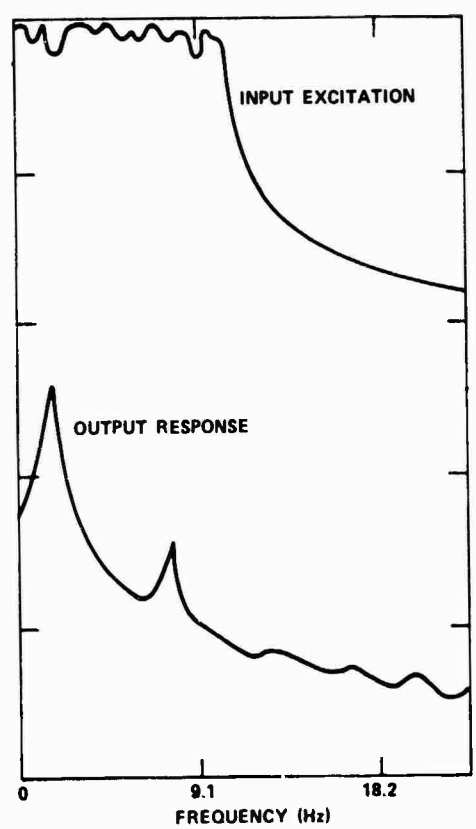

Fig. 8 - Power spectral density curve of the input excitation and output response

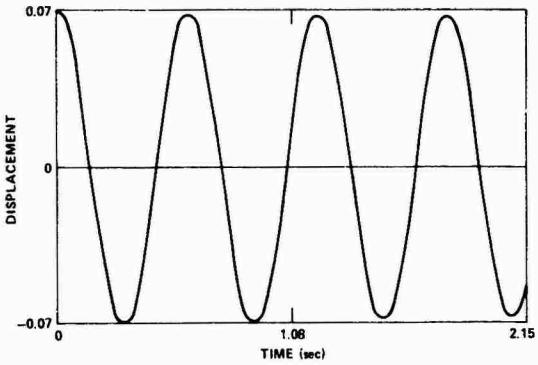

Fig. 9 - Random Decrement signature of the lower frequency mode

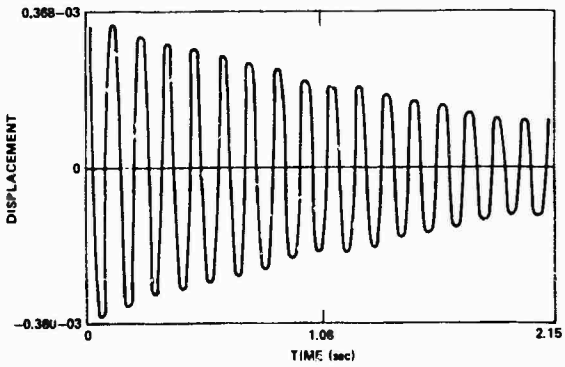

Fig. 10 - Random Decrement signature of the higher frequency mode

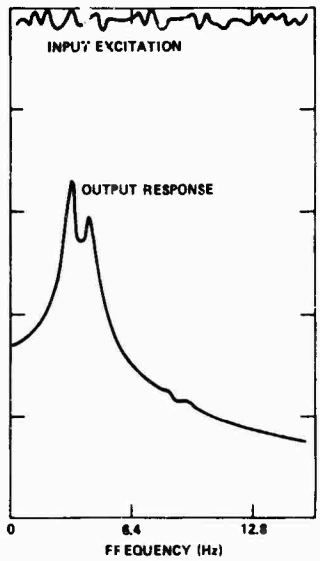

Fig. 11 - P.S.D. curve of input excitation and output response

Each of these Random Decrement signatures represents the free vibration decay curve of one system mode. The natural frequencies and the damping ratios of each mode were then calculated with the use of the logarithmic decrement technique. The same analysis was repeated using a curve fitting computer program.

B. TWO-DEGREE-OF-FREEDOM LUMPED PARAMETER SYSTEM WITH CLOSELY SPACED MODES

The work described in the previous section was repeated for a different set of system parameters.

$M_1 = 1, \quad K_1 = 600, \; C_1 = 0.1$

$M_2 = 0.1, \; K_2 = 50, \; C_2 = 0.2$

These parameters were selected such that the system has two oscillatory modes with closely spaced damped frequencies. Figure 11 shows the power spectral density of the input excitation force $F(t)$ and of the output displacement $x_1(t)$. These two closely spaced modes are difficult to separate by filtering without distorting the response. Figure 12 shows the Random Decrement signature of the output.

This signature now contains contributions from both system modes. The logarithmic decrement technique cannot be used in this case. Instead, we used the curve fitting program to determine the natural frequencies and damping ratios of the system.

C. RESULTS

The results of the analysis when the modes are well separated indicate negligible errors. The results for very closely spaced modes are given in Table 2.

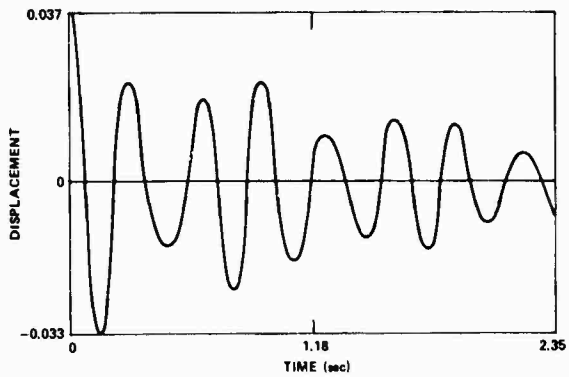

Fig. 12 - Random Decrement signature of model

TABLE 2

RESULTS FOR TWO DEGREE OF FREEDOM SYSTEM WITH CLOSELY SPACED MODES

	DAMPED FREQUENCY		
	Theoretical Value	Random Dec Calculated	Error
First Mode	3.187	3.179	0.25%
Second Mode	4.343	4.278	0.66%
	DAMPED RATIO		
	Theoretical Value	Random Dec Calculated	Error
First Mode	2.36%	2.37%	0.42%
Second Mode	2.48%	2.54%	2.42%

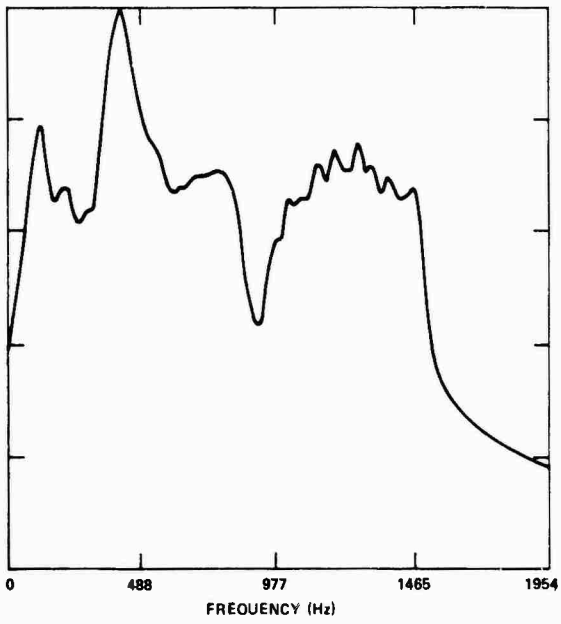

Fig. 13 - P.S.D. curve of response signal of finite element model (Point 1)

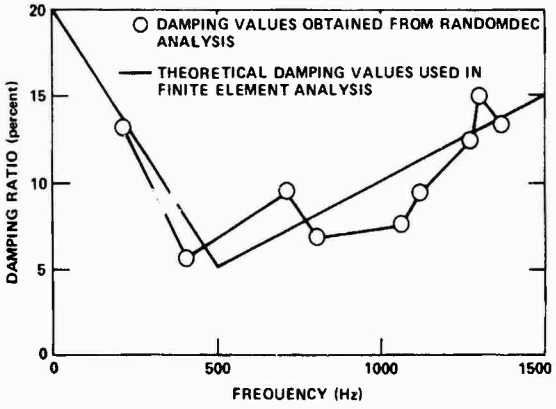

Fig. 14 - Comparison of the obtained damping values with the theoretical damping values used in NASTRAN

COMPLEX FINITE ELEMENT MODEL TESTS

A multidegree of freedom model of a complex structural system was developed with the NASTRAN computer program. The model was excited with a single force F(t) applied at one point, and the dynamic response was simulated with the Newmark beta integration routine. The velocity at two points was saved for further analysis. The force F(t) was simulated by the same computer program which produced the random input excitation of the previous tests.

Figure 13 shows the power spectrum density curve of the velocity response signal. The Random Decrement analysis was applied to all the structural modes that could be identified from this PSD curve. Then the curve fitting routine was used to determine the corresponding model frequencies and damping ratios.

The structural damping values used in the finite element model were preselected to follow the two straight lines shown in Figure 14. The damping values calculated by the Random Decrement method are shown on the same diagram.

DISCUSSION AND CONCLUSIONS

This study has demonstrated that the Random Decrement technique is a useful method in determining modal frequency and damping of complex structural systems.

The main advantage of this technique is that it does not require the knowledge of the input excitation. This technique may prove particularly useful in determining the modal characteristics of large structures that are difficult to vibrate with man-made excitation, or when it is impossible to measure the exciting force. This technique requires only enough natural excitation to produce measurable response. As long as this excitation is random, the Random Decrement analysis technique may be applied.

ACKNOWLEDGEMENT

The research was supported in part by the Office of Naval Research and the United States Geological Survey. Grant No. N-00014-78-C-0675 and by the David Taylor Naval Ship Research and Development Center, Annapolis, Grant No. N61533-80-M-1520.

REFERENCES

1. H.A. Cole, "Method and Apparatus for Measuring the Damping Characteristics of a Structure", United States Patent No. 3,620,069, 1971.

2. H.A. Cole, "On-Line Failure Detection and Damping Measurement of Aerospace Structures by the Random Decrement Signatures", NASA CR-2205, 1973.

3. D.W. Caldwell. "The Measurement of Damping and the Detection of Damage in Linear and Nonlinear Systems by the Random Decrement Technique", Ph.D. Thesis, University of Maryland, 1978.

4. D.W. Caldwell, "The Measurement of Damping and the Detection of Damage in Structures by the Random Decrement Technique", M.S. Thesis, University of Maryland, 1975.

5. J.C.S. Yang, D.W. Caldwell, "Measurement of Damping and the Detection of Damages in Structures by the Random Decrement Technique", 46th Shock and Vibration Bulletin, 1976, pp. 129-136.

6. R.E. Reed, "Analytical Aspects of Randomdec Analysis", AIAA/ASME/ASCE/AHS 20th Structures, Structural Dynamics and Materials Conf., St. Louis, Mo., April 4-6, 1979.

7. R.M. Bennett, and R.N. Desmarais, "Curve Fitting of Aeroelastic Transient Response Data with Exponential Functions", NASA SP-415, Oct. 1975.

8. J.C.S. Yang, M.S. Aggour, N. Oagalakis, F. Miller, "Damping of an Offshore Platform Model by the Random Decrement Method", Proceedings of the Second ASCE/EMD Specialty Conference, Atlanta, Ga., pp. 819-832, (1981).

DAMPED PNEUMATIC SPRING AS SHOCK ISOLATOR:

GENERALIZED ANALYSIS AND DESIGN PROCEDURE

M. S. Hundal
Professor of Mechanical Engineering
The University of Vermont
Burlington, VT 05405

Modeling, response and design procedure for a pneumatic shock isolator are presented. The isolator is a single-acting pneumatic spring with self-damping. The undamped pneumatic spring is also analyzed, the results for which can be more readily used as the starting point in the design process. Parametric studies show the effect of non-dimensional parameters on system response. It is shown that a pneumatic spring and a linear spring isolator experience the same displacement for a short duration pulse.

INTRODUCTION

The use of pneumatic springs for vibration isolation is well established and documented [1-5]. Both passive and active systems are used for this purpose. References to the use of pneumatic spring as a shock isolator are, however, few. Eshleman and Rao [6] investigated six types of shock isolation elements including a pneumatic spring. The paper does not give details of its construction or the analysis. The one paper that deals with the subject in depth is that by Fox and Steiner [7]. They have presented both analytical and experimental results for a passive pneumatic shock isolator, and have shown that a specific geometry yields ideal system response.

The pneumatic spring isolator presented here is conceptually similar to the above. However, the analysis is performed in terms of dimensionless variables and parameters. The results are therefore general in nature and apply to the performance and design of any system of this configuration and type of shock input. An in-depth look at the problem is provided by this study. The method of analysis is similar to that applied to a pneumatic damper-linear spring combination [8].

ANALYSIS

The shock isolator is a single acting pneumatic spring, shown in Figure 1. It consists of a fixed volume chamber and a variable volume chamber, with an orifice connecting the two. Pressures in the two chambers are designated p_1 and p_2, and p_0 is the atmospheric pressure. The equation of motion for the payload of mass m is

$$mx'' = (p_0 - p_1)\, s \qquad (1)$$

where s is the cylinder cross-section area and primes represent differentiation with respect to the physical time, t. Let $d = u - x$, the relative displacement of the mass and piston. Equation of motion can be written as

$$md'' = mu'' + (p_1 - p_0)\, s \qquad (2)$$

The base motion considered here is a constant velocity pulse of a finite duration. We define it by

$$u' = u'_o \text{ for } 0 < t < t_o$$
$$= 0 \text{ for } t > t_o \qquad (3)$$

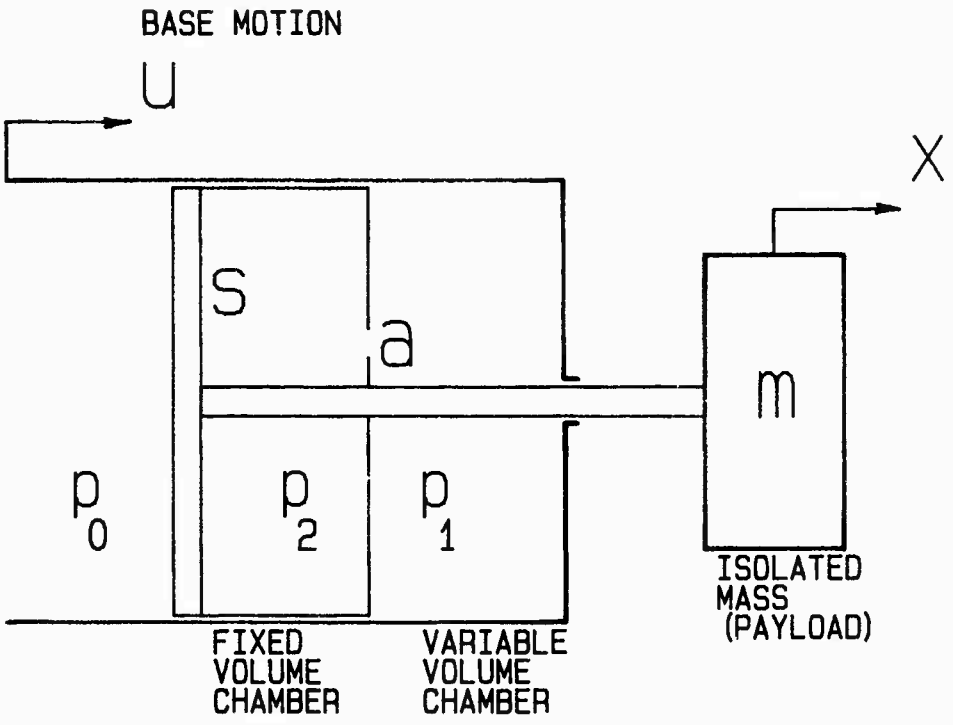

Figure 1. Damped Pneumatic Spring as a Shock Isolator

The flow equations are obtained by using the following basic relationships:

Equation of state

$$m_i = p_i v_i / R\theta_i \qquad (4)$$

Adiabatic process

$$\theta_i/\theta_0 = (p_i/p_0)^{[n-1]/n} \qquad (5)$$

Conservation of mass

$$m'_2 = - m'_1 \qquad (6)$$

In the above m_i , v_i and θ_i are the mass, volume and temperature of air. The subscript i (= 1 or 2) refers to the two chambers, and 0 refers to initial condition. R is the gas constant and n = 1.4 for air. Upon differentiating equation (4) and substituting (5)

$$m'_i = C_1 p_i^{1/n} (n v'_i + v_i p_i^{-1} p'_i) / n \qquad (7)$$

where $C_1 = p_0^{[n-1]/n}/R\ \theta_0$.

Let the initial position of the piston be such that the total volume of the two chambers is sl (i.e., l is the effective cylinder length). Let v_{10} be the initial volume of the right chamber. Then

$$v_1 = v_{10} + sd \ ; \ v'_1 = sd' \qquad (8a)$$

$$v_{10} + v_2 = sl \ ; \ v'_2 = 0 \qquad (8b)$$

Upon substituting the above in equation (7) the flow into each chamber is

$$m'_1 = C_1 p_1^{1/n} [nsd' + (v_{10}+sd) p_1^{-1} p'_1]/n \qquad (9a)$$

$$m'_2 = C_1 v_2 p_2^{[1-n]/n}\ p'_2 / n \qquad (9b)$$

Mass flow rate through an orifice is given in [9]. Denoting the upstream and downstream conditions by the subscripts u and d respectively,

$$m'_d = C_o\ a\ C_2\ p_u / \sqrt{R\ \theta_u} \qquad (10)$$

where a is orifice area and C_o is discharge coefficient. The parameter C_2 is given by

$$C_2 = \{n / [(n+1)/2]^{[n+1]/[n-1]}\}^{1/2}$$

for $p_u/p_d > 1.894$ (11a)

and

$$C_2 = (p_d/p_u)^{1/n}\{[2n/(n-1)].$$
$$[1-(p_d/p_u)^{[n-1]/n}]\}^{1/2}$$

for $p_u/p_d < 1.894$ (11b)

The above equations will now be cast in a dimensionless form. The new variables are defined as follows:

Displacement: $D = d/l$; $X = x/l$; $U = u/l$

Velocity: $\dot{D} = d'/u'_o$; $\dot{X} = x'/u'_o$; $\dot{U} = u'/u'_o$

Acceleration: $\ddot{D} = d''l/u'^2_o$; $\ddot{X} = x''l/u'^2_o$;
$\ddot{U} = u''l/u'^2_o$

Time: $T = t\, u'_o/l$

Pressure: $P_i = p_i/p_0$; $\dot{P}_i = p'_i l/p_0 u'_o$

Here dots represent differentiation with respect to T . The new parameters are:

Mass: $M = m\, u'^2_o/p_0 s\, l$

Area ratio: $S = na\, C_o \sqrt{R\,\theta_0} / s\, u'_o$

Volumes: $V_{10} = v_{10}/s\, l$; $V_2 = v_2/s\, l = 1 - V_{10}$

Pulse length: $T_o = t_o\, u'_o / l$

The pressure equations now take the following form:

For $P_2 > P_1$

$$(V_{10} + D)\dot{P}_1 + n\dot{D}P_1 = C_2 S P_1^{[n-1]/n} P_2^{[n+1]/2n} \quad (12a)$$

$$V_2 \dot{P}_2 = - C_2 S P_2^{[3n-1]/2n} \quad (12b)$$

and, for $P_1 > P_2$

$$(V_{10} + D)\dot{P}_1 + n\dot{D}P_1 = - C_2 S P_1^{[3n-1]/2n} \quad (13a)$$

$$V_2 \dot{P}_2 = C_2 S P_2^{[n+1]/2n} P_1^{[n-1]/n} \quad (13b)$$

The equation of motion becomes

$$M\ddot{D} = M\ddot{U} + P_1 - 1 \quad (14)$$

However, due to the form of the input, it is more convenient to put it in the form

$$M\ddot{X} = 1 - P_1 \quad (15a)$$

$$\dot{D} = \dot{U} - \dot{X} \quad (15b)$$

Equations (12), (13) and (15) are the governing equations for the system. The initial conditions are, at $T = 0$, $D = X = 0$ and $P_1 = P_2 = 1$. The input is $\dot{U} = 1$ for $T < T_o$ and $\dot{U} = 0$ for $T > T_o$. Due to the large excursions of the system during a shock pulse, the equations cannot be linearized and must be solved numerically. This contrasts with the case of vibration isolation where the equations are linearized and analytical solutions obtained [3].

THE UNDAMPED SPRING

Before proceeding with the solution of the above equations, let us consider the response of the pneumatic spring without damping. Such would be the case at the two limiting values of the orifice area, i.e. $a = 0$ and $a = s$. The two cases are similar, the only difference being the volume of entrapped air. The equation of motion for the latter case is

$$mx'' = (p_0 - p)\, s \quad (16)$$

where

$$p = p_0 v_0^n / v^n \quad (17)$$

and

$$v = v_0 + sd = v_0 + s(u - x) \quad (18)$$

Upon substituting the above in equation (17) and using the dimensionless relationships given earlier, the equation of motion becomes

$$M\ddot{X} = 1 - 1/(1 + U - X)^n \quad (19)$$

The initial conditions are $X(0) = \dot{X}(0) = 0$, and the input is $U = T$ for $T < T_o$, and $U = T_o$ for $T > T_o$.

Equation (19) is solved numerically by 4th order Runge-Kutta method. The response is shown in Figure 2 for $M = 1$ and for selected values of T_o. We note that the maximum piston displacement D at the end of the expansion stroke occurs at $T = T_o$ for small values of T_o. The maximum payload acceleration, i.e., $\ddot{X}$, is at the end of the compression stroke. The values depend on T_o and M .

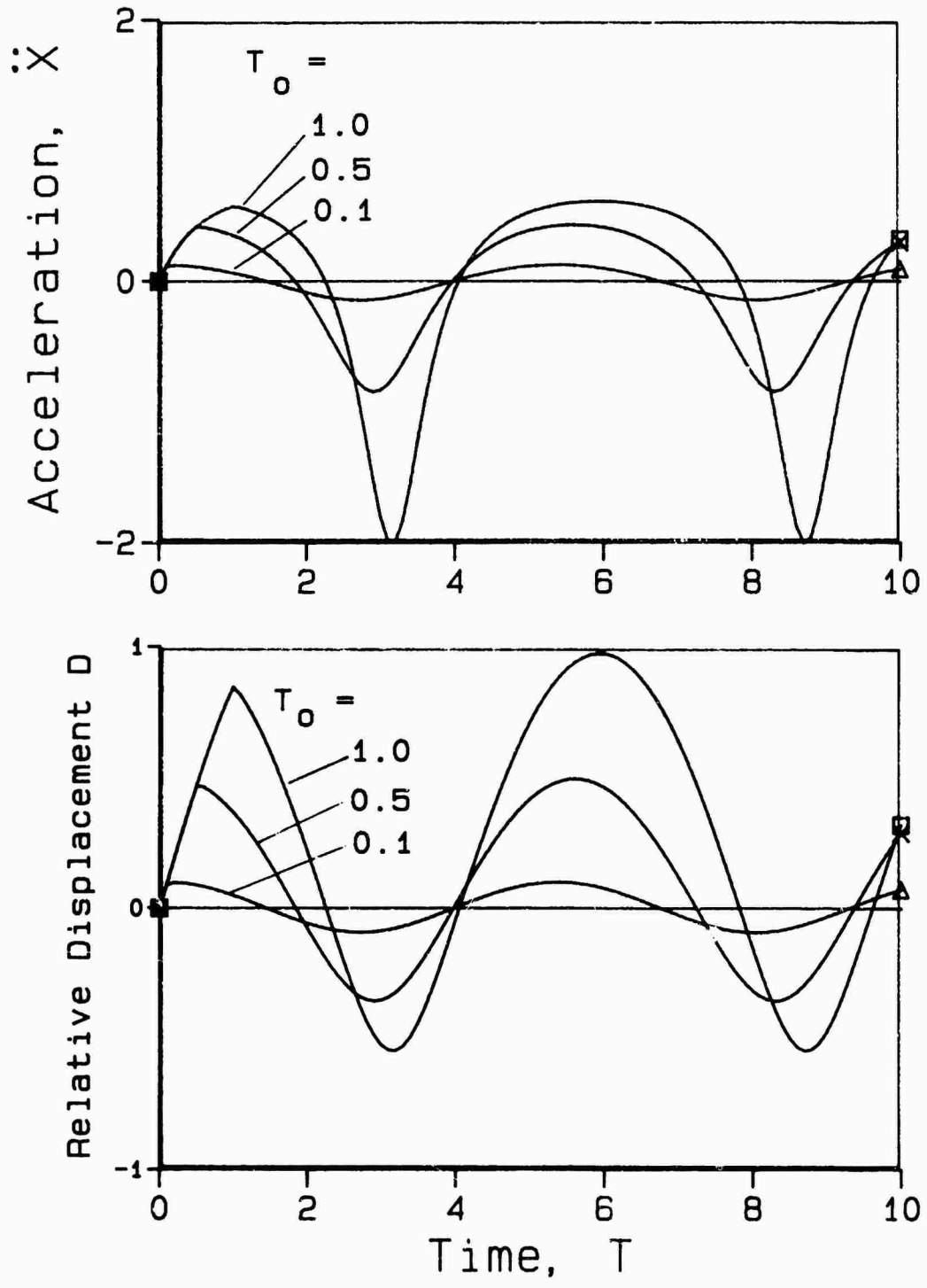

Figure 2. Response of System with Undamped Pneumatic Spring for Different Pulse Durations; M = 1.

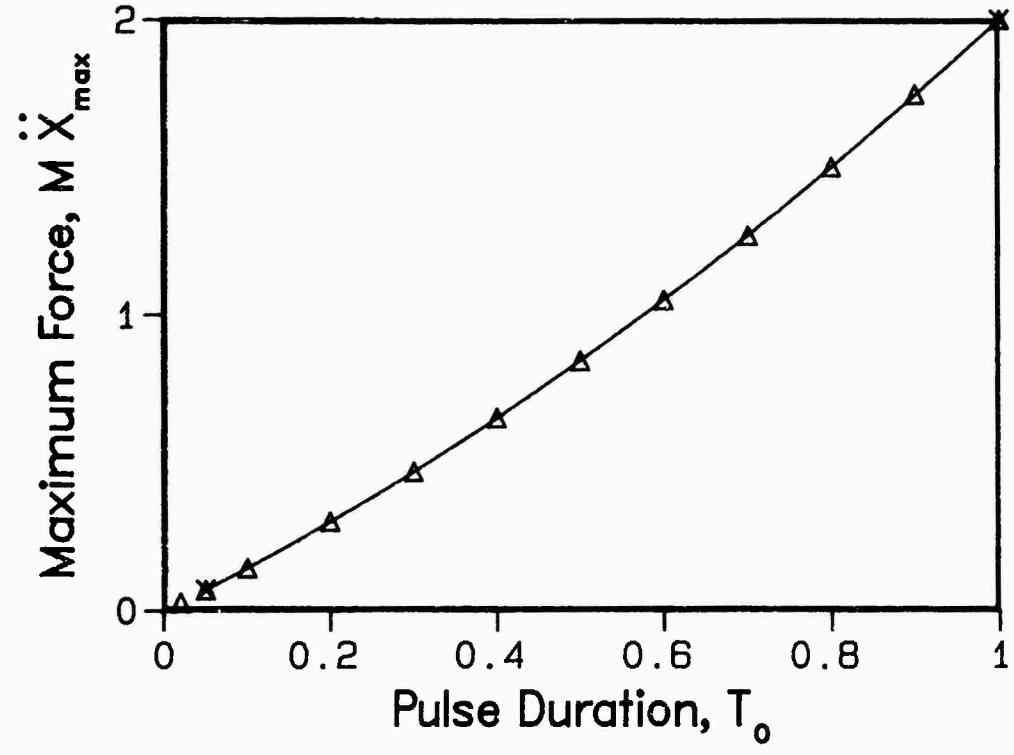

Figure 3. Performance of the System with Undamped Spring

For small values of T_o, equation (19) can be solved analytically to obtain the maximum displacement and acceleration. Since for shock isolation, the pulse duration is much shorter than the natural period of the system, this is a reasonable restriction. Thus during the expansion stroke $p \doteq p_0$ and $\ddot{X} = 0$. Therefore $\dot{D} = \dot{U} = 1$. At $T = T_o$, $D = T_o$ and $\dot{D} = 0$. For $T > T_o$, during the return stroke, since $\ddot{U} = 0$, $\ddot{D} = -\ddot{X}$, and equation (19) becomes

$$M\ddot{D} = 1/(1+D)^n - 1 \qquad (20)$$

Now, using $\ddot{D} = \dot{D}\, d\dot{D}/dD$, the above equation can be integrated to yield

$$M\dot{D}^2/2 = T_o - D - [(1+D)^{1-n} - (1+T_o)^{1-n}]/(n-1) \qquad (21)$$

Let D_m be the displacement at the end of the compression stroke, at which point $\dot{D} = 0$. Upon substituting these in equation (21) we get

$$(1 + D_m)^{1-n} - (1 + T_o)^{1-n} + (n-1)(D_m - T_o) = 0 \qquad (22)$$

which can be solved for D_m for different values of T_o, by a numerical scheme such as half-interval search. Now, since the maximum acceleration occurs at $D = D_m$, it can be found from equation (19), by putting $D_m = U - X$.

The triangle symbols in Figure 3 show a plot of the maximum force as function of T_o. Although these values are valid for an undamped pneumatic spring, they are helpful in the design of a damped shock isolator. By using a least-squares curve fit, the relationship may be expressed explicitly as

$$M\ddot{X}_{max} = 0.001 + 1.38\, T_o + 0.62\, T_o^2 \qquad (23)$$

for the range $0 < T_o < 1$. This is shown by the continuous line in Figure 3.

RESPONSE OF A DAMPED PNEUMATIC SPRING

The governing equations (12), (13) and (15) contain four independent parameters. These are: mass M , area ratio S , volume V_{10} and pulse duration T_o . We wish to study the effect of these parameters on the system response, in particular on the maximum mass acceleration $\ddot{X}_{max}$ and to a lesser extent on the maximum relative displacement D_{max} . Two of these parameters, M and T_o , appeared in the analysis of undamped spring; their effect in the present case is similar. $\ddot{X}_{max}$ is approximately inversely proportional to M and increases with pulse duration T_o . This is shown by the time responses in Figures 4 and 5. The nonlinear nature of the system, as well as the effect of damping is also apparent from these figures. We also note that $D_{max} \leq T_o$; as M increases, D_{max} approaches T_o .

We next look at effects of S and V_{10} . The latter is the ratio of the initial volume of the variable volume chamber to the total volume. Consider the extreme values of V_{10} first. For $V_{10} = 1$ the case reverts to that of an undamped spring. On the other hand, as V_{10} becomes small, there arises the possibility of the piston bottoming out at the end of the compression stroke. Figure 6 shows $\ddot{X}_{max}$ as function of area ratio S , for selected intermediate values of V_{10} . There are several points worth noting from these results.

1. For large values of S the system approaches the undamped case; all curves converge to the value given by Figure 3 for the corresponding M and T_o .
2. Likewise as S approaches 0 , the damping also approaches 0 .
3. The curves exhibit minima for values of S between 0.1 and 1, depending on V_{10} .

The final set of results is shown in Figure 7. Here V_{10} is held constant at 0.5 and the remaining three parameters are varied. As stated earlier, for low and high values of S the system behavior approaches that of the undamped case. In each case a certain value of S yields the optimum response; i.e., a minimum value of $\ddot{X}_{max}$. This minimum value is approximately 80% of the corresponding value for large S .

NUMERICAL EXAMPLES AND DESIGN PROCEDURE

Let us consider an example with the following data:

Payload mass m = 100 kg

Pulse $u'_o = 1$ m/s for $t_o = 0.1$ sec.

It is desired that the maximum mass acceleration be $x''_{max} = 1$ m/s^2. Since the response of an undamped system is given in closed form by equation (23), it can be used as a starting point in the design process. Try a cylinder length l = 1 m . From the definitions of dimensionless quantities we get

$$T_o = t_o u'_o / l = 0.1$$

and

$$\ddot{X}_{max} = x''_{max} l / u'^2_o = 1$$

From equation (23), for $T_o = 0.1$

$$M\ddot{X}_{max} = 0.145$$

thus M = 0.145 . From the definition of M, the piston area is found to be s = 0.0069 m^2 , i.e. a diameter of 9.4 cm. The relative displacement is found as follows: Since $D_{max} \doteq T_o = 0.1 = d_{max}/l$, $d_{max} = 0.1$ m. In order to find the orifice area, first determine the optimum value of S . This will yield a lower $\ddot{X}_{max}$. For S = 0.5 and R = 288 J/kg - K, $\theta_0 = 300$ K , we find that the orifice diameter is 3.2 mm.

It is interesting to note the effect of using a shorter cylinder. Let l = 0.5 m , from which $T_o = 0.2$ and $\ddot{X}_{max} = 0.5$. Equation (23) yields M = 0.6 . The piston area required is s = 0.0033 m^2 , i.e. a diameter of 6.5 cm. Thus a more compact spring yields the same performance. It is also noted that the maximum relative displacement remains the same, i.e., $d_{max} = 0.1$ m .

Let us next evaluate the effect of a different velocity pulse on the isolator of length l = 1 m . Let $u'_o = 0.5$ m/s , with same duration $t_o = 0.1$ sec. We find the new values M = 0.036 and $T_o = 0.05$. From equation (23), $\ddot{X}_{max} = 2$ or $x''_{max} = 0.5$ m/s^2.

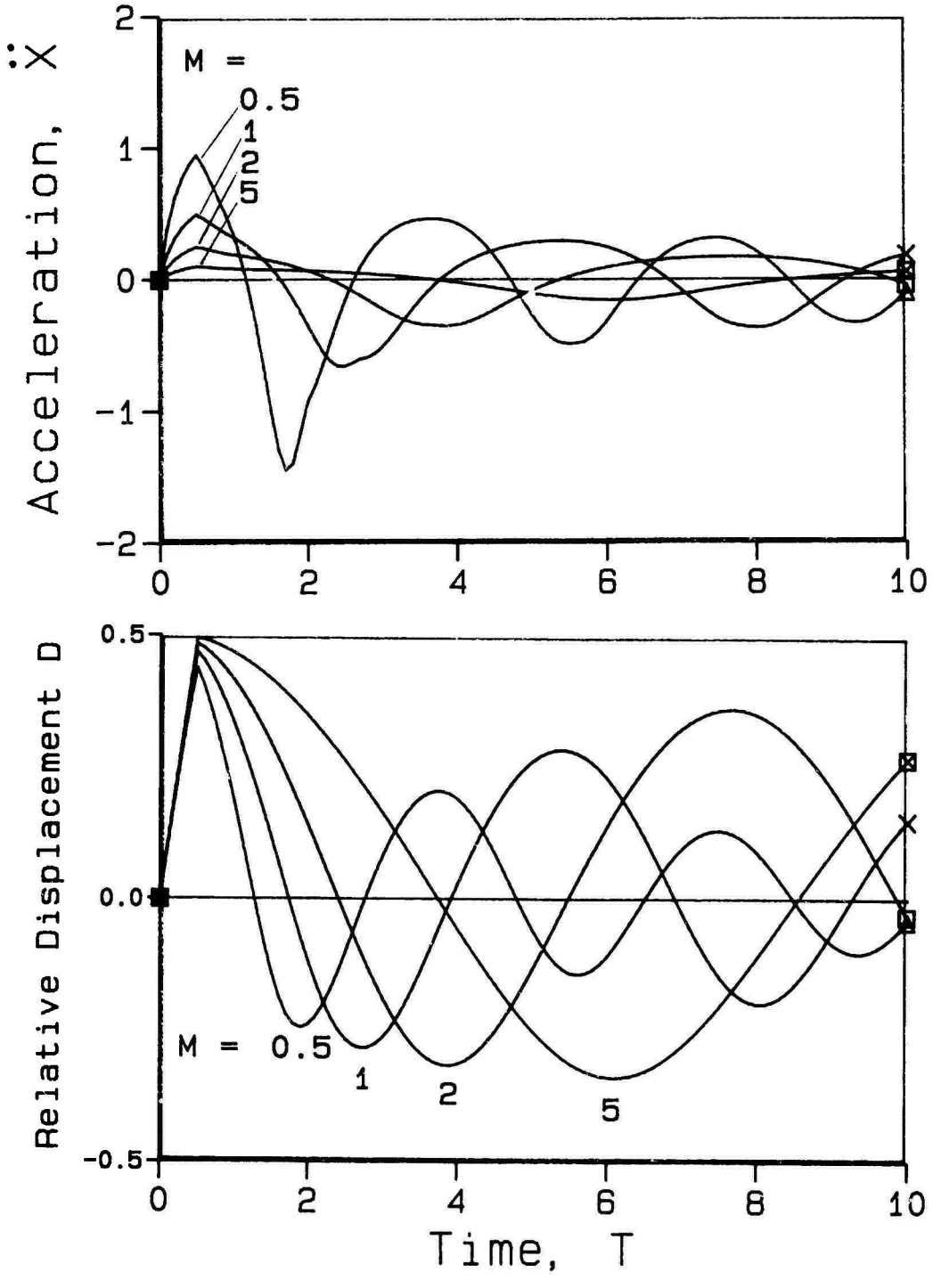

Figure 4. Response of Damped Spring for $S = T_o = V_{10} = 0.5$

Figure 5. Response of Damped Spring for M = 2, S = V_{10} = 0.5

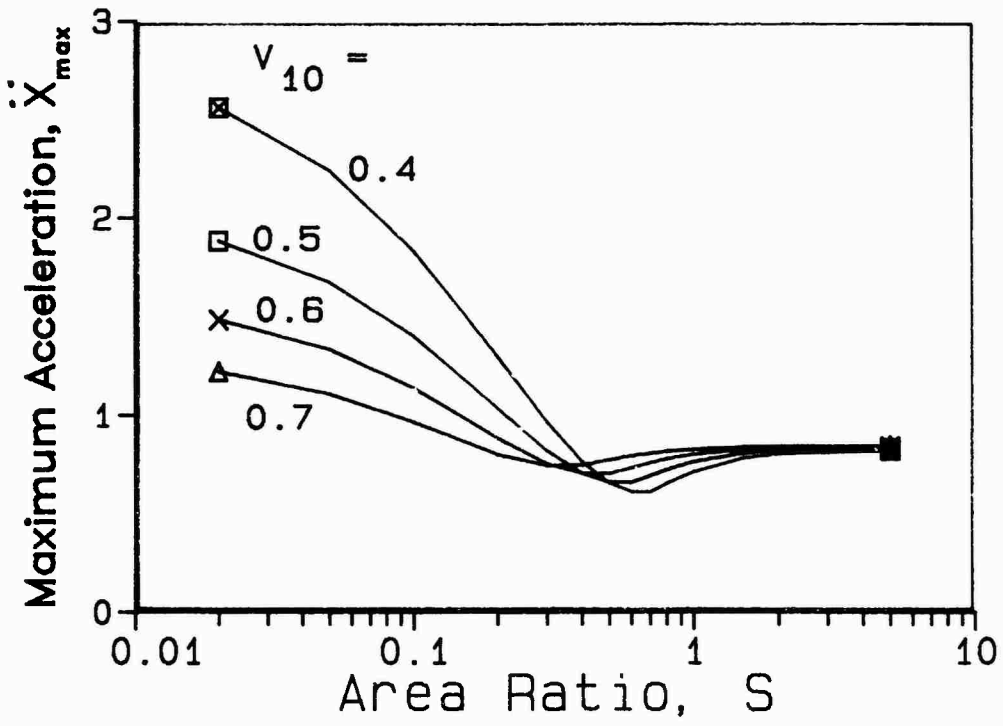

Figure 6. Effect of V_{10} and S on Performance of Damped System. M = 1, T_o = 0.5

Finally we compare the performance of damped pneumatic spring with a shock isolator consisting of linear spring and dashpot in parallel. Results showing the response of a linear isolator to a velocity pulse have not thus far appeared in the published literature. Therefore a separate study was made [10], the results of which are presented here in brief. For a short pulse duration mass acceleration is minimum when no damping is present. Also, the following holds true in this case:

$$x''_{max}/u'_o \doteq \omega_n t_o \doteq d_{max}\omega_n/u'_o$$

where ω_n is the undamped natural frequency. In the present example, for x''_{max} = 1 m/s^2, u'_o = 1 m/s and t_o = 0.1 sec, we find $\omega_n = \sqrt{10}$ rad/sec, and therefore d_{max} = 0.1 m. Thus for the same performance as the damped pneumatic spring, a linear isolator of the same length would be required.

CONCLUSION

A shock isolator consisting of a single-acting self-damped pneumatic spring has been analyzed. The governing equations were cast in a dimensionless form, rendering the results general in nature. Numerical examples were given to illustrate the design process and show the effect of isolator size on performance. Comparison with a linear isolator showed that the two have the same relative displacement for similar performance.

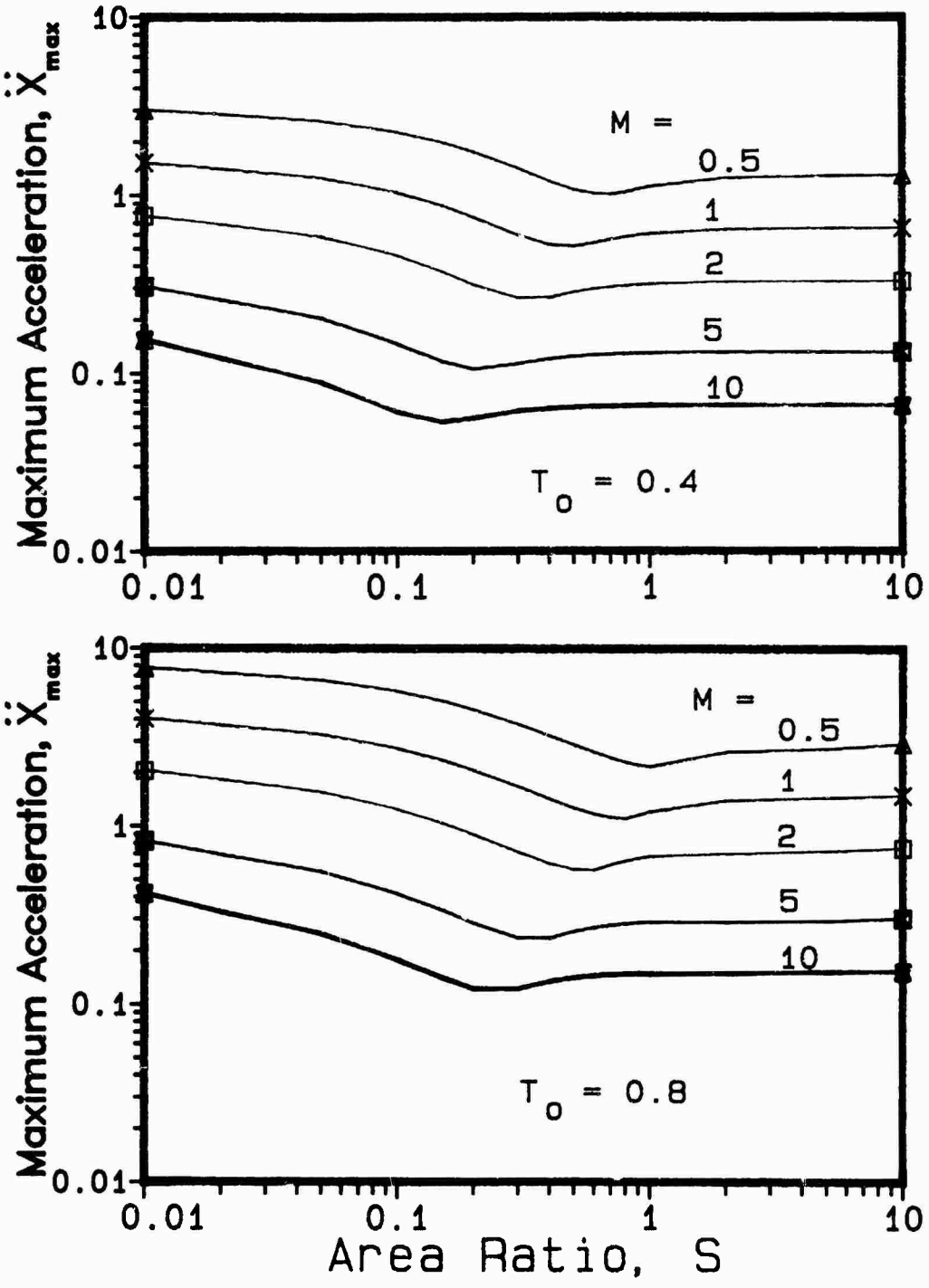

Figure 7. Effect of M, S and T_o on Performance; V_{10} = 0.5

REFERENCES

1. Hirtreiter, A. B., "Air Springs", Machine Design, April 1965, p. 104.

2. Berry, W. S., "The Air Coil Spring", S.A.E. Transactions, Vol. 66, 1958, p. 471.

3. Cavanaugh, R.D., "Air Suspension and Servo-Controlled Isolation Systems", Shock and Vibration Handbook (edited by C.M. Harris and C.E. Crede), McGraw-Hill Book Co., Second Edition, 1976, pp. 33-1 to 33-26.

4. Esmailzadeh, E., "Optimization of Pneumatic Vibration Isolation System for Vehicle Suspension", ASME, J. Mech. Design, Vol. 100, 1978, pp. 500-506.

5. Esmailzadeh, E., "Servo-valve Controlled Pneumatic Suspensions", J. Mech. Engr. Sc., Vol. 21, 1979, pp. 7-18.

6. Eshleman, R.E. and Rao, P.N., "The Responses of Mechanical Shock Isolation Elements to High Rate Input Loading", Shock and Vibration Bull., Vol. 40, pt. 5, 1969, pp. 217-234.

7. Fox, G.L. and Steiner, E., "Transient Response of Passive Pneumatic Isolators", Shock and Vibration Bull., Vol. 42, pt. 4, 1972, pp. 85-91.

8. Hundal, M.S., "Response of a Pneumatic Isolator to Standard Pulse Shapes", Shock and Vibration Bull., Vol. 52, pt. 4, 1982, pp. 161-168.

9. Blackburn, J.F., Reethof, G., and Shearer, J.L., Fluid Power Control, M.I.T. Press, 1960, pp. 215-217.

10. Hundal, M.S., "Response of a Linear Shock Isolator to Velocity Pulse", Journal of Sound and Vibration, 1983 (in press).

MACHINERY DYNAMICS

ANALYTICAL AND EXPERIMENTAL INVESTIGATION OF ROTATING BLADE RESPONSE DUE TO NOZZLE PASSING FREQUENCY EXCITATION

J.S. Rao
Indian Institute of Technology, New Delhi

H.M. Jadvani
Regional Engineering College, Surat

and

P.V. Reddy
Escorts Scientific Research Centre, Faridabad

In this paper, the differential equations of motion of forced vibrations of a pre-twisted, staggered and rotating blade of uniform cross-section are derived using Lagrange's equations. The excitation of the blade is taken in the form of NPF (nozzle passing frequency) excitation. The effect of proportional damping is taken into consideration and the effects of rotary inertia and shear deformation are neglected. The forced vibration response is determined by using modal analysis. A test rig designed to study forced vibration response under NPF is described. In this rig, the NPF excitation is simulated by permanent magnets located at required distances from the blades. The analytical and experimental response at the nozzle passing frequencies is compared and a good agreement has been shown.

INTRODUCTION

Blades constitute the heart of the turbomachines and as such they have been subjected to a very intensive theoretical and experimental study during the last two decades mainly due to the advent of high speed machines. It is known from investigations that the failure of turbine blading is normally due to fatigue and it occurs when vibrations take place at or near resonant conditions of operation. The failure due to fatigue can be catastrophic in the sense that it will involve complete shut down and also additional costs due to redesign and repair. To avoid fatigue, it is absolutely necessary to devise fast and accurate methods to predict fairly the natural frequencies of turbine blading right at the design stage. Extensive literature on turbine blade vibrations is available and the three recent review articles dealing with different aspects may be referred, Jones [1], Rao [2] and Leissa [3].

A typical modern steam turbine may have 3 or 4 rotors, each having several stages and the turbine altogether may have thousands of blades of different characteristics. Hence in such machines, it is not always possible to avoid resonance or near resonant conditions in some stages. Under these conditions, the designer should estimate the blade response and dynamic stresses at resonant conditions. Trumpler et al. [4] discussed the causes of forced vibration of turbine blading and resonant conditions. Prohl [5], assuming damping to be small and the energy input from a prescribed nozzle stimulus is equal to the energy dissipated in damping, developed a method for calculating stresses at resonance of a banded group of turbine buckets. Rao and Carnegie [6] determined the vibration response of rotating blades excited by the harmonic load applied at the free end considering Coriolis forces. Ewins and Sadasiva Rao [7] used the receptance technique to determine the forced vibration response of bladed-discs. Muszynska and Jones [8] have considered the effects of slip

damping at the root and hysteresis damping of the blade material, in determining the response of a stationary blade due to harmonic excitation at the tip. Component modal analysis was used by Srinivasan et al. [9] in the design of a typical fan. Rao et al. [10] used Rayleigh-Ritz method to determine the response of the aerofoil rotating blades due to flow excitation. The NASTRAN or ANSYS programs can be used to determine dynamic stresses of a turbine blade, e.g., Rieger and Nowak [11]. In this paper, the differential equations of motion of forced vibrations of a pretwisted, staggered and rotating blade of uniform cross-section are derived using Lagrange's equations. The excitation is taken in the form of NPF excitation. The effect of proportional damping is taken into consideration and the effects of rotary inertia and shear deformation are neglected. The forced vibration response is determined by using modal analysis.

Free vibration tests on rotating blades were conducted by Carnegie et al. [12], Rao and Banerji [13], and Swaminadham et al. [14]. Measurements of vibrations of steam turbine blades under load were described by Rissone and Burrough [15] and Vincent and Davis [16]. In this paper, the forced vibration phenomenon due to NPF excitation is demonstrated with the nozzles simulated by permanent magnets located at the required distance from the rotating blades. The nozzle passing frequencies are correlated from the Campbell diagram and theoretical and experimental response results are compared.

NOTATIONS

A	area of cross-section of blade
C	torsional stiffness
C_v	proportional damping coefficient
E, G	elastic constants
f_i	bending shape function
F_i	torsional shape function
FCZ	$\frac{1}{2}(n+1) - \frac{1}{2}(n-1)\cos 2\phi\bar{z}$
FSZ	$\frac{1}{2}(n+1) + \frac{1}{2}(n-1)\cos 2\phi\bar{z}$
FFZ	$\bar{R}(1-\bar{z}) + \frac{1}{2}(1-\bar{z}^2)$
I_{xx}, I_{yy}, I_{xy}	moments of area of cross-section about xx and yy axes
I_p	polar moment of area of cross-section
I_{xx}, I_{yy}	principal moments of area of cross-section
I_{cg}	mass moment of inertia per unit length of the blade about an axis passing through centre of gravity
L	length of blade
m	mass per unit length of the blade; harmonic number
n	number of terms in assumed solution
n_s	number of nozzles
p	natural frequency
q_i	generalised coordinate
r_{cg}	$\sqrt{I_{cg}/mL^2}$
R	disc radius
r	I_{yy}/I_{xx}
x, y	deflections of c.g. in xz and yz planes respectively
xx, yy	coordinate axes through c.g.
x_1, y_1	principal axes through c.g.
z	distance measured along Z axis
θ	torsional deflection
ω	rotational frequency
γ	stagger angle
ν	NPF = ωn_s
ϕ	pretwist angle
ρ	density of material of the blade
λ_1^2	mL^4/EI_{xx}
λ_2^2	AC_vL^4/EI_{xx}
λ_3^2	$I_pC_vL^2/EI_{xx}$
λ^2	$m\omega^2L^4/EI_{xx}$
μ^2	C/EI_{xx}
$-$	bar above a quantity denotes its nondimensional value taken with blade length, thus, $\bar{x} = x/L$

ANALYSIS

Neglecting shear deformation and rotary inertia the potential and kinetic energies of a uniform pre-twisted cantilever blade mounted at a stagger angle on a rotating disc are given as

$$U = \frac{1}{2}\int_0^L \left(EI_{xx} y''^2 + 2EI_{xy} x'' y'' + EI_{yy} x''^2 + C\theta'^2 \right) dz \qquad (1)$$

$$T = \frac{1}{2}\int_0^L \Big[m(\dot{x}^2 + \dot{y}^2) + I_{cg}\dot{\theta}^2 - (x'^2 + y'^2)\int_z^L m(R+z)\omega^2 dz + m\omega^2 (x^2 \sin^2\xi + y^2\cos^2\xi - xy \sin 2\xi)\Big] dz \qquad (2)$$

The energy dissipated due to proportional viscous damping is

$$W_d = \frac{1}{2}\int_0^L \Big[AC_v(\dot{x}^2 + \dot{y}^2) + I_p C_v \dot{\theta}^2 - (x'^2 + y'^2)\int_z^L AC_v(R+z)\omega^2 dz + AC_v\omega^2(x^2\sin^2\xi + y^2\cos^2\xi - xy\sin 2\xi)\Big] dz \qquad (3)$$

The excitation due to nozzles is assumed to be point forces acting at the free end of the rotating blade $Z = L$, whose components are taken as $F_x(t)$, $F_y(t)$ in x and y directions respectively and the moment $M(t)$. Work done by external forces is then given by

$$W_F = F_x(t)\,x_L + F_y(t)\,y_L + M(t)\,\theta_L \qquad (4)$$

In the above equation, the force and moment components can be expressed in terms of harmonic components by Fourier analysis. Thus

$$W_F = (a_{0x} + \Sigma a_{mx}\cos m\nu t + \Sigma b_{mx}\sin m\nu t)x_L + (a_{0y} + \Sigma a_{my}\cos m\nu t + \Sigma b_{my}\sin m\nu t)y_L + (a_{0M} + \Sigma a_{mM}\cos m\nu t + \Sigma b_{mM}\sin m\nu t)\theta_L \qquad (5)$$

where

$$a_{0x} = \frac{\nu}{2\pi}\int_0^{2\pi/\nu} F_x(t)\,dt$$

$$a_{mx} = \frac{\nu}{\pi}\int_0^{2\pi/\nu} F_x(t)\cos m\nu t\,dt$$

$$b_{mx} = \frac{\nu}{\pi}\int_0^{2\pi/\nu} F_x(t)\sin m\nu t\,dt$$

etc., (6)

Only six harmonics are considered in this analysis, i.e., $m = 1, 2, \ldots, 6$.

The following shape functions satisfying the boundary conditions, in series form are assumed

$$\bar{x} = \Sigma f_i(\bar{z})\,q_{1i}$$

$$\bar{y} = \Sigma f_i(\bar{z})\,q_{2i}$$

$$\theta = \Sigma F_i(\bar{z})\,q_{3i}$$

$$i = 1, 2, \ldots n \qquad (7)$$

where

$$f_i(\bar{z}) = \frac{1}{6}(i+2)(i+3)\bar{z}^{i+1} - \frac{1}{3}i(i+3)\bar{z}^{i+2} + \frac{1}{6}i(i+1)\bar{z}^{i+3}$$

$$F_i(\bar{z}) = \bar{z}^i - \frac{i}{i+1}\bar{z}^{i+1} \qquad (8)$$

Using Eq. (7) in Eqs. (1) to (4), the following equations of motion can be obtained with the help of Lagrange's equations.

$$[M]\{\ddot{q}\} + [C]\{\dot{q}\} + [K]\{q\} = \{Q_0\} + \sum_m \{Q_m\} e^{im\nu t} + \sum_m \{Q_{m+6}\} e^{i(\frac{\pi}{2} - m\nu t)} \qquad (9)$$

where

$$[M] = \begin{bmatrix} [A] & 0 & 0 \\ 0 & [A] & 0 \\ 0 & 0 & [B] \end{bmatrix}$$

$$A_{ij} = \lambda_1^2 \int_0^1 f_i f_j \, d\bar{z}$$

$$B_{ij} = \lambda_1^2 r_{cg}^2 \int_0^1 F_i F_j \, d\bar{z} \qquad (10)$$

$$[C] = \begin{bmatrix} [D] & 0 & 0 \\ 0 & [D] & 0 \\ 0 & 0 & [E] \end{bmatrix}$$

$$D_{ij} = \lambda_2^2 \int_0^1 f_i f_j \, d\bar{z}$$

$$E_{ij} = \lambda_2^2 \int_0^1 F_i F_j \, d\bar{z} \qquad (11)$$

$$[K] = \begin{bmatrix} [F] & [G] & 0 \\ [G] & [H] & 0 \\ 0 & 0 & [J] \end{bmatrix}$$

$$F_{ij} = \int_0^1 \left[\alpha^2 f_i' f_j' FFZ - \alpha^2 \sin^2 \beta \, f_i f_j + f_i'' f_j'' FSZ \right] d\bar{z}$$

$$G_{ij} = \int_0^1 \left[\tfrac{1}{2}(n-1) f_i'' f_j'' \sin 2\phi \bar{z} + \tfrac{1}{2} \alpha^2 f_i f_j \sin 2\beta \right] d\bar{z}$$

$$H_{ij} = \int_0^1 \left[\alpha^2 f_i' f_j' FFZ - \alpha^2 \cos^2 \beta \, f_i f_j + f_i'' f_j'' FCZ \right] d\bar{z}$$

$$J_{ij} = \mu^2 \int_0^1 F_i' F_j' \, d\bar{z} \qquad (12)$$

$$\{Q_o\} = \frac{L^2}{EI_{xx}} \begin{Bmatrix} a_{ox} f_j \\ a_{oy} f_j \\ a_{oM} F_j / L \end{Bmatrix}_{\bar{z}=1}$$

$$\{Q_m\} = \frac{L^2}{EI_{xx}} \begin{Bmatrix} a_{mx} f_j \\ a_{my} f_j \\ a_{mM} F_j / L \end{Bmatrix}_{\bar{z}=1}$$

$$\{Q_{m+6}\} = \frac{L^2}{EI_{xx}} \begin{Bmatrix} b_{mx} f_j \\ b_{my} f_j \\ b_{mM} F_j / L \end{Bmatrix}_{\bar{z}=1} \qquad (13)$$

$$\{q\} = \begin{Bmatrix} q_{1i} \\ q_{2i} \\ q_{3i} \end{Bmatrix}$$

$i = 1, 2, \cdots n$

$j = 1, 2, \cdots n \qquad (14)$

The natural frequencies and mode shapes are obtained by using standard eigen value subroutines. The forced vibration response due to six harmonics of the exciting force components given in digital form, is obtained by following modal analysis. Computer programs are developed for this purpose using five term solutions in Eq. (7).

EXPERIMENTAL INVESTIGATION

To demonstrate the forced vibration phenomenon due to NPF and check the analysis presented in the previous section, an experimental rig is designed and built. Pretwisted blade of uniform rectangular cross-section is used in the present work. The bladed disk is enclosed in a vacuum chamber and is driven by a 30 KW thyrister controlled D.C. motor. The nozzles are simulated by permanent megnets at required distance from the blades. The excitation force due to these magnets is determined by a magnet calibration set up specially designed for this purpose and the excitation force in yz and xz planes and axial moment on the blade are determined in general digital form at chosen angular intervals. Semiconductor strain gages are used to determine the response in flapwise motion of the blade and signals are monitored through a slip ring to the strain measuring bridge and amplifier. The response is displayed on an oscilloscope screen.

Blade:- A blade pair was prepared from 210 x 80 x 6 mm M.S. plate by first milling and then grinding to the desired dimensions. This piece was then cut into two smaller pieces and the two end surfaces were machined on horizontal milling machine. Each blade was then placed in two attachments, located centrally with the help of packings on the sides and was twisted in a torsion testing machine. The blade was held in the testing machine for a period of 15 minutes after a twist of 60° was imparted, before releasing the grips. After the process of twisting, the top at one of the ends and a length of 9 mm at the other end were cut with hacksaw and the surfaces were machined on the horizontal milling machine.

As the blade is to be mounted on the rotor, a special blade holder was prepared. A piece of 60 mm dia x 20 mm thickness was machined on a lathe and a slot of 10 mm deep and 5 mm wide was then cut on horizontal milling machine. The edges of the slot were finally machined on the shaping machine to an angle of 45° with the the surface of blade holder. Four holes were then drilled and machined. The blade was then located centrally in the blade holder and finally welded to it. The blade holder with the blade welded to it was fastened on the rotor by four L N bolts which were designed to withstand safely a centrifugal force upto a speed of 6000 rpm. Figs. 1 and 2 show 6 different stages of preparation of the blade. Fig. 3 shows the pretwisted blade with blade holder mounted on the rotor.

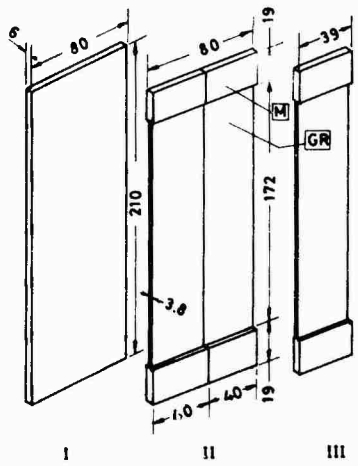

Fig. 1: Stages I, II and III in the preparation of pre-twisted blade.

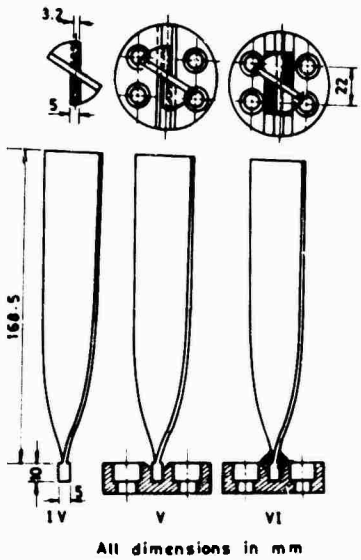

Fig. 2 : Pretwisted blade and blade holder

Fig. 3 : Pre-twisted blade mounted on the rotor

The blade properties are

I_{xx} = 0.010513 cm^4
I_{yy} = 1.521776 cm^4
$\Im$ = 90^o
ϕ = 58^o
C = 35449.79 cm^2/rad
E = 2.11×10^6 kg/cm^2
G = 0.843×10^6 kg/cm^2
L = 16.85 cm
A = 1.232 cm^2
ρ = 0.00786 kg/cm^3

Instrumentation:- Semiconductor strain gauges of silicon are used to sense the bending moment and as such the displacement in yz plane. Two gauges are used at the root of the blade. The gauges are fixed to the blade by araldite and sufficient care is taken to see that the effect of cross-sensitivity is negligibly small. These gauges are connected to the strain measuring bridge in a half bridge circuit. One of the two leads of each strain gauge is connected to a common wire. Thus three leads are taken out from the strain gauges. After the blade is mounted on the rotor, these leads are soldered to three terminals on the rotor and are numbered C, T_1 and T_2. The fourth terminal E on the rotor is for earthing, which is taken from a thin copper strip placed between the blade holder and the rotor before tightening the blade. These four terminals are fixed to the rotor by araldite and are numbered E, C, T_1 and T_2. A 12 way IDM Electronics slip ring is used and the same numbering is given to the terminals coming out of their unit. The wires used for monitoring the signals are perfectly shielded to prevent noise from being picked up in the main signal. An exploded view of the bladed disk with details of connections to the slip ring is given in Fig. 4. A Mini Rack strain measuring bridge is used in conjunction with a sensitive D.C. amplifier and a double beam storage oscilloscope.

Excitation by permanent magnets:- Permanent magnets having a cross-section of 15 x 10 mm made of high energy Alnico alloys with excellent temperature stability are used. These magnets are particularly resistent to demagnetisation from vibrations and shocks and are magnetically oriented in a predetermined direction which is along the axis of the magnet. The two faces are ground.

The magnets are fixed in magnet holders which are machined from an Aluminium bar as shown in Fig. 5. The magnet holder with magnet is fixed in a socket welded in the wall of the vacuum chamber and its axial position

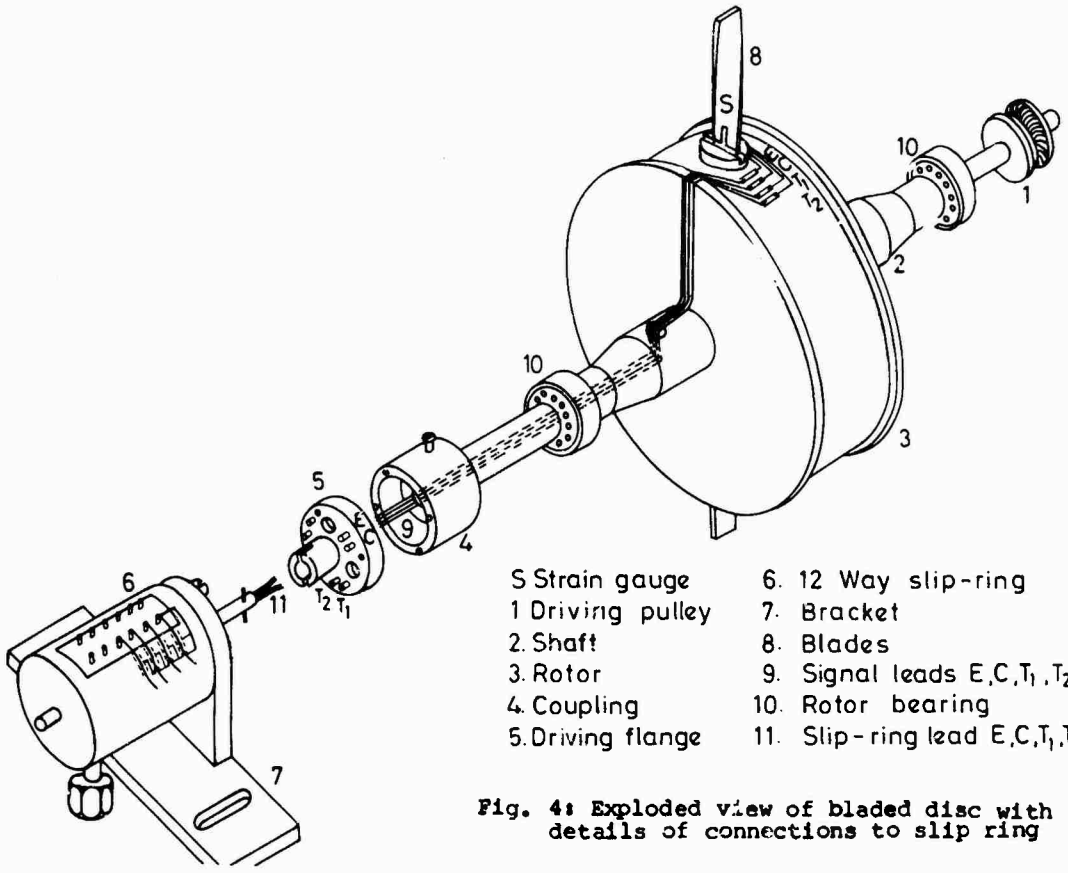

S Strain gauge
1 Driving pulley
2. Shaft
3. Rotor
4. Coupling
5. Driving flange
6. 12 Way slip-ring
7. Bracket
8. Blades
9. Signal leads E,C,T_1,T_2
10. Rotor bearing
11. Slip-ring lead E,C,T_1,T_2

Fig. 4: Exploded view of bladed disc with details of connections to slip ring

is adjusted so as to have a desired clearance between the face of the magnet and the edge of the blade. A steel ring is fixed on the magnet holder to provide an additional locking device for the magnet holder. 12 magnets are used which are spread at equal angular intervals. The lower half of the vacuum chamber with the permanent magnets is shown in Fig. 6. The complete vacuum chamber with magnet holders and slip ring is shown in Fig. 7.

Test Rig:- Fig. 8 shows the schematic arrangement in plan of the test rig with the driving motor. The rig essentially consists of a rotor on which the blade ring is sandwiched between two outer sections. The three sections are coupled together by eight axial bolts, the axis of the rotor being aligned horizontally in two roller bearings. All the rotating parts are made from EN 24 steel which permits the safe operation of the rig upto 8000 RPM. The rotor diameter is 32.4 cm and a provision is made on the blade ring to accommodate four blades at 90° angular intervals.

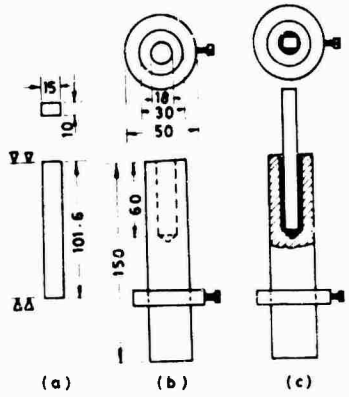

All dimension in mm

Fig. 5 : (a) Permanent Magnet (Alnico)

(b) Magnet holder with locking ring

(c) Assembly of Magnet and magnet holder with locking ring.

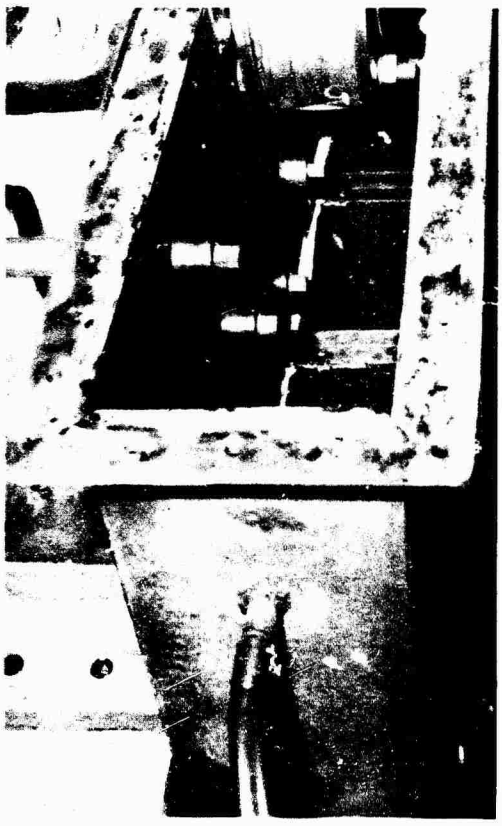

Fig. 6 : Lower half of vacuum chamber with permanent magnets.

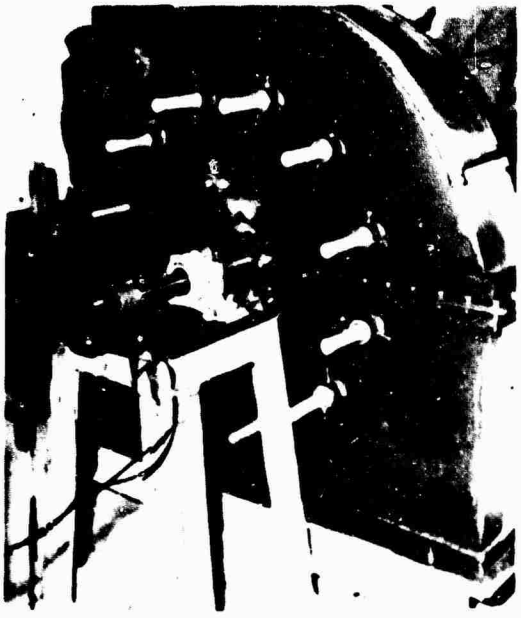

Fig. 7 : Complete vacuum chamber with magnet holders and slip ring.

The bladed disk is enclosed in a vacuum chamber which is fabricated from 6 mm M.S. plate. It is made in two parts separated by a parting plane. The top half could be lifted whenever required. In order to prevent leakage of air from outside, the parting plane flanges are made from 25 x 6 mm angle sections and the two halves are bolted together by 10 mm bolts at a pitch of 60 mm. A 2 mm thick rubber lining is provided at the parting plane. The bottom of the vacuum chamber is closed by welding a 3 mm M.S. plate reinforced by angle sections at six places across the width. This bottom flange is directly mounted on channnel sections. In order to seal the vacuum chamber at the two holes from where the rotor shaft comes out of it, two semi-circular rubber seals having the same internal diameter as the diameter of the shaft are fixed to the vacuum chamber, leaving practically no radial clearance between the shaft and seals. Twelve holes of 45 mm dia are drilled on one side wall at a pitch radius of 320 mm at 30° angular intervals and twelve sockets fixed to receive the magnet holders. A 70 HP vacuum pump is used to obtain a difference of mercury level of 30 cms.

Magnet calibration :- Fig. 9 shows a pictorial view of experimental set up to determine the forcing functions $F_x(t)$ and $F_y(t)$. Vertical rods R_1 and R_2 support a horizontal bar of square cross-section on the platform. Sliders A and B can slide freely on the horizontal bar. The slider A is locked in one extreme position by a screw S near the rod R_1. Slider B carries a magnet holder and a pointer P which indicates its position on the scale fixed on the horizontal bar. A threaded screw passes through the fixed slider A and a hand wheel is keyed to this screw at one end. At the other end of the screw is a ball and socket joint D which causes the slider B move to and fro on the horizontal bar by the rotation of the hand wheel H.

The blade end can be rotated on the sensing rod so that the correct position of the blade at the free end could be adjusted. The end of the sensing rod is thinned and two semiconductor type strain gauges, one in front and the other at the back are fixed so as to sense the bending moment. Care has been taken to see

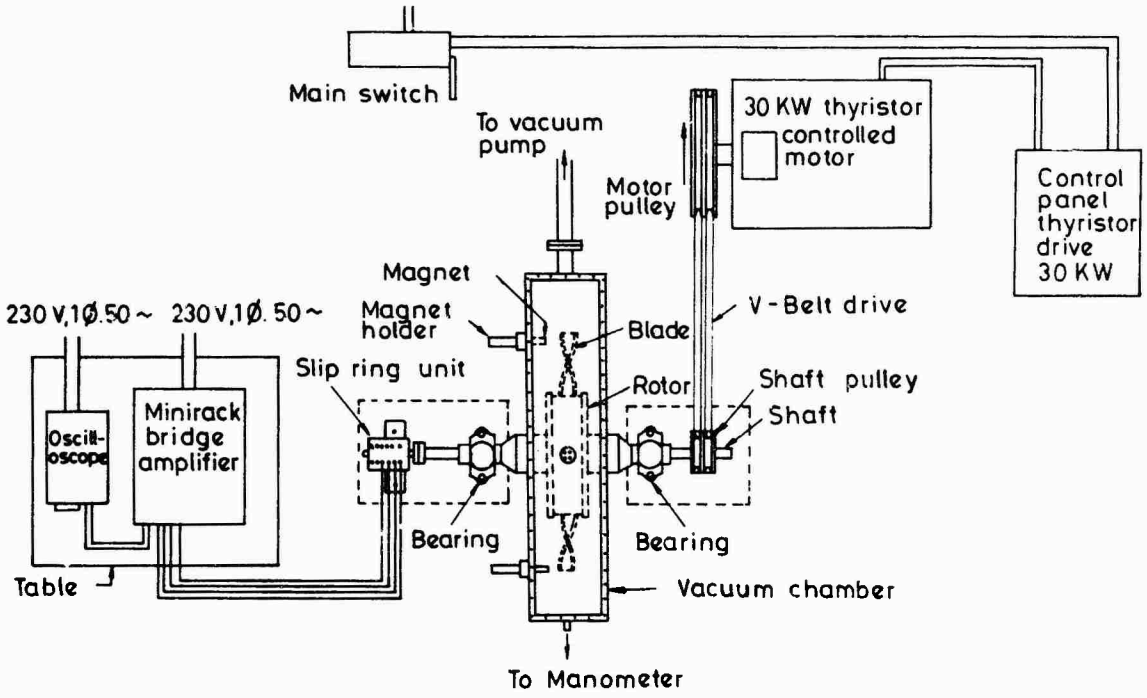

Fig. 8 : Schematic layout of the test rig.

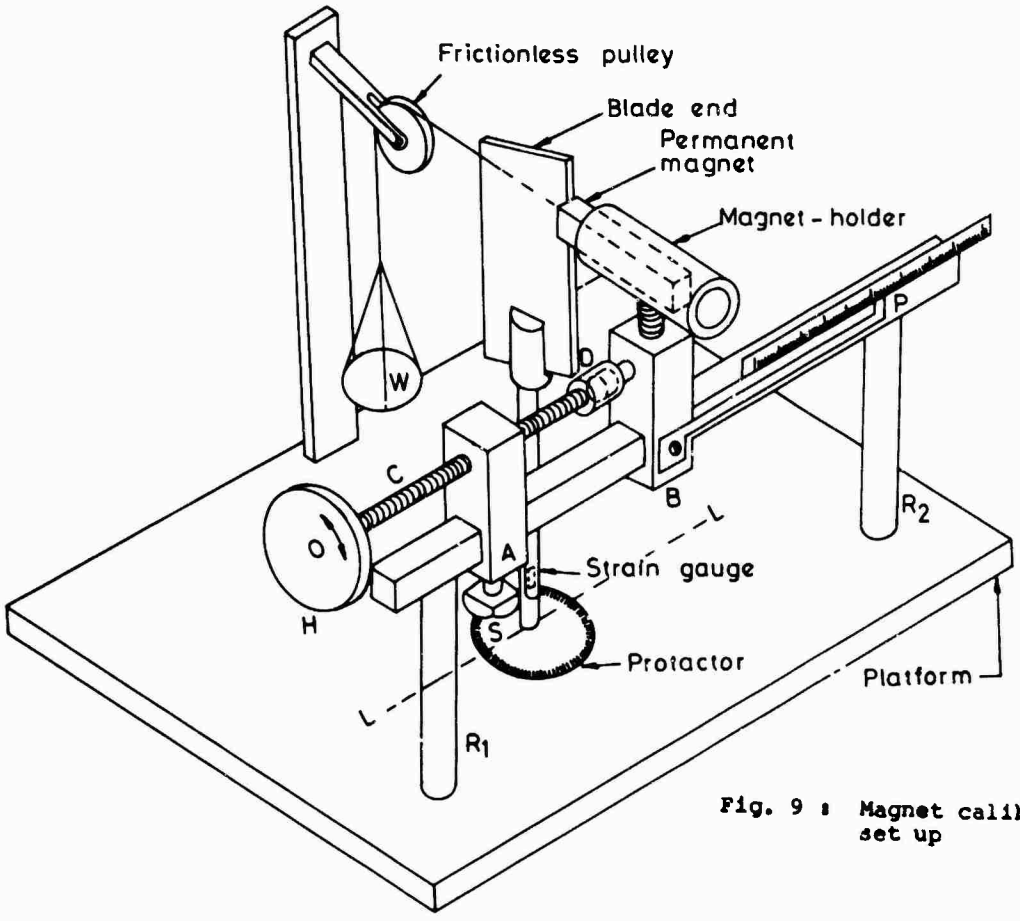

Fig. 9 : Magnet calibration set up

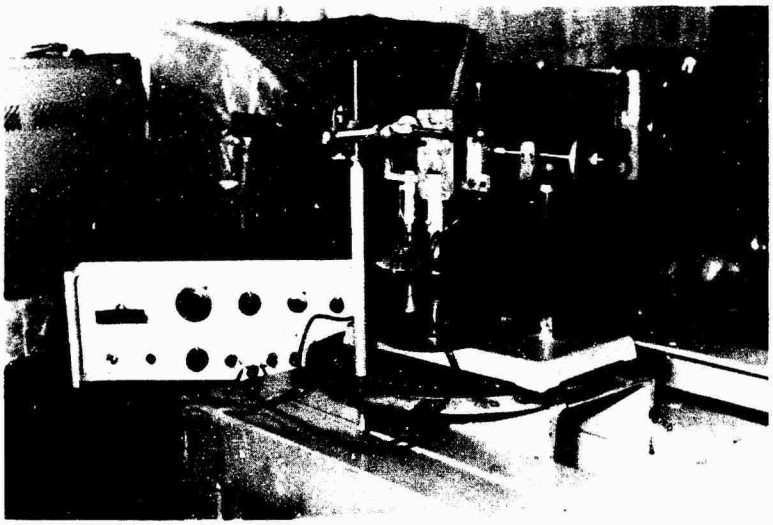

Fig. 10 : Magnet calibration set up.

that the gauges are mounted precisely such that the effect of cross-sensitivity is reduced to a minimum. A protractor is fixed at the end of the sensing rod such that zero degree line is parallel to the plane of the strain gauges. The permanent magnet can be adjusted in its magnet holder on the slider B so that the clearance between the nearest edge of the blade and the face of the magnet can be adjusted tc any desired value.

To balance the magnetic attractive force on the blade at any position of the magnet, a light string is attached at the centre line of the blade at the free end. This spring passes around a frictionless pulley and carries a light pan W of aluminium for placing weights. Fig. 10 shows the photograph of the magnet calibration set up.

To determine the force $F_y(t)$, the position of the plane of the strain gauges at the end of the sensing rod is so adjusted it is parallel to the chord of the blade at the root, with the help of line LL marked parallel to the horizontal rod. The plane of the blade at the top of the sensing rod is also adjusted such that it is parallel to the chord of the actual blade at the free end. Next the position of pulley is also adjusted such that the string remains perpendicular to the plane of the strain gauges. After having made these adjustments, the magnet holder is brought nearer the blade by rotating the handwheel till the pointer of voltmeter just starts moving from zero position. The scale is now adjusted on the rod such that the zero reading on the scale coincides with the position of pointer P. At 2 mm intervals of slider B from this position, the magnetic attractive force on the blade is recorded by balancing the voltmeter reading with the help of placing weights in the pan. To determine, the forcing function $F_x(t)$, the plane of the gauges is now made perpendicular to its previous position and the experiment repeated. Knowing F_y and F_x at each location (i.e., moment arms), the moment $M(t)$ is computed. The values thus obtained for a typical setting are given in Figs. 11 to 13.

Test Procedure:- The test rotor is first balanced using two plane rigid rotor balancing procedure with the help of B & K field balancing kit. The vacuum chamber is then assembled and perfectly sealed to obtain a vacuum of 30 cm mercury with the help of 70 HP vacuum pump. The strain bridge is then balanced. The thyristor controlled D.C. motor was then switched on and the rotor run to a desired speed. The rotor speed was measured by a tachometer and the amplitude of the wave form measured on the oscilloscope screen. It has been found that the response is purely harmonic at or near resonant conditions.

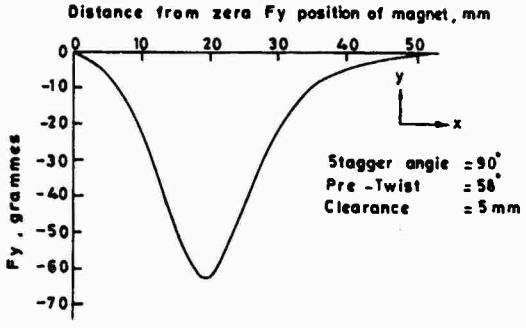

Fig. 11 : Magnetic Attractive force F_y

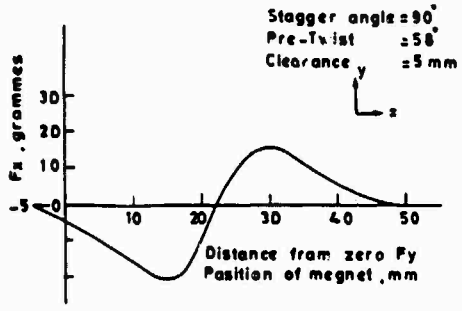

Fig. 12 : Magnetic Attractive force F_x

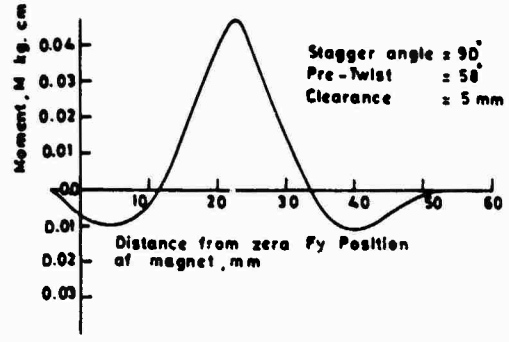

Fig. 13 : Moment M

ANALYTICAL RESULTS

For the blade data given earlier, the computer program developed is run to obtain the natural frequencies and forced vibration response. Fig. 14 gives the Cambell diagram of the blade for the first four bending-bending coupled modes and one torsional mode. Figs. 15 to 17 show the variation of bending-bending and torsional deflection amplitudes at the free end of the blade for a blade nozzle gap of 19 mm in the range of rotor speeds 150 - 1600 rpm. It can be observed that the peak values of deflections occur when the rotor speed reaches the critical values of inter-section of natural frequency curves and nozzle passing frequency lines as shown in the Cambell diagram. The intensity of resonance depends upon the order of NPF, e.g., in flap-wise bending the response is more pronounced at I NPF (477.6 rpm) compared to that at II NPF (238.5 rpm). The effect of damping ratio (DR = 0.01) is shown in Fig. 18 for bending-bending torsional deflections in the vicinity of two critical rotor speeds of 477.5 rpm and 1051 rpm.

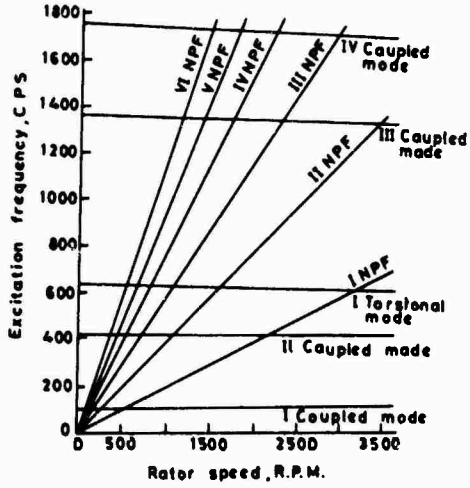

Fig. 14 : Campbell diagram

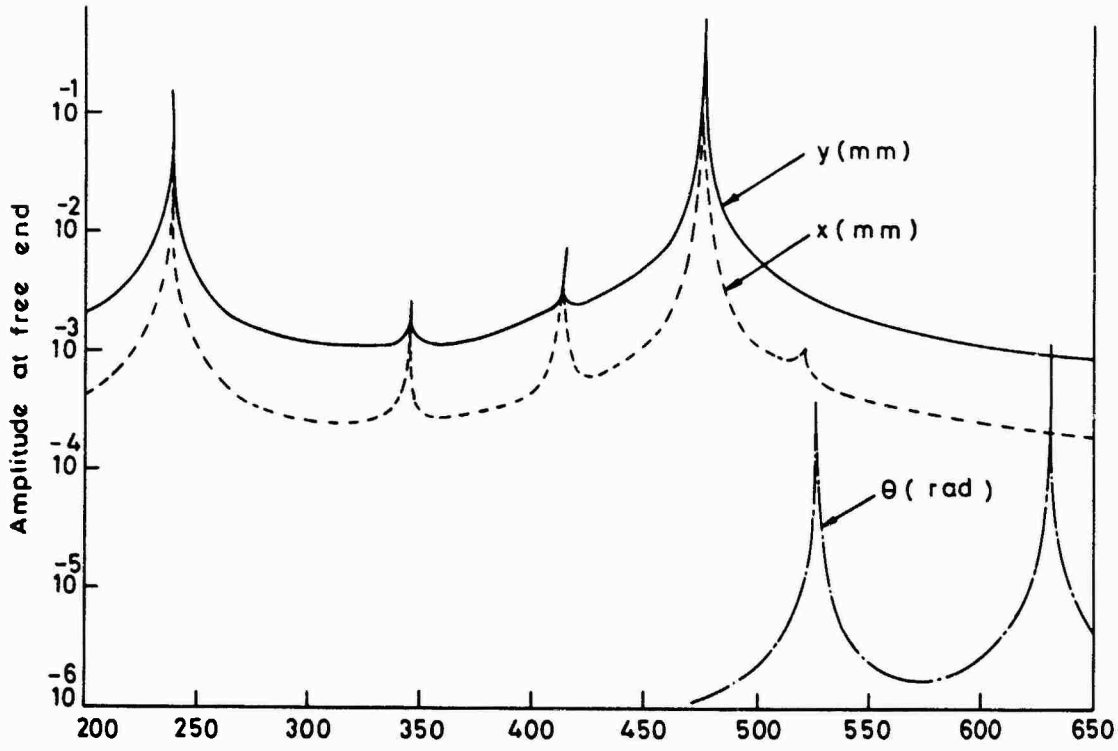

Fig. 15 : Blade response (speed range 200 - 650 rpm)

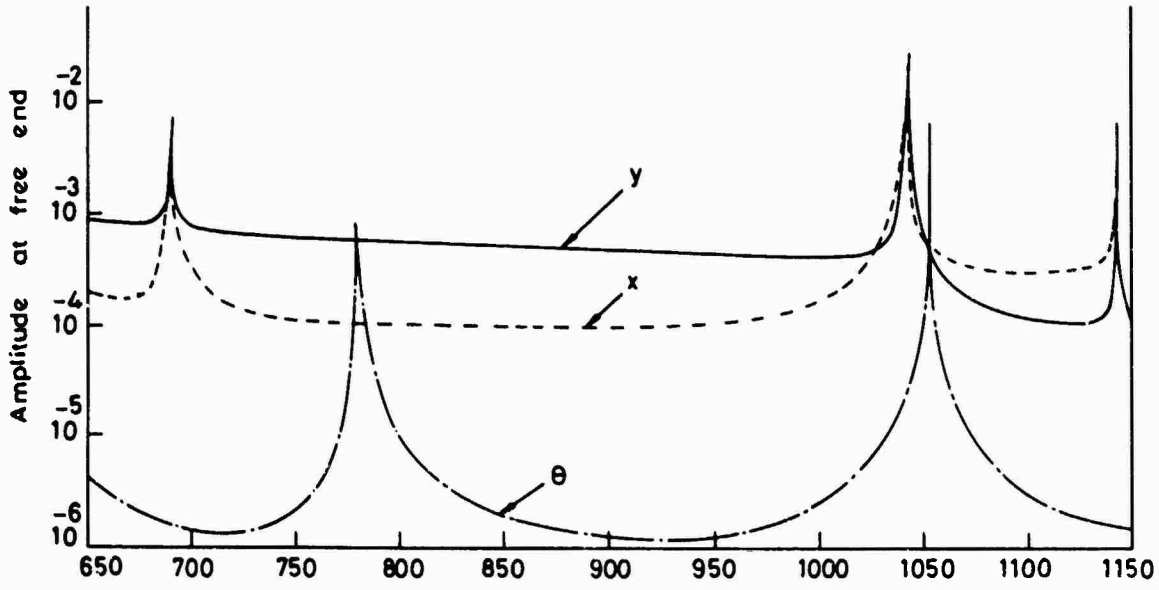

Fig. 16 Blade response (Speed range 650 - 1150 rpm)

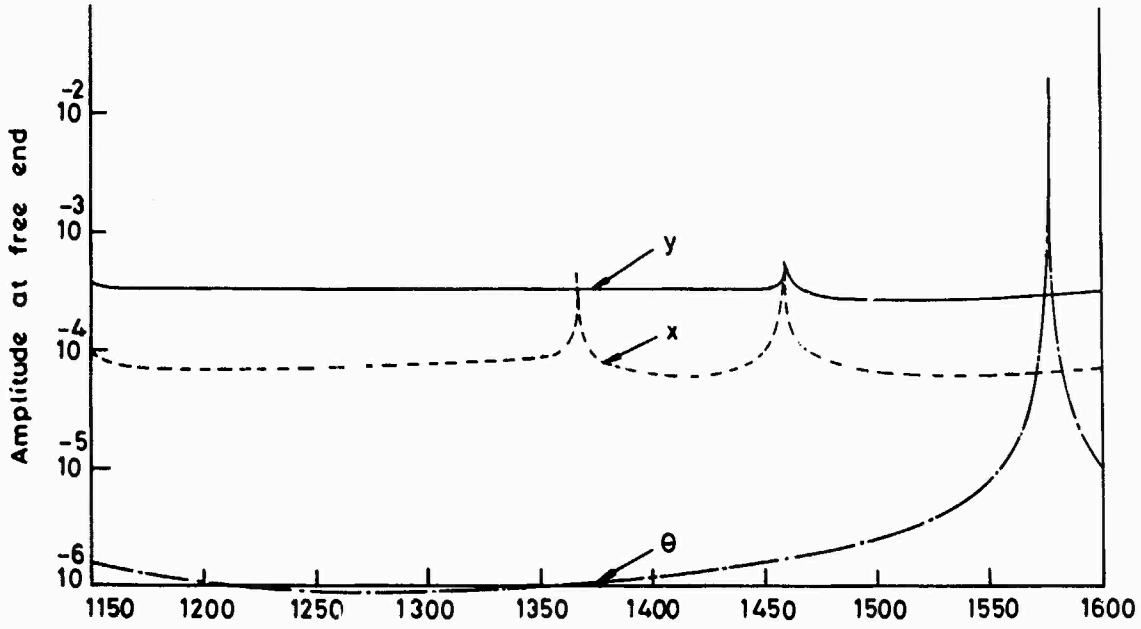

Fig. 17: Blade response (speed range 1150 - 1600 rpm)

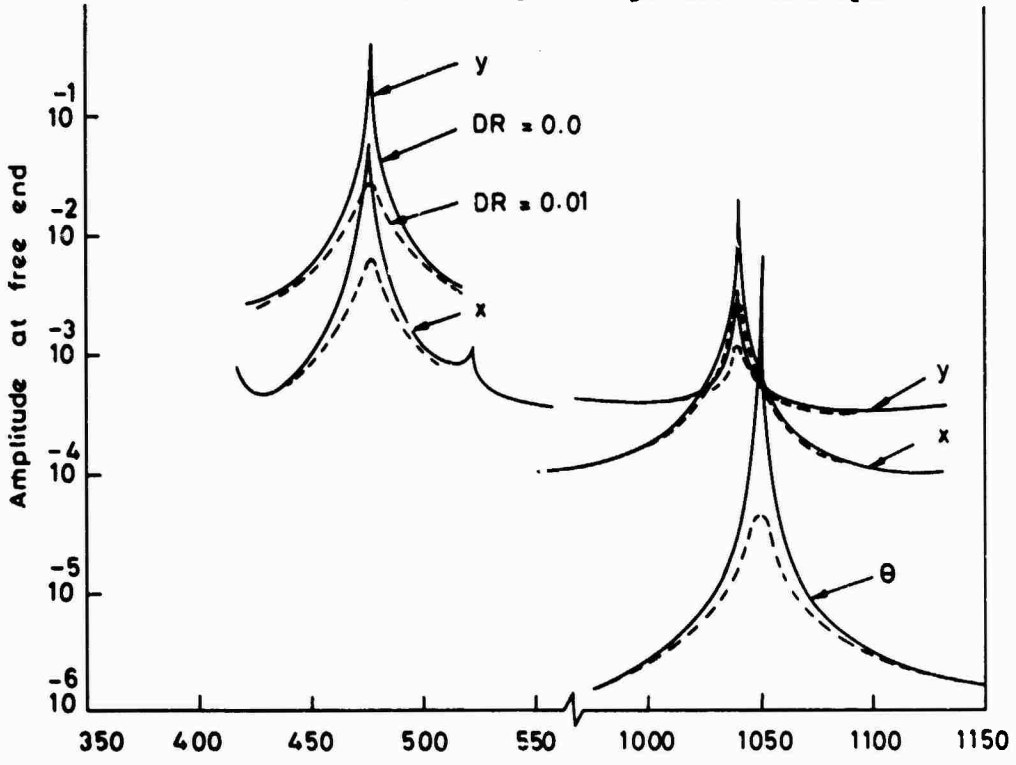

Fig. 18 : Effect of damping on blade response.

EXPERIMENTAL RESULTS

Figs. 19 to 21 give plots of results obtained directly from the tests described before. The peaks of the response curve show the resonance of the blade corresponding to the frequencies on the Campbell diagram in Fig. 14. Because of the type of arrangement of the gauges, the torsional mode could not easily be sensed. Also the response at resonances of coupled modes with higher harmonics of NPF was quite low and could not be easily detected.

COMPARISON OF RESULTS

Table 1 gives the analytical and experimental values of the rotor speeds at which resonance occurs. The experimental values of rotor speeds observed are in good agreement with the theoretical values.

The response results obtained in the first flapwise mode are compared with the analytical results by calibrating the gauges as follows. A light string is connected at the free end of the blade and this passes round a frictionless pulley. At the other end of the string is provided a pan for placing weights. The deflection of the free end in flapwise motion due to the weight on the pan is measured by the expansion of the dial gauge spindle placed behind the blade and the corresponding beam deflection on the oscilloscope screen is recorded directly. Using a calibration curve thus obtained, the experimental results are compared with analytical values in Fig. 22, which shows a very good agreement between them.

CONCLUSIONS

The differential equations of motion of forced vibrations of pretwisted uniform cross-section blades mounted at a stagger angle on a rotating disk are derived using Largange's equations. The blade excitation is taken in the form of NPF excitation as typical to a turbomachine. The force components can be given in general digital form and six harmonic components of NPF are accounted in the analysis. The effect of proportional damping is also included. Higher order effects due to shear and rotary inertia are not accounted. A general computer program is developed to determine coupled bending-bending and uncoupled torsional frequencies and the forced vibration response by using modal analysis.

A special test rig is designed to demonstrate the phenomenon of NPF excitation. The nozzles are simulated by permanent magnets located at required distance from the blades.

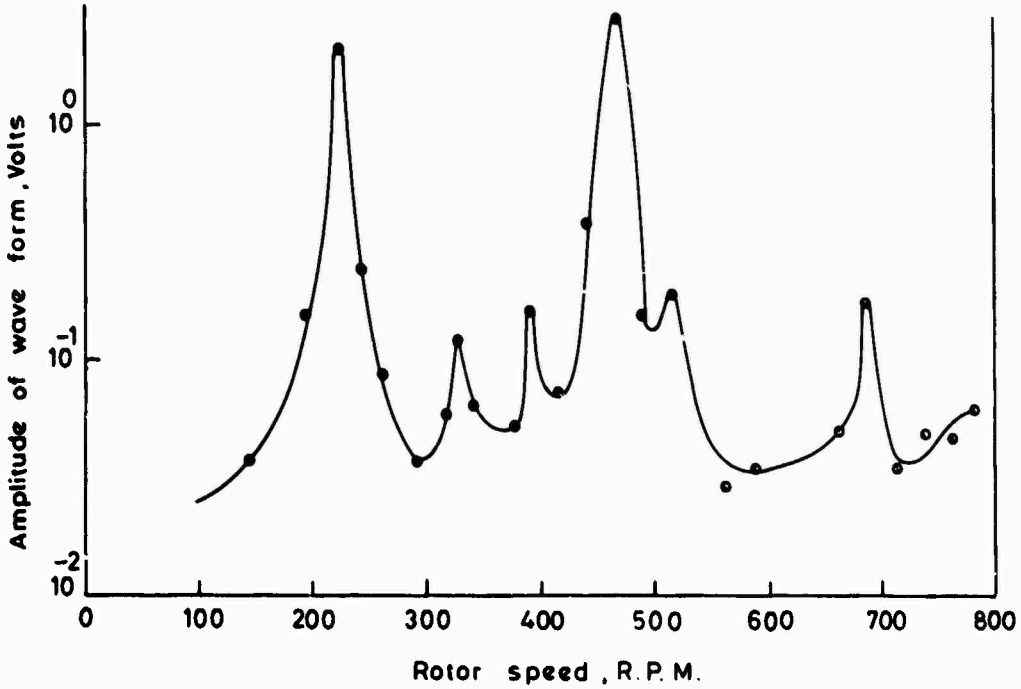

Fig. 19 : Experimental response of the blade (speed range 0 - 800 rpm)

Using the calibration set up, the excitation force components are defined for the magnet passing frequency excitation. The experimental observations are shown to be in good agreement with the analytical values obtained from the computer program.

ACKNOWLEDGEMENTS

The financial grant provided by ARDB panel of Ministry Defence, is greatly appreciated. The authors are also thankful to Dr. Ronald L Eshleman for presenting this paper on their behalf.

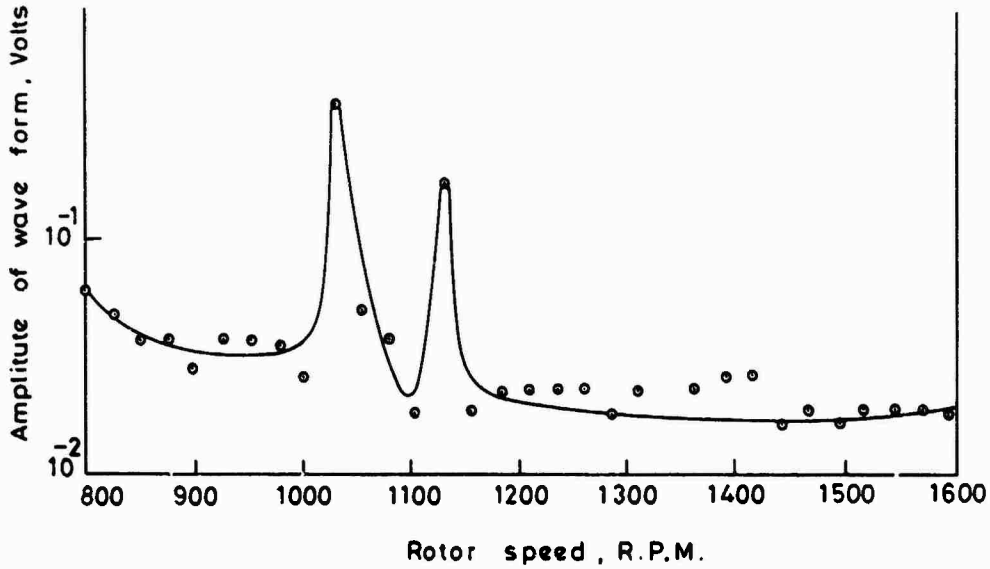

Fig. 20 : Experimental response of the blade (speed range 800-1600 rpm)

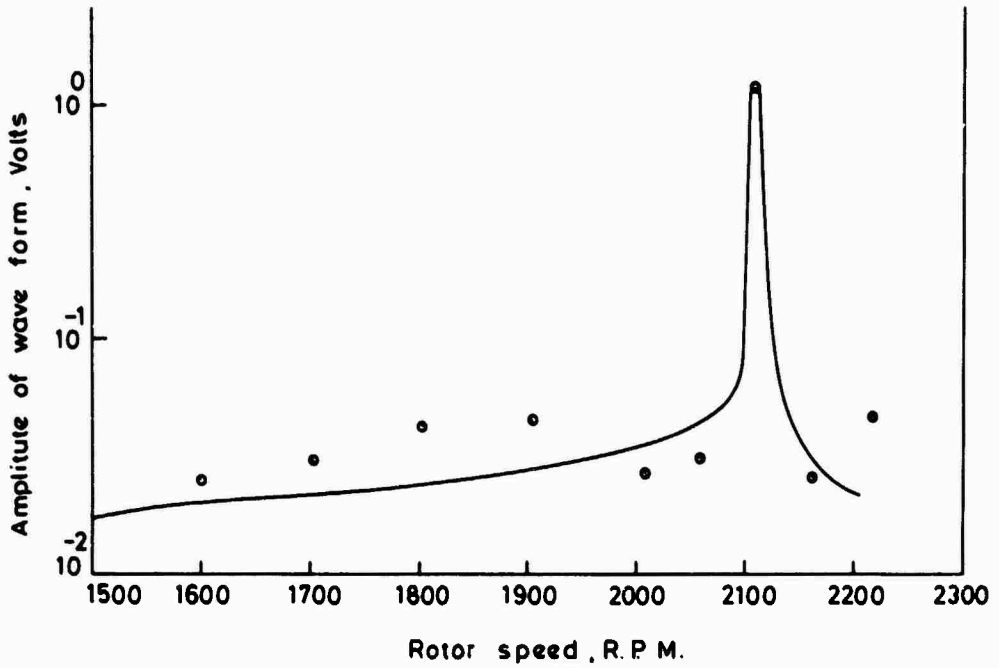

Fig. 21 : Experimental response of the blade (speed range 1500-2300 rpm)

TABLE 1

Comparison of Theoretical and Experimental Values of Rotor Speeds at which Resonance Occurs (RPM)

No.	Theory	Mode	NPF	Experiment	% Error
1	238.5	I coupled	II	230.0	3.56
2	343.3	II coupled	VI	-	
3	414.0	II coupled	V	400.0	3.38
4	477.5	I coupled	I	470.0	1.57
5	519.0	II coupled	IV	-	
6	525.0	I torsional	VI	-	
7	630.0	I torsional	V	-	
8	690.0	II coupled	III	700.0	-1.45
9	788.0	I torsional	IV	-	
10	1040.0	II coupled	II	1025.0	1.40
11	1051.0	I torsional	III	-	
12	1132.0	III coupled	VI	1125.0	0.61
13	1366.0	III coupled	V	-	
14	1458.0	IV coupled	VI	-	
15	1576.0	I torsional	II	-	
16	1708.0	III coupled	IV	-	
17	1755.0	IV coupled	V	-	
18	2121.5	II coupled	I	2125.0	-0.16

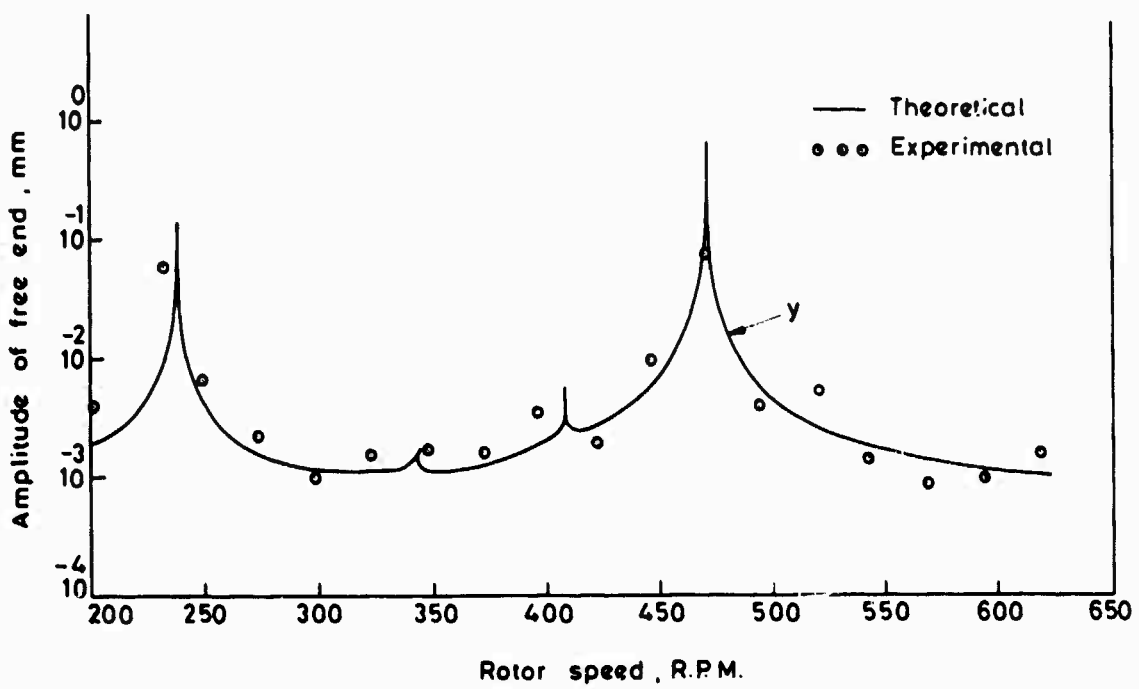

Fig. 22 : Comparison of theoretical and experimental results.

REFERENCES

1. D.I.G. Jones, "Two Decades of progress in Damping Technology", Aircraft Engrg., January 1979, p.9.

2. J.S. Rao, "Turbomachine Blade Vibration", The Shock and Vibration Digest, February, 1980, p. 19.

3. A.W. Leisse, "Vibrational Aspects of Rotating Turbomachinery Blades", App. Mech. Reviews, May 1981, p. 629.

4. W.E. Trumpler, et al., "Turbine Blade Vibration and Strength", Trans. ASME, Vol.77, 1955, p.337.

5. M.A. Prohl, "A Method for Calculating Vibration Frequency and Stress of a Banded Group of Turbine Buckets", Trans. ASME, Vol. 80, 1958, p. 169.

6. J.S. Rao, and W. Carneige, "Nonlinear Vibrations of Cantilever Blades by Ritz Averaging Process", J. Royal Aero. Soc., Vol. 76, 1972, p. 556.

7. D.J. Ewins, and V.V.K. Sadasiva Rao, "The Effect of Aerodynamic Damping on the Forced Response of Bladed Discs", Report No.2, S.R.C. Contract B/RG 5103.8, Imperical College of Science and Technology, London, May 1976

8. A. Muszynska, and D.I.G. Jones, "On Discrete Modelization of Response of Blades with Slip and Hysteretic Damping", Proc. 5th Congress on TPM, ASME Publ. July 1979, p. 641.

9. A.V. Srinivasan, et al., "Dynamic Analysis of an Assembly of Shrouded Blades Using Component Modes", J. Mech. Des., Trans. ASME, Vol. 100, 1978, p. 520.

10. J.S. Rao, et al., "Unsteady Force-Blade Response", Project Report 1978-79, Aero R&D Board, Ministry of Defence, India, 1979.

11. N.F. Rieger and W.J. Nowak, Analysis of Fetigue Stresses in Steam Turbine Blade Groups", EPRI Seminar on Steam Turbine Availability, Palo Alto, Jan. 1977.

12. W. Carneige, et al., "Vibration Characteristics of Turbine Bladind under Rotetion-Results of an Initial Investigetion and Details of High Speed Test Installation", App. Mech. Conv., Proc. I, Mech.E., April 1966, p. 124.

13. J.S. Rao, and S. Banjerji, "Coupled Bending Torsion Vibrations of Rotating Blades", ASME 76-GT-43.

14. M. Swaminetham, et al., "Identificetion of Resonant Frequencies of Rotating Beams with the use of PZT Crystals", Expt. Mech., Vol. 19, 1979, p.76.

15. R.F., Rissone, end H.L. Burrough, "Measurement of Blade Vibration in e Steam Turbine under Load", Engineer, Vol. 217, 1966, p. 209.

16. D. Vincent, and S.P. Davis, Radio Telemetry for Strain Measurement in Turbines", Reprint 149, Westinghouse Electric Corpn., Philadelphie, 1973.

PREDICTION OF CRITICAL SPEEDS, UNBALANCE AND NONSYNCHRONOUS FORCED RESPONSE OF ROTORS

P. Berthier, G. Ferraris, M. Lalanne
I.N.S.A.
Laboratoire de Mécanique des Structures
E.R.A. C.N.R.S. 911
20, avenue Albert Einstein
69621 Villeurbanne - France

The dynamic behavior of rotors must be accurately predicted today at the design stage of construction of rotating machinery. Here the general equations of rotors consisting of symmetric shafts, rigid discs and non symmetric bearings are presented. These equations are obtained by using a finite element technique and solved with a modal method.
Two industrial applications, a gaz turbine and a centrifugal compressor, are presented for which the critical speeds, unbalance and non synchronous forced response are calculated.

INTRODUCTION

It is now more and more necessary in the design of rotating machinery to predict accurately the dynamic behavior of rotors. This means that in general the variation of natural frequencies versus speed of rotation which gives the critical speeds, the unbalance and nonsynchronous forced response have to be calculated.

For the last ten years various studies including the mathematical modelisation of rotors and the resolution of these equations have been performed. In |1| and |2| the authors have used the transfer matrix technique. In |3|, ..., |12| the authors have generally written the equations of motion, used the finite element technique and frequently reduced the number of degrees of freedom by a substructures or a modal method.

In this paper an approach of the predominant effects occuring in steady state linear dynamics of rotors is presented. At first kinetic, strain energies and external forces for rotor elements, i.e. rigid discs, beams and bearings, are given. Then using Lagrange's equations the differential system of the rotor is obtained. The number of degrees of freedom of the equations is reduced by using the modes of the system at rest. The computer program written has been used for predicting the behavior of industrial examples such as a gas turbine and a centrifugal compressor which are presented in this paper.

DYNAMIC ANALYSIS

The rotor is composed with the following elements :

- symmetric rigid discs
- symmetric beam elements
- non symmetric viscous damped bearings

and rotates at a constant speed. The equations of motion are obtained from Lagrange's equations :

$$\frac{d}{dt}\left(\frac{\partial T}{\partial \dot{q}_i}\right) - \frac{\partial T}{\partial q_i} + \frac{\partial U}{\partial q_i} - Q_i = 0 \qquad (1)$$

with T, kinetic energy
U, strain energy
q_i, Q_i, respectively i^{th} generalised coordinate and force.

Kinetic energy

- Disc, (Fig.1)

In what follows :

u, w are the displacement components of the center of inertia of both disc and shaft cross section,
XYZ is the fixed frame of reference,
xyz is a rotating frame fixed to the disc or to the shaft,
OY is the axis of the rotor at rest. The displacements from the equilibrium position, that is the angles

$\theta = \frac{\partial w}{\partial y}$ and $\psi = -\frac{\partial u}{\partial y}$, are small and $\phi = \Omega t$.

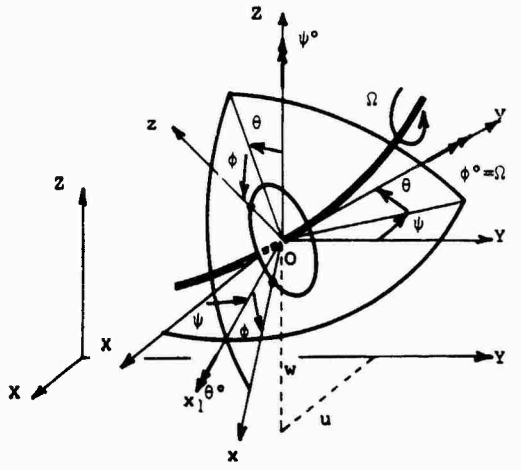

Fig.1 : Reference frames.

The disc is fixed in the xz plane of the rotating frame xyz end the angular velocity vector $\vec{\Omega}$ of xyz with respect to XYZ expressed by its components in xyz is :

$$\vec{\Omega} = \psi^{\circ}\vec{z} + \theta^{\circ}\vec{x}_1 + \phi^{\circ}\vec{y} \qquad (2)$$

$$= \begin{vmatrix}\Omega_x\\ \Omega_y\\ \Omega_z\end{vmatrix} = \begin{vmatrix}-\psi^{\circ}\cos\theta\sin\phi + \theta^{\circ}\cos\phi\\ \phi^{\circ} + \psi^{\circ}\sin\theta\\ \psi^{\circ}\cos\theta\cos\phi + \theta^{\circ}\sin\phi\end{vmatrix} \qquad (3)$$

The kinetic energy of the disc is then :

$$T_D = \frac{M_D}{2}(u^{\circ 2}+w^{\circ 2}) + \frac{1}{2}(I_{Dx}\Omega_x^2 + I_{Dy}\Omega_y^2 + I_{Dz}\Omega_z^2) \qquad (4)$$

with, $I_{Dx} = I_{Dz}$, diametral mass moment of inertie
$I_{Dy} = 2I_{Dx}$, poler mass moment of inertia
M_D, mass.

Taking into account the angular assumptions and (3), equation (4) becomes :

$$T_D = \frac{M_D}{2}(u^{\circ 2}+w^{\circ 2}) + \frac{I_{Dx}}{2}(\theta^{\circ 2}+\psi^{\circ 2}) + I_{Dy}\Omega\psi^{\circ}\theta + \frac{I_{Dy}\Omega^2}{2} \qquad (5)$$

where u, w, θ, ψ are generalised coordinetes. If (1) is used, equation (5) gives the disc matrices. The dstsrmination of the clessicel mass matrix is obtained by the first two terms, the entisymmetric Coriolis matrix which cen have a very significant effect by the third. The fourth term, being a constant, has no influence. These matrices are presented in |3| or |12|.

- Beam element

The extension of equation (5) to a constant cross section beam element of length L gives :

$$T_B = \frac{\rho S}{2}\int_0^L (u^{\circ 2}+w^{\circ 2})dy + \frac{\rho I}{2}\int_0^L (\psi^{\circ 2}+\theta^{\circ 2})dy + \rho I_p \Omega\int_0^L \psi^{\circ}\theta\, dy + \frac{\rho I_p L\Omega}{2} \qquad (6)$$

with : ρ, mass per unit volume
S, cross section area
I, diametral area moment of inertia of the cross section
I_p, polar area moment of inertia of the cross section.

The finite element technique is used and the nodal displacement vectors, (Fig.2), are :

$$\delta_u = |u_1, \psi_1, u_2, \psi_2|^t$$
$$\delta_w = |w_1, \theta_1, w_2, \theta_2|^t \qquad (7)$$

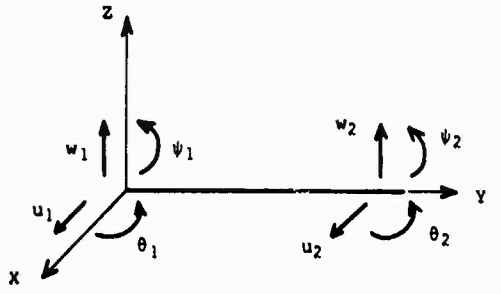

Fig.2 : Beam finite element.

The displecement functions are :

$$u = N_1(y)\,\delta_u \quad , \quad w = N_2(y)\,\delta_w \qquad (8)$$

where

$$N_1(y) = \left[1 - \frac{3y^2}{L^2} + \frac{2y^3}{L^3} \; ; \; -y + \frac{2y^2}{L} - \frac{y^3}{L^2} \; ; \; \frac{3y^2}{L^2} - \frac{2y^3}{L^3} \; ; \; \frac{y^2}{L} - \frac{y^3}{L^2}\right]$$

$$N_2(y) = \left[1 - \frac{3y^2}{L^2} + \frac{2y^3}{L^3} \; ; \; y - \frac{2y^2}{L} + \frac{y^3}{L^2} \; ; \; \frac{3y^2}{L^2} - \frac{2y^3}{L^3} \; ; \; -\frac{y^2}{L} + \frac{y^3}{L^2}\right] \qquad (9)$$

Introducing (7), (8), (9) in equation (6) gives :

$$T_B = \frac{\rho S}{2}\int_0^L (\delta_u^{\circ t}\ N_1^t N_1\ \delta_u^\circ + \delta_w^{\circ t}\ N_2^t N_2\ \delta_w^\circ)dy + \frac{\rho I}{2}\int_0^L (\delta_u^{\circ t}\ \frac{dN_1^t}{dy}\frac{dN_1}{dy}\ \delta_u^\circ + \delta_w^{\circ t}\ \frac{dN_2^t}{dy}\frac{dN_2}{dy}\ \delta_w^\circ)dy + \rho\ I_p\ \Omega \int_0^L \delta_u^{\circ t}\ \frac{dN_1^t}{dy}\frac{dN_2}{dy}\ \delta_w\ dy + \frac{\rho\ I_p\ L\ \Omega^2}{2} \quad (10)$$

The first integral gives the predominant mass matrix, the second the secondary effect of rotatory inertia. The third integral leads to the Coriolis matrix and the fourth term being a constant has no influence. These matrices are presented in |3| or |12|.

Strain energy

The general expression for the strain energy is

$$U = \frac{1}{2}\int_\tau \varepsilon^t \sigma\ d\tau \quad (11)$$

where ε and σ are respectively the strain and stress vector. Here :

$$\sigma = D\,\varepsilon = E\,\varepsilon \quad (12)$$

with E, the Young's modulus.

Let u^*, v^*, w^* be the components of the displacement of a point P of the cross section in the reference frame attached to the undeformed cross section of the beam, (Fig.3). The bending strain is :

$$\varepsilon = -x\frac{\partial^2 u^*}{\partial y^2} - z\frac{\partial^2 w^*}{\partial y^2} \quad (13)$$

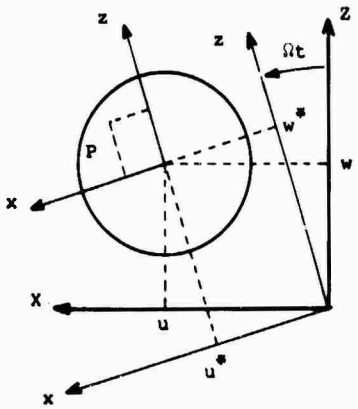

Fig.3 : Shaft reference frames.

As Ox and Oz are axis of symmetry, introducing equations (12) and (13) in equation (11) gives :

$$U = \frac{1}{2}\int_0^L EI_x \left(\frac{\partial^2 w^*}{\partial y^2}\right)^2 dy + \frac{1}{2}\int_0^L EI_z \left(\frac{\partial^2 u^*}{\partial y^2}\right)^2 dy \quad (14)$$

where EI_x and EI_z are respectively the bending rigidity about the z and x axis. Equation (14) has to be written with displacements expressed in the fixed frame XYZ in order to have a set of generalised coordinates. The displacement u^*, w^* and u, w are such as :

$$\begin{aligned} w^* &= w\cos\Omega t + u\sin\Omega t \\ u^* &= -w\sin\Omega t + u\cos\Omega t \end{aligned} \quad (15)$$

The substitution of (15) into equation (14) gives :

$$U = \frac{E}{2}\int_0^L \left[I_x\left(\cos\Omega t\frac{\partial^2 w}{\partial y^2} + \sin\Omega t\frac{\partial^2 u}{\partial y^2}\right)^2 + I_z\left(-\sin\Omega t\frac{\partial^2 w}{\partial y^2} + \cos\Omega t\frac{\partial^2 u}{\partial y^2}\right)^2\right] dy \quad (16)$$

For a symmetric shaft $I_x = I_z = I$, the periodic coefficients of (16) dissapear and the expression of the strain energy is :

$$U = \frac{EI}{2}\int_0^L \left[\left(\frac{\partial^2 u}{\partial y^2}\right)^2 + \left(\frac{\partial^2 w}{\partial y^2}\right)^2\right] dy \quad (17)$$

Using now (7), (8), (9), equation (17) can be written as :

$$U = \frac{EI}{2}\int_0^L \left[\delta_u^t\ \frac{d^2N_1^t}{dy^2}\frac{d^2N_1}{dy^2}\ \delta_u + \delta_w^t\ \frac{d^2N_2^t}{dy^2}\frac{d^2N_2}{dy^2}\ \delta_w\right] dy \quad (18)$$

This integral gives the classical stiffness matrix which is, as the matrices due to axial force or shear effect, presented in |3| or |12|. The pulsating torque influence has been shown in |13| and the corresponding matrices are in |4|.

Bearings

The two components of the force on the shaft due to hydrodynamic bearings have the well known general expression |14| :

$$\begin{vmatrix} F_u \\ F_w \end{vmatrix} = -\begin{vmatrix} k_{XX} & k_{XZ} \\ k_{ZX} & k_{ZZ} \end{vmatrix}\begin{vmatrix} u \\ w \end{vmatrix} - \begin{vmatrix} c_{XX} & c_{XZ} \\ c_{ZX} & c_{ZZ} \end{vmatrix}\begin{vmatrix} u^\circ \\ w^\circ \end{vmatrix} \quad (19)$$

where the two matrices are respectively the stiffness and the viscous damping matrices, generally non symmetric, i.e. $k_{XZ} \neq k_{ZX}$ and $c_{XZ} \neq c_{ZX}$.

Unbalance and nonsynchronous force

The force due to unbalance is easily obtained from the application of (1) to the expression of the kinetic energy of the mass unbalance. For an another kind of force which can be for example constant or nonsynchronous it is necessary to determine the expressions of their virtual work.

Solution of the equations

If X is the N order generalized coordinate displacement vector, the differential equation system of the rotor can be written as :

$$M\ddot{X} + C\dot{X} + KX = F_1 + F_2 \sin \Omega t + F_3 \cos \Omega t + F_4 \sin a\,\Omega t + F_5 \cos a\,\Omega t \quad (20)$$

with M, symmetric mass matrix
K, stiffness matrix consisting of symmetric matrices of the beam elements and non symmetric matrices of the bearings
C, matrix consisting of antisymmetric matrices due to Coriolis effect and non symmetric matrices due to the bearings
F_1, constant force such as gravity
F_2,F_3, force due to unbalance
F_4,F_5, force due to nonsynchronous effect
a, coefficient.

In this work the solution of (20) is obtained from a modal method which uses the modes of the system at rest to reduce the number of degrees of freedom. These modes come from :

$$M\ddot{X} + KX = 0 \quad (21)$$

The matrix K is non symmetric, then the modes of (21) are obtained by using the Q.R. algorithm. This gives the n first eigenvectors (n << N) used to perform the change of variables :

$$X = \phi\, p \quad (22)$$

ϕ, N.n transformation matrix. With (22), equation (20) becomes :

$$\phi^t M \phi\, \ddot{p} + \phi^t C \phi\, \dot{p} + \phi^t K \phi\, p = \phi^t F_1 + \phi^t (F_2 \sin \Omega t + F_3 \cos \Omega t) + \phi^t (F_4 \sin a\,\Omega t + F_5 \cos a\,\Omega t) \quad (23)$$

which, when p is known, will give X. The natural frequencies versus speed of rotation are obtained by using the Q.R. algorithm for solving :

$$\phi^t M \phi\, \ddot{p} + \phi^t C \phi\, \dot{p} + \phi^t K \phi\, p = 0 \quad (24)$$

The steady state response to the force $\phi^t F_1$ is obtained from the solution of

$$\phi^t K \phi\, p = \phi^t F_1 \quad (25)$$

The steady state responses to the forces $\phi^t (F_2 \sin \Omega t + F_3 \cos \Omega t)$ or $\phi^t (F_4 \sin a\,\Omega t + F_5 \cos a\,\Omega t)$ are obtained by identification of the solutions of the form $p = \alpha \sin \Omega t + \beta \cos \Omega t$ or $p = \alpha \sin a\,\Omega t + \beta \cos a\,\Omega t$.

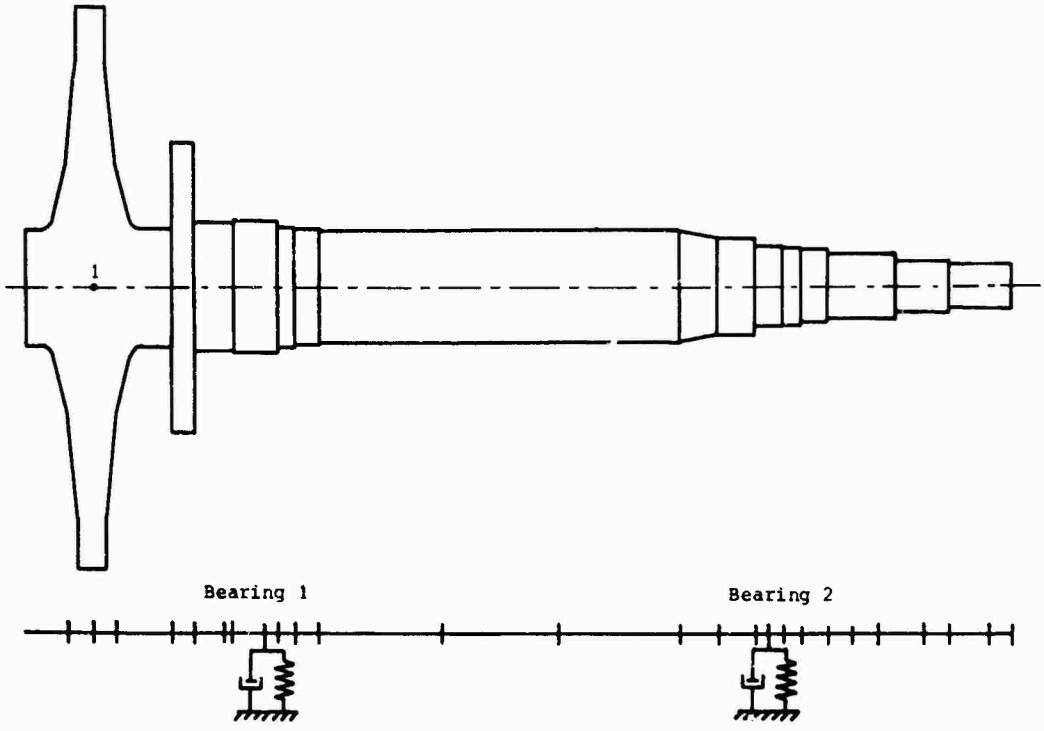

Fig.4 : Gaz turbine and finite element modelisation.

APPLICATIONS

Two industrial examples are presented in what follows. The S.I. units are used.

Gas Turbine (GT)

In figure 4, the rotor and its finite element modelisation are presented. The two bearings are different and for each of them two types of characteristics have been used. In case 1 the two bearings are symmetric, in case 2 they are not. Their characteristics are as follows :

	Bearing 1		Bearing 2	
	k_{XX} N/m	K_{ZZ} N/m	k_{XX} N/m	k_{ZZ} N/m
Case 1	0.74×10^9	0.74×10^9	0.45×10^9	0.45×10^9
Case 2	0.37×10^9	0.74×10^9	0.225×10^9	0.45×10^9

For both cases $k_{XZ} = k_{ZX} = 0$. Two values are given, for the viscous damping coefficient, which are identical, for both bearings and are supposed to be either $c_{XX} = c_{ZZ} = 0.6 \times 10^3$ (N/m/s) or $c_{XX} = c_{ZZ} = 0.6 \times 10^4$ (N/m/s) with in both cases the cross coupling terms equal to zero : $c_{XZ} = c_{ZX} = 0$.

The solution of the natural frequencies of the undamped rotor versus speed of rotation is presented in Figure 5 and Figure 6 which correspond respectively to the cases 1 and 2. These results show in the range 0-30000 rpm one critical speed due to unbalance in the case 1 and three critical speeds in the case 2.

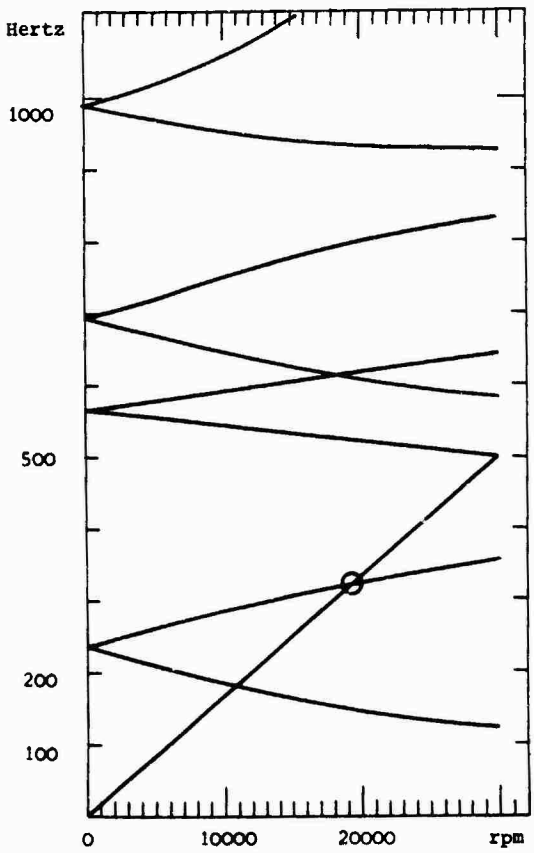

Fig.5 : GT. Case 1. Natural frequencies versus speed of rotation.

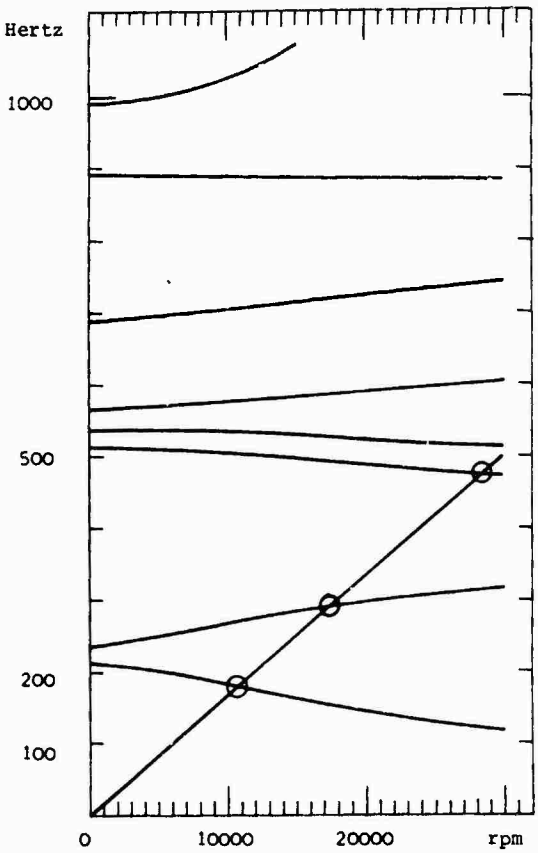

Fig.6 : GT. Case 2. Natural frequencies versus speed of rotation.

Then the effect due to an unbalance of 270 g.mm situated in 1, (Fig.4), that is in the plane of symmetry of the disc is calculated. In Figures 7 and 8 the displacement amplitude of the point 1 versus the speed of rotation is presented. The critical speeds predicted appear clearly and the amplitude of the response is very large for the two value of the damping. Obviously the rotor must be driven far from the critical speeds.

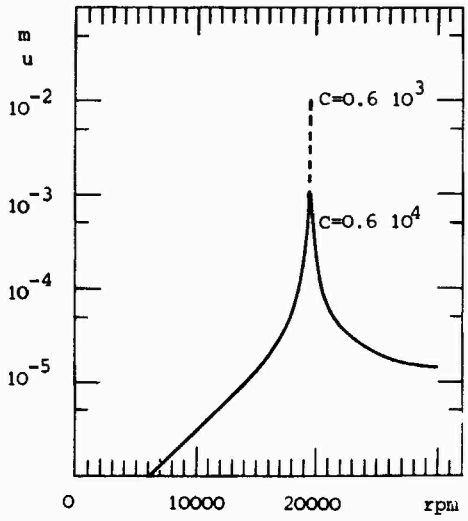

Fig.7 :GT. Case 1. Unbalance response.

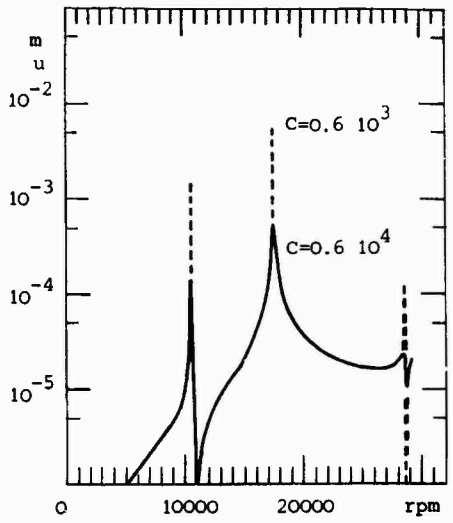

Fig.8 : GT. Case 2. Unbalance response.

Centrifugal Compressor (CC)

The rotor and its finite element modelisation are presented in Fig.9. At first the variation of the natural frequencies versus the bearing stiffness is given at rest and at operating speed. The stiffnesses are supposed to have no cross coupling terms and to be identical, (Fig.10). The continuous lines correspond to the

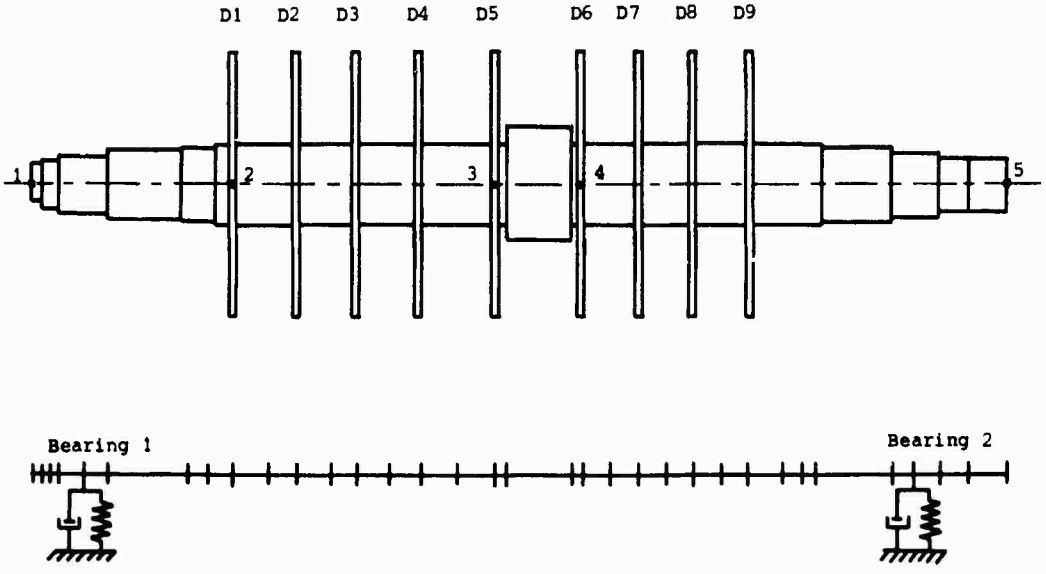

Fig.9 : Centrifugal compressor and finite element modelisation.

rotor at rest, the dotted lines to the frequency split due to the Coriolis effect.

Then the unbalance effect due to four possible unbalances is calculate and the displacement of point 2 is given. The values of the stiffnesses and viscous damping coefficients are as follows :

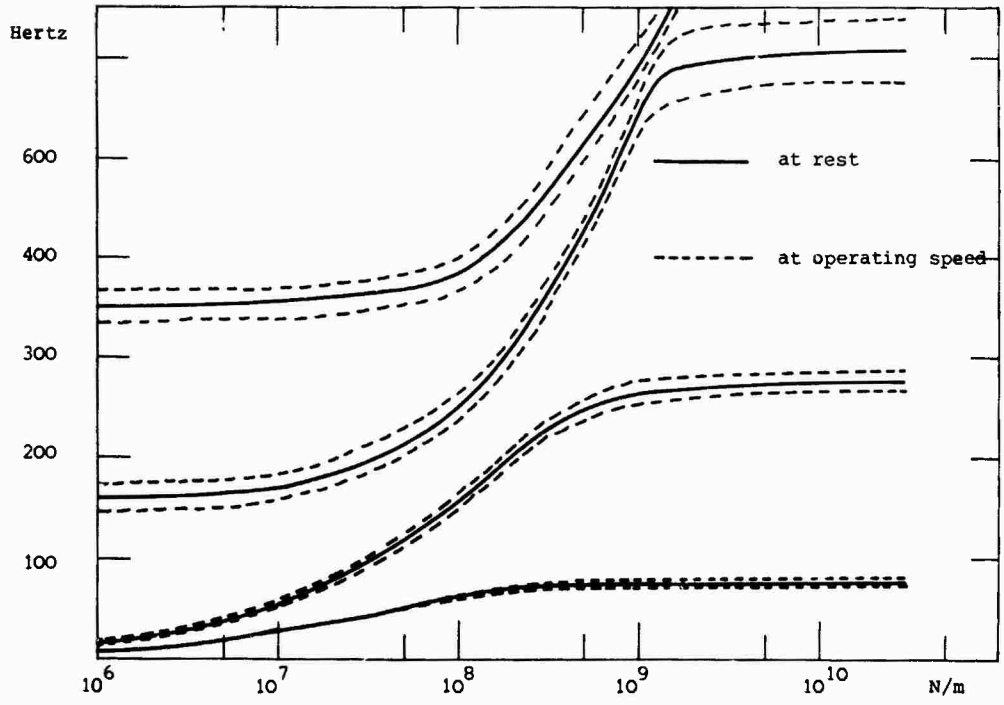

Fig.10 : CC. Natural frequencies versus bearing stiffness.

Speed rpm	5000	10000	20000
k_{XX}(N/m)	$4x10^7$	$6x10^7$	$7x10^7$
k_{ZZ}	$1.2x10^8$	$1.2x10^8$	$1.2x10^8$
k_{XZ}	$-1.1x10^5$	$-5x10^6$	$-1x10^6$
k_{ZX}	$1.1x10^5$	$5x10^6$	$1x10^6$
c_{XX}(N/m/s)	$1.05x10^4$	$6.5x10^4$	$6x10^4$
c_{ZZ}	$4.2x10^3$	$2.5x10^3$	$2.3x10^3$
c_{XZ}	$1.7x10^3$	$3.2x10^3$	$4.2x10^3$
c_{ZX}	$-1.7x10^3$	$-3.2x10^3$	$-4.2x10^3$

The characteristics at 5000 rpm were used for the speed lower than 7500 rpm. The characteristics at 10000 rpm were used in the calculation for the speeds between 7500 and 15000 rpm. The characteristics at 20000 rpm were used for speeds above 15000 The results (Fig.11), shows discontinuities around 7500 rpm because characteristics at 5000 and 10000 are significantly different.

The main practical conclusion is that for the range of speed of rotation considered the amplitude of the response to unbalance is always limited because of the viscous damping.

The displacement at point 3, when the rotor at operating speed is subjected to two identical nonsynchronous forces of amplitude 50 N at the points 3 and 4, has been predicted as a function of the forcing frequency of the nonsynchronous force and is given (Fig.12).

CONCLUSION

The equations of symmetric rotors composed of beam elements, rigid discs and supported by nonsymmetric viscous damped bearings have been presented. They have been solved using the modes of the structure at rest.

Two industrial exemples have been presented the prediction of their behaviour shows that for the Gas Turbine the speed of rotation must be far from a critical speed and that for the centrifugal compressor the damping induced by the bearings is sufficient to maintain independently of the speed of rotation the unbalance response at a low level.

AKNOWLEDGEMENTS

This work has been supported by CREUSOT-LOIRE The authors are indebted for permission to publish this paper.

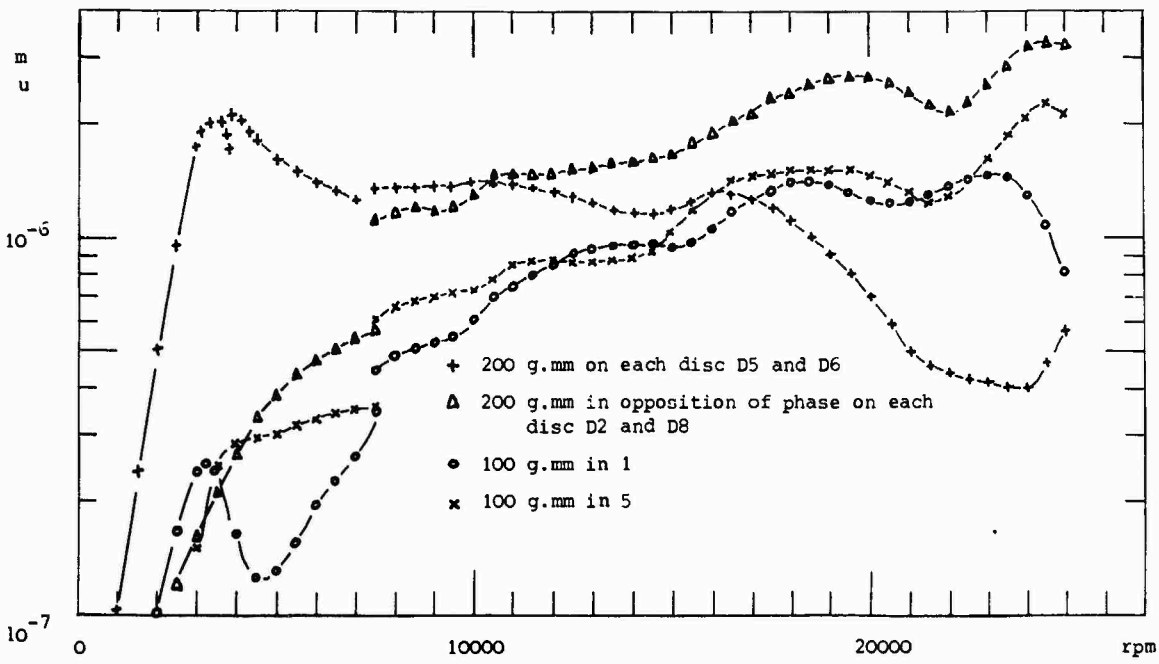

Fig.11 : CC. Unbalance response at point 2 versus speed of rotation.

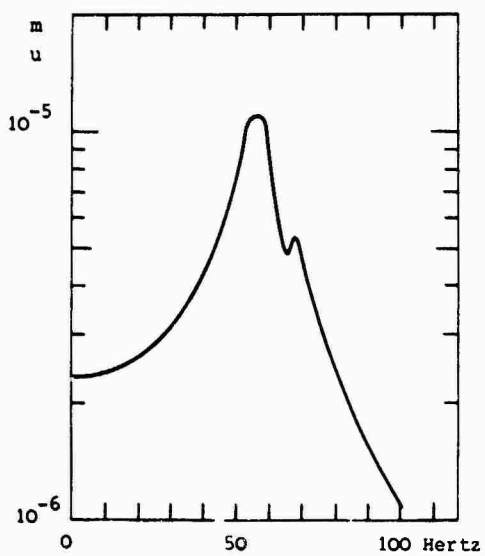

Fig.12 : CC. Non synchronous response at point 3 versus forcing frequency.

REFERENCES

|1| J.W. Lundt, "Critical speed, stability and response of a geared train of rotors", J. Mech. Des., Trans. A.S.M.E., pp.535-539, (1978).

|2| W.D. Pilkey, J.S.S. Trenkowski, P.Y. Chang, "Transient response of a rotor in damped bearings", J. Mech. Des., Trans. A.S.M.E., pp.257-265, (1978).

|3| H.D. Nelson, J.M. Mc. Vaugh, "The dynamic of rotor bearing systems using finite elements", J. Eng. Ind., Trans. A.S.M.E., pp.593-600, (1976).

|4| E.S. Zorzi, H.D. Nelson, "The dynamic of rotor bearing system with axial torque using finite element approach", J. Mech. Des., Trans. A.S.M.E., pp.158-161, (1980).

|5| K.E. Rouch, J.S. Kao, "Dynamic reduction in rotor dynamics by the finite element method", J. Mech. Des., Trans. A.S.M.E., pp.360-368, (1980).

|6| D.W. Childs, "A modal transient simulation model for flexible axisymetric rotors", J. Eng. Ind., Trans. A.S.M.E., pp.312-319, (1976).

|7| A.J. Dennis, R.H. Erikson, L.H. Settelman, "Transient response analysis of damped rotor systems by the normal mode method", A.S.M.E. paper 75 GT 58.

|8| D.A. Glasgow, H.D. Nelson, "Stability analysis of rotor bearing systems using component mode synthesis", J. Mech. Des. Trans. A.S.M.E., pp.352-359, (1980).

|9| H.D. Nelson, W.L. Meacham, "Transient analysis of rotor bearing systems using component mode synthesis", A.S.M.E., paper 81 GT 110.

|10| D.F. Li, E.J. Gunther, "Component mode synthesis of large rotor systems", A.S.M.E. paper 81 GT 147.

|11| Y. Birembaut, J. Peigney, "Predictions of dynamic properties of rotor supported by hydrodynamic bearings using the finite element method", Comp. and Struc., pp.483-486, (1980).

|12| D.M. Tran, "Etude du comportement dynamique des rotors flexibles", Thèse de D.I., (1981).

|13| R.L. Eshleman, R.A. Eubanks, "On the critical speed of a continuous rotor", J. Eng. Ind., Trans. A.S.M.E., pp.1180-1188, (1969).

|14| D. Nicolas, N. Abdul-Wahed, "Les paliers non symétriques à géométrie fixe-aspect dynamique", Méc., Mat., Elec., n°347/348,(1978).

|15| F.M. Dimentberg, "Flexural vibration of rotating shafts", Butterworth, (1961).

|16| A. Tondl, "Some problems of a rotordynamics", Chapmann and Hall, (1965).

|17| R.G. Loewy, W.J. Piarully, "Dynamics of rotating shafts", Shock and Vib. Monography, n°4, (1969).

|18| N.F. Rieger, J.F. Crofoot, "Vibration of rotating machinery", (1977).

|19| R. Bigret, "Vibration des machines tournantes et des structures", Tech. et Doc., (1980).

DISCUSSION

Mr. Bhat (Concordia University): You used the modes of the system at rest to obtain the unbalanced response. For the actual system, which is a non-self adjoint system, are the modes of the system at rest the actual modes? They are not the orthoagonal modes of the system, and they won't be orthagonal. By using the modes of the original system at rest will it give the proper unbalanced response?

Mr. LaLanne: We used modes of the system at rest, and that is what I have presented. You have obviously a system which is a non-diagonal system. Was that your question? At first it is a non-diagonal system, but it is a very small size system. What I mean by small size system is that we have somewhere around twenty equations, maybe a few more. When you want to get unbalanced response, we have to solve the system systematically for different values of the speed of rotation, omega, and look for a solution which has components in sin wt and cos wt. We have also solved the equations using the modes of the system in another way that makes the problem much more difficult to solve. For an existing rotor, of two or three hundred degrees of freedom, this leads to an increase of computer time, and after an explanation and using the results of a hundred or twenty, thirty, and so forth, it does not give significantly different results.

Mr. Bhat: Have you also tried modal analysis in phase space, considering the modes of the adjoint system?

Mr. LaLanne: Yes.

Mr. Bhat: And it didn't give results?

Mr. LaLanne: No.

UNBALANCE RESPONSE OF A SINGLE MASS ROTOR MOUNTED ON DISSIMILAR HYDRODYNAMIC BEARINGS

R. Subbiah, R.B. Bhat and T.S. Sankar

Department of Mechanical Engineering
Concordia University
Montreal, Quebec, Canada

The critical speeds and unbalance response of a single mass rotor, mounted on dissimilar fluid-film bearings at the ends, are studied. The direct and cross-coupled coefficients of stiffness and damping at the bearings are included in the analysis, which are expressed as polynomials in Sommerfeld number. The equations of motion are obtained by Lagrangian approach. The resulting equations of motion are solved to obtain the unbalance response and critical speeds. Numerical results are obtained for a laboratory model of a single mass rotor and the effects of various parameters of the system on the response are investigated. The response of the rotor at the bearing locations are also obtained.

NOMENCLATURE

$C_\alpha, C_\beta, C_\gamma$ = shaft damping at the disk position

D = damping energy

I_d = transverse moment of inertia of the disk

I_x = polar moment of inertia of the disk

L = Lagrangian

T = kinetic energy

V = potential energy

a = disk eccentricity

c_1, c_2 = bearing clearances for the left and right end bearings

$c_{y_1}, c_{y_2}, c_{z_1}, c_{z_2}$ = direct damping coefficients for bearings

$c_{yz_1}, c_{yz_2}, c_{zy_1}, c_{zy_2}$ = cross-coupled damping coefficients for bearings

$k_{y_1}, k_{y_2}, k_{z_1}, k_{z_2}$ = direct stiffness coefficients for bearings

$k_{yz_1}, k_{yz_2}, k_{zy_1}, k_{zy_2}$ = cross-coupled stiffness coefficients for bearings

ℓ = total length of the rotor shaft

ℓ_1, ℓ_2 = distances to the disk from the left and right ends of the bearings respectively

m = mass of the disk

y_1, y_2 = displacement at the bearings in y-direction

z_0, y_0 = displacement at the disk location

z_1, z_2 = displacement at the bearings in z-direction

ω = constant speed of the shaft

α, β, γ = shaft stiffness at the disk position

α = force per unit displacement

β = moment per unit angular displacement

γ = force per unit angular displacement or moment per unit deflection

θ_z, θ_y = local deviational angles at the disk of the distorted shaft tangent

INTRODUCTION

The dynamic response of rotors to residual unbalance is of vital interest in industry. In the vicinity of the critical speeds of the rotor, the response is quite large and hence, the normal steady state operating speeds of the rotor must be away from these speeds. When the rotors are mounted on hydro dynamic bearings, the evaluation of the damped critical speeds and the unbalance

response is quite complicated due to the asymmetry in the direct and cross-coupled stiffness and damping coefficients in the horizontal and vertical directions. Also, these coefficients are dependent on the operating speed of the rotor.

Different techniques were developed by various investigators to predict the critical speeds and unbalance of the rotor system. For example, Lund [1] used Prohl-Myklestad methods to determine the unbalance response of the rotor systems while Nelson and McVaugh [2] adopted finite element approach. Response of rotors in the fundamental rigid support mode region has been investigated by Rao [3], Rao, Bhat and Sankar [4] employing a Jeffcott rotor model. In their investigations, the rotor disk was at the center of the shaft and the fluid-film bearings which support the rotor at the two extreme ends were assumed to be identical. Their study was limited to response evaluation for synchronous whirl conditions only. However, in practice, the rotor may not be mounted exactly at the shaft center and the bearings supporting the rotor ends may not be identical, which may be due to practical limitations imposed in the design stage or due to tolerances in production. When the disk is not at the center or when the bearings are not identical, the rotor is likely to exhibit a coupled type of behaviour with the two ends of the rotor having different orbital motions. Unstable vibrations of an unsymmetric rotor system were studied by Yamamoto, Ota and Kono [5]. Also, an asymmetrically mounted rotor on dissimilar bearings was investigated by Ardayfio and Frohrib [6] using energy methods. But, their investigation did not include the cross-coupled stiffness of the fluid-film bearings. Moreover, the damping in the bearings was ignored in their approach.

A study of the response at the bearing locations is not reported in literature. If this response exceeds the bearing clearance, the rotor cannot operate satisfactorily and the bearing will fail. Hence, the bearings have to be designed considering the rotor response at the bearing locations.

In the present investigation, an energy method is used to develop the system model and Lagrange's equations are utilized to derive the equations of motion. The dissimilarity in bearings is achieved by having different bearing clearances at the two ends and by varying the disk position. The damped critical speeds and unbalance response of a laboratory model of a single mass rotor are studied for different combinations of clearances for the two bearings and for different disk positions. Orbital diagrams at the disk location and at the two bearings are obtained.

MATHEMATICAL MODEL AND ANALYSIS

The typical single mass rotor supported on hydro dynamic bearings at its two extreme ends is shown in Fig. 1. The disk is located at any position along the length of the rotor. The kinetic and potential energies for the given rotor system are set up and, using Lagrange's method, equations of motion are derived.

Lagrange's equation of motion is given by

$$\frac{d}{dt}\left(\frac{\partial L}{\partial \dot{q}}\right) - \frac{\partial L}{\partial q} + \frac{\partial D}{\partial \dot{q}} = 0$$

This results in four dynamical equations and four constraint equations. The final form of equations are given here and the detailed derivations are shown in Appendix I.

The dynamical equations are

$$m\frac{d^2}{dt^2}(z_0 + a\cos\omega t) + \alpha(z_0 - \frac{\ell_1}{\ell}z_2 - \frac{\ell_2}{\ell}z_1) + \gamma(\theta_z - \frac{z_2-z_1}{\ell}) + C_\alpha(\dot{z}_0 - \frac{\ell_1}{\ell}\dot{z}_2 - \frac{\ell_2}{\ell}\dot{z}_1) + C_\gamma(\dot{\theta}_z - \frac{\dot{z}_2-\dot{z}_1}{\ell}) = 0 \quad (1)$$

$$m\frac{d^2}{dt^2}(y_0 + a\sin\omega t) + \alpha(y_0 - \frac{\ell_1}{\ell}y_2 - \frac{\ell_2}{\ell}y_1) + \gamma(\theta_y - \frac{y_2-y_1}{\ell}) + C_\alpha(\dot{y}_0 - \frac{\ell_1}{\ell}\dot{y}_2 - \frac{\ell_2}{\ell}\dot{y}_1) + C_\gamma(\dot{\theta}_y - \frac{\dot{y}_2-\dot{y}_1}{\ell}) = 0 \quad (2)$$

$$I_d\ddot{\theta}_z + I_x\omega\dot{\theta}_y + \gamma(z_0 - \frac{\ell_1}{\ell}z_2 - \frac{\ell_2}{\ell}z_1) + \beta(\theta_z - \frac{z_2-z_1}{\ell}) + C_\gamma(\dot{z}_0 - \frac{\ell_1}{\ell}\dot{z}_2 - \frac{\ell_2}{\ell}\dot{z}_1) + C_\beta(\dot{\theta}_z - \frac{\dot{z}_2-\dot{z}_1}{\ell}) = 0 \quad (3)$$

$$I_d\ddot{\theta}_y - I_x\omega\dot{\theta}_z + \gamma(y_0 - \frac{\ell_1}{\ell}y_2 - \frac{\ell_2}{\ell}y_1) + \beta(\theta_y - \frac{y_2-y_1}{\ell}) + C(\dot{y}_0 - \frac{\ell_1}{\ell}\dot{y}_2 - \frac{\ell_2}{\ell}\dot{y}_1) + C_\beta(\dot{\theta}_y - \frac{\dot{y}_2-\dot{y}_1}{\ell}) = 0 \quad (4)$$

The constraint equations are

$$-\alpha\frac{\ell_2}{\ell}(z_0 - \frac{\ell_1}{\ell}z_2 - \frac{\ell_2}{\ell}z_1) + \gamma[-\frac{\ell_2}{\ell}(\theta_z - \frac{z_2-z_1}{\ell}) + \frac{1}{\ell}(z_0 - \frac{\ell_1}{\ell}z_2 - \frac{\ell_2}{\ell}z_1)] + \frac{\beta}{\ell}(\theta_z - \frac{z_2-z_1}{\ell}) + k_{z_1}\cdot z_1 + k_{zy_1}\cdot y_1 - C_\alpha\frac{\ell_2}{\ell}(\dot{z}_0 - \frac{\ell_1}{\ell}\dot{z}_2 - \frac{\ell_2}{\ell}\dot{z}_1) + C_\gamma[-\frac{\ell_2}{\ell}(\dot{\theta}_z - \frac{\dot{z}_2-\dot{z}_1}{\ell}) + \frac{1}{\ell}(\dot{z}_0 - \frac{\ell_1}{\ell}\dot{z}_2 - \frac{\ell_2}{\ell}\dot{z}_1)] + \frac{C_\beta}{\ell}(\dot{\theta}_z - \frac{\dot{z}_2-\dot{z}_1}{\ell}) + c_{z_1}\cdot\dot{z}_1 + c_{zy_1}\cdot\dot{y}_1 = 0 \quad (5)$$

$$-\alpha\frac{\ell_1}{\ell}\left(z_o-\frac{\ell_1}{\ell}z_2-\frac{\ell_2}{\ell}z_1\right)+\gamma\left[-\frac{\ell_1}{\ell}\left(\theta_z-\frac{z_2-z_1}{\ell}\right)\right.$$

$$\left.-\frac{1}{\ell}\left(z_o-\frac{\ell_1}{\ell}z_2-\frac{\ell_1}{\ell}z_1\right)\right]-\frac{\beta}{\ell}\left(\theta_z-\frac{z_2-z_1}{\ell}\right)$$

$$+k_{z_2}\cdot z_2+k_{zy_2}\cdot y_2-\frac{C_\alpha\ell_1}{\ell}\left(\dot{z}_o-\frac{\ell_1}{\ell}\dot{z}_2-\frac{\ell_2}{\ell}\dot{z}_1\right)$$

$$+C_\gamma\left[-\frac{\ell_1}{\ell}\left(\dot{\theta}_z-\frac{\dot{z}_2-\dot{z}_1}{\ell}\right)-\frac{1}{\ell}\left(\dot{z}_o-\frac{\ell_1}{\ell}\dot{z}_2-\frac{\ell_2}{\ell}\dot{z}_1\right)\right]$$

$$-\frac{C_\beta}{\ell}\left(\dot{\theta}_z-\frac{\dot{z}_2-\dot{z}_1}{\ell}\right)+c_{z_2}\cdot\dot{z}_2+c_{zy_2}\cdot\dot{y}_2=0 \qquad (6)$$

$$-\alpha\frac{\ell_2}{\ell}\left(y_o-\frac{\ell_1}{\ell}y_2-\frac{\ell_2}{\ell}y_1\right)+\gamma\left[-\frac{\ell_2}{\ell}\left(\theta_y-\frac{y_2-y_1}{\ell}\right)\right.$$

$$\left.+\frac{1}{\ell}\left(y_o-\frac{\ell_1}{\ell}y_2-\frac{\ell_2}{\ell}y_1\right)\right]+\frac{\beta}{\ell}\left(\theta_y-\frac{y_2-y_1}{\ell}\right)$$

$$+k_{y_1}\cdot y_1+k_{yz_1}\cdot z_1-C_\alpha\frac{\ell_2}{\ell}\left(\dot{y}_o-\frac{\ell_1}{\ell}\dot{y}_2-\frac{\ell_2}{\ell}\dot{y}_1\right)$$

$$+C_\gamma\left[-\frac{\ell_2}{\ell}\left(\dot{\theta}_y-\frac{\dot{y}_2-\dot{y}_1}{\ell}\right)+\frac{1}{\ell}\left(\dot{y}_o-\frac{\ell_1}{\ell}\dot{y}_2-\frac{\ell_2}{\ell}\dot{y}_1\right)\right]$$

$$+\frac{C_\beta}{\ell}\left(\dot{\theta}_y-\frac{\dot{y}_2-\dot{y}_1}{\ell}\right)+c_{y_1}\cdot\dot{y}_1+c_{yz_1}\cdot\dot{z}_1=0 \qquad (7)$$

$$-\alpha\frac{\ell_1}{\ell}\left(y_o-\frac{\ell_1}{\ell}y_2-\frac{\ell_2}{\ell}y_1\right)+\gamma\left[-\frac{\ell_1}{\ell}\left(\theta_y-\frac{y_2-y_1}{\ell}\right)\right.$$

$$\left.-\frac{1}{\ell}\left(y_o-\frac{\ell_1}{\ell}y_2-\frac{\ell_2}{\ell}y_1\right)\right]-\frac{\beta}{\ell}\left(\theta_y-\frac{y_2-y_1}{\ell}\right)$$

$$+k_{y_2}\cdot y_2+k_{yz_2}\cdot z_2-C_\alpha\frac{\ell_1}{\ell}\left(\dot{y}_o-\frac{\ell_1}{\ell}\dot{y}_2-\frac{\ell_2}{\ell}\dot{y}_1\right)$$

$$+C_\gamma\left[-\frac{\ell_1}{\ell}\left(\dot{\theta}_y-\frac{\dot{y}_2-\dot{y}_1}{\ell}\right)-\frac{1}{\ell}\left(\dot{y}_o-\frac{\ell_1}{\ell}\dot{y}_2-\frac{\ell_2}{\ell}\dot{y}_1\right)\right]$$

$$-\frac{C_\beta}{\ell}\left(\dot{\theta}_y-\frac{\dot{y}_2-\dot{y}_1}{\ell}\right)+C_{y_2}\cdot\dot{y}_2+C_{yz_2}\cdot\dot{z}_2=0 \qquad (8)$$

Let $\{Z\}$ be the displacement vector with elements z_o, y_o, θ_z, θ_y, z_1, y_1, z_2, y_2. Then, the equation of motion of the rotor system can be written in matrix form as

$$[M]\{\ddot{Z}\}+[C]\{\dot{Z}\}+[K]\{Z\}=\{F\} \qquad (9)$$

where [M], [C] and [K] are mass, damping and stiffness matrices, respectively, and are given in appendix II.

Considering the undamped, homogeneous case of equation (9), the eigenvalues may be obtained from the equation

$$[K]-\omega^2[M]=0 \qquad (10)$$

When one of the eigenvalues is equal to the rotor speed, that eigenvalue is a critical speed of the rotor. However, since damping is quite significant in fluid film bearings, critical speeds obtained by this method will not be exact. Damped critical speeds can be found from the unbalance response plots by locating the speed corresponding to the peak response.

The vector of unbalance force, F is written as

$$\{F\}=\{F_c\}+\{F_s\} \qquad (11)$$

where

$$\{F_c\}=[f_o\cos\omega t,\ 0,\ 0,\ 0,\ 0,\ 0,\ 0,\ 0]^T$$

$$\{F_s\}=[0,\ f_o\sin\omega t,\ 0,\ 0,\ 0,\ 0,\ 0,\ 0]^T$$

and $f_o=ma\omega^2$.

The steady state solution may be written as

$$\{Z\}=\{Z_c\}+\{Z_s\} \qquad (12)$$

where

$$\{Z_c\}=\{Z\}\cos\omega t$$

$$\{Z_s\}=\{Z\}\sin\omega t \qquad (13)$$

Substitution of equation (11) to (13) in equation (9) yields

$$\begin{Bmatrix}Z_c\\ \hline Z_s\end{Bmatrix}=\begin{bmatrix}[K] & -\omega^2[M] & [C]\\ -[C] & [K] & -\omega^2[M]\end{bmatrix}^{-1}\begin{Bmatrix}F_c\\ F_s\end{Bmatrix} \qquad (14)$$

The solution of equations (12), (13) and (14) can be expressed as

$$z_o=z_{oc}\cos\omega t+z_{os}\sin\omega t$$

$$y_o=y_{oc}\cos\omega t+y_{os}\sin\omega t \qquad (15)$$

at the disk location.

At the bearing location, the solution is found as

$$z_1=z_{1c}\cos\omega t+z_{1s}\sin\omega t$$

$$y_1=y_{1c}\cos\omega t+y_{1s}\sin\omega t$$

$$z_2=z_{2c}\cos\omega t+z_{2s}\sin\omega t$$

$$y_2=y_{2c}\cos\omega t+y_{2s}\sin\omega t \qquad (16)$$

The out of balance response is the vector sum of responses in z and y directions and is expressed non-dimensionally as

$$r=(z+iy)/a \qquad (17)$$

From (15) the forward and backward whirl amplitude of the disk is given by

$$z_o = z_{oc} \frac{e^{i\omega t} + e^{-i\omega t}}{2} + z_{os} \frac{e^{i\omega t} - e^{-i\omega t}}{2i}$$

$$y_o = y_c \frac{e^{i\omega t} + e^{-i\omega t}}{2} + y_{os} \frac{e^{i\omega t} - e^{-i\omega t}}{2i}$$

$$r = z_o + iy_o$$

$$r = r^+ e^{i\omega t} + r^- e^{-i\omega t}$$

where r^+ and r^- are respectively the forward and backward whirl amplitudes at the disk location, and these quantities together with the respective phase angles are useful in determining the whirl direction. Proceeding on similar lines, the whirl direction at the bearing locations can be determined.

NUMERICAL RESULTS

The above analysis is used to obtain the damped critical speeds and the normalized unbalance response of a single mass rotor, the details of which are given in Table I. The dissimilarity in bearings is achieved with different combinations of bearing clearances at the two ends. In hydrodynamic bearings, the variations in bearing clearances alter the Sommerfeld number which in turn, influences the bearing stiffness and damping coefficients.

The effect of dissimilarity in bearings on the damped critical speeds and unbalance response of the rotor are investigated for different rotor configurations, which are given in Table II. Results are given in figures 2 and 3 for the unbalance response. Orbital diagrams for two specific cases are shown in figures 5 to 7. The individual cases, shown in Table II, are discussed below. Proceeding on similar lines, the whirl direction at the bearing locations can be determined.

Case No. 1

The variation of unbalance response for this case, when the disk is at the center of the shaft and β and γ being zero, is shown in Fig. 2. The clearance at the left end, c_1, is kept constant at 0.0000533m and the clearance at the right end, c_2, is varied. Five different values are considered for c_2 as shown in Table II. Except for the c_2 value of 0.000188m which exhibits a double peak, all other clearances show only a single peak. Moreover, the peak amplitude of the response drops down considerably while the peaks themselves shift towards lower speeds, as the c_2 values are increased.

Case No. 2

Unbalance response for the case of central disk and c_1 value kept at 0.000188m, is shown for different values of c_1 in Fig. 3. It shows double peaks for all c_1 values and the peak amplitude of the response again drops down considerably for increasing values of c_1. The response peaks shift towards left thereby lowering the damped critical speed. A very interesting observation here is that the amplitudes for the different c_1 values are almost the same for the speed range between 2100 rpm and 2200 rpm. This is so because, for the corresponding range of Sommerfeld numbers, the direct damping coefficients along the y direction increase and the direct stiffness coefficients along the z direction decrease, and hence the net effect is to keep the amplitude at approximately constant level.

The variation of critical speeds with the bearing clearance parameter is shown in Fig. 4 when the disk is at the shaft center. It is seen that there is a range of clearance values where the rotor has two distinct critical speeds and out of this range, both the critical speeds are coalesced into one.

The orbital diagrams are shown in Figs. 5 to 7 for the case of central disk with the c_1 and c_2 values being 0.000188m. Figure 5 shows the orbital diagram for the rotor speed of 1800 rpm which lies below the first critical speed. It is seen that the forward component is predominant, and hence the net effect is to make the rotor whirl in the forward direction. The orbital diagram for the rotor speed of 2400 rpm, which lies between the two critical speeds is shown in Fig. 6. It shows that the forward amplitude decreases whereas the backward amplitude increases. However, the net effect is to keep the rotor whirl in the forward direction. The damped critical speeds for this case were 2000 rpm and 2700 rpm as can be seen from Fig. 3. Since damping is also included, the change from forward whirl to backward whirl does not take place at the first critical speed itself unlike the case of an undamped rotor. The rotor motion tends towards a backward whirl in between the two criticals, however, since the second critical speed approaches, before that could happen, the rotor continues to move in the forward direction only. The orbital diagram for the rotor shaft at the bearing location is also shown in Figs. 5 and 6. For this case of the rotor, only synchronous whirl is present and hence, the shaft at the bearing location whirls in the same manner as that of the disk, however, with different amplitude.

Orbital diagrams for the case of central disk and unequal bearing clearances at the two ends, are shown in Fig. 7. In this case, the rotor exhibits only synchronous whirl, however, the motion at the two bearing locations have different amplitudes and they are not in phase with each other and with the disk motion. This is due to the different stiffness and damping values at the two bearings.

Case No 3

In this case, the dissimilarity in bearings

is caused by a noncentral disk, with all the geometrical parameters of the bearings being identical. The noncentral disk exerts different loads on the two bearings and hence the Sommerfeld numbers for the two bearings will be different. The unbalance response of the rotor is shown in Fig. 8, when the two bearing clearances are kept at 0.0000533m and the disk position along the shaft is varied. As the disk is moved away from the center, the response decreases. There is a small peak in each of the response curves, however, the response goes on increasing with speed beyond this peak. The curve tends to flatten at very high speeds.

The orbital diagrams at the disk location and at the bearings are shown in Fig. 9 when $\ell_1 = 0.3105$m and $\ell_2 = 0.2$m at 4000 rpm. In this case, the response at the bearings is more than the bearing clearance, suggesting that the rotor cannot be operated at this speed. It was found that the response at the bearings were less than the clearance for a rotor speed above 7500 rpm. It was also found that when the clearances or the disk weight were increased, thus increasing the Sommerfeld number, the likelihood of the response at the bearings exceeding the clearance increased.

Even in the case of rotors with central disk, there are speeds at which the response at the bearing location is more than the bearing clearance. The present investigation considers linear stiffness and damping coefficients for the fluid film in the bearings. When the response at the bearing locations are of the order of the bearing clearance, a linear anaylsis is not enough to study the rotor behaviour. However, on the basis of a linear analysis, it seems that the rotor cannot operate satisfactorily under such conditions.

CONCLUSIONS

The critical speeds and the unbalance response of a single mass rotor supported on dissimilar hydrodynamic bearings at the two ends are studied. Five different bearing clearances are used at one end of the bearing, keeping the clearance constant at the other end. The influence of disk location on the rotor behaviour is also studied. Based on the results presented, it can be observed that a rotor with dissimilar bearings at the two ends, exhibits synchronous whirl only. However, the rotor response at the two bearing locations will have different magnitudes and phase. The dissimilarity in the two bearings, introduced in this study by having different clearances, influences the unbalance response significantly, and the peak response speeds to some extent. Also, the rotor may change its behaviour from having a single peak in its response to that of a double peak or vice versa. A study of the response at the bearing locations is very important, since, if this exceeds the bearing clearance, the rotor cannot operate satisfactorily.

ACKNOWLEDGEMENTS

This investigation was supported in part by Grant A1375 and A7104 from the Natural Sciences and Engineering Research Council of Canada.

REFERENCES

1. J.W. Lund, "Rotor Bearings Dynamics Design Technology, Part V: Computer Program Manual for Rotor Response and Stability", Mechanical Technology Inc., Latham, N.Y., U.S.A., AFAPL-Tr-65-45, 1965.

2. H.D. Nelson and J.N. McVaugh, "The Dynamics of Rotor Bearing Systems Using Finite Elements", Journal of Engineering for Industry, A.S.M.E., Vol. 98, p. 593, 1976.

3. J.S. Rao, "Conditions for Backward Synchronous Whirl of a Flexible Rotor in Hydrodynamic Bearings", Mechanism and Machine Theory Journal, Vol. 17, No. 2, pp. 143-152, 1982.

4. J.S. Rao, R.B. Bhat and T.S. Sankar, "Effect of Damping on the Synchronous Whirl of a Rotor in Hydrodynamic Bearings", Transactions of CSME, Vol. 6, No. 3, 1981.

5. T. Yamamoto, H. Ota and K. Kono, "On the Unstable Vibrations of a Shaft with Unsymmetrical Rotor", Applied Mechanics, p. 313, June 1968.

6. D. Ardayfio and D.A. Frohrib, "Vibration of an Asymmetrically Mounted Rotor with Gyroscopic Effects", Transactions of the ASME, Journal of Engineering for Industry, p. 327, Feb. 1976.

TABLE I

Details of the Rotor

ROTOR WEIGHT	103.8 N
DISK WEIGHT	88.96 N
TYPE OF BEARINGS	PLAIN CYLINDRICAL
BEARING DIAMETER	0.0254 m
BEARING L/D RATIO	1
VISCOSITY OF OIL	0.0241 N.sec/m^2
TOTAL LENGTH OF ROTOR	0.5105 m
MODULUS OF ELASTICITY OF SHAFT	1.96623×10^{11} N/m^2
SHAFT DIAMETER	0.022 m

TABLE II

Rotor Configurations

CASE NO.	OISK WT in N	ℓ_1 in m	ℓ_2 in m	β N.m/rad	γ N/rad	c_1 in m	c_2 in m
1	89	0.25525	0.25525	0	0	0.0000533	i) 0.0000533 ii) 0.0000833 iii) 0.0001133 iv) 0.0001433 v) 0.000188
2	89	0.25525	0.25525	0	0	i) 0.0000533 ii) 0.0000833 iii) 0.0001133 iv) 0.0001433 v) 0.000188	0.000188
3	21.88	0.3105 0.3605 0.4105	0.2 0.15 0.10	4.66×10^4	-5.06×10^5	0.0000533	0.0000533

APPENDIX I

The kinetic energy of the rotor shown in Fig. 1 is

$$T = \frac{1}{2} m(\dot{z}_0^2 + \dot{y}_0^2) + \frac{1}{2} I_u(\dot{\theta}_z^2 + \dot{\theta}_y^2) + \frac{1}{2} I_x[\omega^2 + \omega(\dot{\theta}_z\theta_y - \dot{\theta}_y\theta_z)] \quad \text{(AI-1)}$$

The potential energy is

$$\begin{aligned} V = {} & \frac{\alpha}{2}\left(z_0 - \frac{\ell_1}{\ell} z_2 - \frac{\ell_2}{\ell} z_1\right)^2 + \left(y_0 - \frac{\ell_1}{\ell} y_2 - \frac{\ell_2}{\ell} y_1\right)^2 \\ & + \gamma\left[\left(z_0 - \frac{\ell_1}{\ell} z_2 - \frac{\ell_2}{\ell} z_1\right)\left(\theta_z - \frac{z_2 - z_1}{\ell}\right)\right. \\ & \left. + \left(y_0 - \frac{\ell_1}{\ell} y_2 - \frac{\ell_2}{\ell} y_1\right)\left(\theta_y - \frac{y_2 - y_1}{\ell}\right)\right] \\ & + \frac{\beta}{2}\left[\left(\theta_z - \frac{z_2 - z_1}{\ell}\right)^2 + \left(\theta_y - \frac{y_2 - y_1}{\ell}\right)^2\right] \\ & + \frac{1}{2}\left[k_{z_1} \cdot z_1^2 + k_{z_2} \cdot z_2^2 + k_{y_1} \cdot y_1^2 + k_{y_2} \cdot y_2^2\right] \\ & + (k_{zy_1} \cdot y_1) z_1 + (k_{zy_2} \cdot y_2) z_2 + (k_{yz_1} \cdot z_1) y_1 \\ & + (k_{yz_2} \cdot z_2) y_2 \end{aligned} \quad \text{(AI.2)}$$

$$\begin{aligned} D = {} & \frac{C_\alpha}{2}\left(\dot{z}_0 - \frac{\ell_1}{\ell} z_2 - \frac{\ell_2}{\ell} \dot{z}_1\right)^2 + \left(\dot{y}_0 - \frac{\ell_1}{\ell} y_2 - \frac{\ell_2}{\ell} \dot{y}_1\right)^2 \\ & + C_\gamma\left[\left(\dot{z}_0 - \frac{\ell_1}{\ell} \dot{z}_2 - \frac{\ell_2}{\ell} \dot{z}_1\right)\left(\dot{\theta}_z - \frac{\dot{z}_2 - \dot{z}_1}{\ell}\right)\right. \\ & \left. + \left(\dot{y}_0 - \frac{\ell_1}{\ell} \dot{y}_2 - \frac{\ell_2}{\ell} \dot{y}_1\right)\left(\dot{\theta}_y - \frac{\dot{y}_2 - \dot{y}_1}{\ell}\right)\right] \\ & + \frac{C_\beta}{\ell}\left[\left(\dot{\theta}_z - \frac{\dot{z}_2 - \dot{z}_1}{\ell}\right)^2 + \left(\dot{\theta}_y - \frac{\dot{y}_2 - \dot{y}_1}{\ell}\right)\right] \\ & + \frac{1}{2}\left[c_{z_1} \cdot \dot{z}_1^2 + c_{z_2} \cdot \dot{z}_2^2 + c_{y_1} \cdot \dot{y}_1^2 + c_{y_2} \cdot \dot{y}_2^2\right] \\ & + (c_{zy_1} \cdot \dot{y}_1)\dot{z}_1 + (c_{zy_2} \cdot \dot{y}_2)\dot{z}_2 + (c_{yz_1} \cdot \dot{z}_1)\dot{y}_1 \\ & + (c_{yz_2} \cdot \dot{z}_2)\dot{y}_2 \end{aligned} \quad \text{(AI.3)}$$

The Lagrangian equation for z_1 component can be written as

$$\frac{\partial L}{\partial z_1} - \frac{\partial D}{\partial \dot{z}_1} = 0$$

$$\frac{\partial T}{\partial z_1} - \frac{\partial V}{\partial z_1} - \frac{\partial D}{\partial \dot{z}_1} = 0$$

Since

$$\frac{\partial T}{\partial z_1} = 0, \quad \frac{\partial V}{\partial z_1} + \frac{\partial D}{\partial \dot{z}_1} = 0$$

Similar expressions are applicable for z_2, y_1 and y_2 components. Therefore, constraint equations in z-direction are

$$\begin{aligned} \frac{\partial V}{\partial z_1} = {} & -\alpha \frac{\ell_2}{\ell}\left(z_0 - \frac{\ell_1}{\ell} z_2 - \frac{\ell_2}{\ell} z_1\right) + \gamma\left[-\frac{\ell_2}{\ell}\left(\theta_z - \frac{z_2 - z_1}{\ell}\right)\right. \\ & \left. + \frac{1}{\ell}\left(z_0 - \frac{\ell_1}{\ell} z_2 - \frac{\ell_2}{\ell} z_1\right)\right] \\ & + \frac{\beta}{\ell}\left(\theta_z - \frac{z_2 - z_1}{\ell}\right) + k_{z_1} \cdot z_1 + k_{zy_1} \cdot y_1 = 0 \end{aligned}$$

$$\frac{\partial D}{\partial \dot{z}_1} = -C_\alpha \frac{\ell_2}{\ell}\left(\dot{z}_0 - \frac{\ell_1}{\ell}\dot{z}_2 - \frac{\ell_2}{\ell}\dot{z}_1\right) + C_\gamma\left[-\frac{\ell_2}{\ell}\left(\dot{\theta}_z - \frac{\dot{z}_2-\dot{z}_1}{\ell}\right) + \frac{1}{\ell}\left(\dot{z}_0 - \frac{\ell_1}{\ell}\dot{z}_2 - \frac{\ell_2}{\ell}\dot{z}_1\right)\right] + \frac{C_\beta}{\ell}\left(\dot{\theta}_z - \frac{\dot{z}_2-\dot{z}_1}{\ell} + C_{z_1}\cdot\dot{z}_1 + C_{zy_1}\cdot\dot{y}_1\right) = 0$$

$$\frac{\partial v}{\partial z_1} = -\frac{\alpha\ell_1}{\ell}\left(z_0 - \frac{\ell_1}{\ell}z_2 - \frac{\ell_2}{\ell}z_1\right) + \gamma\left[-\frac{\ell_1}{\ell}\left(\theta_z - \frac{z_2-z_1}{\ell}\right) - \frac{1}{\ell}\left(z_0 - \frac{\ell_1}{\ell}z_2 - \frac{\ell_2}{\ell}z_1\right)\right] - \frac{\beta}{\ell}\left(\theta_z - \frac{z_2-z_1}{\ell}\right) + k_{z_2}\cdot z_2 + k_{zy_2}\cdot y_2 = 0$$

$$\frac{\partial D}{\partial \dot{z}_2} = -\frac{C_\alpha \ell_1}{\ell}\left(\dot{z}_0 - \frac{\ell_1}{\ell}\dot{z}_2 - \frac{\ell_2}{\ell}z_1\right) + C_\gamma\left[-\frac{\ell_1}{\ell}\left(\dot{\theta}_z - \frac{\dot{z}_2-\dot{z}_1}{\ell}\right) - \frac{1}{\ell}\left(\dot{z}_0 - \frac{\ell_1}{\ell}\dot{z}_2 - \frac{\ell_2}{\ell}\dot{z}_1\right)\right] - \frac{C_\beta}{\ell}\left(\dot{\theta}_z - \frac{\dot{z}_2-\dot{z}_1}{\ell}\right) + k_{z_2}\cdot\dot{z}_2 + k_{zy_2}\cdot\dot{y}_2 = 0$$

APPENDIX II

$$\alpha = \frac{3EI\ell}{\ell_1^2\ell_2^2}$$

$$\beta = \frac{\text{moment}}{\text{angular displacement}} = \frac{3EI\ell}{(\ell_1^2 + \ell_2^2 - \ell_1\ell_2)}$$

$$\gamma = \frac{\text{moment}}{\text{deflection}} = \frac{3EI\ell}{\ell_1\ell_2(\ell_1-\ell_2)}$$

where $I = \frac{\pi}{64}$ x diameter of the shaft.

Mass Matrix [M]

$$\begin{bmatrix} m & 0 & 0 & 0 \\ 0 & m & 0 & 0 \\ 0 & 0 & I_d & 0 \\ 0 & 0 & 0 & I_d \end{bmatrix}$$

Stiffness Matrix [K]

$$\begin{bmatrix}
\alpha & 0 & \gamma & 0 & \left(-\frac{\alpha\ell_2}{\ell}+\frac{\gamma}{\ell}\right) & 0 & -\left(\frac{\alpha\ell_1}{\ell}+\frac{\gamma}{\ell}\right) & 0 \\
0 & \alpha & 0 & \gamma & 0 & \left(-\frac{\alpha\ell_2+\gamma}{\ell}\right) & 0 & -\left(\frac{\alpha\ell_1+\gamma}{\ell}\right) \\
\gamma & 0 & \beta & 0 & \left(-\frac{\gamma\ell_2+\beta}{\ell}\right) & 0 & -\left(\frac{\gamma\ell_1+\beta}{\ell}\right) & 0 \\
0 & \gamma & 0 & \beta & 0 & \left(-\frac{\gamma\ell_2+\beta}{\ell}\right) & 0 & -\left(-\frac{\gamma\ell_1+\beta}{\ell}\right) \\
\left(-\frac{\alpha\ell_2+\gamma}{\ell}\right) & 0 & \left(-\frac{\gamma\ell_2+\beta}{\ell}\right) & 0 & (a_1 + k_{z_1}) & k_{zy_1} & a_2 & 0 \\
0 & \left(-\frac{\alpha\ell_2+\gamma}{\ell}\right) & 0 & \left(-\frac{\gamma\ell_2+\beta}{\ell}\right) & k_{yz_1} & (a_1 + k_{y_1}) & 0 & a_2 \\
-\left(\frac{\alpha\ell_1+\gamma}{\ell}\right) & 0 & -\left(\frac{\gamma\ell_1+\beta}{\ell}\right) & 0 & a_2 & 0 & (a_3 + k_{z_2}) & k_{zy_2} \\
0 & -\left(\frac{\alpha\ell_1+\gamma}{\ell}\right) & 0 & -\left(\frac{\gamma\ell_1+\beta}{\ell}\right) & 0 & a_2 & k_{yz_2} & (a_3 + k_{y_2})
\end{bmatrix}$$

where $a_1 = \frac{\alpha\ell_2^2 - 2\gamma\ell_2 + \beta}{\ell^2}$ $\quad a_2 = \frac{\alpha\ell_1\ell_2 - \gamma(\ell_1 - \ell_2) - \beta}{\ell^2}$ and $a_3 = \frac{\alpha\ell_1^2 + 2\gamma\ell_1 + \beta}{\ell^2}$

Damping Matrix [C]

$$
\begin{bmatrix}
C_\alpha & 0 & C_\gamma & 0 & \left(-\frac{C_\alpha \ell_2 + C_\gamma}{\ell}\right) & 0 & -\left(\frac{C_\alpha \ell_1 + C_\gamma}{\ell}\right) & 0 \\
0 & C_\alpha & 0 & C_\gamma & 0 & \left(-\frac{C_\alpha \ell_2 + C_\gamma}{\ell}\right) & 0 & -\left(\frac{C_\alpha \ell_1 + C_\gamma}{\ell}\right) \\
C_\gamma & 0 & C_\beta & (I_x\omega) & \left(-\frac{C_\gamma \ell_2 + C_\beta}{\ell}\right) & 0 & -\left(\frac{C_\gamma \ell_1 + C_\beta}{\ell}\right) & 0 \\
0 & C_\gamma & (-I_x\omega) & C_\beta & 0 & \left(-\frac{C_\gamma \ell_2 + C_\beta}{\ell}\right) & 0 & -\left(\frac{C_\gamma \ell_1 + C_\beta}{\ell}\right) \\
\left(-\frac{C_\gamma \ell_2 + C_\gamma}{\ell}\right) & 0 & \left(-\frac{C_\gamma \ell_2 + C_\beta}{\ell}\right) & 0 & (b_1 + c_{z_1}) & c_{zy_1} & b_2 & 0 \\
0 & \left(-\frac{C_\alpha \ell_2 + C_\gamma}{\ell}\right) & 0 & \left(-\frac{C_\gamma \ell_2 + C_\beta}{\ell}\right) & c_{yz_1} & (b_1 + c_{y_1}) & 0 & b_2 \\
-\left(\frac{C_\alpha \ell_1 + C_\gamma}{\ell}\right) & 0 & -\left(\frac{C_\gamma \ell_1 + C_\beta}{\ell}\right) & 0 & b_2 & 0 & (b_3 + c_{z_2}) & c_{zy_2} \\
0 & -\left(\frac{C_\alpha \ell_1 + C_\gamma}{\ell}\right) & 0 & -\left(\frac{C_\gamma \ell_1 + C_\beta}{\ell}\right) & 0 & b_2 & c_{yz_2} & (b_3 + c_{y_2})
\end{bmatrix}
$$

where $b_1 = \dfrac{C_\alpha \ell_2^2 - 2C_\gamma \ell + C_\beta}{\ell^2}$ $\quad b_2 = \dfrac{C_\alpha \ell_1 \ell_2 - C_\gamma(\ell_1 - \ell_2) - C_\beta}{\ell^2}$ and $b_3 = \dfrac{C_\alpha \ell_1^2 + 2C_\gamma \ell_1 + C_\beta}{\ell^2}$

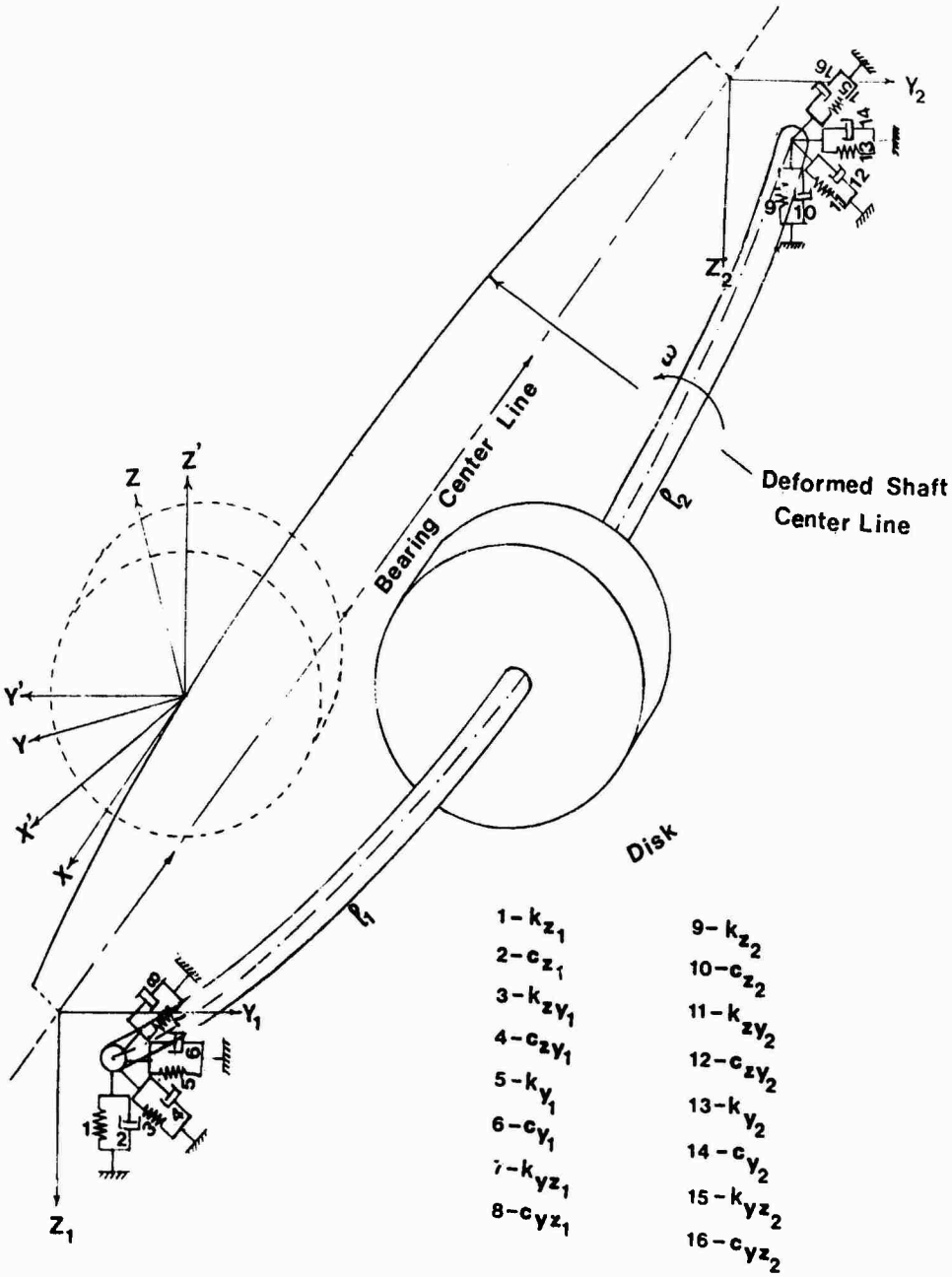

Fig. 1 - A single mass rotor on fluid-film bearings.

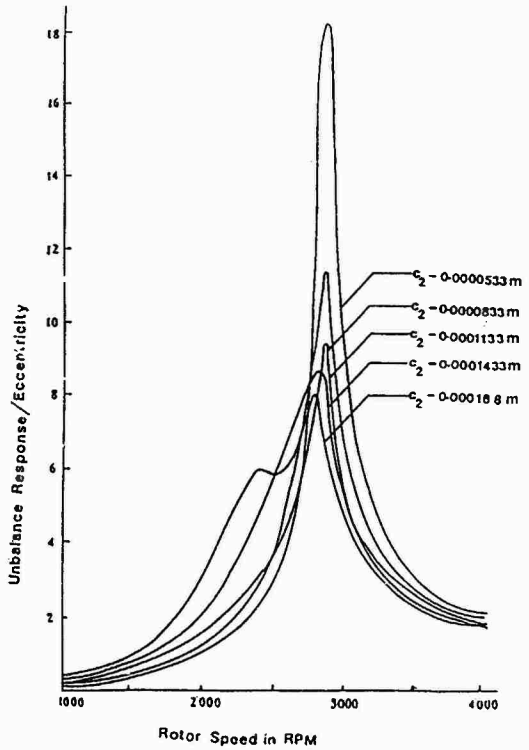

Fig. 2 - Unbalance response of rotor (central disk, β=0, γ=0, c_1=0.0000533 m)

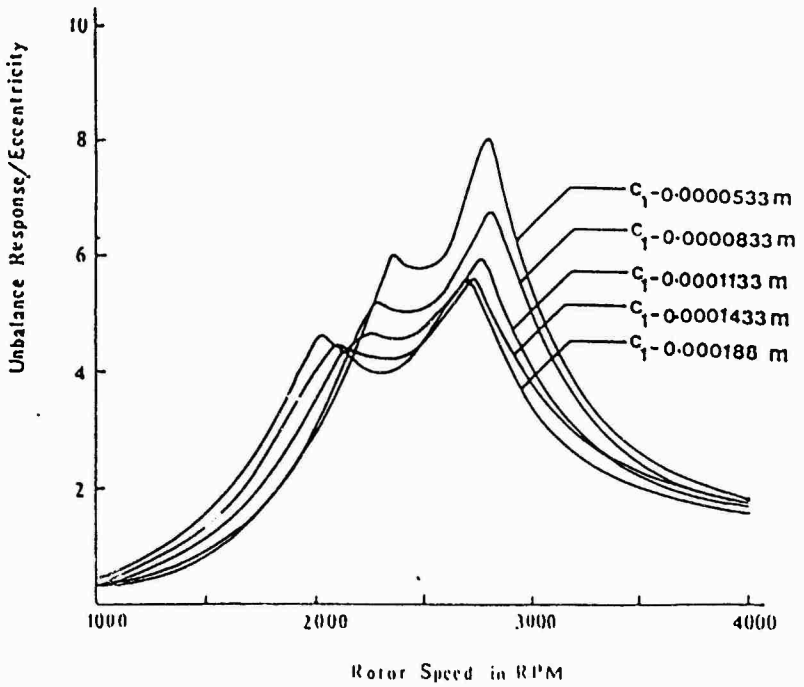

Fig. 3 - Unbalance response of rotor (central disk, β=0, γ=0, c_2=0.000188 m)

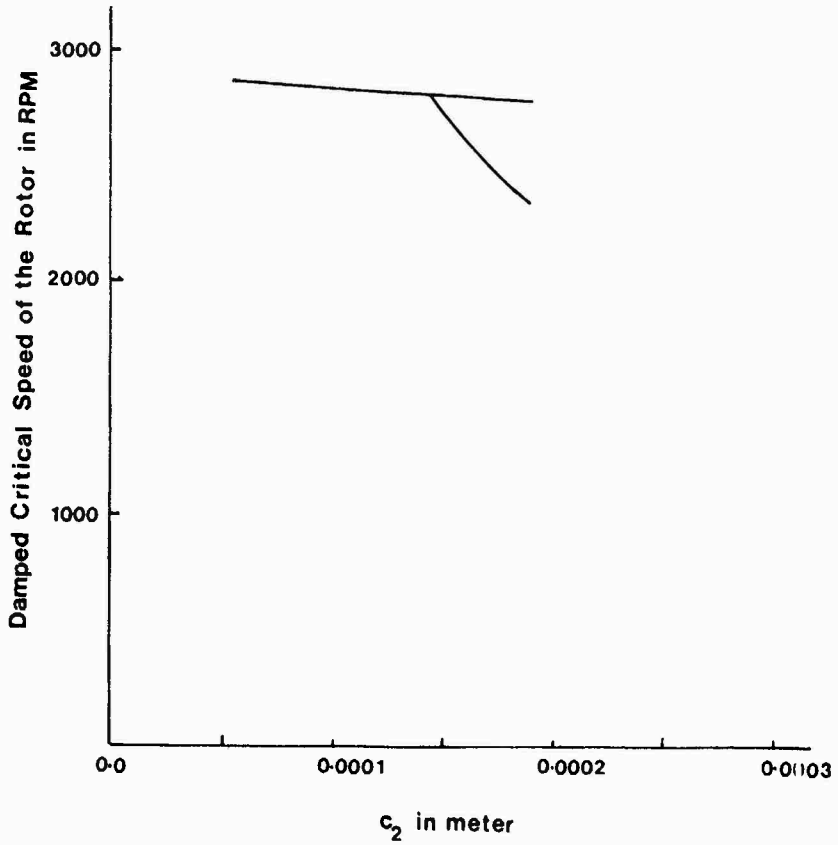

Fig. 4 - Variation of critical speeds of the rotor (central disk, β=0, γ=0, c_1=0.0000533 m)

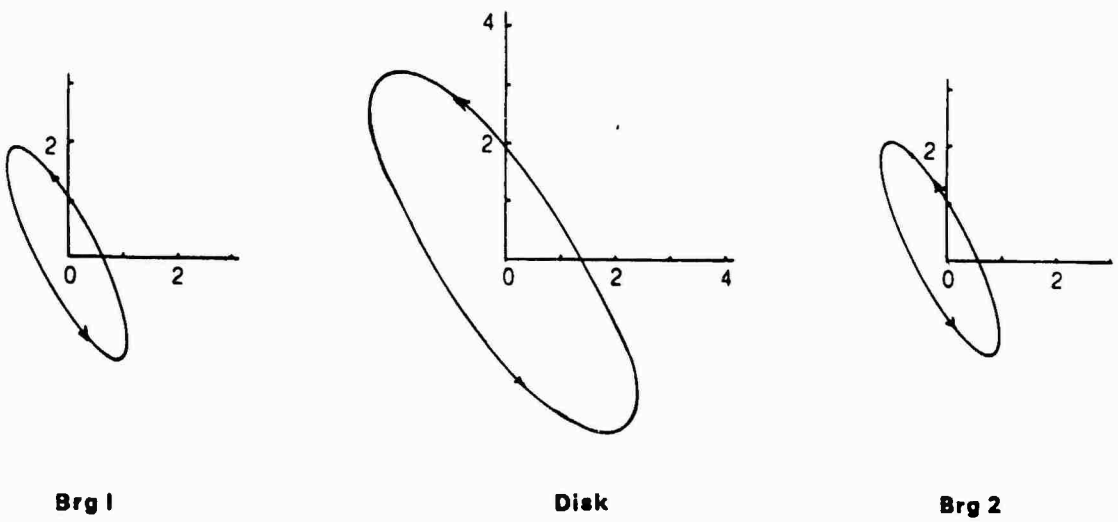

Fig. 5 - Orbital diagram (central disk, β=0, γ=0, $c_1 = c_2$=0.000188 m and rotor speed = 1800 rpm)

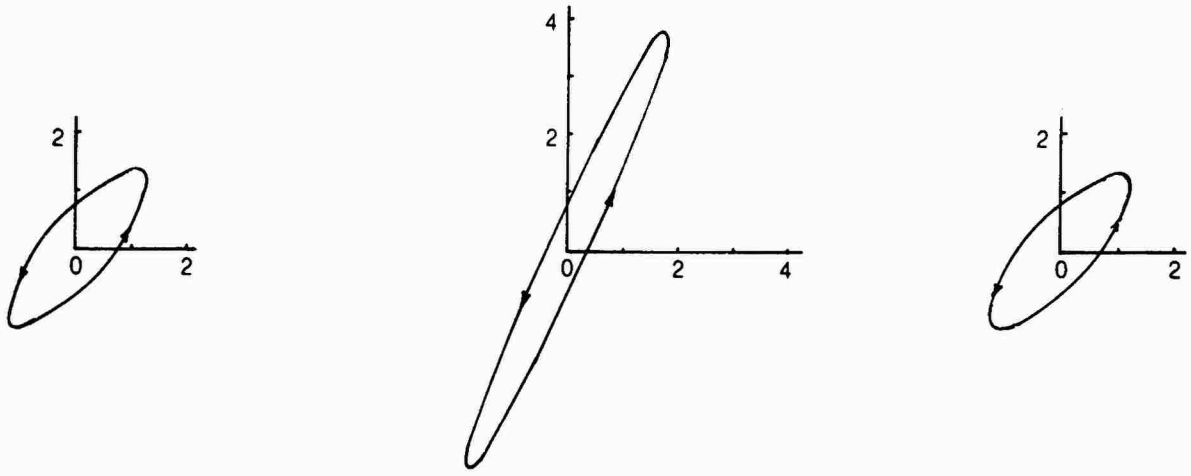

Fig. 6 - Orbital digram (central disk, β=0, γ=0, $c_1 = c_2$=0.000188 m and rotor speed = 2400 rpm)

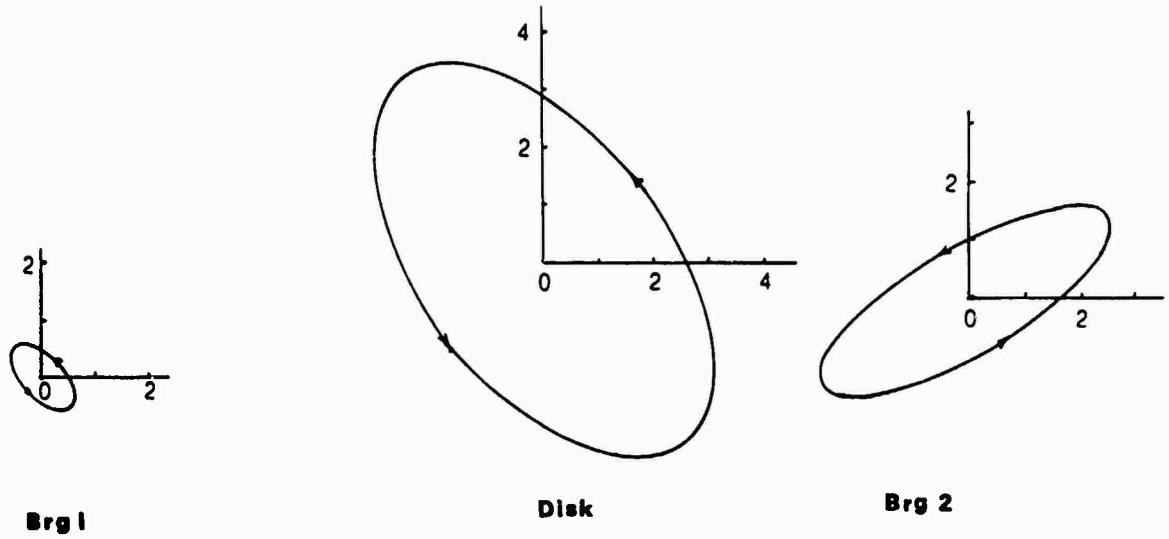

Fig. 7 - Orbital diagram (central disk, β=0, γ=0, c_1 = 0.0000833 m, c_2 = 0.000188 m and rotor speed = 1500 rpm)

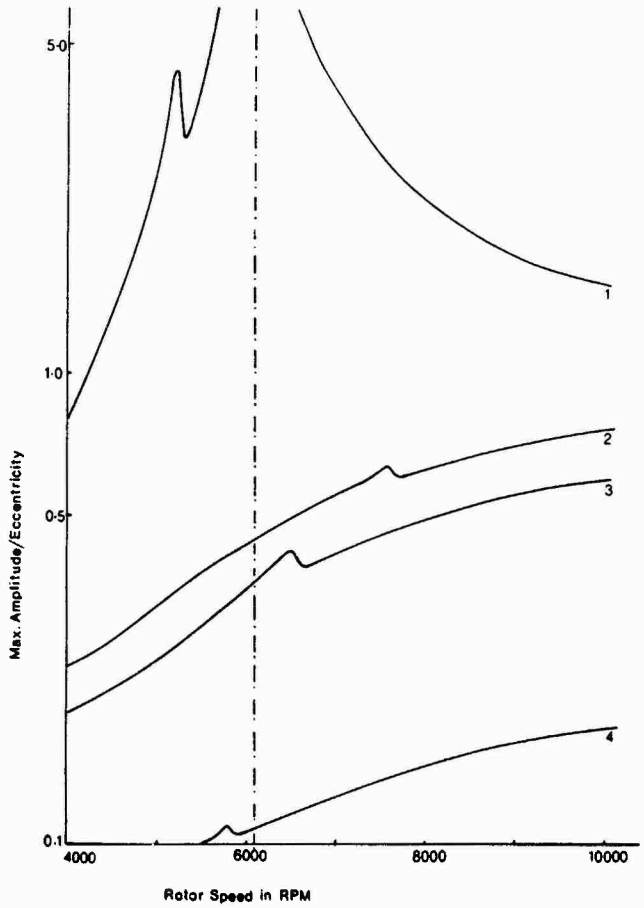

Fig. 8 - Unbalance response of rotor 1-($\ell_1 = 0.25525\,m$, $\ell_2 = 0.25525\,m$, $c_1 = c_2 = 0.0000533\,m$ 2 - $\ell_1 = 0.3105\,m$, $\ell_2 = 0.2\,m$, $c_1 = c_2 = 0.0000533\,m$; 3 - $\ell_1 = 0.3505\,m$, $\ell_2 = 0.16\,m$, $c_1 = c_2 = 0.0000533\,m$, 4 - $\ell_1 = 0.4105\,m$, $\ell_2 = 0.1\,m$, $c_1 = c_2 = 0.0000533\,m$)

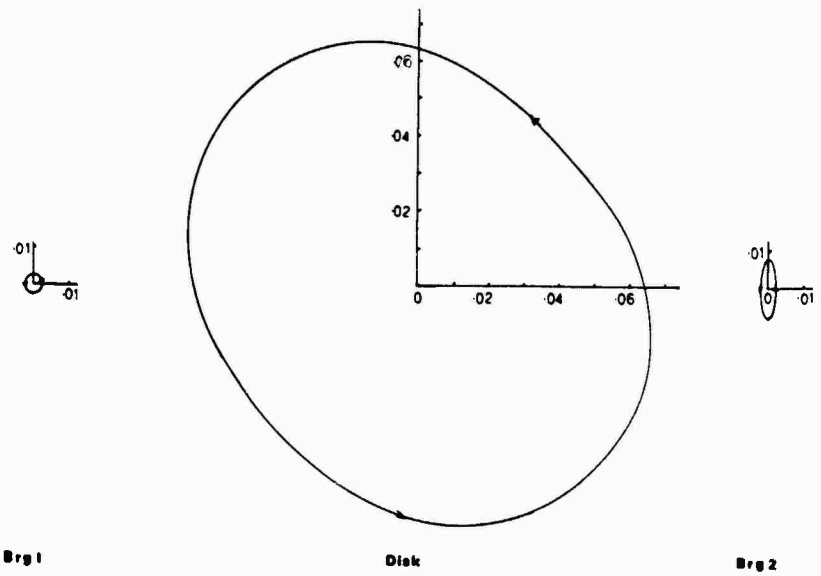

Fig. 9 - Obital diagrams ($\ell_1 = .3105\,m$, $\ell_2 = 0.2000\,m$, $c_1 = c_2 = 0.0000533\,m$ and rotor speed = 4000 rpm)

NONLINEAR COUPLING RESPONSES TO VARIABLE FREQUENCY EXCITATIONS

F. H. Wolff and A. J. Molnar
Engineering-Analytical Dynamics Corp.
Trafford, Pennsylvania 15085

Effects of a nonlinear coupling with a hardening torque-deflection characteristic on shaft torsional vibrations from a variable frequency excitation are calculated. Amplitudes for an accelerating excitation frequency are greater than amplitudes predicted by linear theory; whereas, amplitudes for a decelerating excitation frequency are less than amplitudes predicted by linear theory. With a nonlinear coupling both harmonic and subharmonic vibrations can occur when more than one vibration mode is involved.

INTRODUCTION

Rotating machinery designers must be concerned with resonant conditions in their equipment. System detuning will avoid many serious problems; i.e., changing natural frequencies by modifying physical inertia or stiffness properties. Also, sufficient damping will generally limit vibrations from resonance to acceptable levels. The nature of some excitations makes it virtually impossible to avoid quasi-resonant conditions; e.g., salient pole synchronous motors during start up contain a twice slip frequency pulsating component of air gap torque which for most systems is certain to pass through at least one torsional natural frequency. For a 60 Hz electrical supply, the twice slip frequency component will vary from 120 Hz to dc.

Nonlinear couplings where stiffness varies as the load changes are frequently considered for detuning. The "natural" frequency will vary as the level of vibration changes; accordingly, a system near resonance may be detuned. On the other hand with an excitation frequency slightly greater than the "natural" frequency, the "natural" frequency could be increased bringing it closer yet to the excitation frequency. For a constant frequency excitation the nonlinear effect will be favorable most of the time; however, what about the influence of nonlinear couplings when the excitation frequency is changing.

This study quantitatively defines the effects of nonlinear couplings on vibrations because of accelerating or decelerating input frequencies. For simplicity a two inertia torsional model was considered initially because only one vibration mode would be involved. Finally, to determine the influence of more than one vibration mode a three inertia model was analyzed. The transient results (shaft torques) are given in per unit where 1 per unit equals 578,000 in-lbs (rated motor torque).

A fourth-order Runge-Kutta numerical integration routine with controlled error was used to make the transient calculations. The error limit for the discrete integration steps was set at .001.

NONLINEAR COUPLING CHARACTERISTICS

Figure 1 shows a typical torque-deflection curve of a nonlinear coupling whose characteristics (Table 1) are in the range of those commercially available. When the coupling stiffness property is compared to the torque-deflection curve of a linear shaft section, the nonlinearity is seen to be gradual (Fig. 1).

TABLE 1
Nonlinear Coupling Torque-Deflection Characteristics

Angle of Twist (deg)	(10^{-3} rad)	Torque (10^6 in-lbs)	Stiffness, k (10^6 in-lb/rad)
0	0	0	37.6
0.14	2.44	0.092	37.6
0.58	10.04	0.378	40.6
0.90	15.71	0.608	43.2
1.10	19.20	0.758	55.3
1.25	21.80	0.902	65.0
2.00	35.00	1.760	65.0

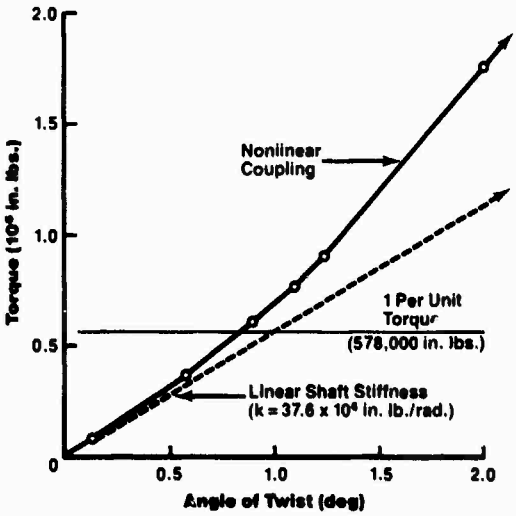

Fig. 1—Nonlinear coupling and linear shaft torque-deflection characteristics

ACCELERATING AND DECELERATING EXCITATIONS

Accelerating or decelerating excitation frequencies appear in many physical systems:

(1) unbalance centrifugal forces of rotating equipment as the equipment speed is being increased (accelerating) or decreased (decelerating).

(2) harmonic (6th, 12th, etc.) air gap torques of adjustable speed synchronous or induction motors as the motor speed is varied (accelerating or decelerating).

The air gap torque of a salient pole synchronous motor exhibits a variable frequency torsional excitation during a line start. In addition to the steady driving torque and a short lived line frequency pulsating torque, a twice slip frequency oscillating component is present. The twice slip frequency torque pulsation which varies from 120 Hz to dc for a 60 Hz supply is an example of a decelerating excitation frequency (Fig. 2A). If the motor is designed to start in 8 seconds, the average decelerating rate can be taken to be

$$h = -\frac{120 \text{ Hz}}{8 \text{ sec}} = -15 \text{ Hz/sec} \qquad (1)$$

Even though the amplitude of 1 per unit (Fig. 2A) is larger than expected in most synchronous motors, it was selected so that the shaft responses in per unit would be (1/2) amplification factors (2 equal inertia). Figure 2B shows an accelerating excitation frequency torque with the same average rate (15 Hz/sec).

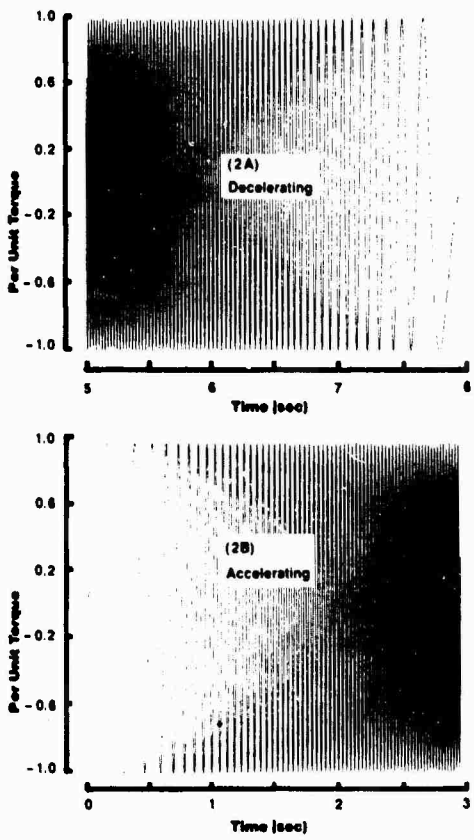

Fig. 2—Decelerating and accelerating of frequency excitation torques

TWO INERTIA MODEL RESULTS

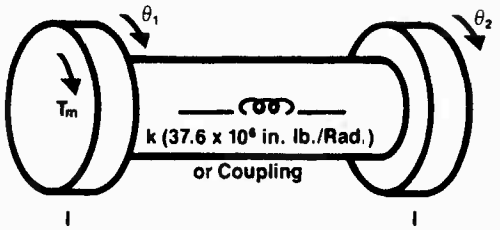

$T_m = (1.0)(578000)\,\mathrm{Sin}\,\Theta(t)$

$$\Theta(t) = \begin{cases} (2\pi f)\, t^2 / T_S; \text{ accelerating} \\ 2(2\pi f)\left[1 - \frac{t}{2T_S}\right] t; \text{ decelerating} \end{cases}$$

$f = 60$ hz, $T_S = 8$ sec.-time to start

$$\frac{d^2\theta}{dt^2}(t) = \begin{cases} 2\pi \frac{2f}{T_S}; \text{ accelerating} = \frac{2f}{T_S} \text{ hz/sec.} \\ -2\pi \frac{2f}{T_S}; \text{ decelerating} = -\frac{2f}{T_S} \text{ hz/sec.} \end{cases}$$

$$I = \begin{cases} 4760; \text{ 20 hz natural frequency} \\ 528.9; \text{ 60 hz natural frequency} \end{cases}$$

Fig. 3—2 inertia model

F. M. Lewis [1] and others [2], [3] have shown that decelerating through a resonance produces responses slightly larger than accelerating through a resonance. Lewis's estimate of resonance factor Q for an undamped single degree of freedom system with a natural frequency f_n (Hz) is

$$Q = 3.67\ \sqrt{q} \pm \frac{\sqrt{2}}{4} \text{ for } \begin{matrix} + \text{ deceleration} \\ - \text{ acceleration} \end{matrix} \quad (2)$$

where q is a measure of the rate of acceleration or deceleration according to

$$q = \frac{f_n^2}{h} \quad (3)$$

For a 2 inertia model (Fig. 3) with equal inertias the per unit shaft response will be 1/2 the amplification factor since only 1/2 of the input excites the mode. For a linear shaft section with a 20 Hz natural frequency the peak shaft torque (9.60, Fig. 4) corresponding to the decelerating input was slightly larger than the peak (9.35, Fig. 5) recorded during the accelerating case. On the contrary when the linear shaft section is replaced by the nonlinear coupling (Fig. 1), the transient shaft torques during

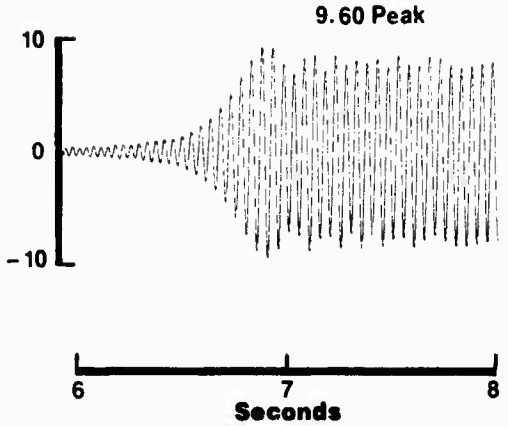

Fig. 4—Per unit linear shaft (20 hz, Fig. 3) response torque to decelerating excitation torque, $\zeta = 0$.

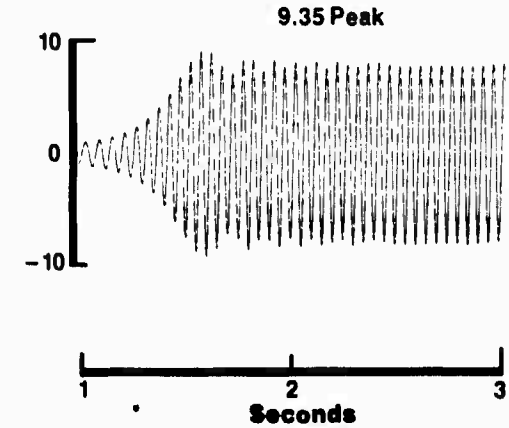

Fig. 5—Per unit linear shaft (20 hz, Fig. 3) response torque to accelerating excitation torque, $\zeta = 0$.

accelerating were the greatest (12.25, Fig. 6) while the peak shaft torque (7.7, Fig. 7) corresponding to the decelerating input was the smallest. Note, these results are for a coupling which gets stiffer with vibration amplitude; whereas, a softening coupling may give opposite results.

The transient shaft torques (Fig. 8) for a 60 Hz natural frequency with light damping (ζ=.005) show what happens. For example, during the accelerating input the natural frequency is steadily increased because of the stiffening effect of the nonlinear coupling as the level of vibration increases as resonance is approached. In effect, the natural frequency is pushed ahead of the excitation frequency

causing more cycles at or near resonance (Fig. 8B), hence, a larger response. Furthermore, more cycles of large vibration occur with the nonlinear coupling - an important fatigue consideration. For the decelerating excitation (Fig. 9) the opposite occurs: while the nonlinear coupling tends to increase the natural frequency, the input frequency is decreasing giving a net smaller q or deceleration rate. Hence, a buildup occurs that is smaller than linear theory predicts (16.75 peak with coupling compared to 20.75 with linear shaft).

Figure 10 shows the maximum shaft torques (Table 2) of the 2 inertia model (20 Hz natural frequency) for both a linear shaft section and a nonlinear

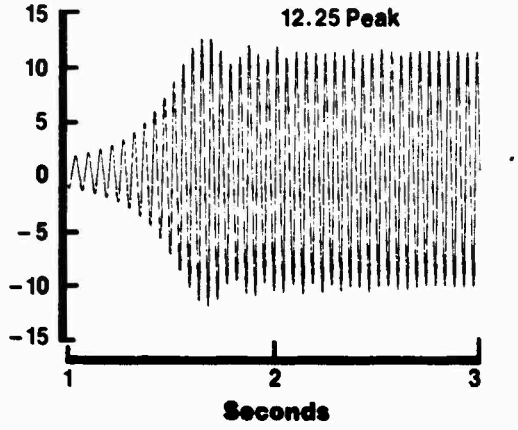

Fig. 6—Per unit nonlinear cplg. (20 hz, Fig. 3) response torque to accelerating excitation torque, $\zeta = 0$.

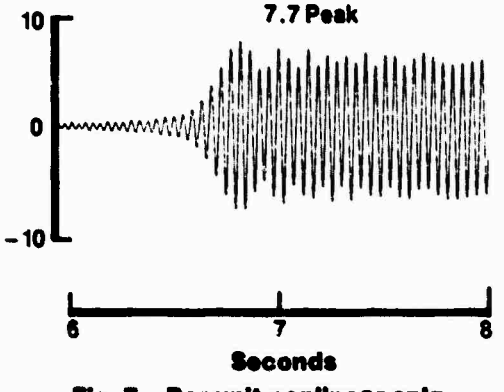

Fig. 7—Per unit nonlinear cplg. (20 hz, Fig. 3) response torque to decelerating excitation torque, $\zeta = 0$.

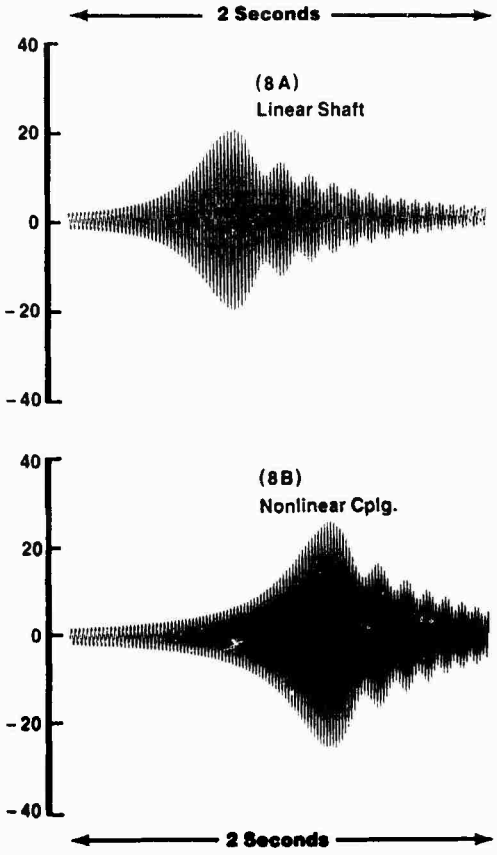

Fig. 8—Per unit response (60 hz, Fig. 3) torques to accelerating excitation torque, $\zeta = .005$.

coupling for both accelerating and decelerating excitation frequencies. The nonlinear coupling (with hardening characteristic) is ineffective for detuning when an accelerating input is considered; however, the coupling effectively detunes for the decelerating input. The differences are less evident as damping increases.

Figure 11 shows normalized peak shaft torques; i.e., ratios (Table 3) of peak coupling torques to linear shaft torques during variable frequency excitations for both 20 Hz and 60 Hz natural frequencies. For the undamped case both natural frequency peak responses are about 30% greater with the nonlinear coupling with an accelerating excitation, while the coupling reduces the peak responses by 20% for the 20 Hz natural frequency and 28% for the 60 Hz case with a decelerating input. Once again, as damping is increased the nonlinear coupling effects are less.

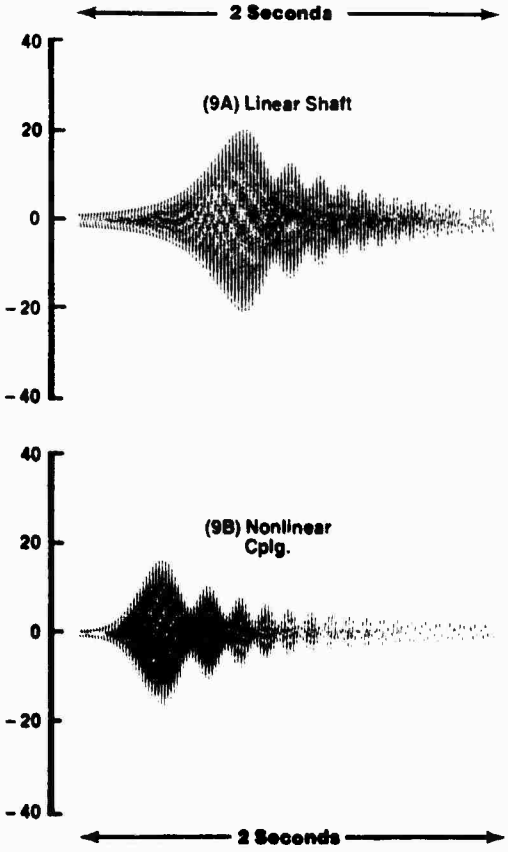

Fig. 9—Per unit response (60 hz, Fig. 3) torques to decelerating excitation torque, $\zeta = .005$.

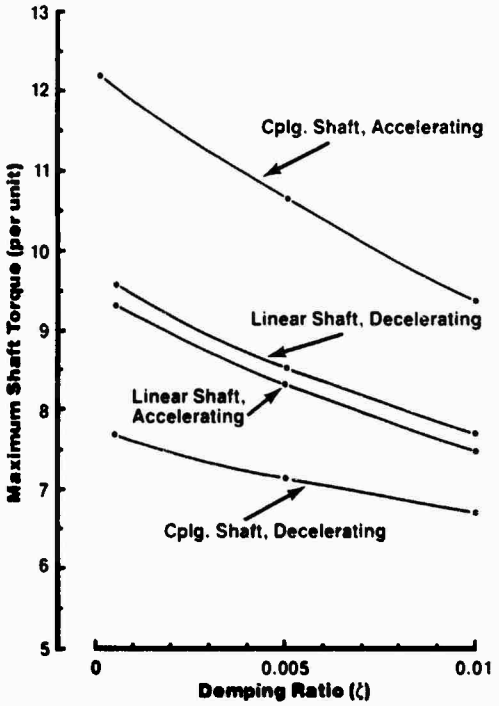

Fig. 10—Maximum shaft torques of 2 inertia model for accelerating and decelerating inputs as a function of damping, 20 hz natural frequency.

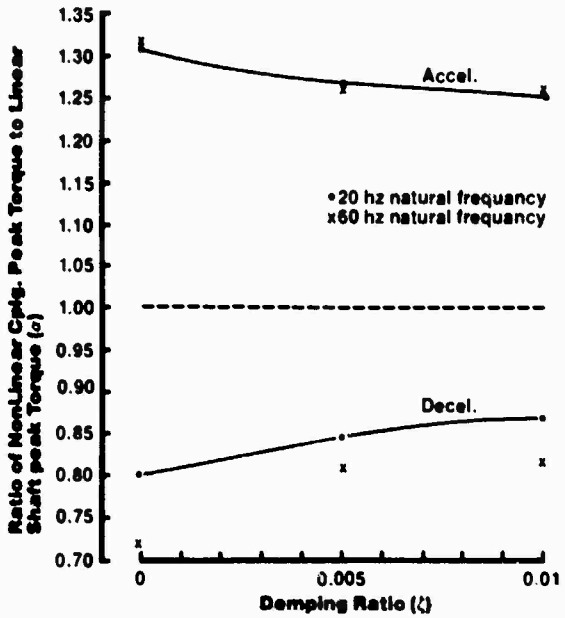

Fig. 11—Ratio of nonlinear cplg. peak torque to linear shaft peak torque of 2 inertia model for accelerating and decelerating inputs

TABLE 2
Maximum Shaft Torques of 2 Inertia Model For Accelerating and Decelerating Excitation

Natural Frequency (f_n)	Damping Ratio (ζ)	Shaft Section	Excitation Frequency	Maximum Shaft Torque (per unit)
20	0	Cplg.	Accel.	12.25
↓	↓	Linear	Accel.	9.35
		Linear	Decel.	9.6
		Cplg.	Decel.	7.7
	0.005	Cplg.	Accel.	10.7
	↓	Linear	Accel.	8.4
		Linear	Decel.	8.55
		Cplg.	Decel.	7.2
	0.01	Cplg.	Accel.	9.4
	↓	Linear	Accel.	7.5
		Linear	Decel.	7.75
		Cplg.	Decel.	6.75
60	0	Cplg.	Accel.	37.5
↓	↓	Linear	Accel.	28.5
		Linear	Decel.	30.0
		Cplg.	Decel.	21.7
	0.005	Cplg.	Accel.	26.0
	↓	Linear	Accel.	20.5
		Linear	Decel.	20.75
		Cplg.	Decel.	16.75
	0.01	Cplg.	Accel.	19.4
	↓	Linear	Accel.	15.4
		Linear	Decel.	15.9
		Cplg.	Decel.	12.9

TABLE 3
Ratio of Nonlinear Cplg. Peak Torque to Linear Shaft Peak Torque of 2 Inertia Model for Accelerating and Decelerating Excitation

Natural Frequency (f_n)	Damping Ratio (ξ)	Ratio of Nonlinear Cplg. Peak Torque To Linear Shaft Peak Torque (γ)	
		Accelerating	Decelerating
20	0	1.31	0.80
↓	0.005	1.27	0.84
	0.01	1.25	0.87
60	0	1.32	0.72
↓	0.005	1.268	0.807
	0.01	1.260	0.811

TABLE 4
Peak Shaft Torques of 3 Inertia Model (Fig. 12)

Shaft Coupling	Peak Shaft Torques (per unit)			
	Shaft (1)		Shaft (2)	
	Decelerating Excitation	Accelerating Excitation	Decelerating Excitation	Accelerating Excitation
Linear	4.0		3.25	
Nonlinear	6.25	7.7	2.88	3.5

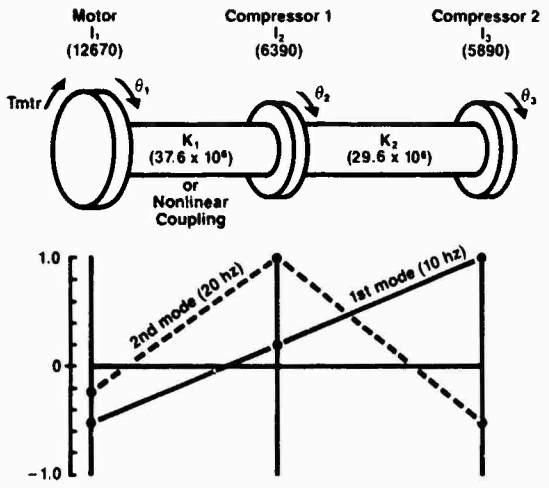

Mode No	Natural Frequency f_n (hz)	Generalized Inertia IG_n	Generalized Stiffness KG_n	Transpose of Modal Matrix $[\Phi]^T$ $\phi 0, n$	$\phi 1, n$	$\phi 2, n$
0	free/free	24950	0	1.000	1.000	1.000
1	10.09	10205	41.0×10^6	-0.566	0.200	1.000
2	19.18	8890	128.8×10^6	-0.258	1.000	-0.531

Fig. 12—Three inertia model, vibration modes, and generalized normal mode data

THREE INERTIA MODEL RESULTS

To study the effects of an additional vibration mode, a synchronous motor-axial flow compressor drive train (Fig. 12) was analyzed. With a linear motor shaft there are 2 vibration modes - 10 Hz and 20 Hz (Fig. 12). Figure 13 shows both linear shaft torque responses for a decelerating excitation frequency and a damping ratio ζ=.005. The response of each mode as they are decelerated through are nearly independent of each other; i.e., by the time the 10 Hz mode is in resonance the earlier 20 Hz vibration has almost disappeared. Since the 10 Hz mode is easier to excite (mode shape and generalized stiffness of Fig. 12), the 10 Hz vibration is stronger. Peak shaft torques (Table 4) were 4 per unit and 3.25 per unit for shafts 1 and 2, respectively; both occurring during the 10 Hz quasi-resonance.

When the linear motor shaft section (shaft 1) is replaced with a nonlinear coupling (Fig. 1) and a decelerating input is applied, the peak shaft 1 torque (6.25 per unit, Table 4) increased while the peak shaft 2 torque (2.88 per unit, Table 4) decreased. The shaft time histories (Fig. 14) show evidence of a 20 Hz vibration during the 10 Hz quasi resonance condition. The

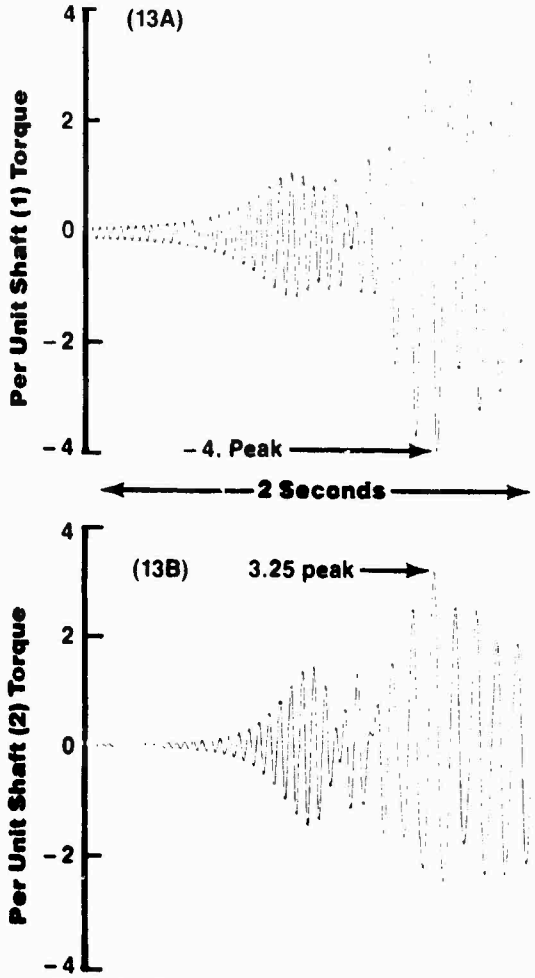

Fig. 13—Per unit shaft (Fig. 12) torque responses to a decelerating excitation torque, ζ=.005.

phasing of mode shapes (Fig. 12) indicate that while a 20 Hz vibration will strengthen the 10 Hz vibration of shaft 1 it will subtract from the vibration of shaft 2.

For an accelerating input both shaft responses (Fig. 15) are greater; e.g., peak shaft torques are 7.7 per unit (shaft 1) and 3.5 per unit (shaft 2) - Table 4. The maximum response of shaft 1 occurs during the pass through the 20 Hz mode (Fig. 15A); however, the time history has a large 10 Hz component which is being excited subharmonically because of the nonlinearity.

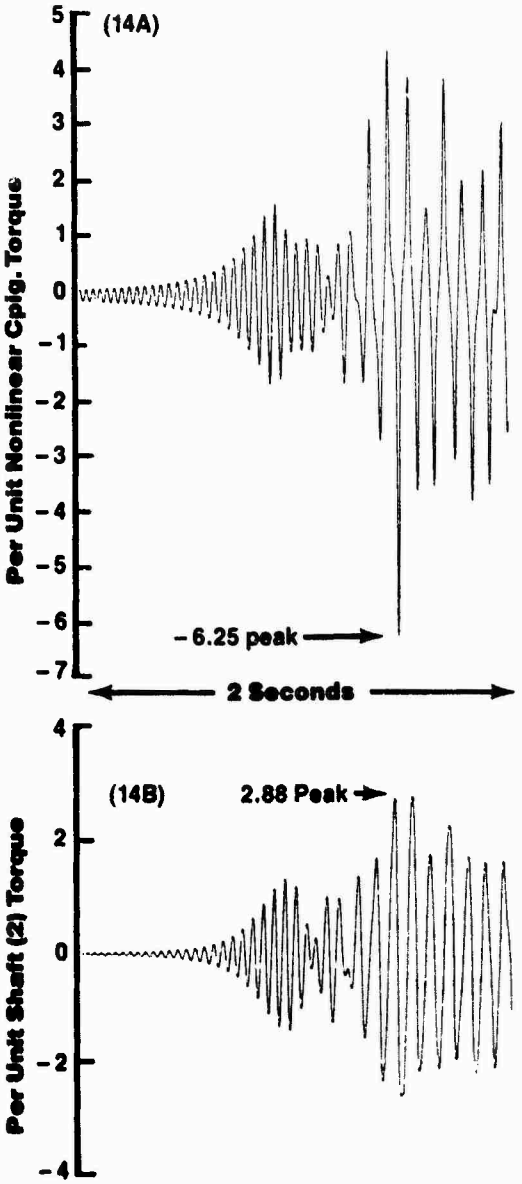

Fig. 14—Per unit nonlinear cplg. and shaft (Fig. 12) torque responses to a decelerating excitation torque, $\zeta = .005$.

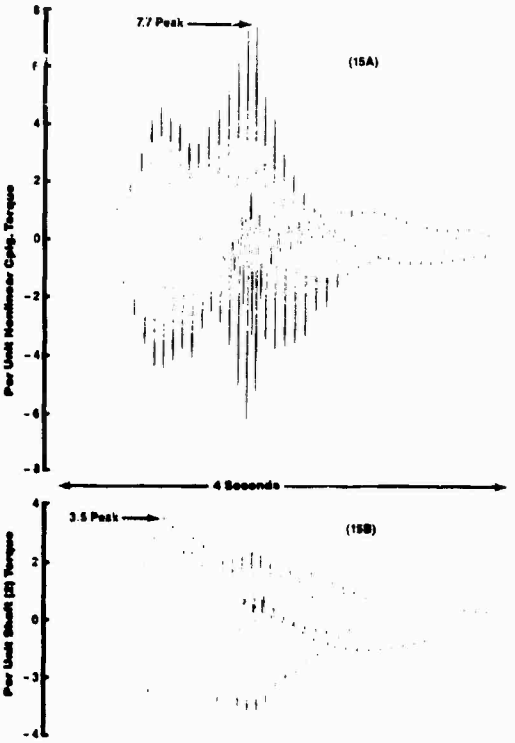

Fig. 15—Per unit nonlinear cplg. and shaft (Fig. 12) torque responses to an accelerating excitation torque, $\zeta = .005$.

CONCLUSIONS

A nonlinear coupling with a stiffness property that increases with vibration level may either strengthen or reduce vibration responses to variable frequency excitations.

1. For an accelerating excitation, the tendency is to push the "natural" frequency ahead of the excitation frequency causing a greater number of cycles (closer to steady state) and, hence, a greater buildup than predicted by linear theory: for a decelerating excitation, the converse is true.

2. For one mode of vibration the nonlinear coupling peak response can be as much as 28% less than a linear shaft response for a decelerating excitation.

3. For one mode of vibration the nonlinear coupling peak response can be 31% greater than a linear shaft response for an accelerating excitation.

4. When a second vibration mode was introduced the nonlinear coupling gave a greater peak response for the decelerating excitation, also. A subharmonic excitation of the lower mode while the second mode was being accelerated through gave a peak coupling response that was almost twice as large as the peak linear response.

REFERENCES

1. F.M. Lewis, "Vibration During Acceleration Through a Critical Speed," ASME, Applied Mechanics Division, APM-54-24 (1932).

2. J.G. Baker, "Mathematical Machine Determination of the Vibration of Accelerated Unbalance Rotor," Trans. ASME, 1939, p. A-154.

3. F.H. Wolff, A.J. Molnar, and A.C. Hagg, "Accelerating Through Resonance of Multi-Degree of Freedom Systems," Shock and Vibration Bulletin No. 47, Part 2, Sept. 1977.

DISCUSSION

Mr. Lyon (M.I.T.): Did you see any evidence of any jump phenomena in this study? I have experienced a rundown of motors where there were nonlinear springs where you would get jumps in the response.

Mr. Wolfe: No. We did not see any jump phenomena in the two cases of the simple single degree of freedom system, and adding the additional mode for this particular example. I am trying to remember if the fact that it doesn't occur has anything to do with the accelerating or decelerating rate. With the hardening coupling, you would expect to see it rise, then jump down, the bent over knee. But that effect is less with damping; it doesn't show up as much because damping rounds out the curve and gives you a smaller instability region even in the nonlinear case, I think.

Mr. Bingman (Wright-Patterson AFB): When you say accelerating or decelerating, are you referring to increasing the input frequency rate, passing through the resonance, or decreasing the rate of your frequency?

Mr. Wolfe: Yes, the accelerating and decelerating referred to changing the input frequencies.

Mr. Bingman: It is reasonable then, that as you change your input frequency by accelerating, and if you have a hardening spring, you are dwelling longer at this quasi-resonance as you are increasing the frequency because you have a stiff spring. But the numbers you showed, your 31% or 28% difference, aren't those subject to that rate of change?

Mr. Wolfe: Yes. This was a fairly fast acceleration rate. It was typical; 15 Hz per second is typical for a synchronous motor application.

Mr. Bingman: If your rate of change was quite a bit different, then wouldn't those numbers change?

Mr. Wolfe: Yes, those numbers would change.

Mr. Eshleman (The Vibration Institute): Did you use the same damping in the two modes that you went through? In some synchronous motor applications you actually go through the second mode first. In other words, you apparently come down in frequency while you increase the speed. I have seen that the second mode is well damped, but then the first mode has a lot of response.

Mr. Wolfe: The damping ratios were the same in both modes. The example I showed was .005 damping ratio for both modes. It is a simple example, but keeping it simple allows you to take a more thorough look at what is happening.

SIMPLE APPROXIMATE MODELS FOR A CLASS OF STRUCTURES

A. J. Molnar and F. H. Wolff
Engineering-Analytical Dynamics Corp.
Trafford, Pennsylvania 15085

A two mass approximate model for investigating the interaction for a class of structures in a particular frequency range is developed. The method is applicable to both analytical finite element type models as well as physical structures where vibration response data are available.

INTRODUCTION

In these times of large finite element structural analyses and Fast Fourier Analyzers for detailed analyses of test data, there is still a need for engineering approximations and judgement, which in many instances, results in more insight and less costs.

A two mass approximate model derived in this paper is most applicable for economically studying the interactions of two structures in a frequency range where one mode of each structure dominates in the same particular coordinate direction (class of structures). Systems where the exciting forces are essentially at a fixed frequency such as those involving synchronous machinery are candidates for this type of analysis - where the exciting frequency may be too close to a natural resonant frequency. Changes in the system necessary to move the resonance can be evaluated through an economical parametric study of a two mass model. Only the most promising or practical changes would or could then be evaluated with more complex finite element analyses or testing.

DEVELOPMENT OF APPROXIMATE MODEL

As previously mentioned this type of analysis can be most useful where the exciting frequency is fixed and is too close to a basic structural frequency. Figure 1 shows the steady state response at a particular node from a finite element analysis of a large structure between 50 and 70 Hz. The node is on the main structure and comparison of the two responses shows the dynamic effect from addition of the substructure. In this case damping of the main structure comes primarily from bearing oil films which support the machine rotor. The exciting force is at or near 60 Hz. In order to reduce the vibration response level in the neighborhood of 60 Hz, a dynamic vibration absorber (substructure) tuned to 60 Hz was attached to the finite element model of the main structure. The resulting change in response is shown by the main + substructure curve in Figure 1. Comparing the two responses in Figure 1 indicates a behavior similar to classical one and two-degree-of-freedom systems and we proceed to develop a two-degree-of-freedom model which has similar dynamic behavior.

Figure 2 shows schematically a two mass model where f_{11} is the resonant modal frequency of the main structure and f_{22} is the modal frequency of the substructure attached to a fixed base. Resonant frequencies (undamped) of the two mass model in Figure 2 are determined from equation (1) [1].

$$f^4 - [f_{11}^2 + (1+\mu) f_{22}^2] f^2 + f_{11}^2 f_{22}^2 = 0 \quad (1)$$

where

$$f_{11} = \frac{1}{2\pi}\sqrt{\frac{K_1}{M_1}},\ f_{22} = \frac{1}{2\pi}\sqrt{\frac{K_2}{M_2}} \text{ and } \mu = \frac{M_2}{M_1}$$

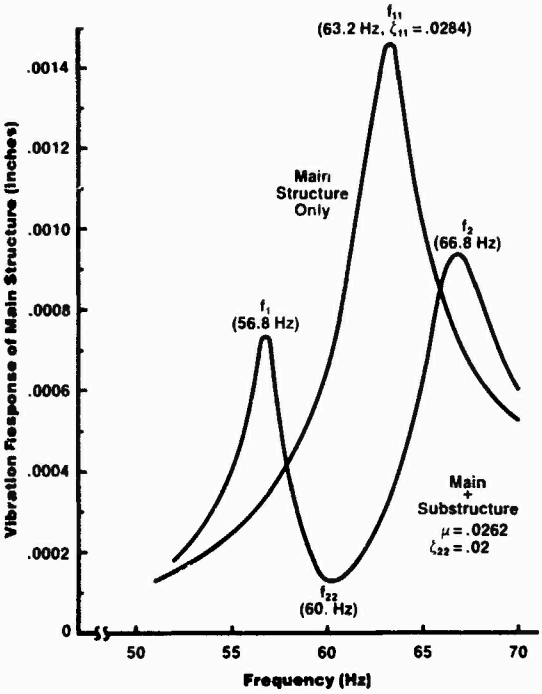

Fig.1—Comparison of main structure vibration with and without substructure.

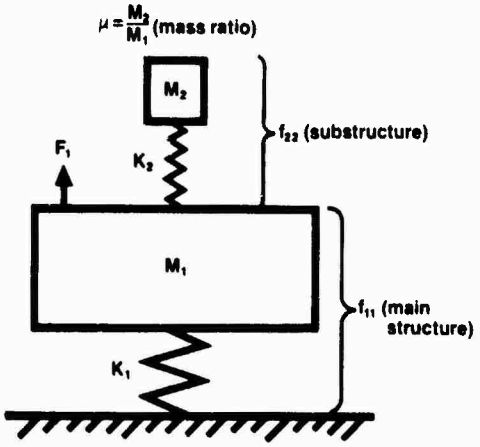

Fig. 2—Two mass model for approximating interaction between structures.

The roots of equation (1), $f^2 = f_1^2$, f_2^2 are the resonant frequencies; therefore,

$$(f^2-f_1^2)(f^2-f_2^2) = \tag{2}$$

$$f^4 - [f_1^2+f_2^2]\, f^2 + f_1^2 f_2^2 = 0$$

The polynomial equations (1) and (2) are equal; therefore, the coefficients are equal so equating coefficients gives:

$$f_{11}^2 + (1+\mu)\, f_{22}^2 = f_1^2+f_2^2 \quad \text{and} \tag{3}$$

$$f_{11}^2 f_{22}^2 = f_1^2 f_2^2$$

or

$$\mu = \frac{f_1^2 + f_2^2 - f_{11}^2}{f_{22}^2} - 1 \tag{4}$$

and

$$f_{11} f_{22} = f_1 f_2 \tag{5}$$

From the response data in Figure 1, f_{11} = 63.2 Hz, f_{22} = 60. Hz, f_1 = 56.8 Hz and f_2 = 66.8 Hz. Substituting in equation (4) gives:

$$\mu = \frac{56.8^2 + 66.8^2 - 63.2^2}{60.^2} - 1 = .0262$$

For this case M_2 = 2700 lb/g $\approx$ 7.0 (lb-sec^2/in) (absorber mass), therefore

$$M_1 = \frac{M_2}{\mu} = \frac{7.0}{.0262} \approx 267.2 \text{ (lb-sec}^2\text{/in)}$$

or the effective weight of the main structure at the location the response was measured is 103130 lbs. Therefore,

$$K_1 = 267.2\ (2\pi\ 63.2)^2 = 42.1(10)^6 \text{ lb/in}$$

also

$$K_2 = 7.\ (2\pi\ 60)^2 = .994(10)^6 \text{ lb/in.}$$

Parameters for the approximate two mass model (Figure 2) have been derived from the system response curves in Figure 1 and knowing that a 2700 lb dynamic vibration absorber was attached to the main structure.

In summarizing, using equation (4) and the definitions of f_{11} and f_{22} a model can be constructed by knowing any three of the four quantifies f_1, f_2, f_{11} or f_{22} and one of the four quantities K_1, M_1, K_2 or M_2. A qualitative analysis

can be performed without knowing any of the latter four quantities.

In the previous example all of the quantities f_1, f_2, f_{11} and f_{22} were known; however, only three are required since the fourth can be found from equation (5). In many cases only three of the quantities are available.

DAMPING

Although the approximate model was developed without damping, reasonable amounts of damping have little effect on the method and damping can be added to the two mass model later as indicated by tests or finite element calculation of the system. The model was derived primarily from frequency data which is not sensitive to small amounts of damping.

ANALYSIS OF APPROXIMATE MODEL

The approximate model derived from response data in Figure 1 will be analyzed and the results compared to Figure 1. We will first add damping as indicated by the sharpness of resonance at 63.2 Hz which indicates a damping ratio of $\zeta_{11} = .0284$. Thus damping of

$$C_{11} = \zeta_{11}\ 2\ \sqrt{K_1 M_1} = 6024 \text{ lb-sec/in}$$

is used to represent damping of the main structure. The damping in the dynamic absorber by design was $\zeta_{22} = .02$, therefore

$$C_2 = \zeta_{22}\ 2\ \sqrt{K_2 M_2} = 105.5 \text{ lb-sec/in.}$$

Adding this damping to the approximate model and calculating the steady state response to $F_1 = 3492 \sin 2\pi f_i t$ lbs on M_1 where f_i varies from 50 to 70 Hz, the results are shown in Figure 3. The magnitude of F_1 is determined so that the peak response on M_1 matches the main structure at 63.2 Hz. Comparing Figure 1 to Figure 3 indicates the approximate model represents the dynamic behavior of original structure well.

PARAMETRIC EVALUATIONS

The approximate model can be readily used to econmically study variations in parameters and how they affect the response in this particular frequency range (50-70 Hz in this case). For example, Figure 4 shows how variations in substructural damping (dynamic absorber) affect the response of the main structure using the approximate model. In this case, a dynamic absorber design was selected corresponding to curve D. Promising changes guided by parametric studies on approximate models can be checked by a limited number of cases using more complex finite element or testing methods. In this case a dynamic vibration absorber was designed to reduce the vibration level in the region of 60 Hz.

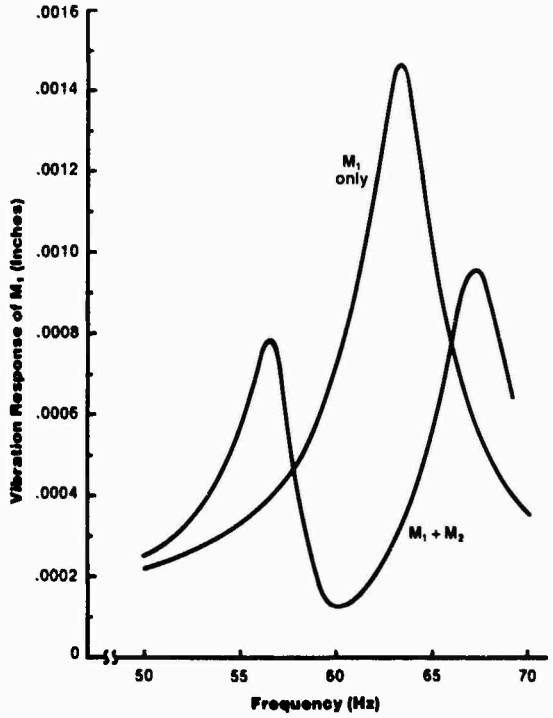

Fig. 3—Comparison of response of M_1 with and without M_2 for approximate model.

The previous case involved studying a small substructure that is $\mu = .0262$ over a narrow frequency range. This method also works well with larger values of μ and larger system changes and parametric curves such as those shown in Figure 5 can be used to predict resonant frequencies over a wider frequency range; however, it becomes more difficult to distinguish the main structure and substructure modes which are interacting dynamically.

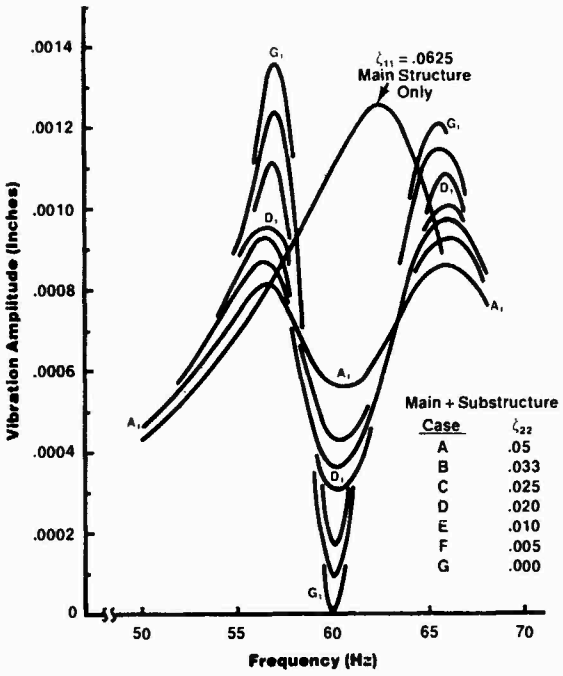

Fig. 4—Parametric study of substructural damping using approximate model.

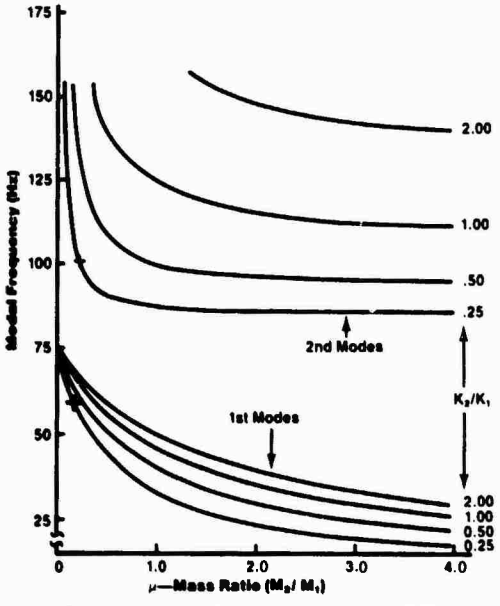

Fig. 5—Parametric study of larger stiffness and mass ratio effects on modal frequencies.

DISCUSSION

Having determined the approximate model and performed variations of parameter to determine a structural design or redesign, the interpretation of the meaning of the K's and M's may require considerable engineering judgement. In the case of a dynamic vibration absorber, used in this paper for the substructure, the interpretation is straight forward since the substructure is a simple spring-mass oscillator. For more complex structures the use of modal effective mass and stiffness and mode shapes along with engineering judgement are required to relate the parameters of the approximate model to the actual structure [2], [3].

CONCLUSIONS

An approximate two mass model has been derived for studying the interaction between a class of structures in an economical manner. Parametric studies of the approximate model can be a valuable aid in determining required changes in the actual structures.

The method is especially useful in designing dynamic vibration absorbers for large complex structures.

REFERENCES

1. W.T. Thomson, "Vibration Theory and Applications," Prentice-Hall Inc., Englewood Cliffs, NJ, 1965.

2. F.H. Wolff and A.J. Molnar, "Reduced System Models Using Modal Oscillators for Subsystems (Rationally Normalized Modes)," Shock and Vibration Bulletin No. 48, Sept. 1978.

3. B.K. Wada, R. Bamford, and J.A. Garba, "Equivalent Spring-Mass Systems: A Physical Interpretation," Shock and Vibration Bulletin No. 42, January 1972.

SOURCE SIGNATURE RECOVERY IN REVERBERANT STRUCTURES

Richard H. Lyon
Massachusetts Institute of Technology
Cambridge, Massachusetts 02139

The use of vibration or acoustical signals to reveal operational parameters or developing faults of a machine is very attractive. If one wishes to monitor a number of sources of vibration in a machine, then either a multiplicity of sensors must be used or individual sensors must each monitor several sources. If information is to be determined from sensors that are not close to sources, then the effects of the propagation on the vibration signal may become troublesome. The conversion of remotely sensed vibration or sound to a source signal generally involves some form of inverse filter transfer function which has a magnitude and phase; evidence shows that the phase is more important. Our work has concentrated on the phase, its estimation and its measurement in complex structures. The phase of measured transfer functions, even in very reverberant systems, has a strong tendency to have a lag that increases with increasing frequency. We discuss the reason for this phase trend, and its significance in defining the appropriate inverse filter.

INTRODUCTION

The use of vibration or acoustical signals to reveal operational parameters (load, fuel/air mixture, etc.) of a machine or developing faults (wear, fatigue, loss of lubricant) is very attractive. There is a sizable industry that has developed around this idea, using broad-band or filtered vibration or sound levels to indicate faults. In existing applications, the sensor is usually placed as close as possible to the source being monitored (at the bearing cap, for example) and the mean square (m.s.) level is read.

If one wishes to monitor a number of sources of vibration in a machine, then either a multiplicity of sensors must be used or individual sensors must each monitor several sources. Actually, of course, a single sensor will always pick up vibrations from several sources, so the distinction may be artificial. In any case, if information is to be determined from sensors that are not close to sources, then the effects of the propagation on the vibration signal may become troublesome and have to be dealt with.

The conversion of remotely sensed vibration or sound to a source signal generally involves some form of inverse filtering. The filter transfer function has a magnitude and phase, but experimental evidence shows that the phase is more important in source signal recovery. Generally, there has been much more concern with the magnitude of transfer functions than the phase because of concern with noise problems, for which one may ignore the phase.

Recently, our work at MIT has concentrated on the phase, its estimation and its measurement in complex structures. The phase of measured transfer functions, even in very reverberant systems, has a strong tendency to have a lag that increases with increasing frequency. It is the purpose of this report to discuss the reason for this phase trend, and its significance in defining the appropriate inverse filter.

II. SIGNAL TRANSMISSION IN REVERBERANT STRUCTURES

To illustrate, consider the pressure fluctuation in the cylinder of a diesel engine and the resulting vibration pulse on the casing, both shown in Fig. 1 [1]. The pressure pulse has a simple waveform, and can reveal a number of features of the compression and combustion process. By contrast, the vibration pulse is too complex to show variations in operation parameters.

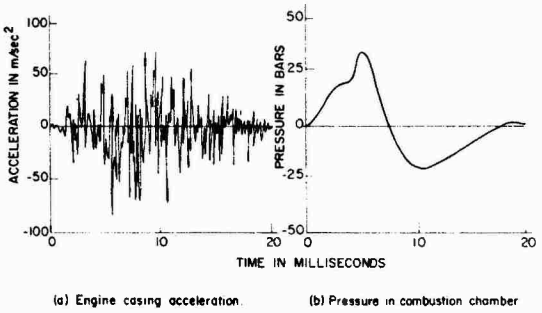

Fig. 1: Cylinder Pressure and Casing Vibration Pulses Resulting from Diesel Combustion

If the Fourier transform of the applied force $f(t)$ is $F(\omega) = |F|e^{j\alpha}$ and the measured velocity $v(t)$ has a transform $V(\omega) = |V|e^{j\psi}$, the transfer mobility is

$$Y(\omega) = |Y|e^{j\phi} = (|V|/|F|)e^{j(\psi-\alpha)}. \qquad (1)$$

In Fig. 2, we show the values of $|Y|$ and ϕ determined from the force and vibration signals in Fig. 1. The magnitude of Y shows the variations that are typical of multimodal reverberant systems. The magnitude of Y can be estimated using statistical energy analysis (SEA). The input power to the structure $\langle F^2\rangle \pi/2 \; n(\omega)/M$ must equal the dissipated energy due to the losses $M\langle v^2\rangle\omega\eta$ resulting in [3]

$$|Y|^2 = \frac{\langle v^2\rangle}{\langle F^2\rangle} = \frac{\pi n(\omega)}{2M^2\omega\eta} \qquad (2)$$

where $n(\omega)$ is the modal density, M is the mass, and η is the loss factor for the structure.

The phase function in Fig. 2 fluctuates between $\pm\pi$ at low frequencies, but a sawtooth like pattern develops at high frequencies, which represents a monotonic increase in phase lag ϕ as the frequency increases, superimposed on fine scale fluctuations in phase. It is clear that both the average phase trend and the fluctuations in phase around the trend can affect the form of $v(t)$. A linear dependence

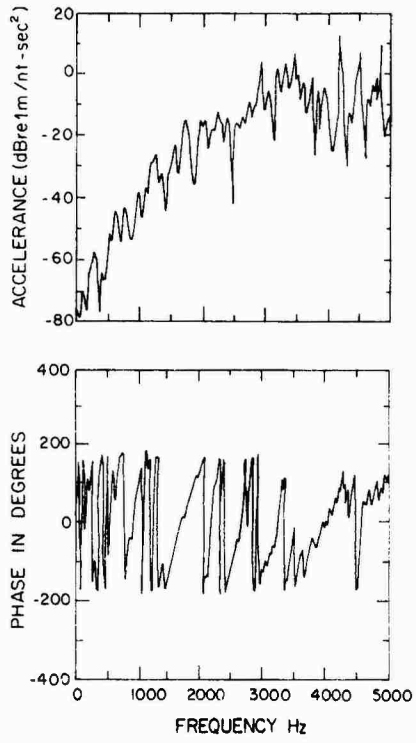

Fig. 2: Magnitude and Phase of Transfer Function from Cylinder Pressure to Casing Vibration

on phase with frequency represents a simple time delay, but any other functional form will cause the signal to change shape as it propagates. The phase trend is the part of the phase variation that is discussed in this paper. We do not have a way of dealing with fine scale variations at the present time.

III. ESTIMATION OF THE PHASE TREND

In another paper [2], we have made arguments for the following points relevant to the phase trend

(a) Transmission functions for structures are minimum phase, i.e., poles and zeroes both have positive dissipation

(b) As a result of (a), the phase trend $\phi(\omega)$ is $-\pi(N_p-N_z)$ where N_p and N_z are the numbers of poles and zeroes respectively up to frequency ω.

(c) The likelihood of a zero is about one-half that of a pole so that $N_z \doteq \frac{1}{2} N_p$ and

$$\overline{\phi}(\omega) \doteq -\tfrac{1}{2} N_p. \qquad (3)$$

Parenthetically, we note that the group delay $\tau = -\phi'(\omega)$ due to the phase trend is given by

$$\tau \triangleq \tfrac{1}{2}\,\pi n(\omega) = \tfrac{1}{2}\,\pi n(k)\,\frac{dk}{d\omega} = \pi n(k)/2c_g$$

where $n(k)$ is the modal density in wave number and c_g is the group or energy speed. Then

$$c_g\tau = \frac{\pi}{2}\,n(k) = d_E \qquad (4)$$

which may be interpreted as the average distance traveled by a packet of energy in going from the source to the observation point. For a two-dimensional structure such as a plate of area A,

$$d_E = \frac{\pi}{2}\,n(k) = \tfrac{1}{4}\,kA, \qquad (5)$$

which is generally much longer than the mean free path.

Computations of phase lag were carried out on a rectangular plate for various source to receiver distances. The results of these calculations are shown in Fig. 3. From these results several points are clear. First of all, the phase lag is much greater than kr (Ref. 2 shows that kr is the proper phase lag for one-dimensional systems, but not for systems of higher dimensionality). Second the phase lag does depend on r to a degree, and finally, the phase lag is not linear, as Eq. (2) would predict.

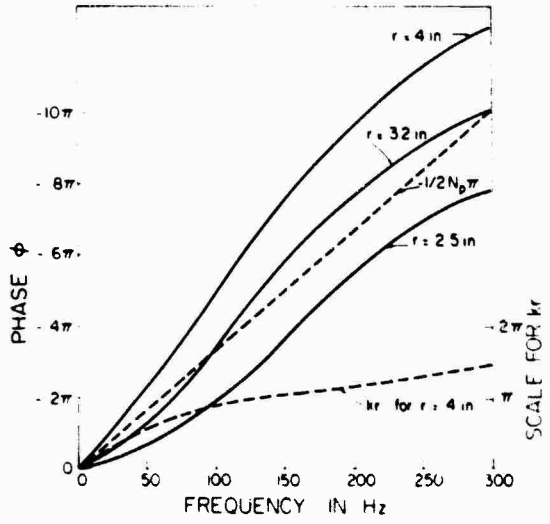

Fig. 3: Phase Lag Computed for a Simply Supported Plate

It is shown in Ref. 2 that if the transfer function is expressed in a modal expansion

$$Y(\omega) = \text{const.} \sum_M \frac{\psi_M(x_s)\psi_M(x_0)}{\omega^2-\omega_M^2}, \qquad (6)$$

where $\psi_M = \sin m_1\pi x_1/\ell_1 \sin m_2\pi x_2/\ell_2$ for a rectangular supported plate of dimensions ℓ_1,ℓ_2, then a zero occurs between the ordered poles ω_M, ω_{M+1} if the numerator or residues do not change sign. Thus, since we know in an approximate way at least the number of poles, a better estimate of the zeroes is needed to determine phase.

Consider the sign of the combination $\sin kr \sin k(x+\delta)$ as a function of k for fixed x, $x+\delta$. The period of the first factor is $2\pi/x$ and the second $2\pi/(x+\delta)$. This product will be positive until the zero at $k = \pi/(x+\delta)$, negative until $k = \pi/x$, etc. as shown in Fig. 4. As long as the region of negative residue is much smaller than the lattice spacing π/ℓ, the numerators in Eq. (6) will not change sign, zeroes will occur between the poles, and the transfer function will not accumulate phase. The negative residue region will continue to grow as wavenumber and frequency increase until the n^{th} negative region is comparable to lattice spacing, $\pi/\ell = n\pi\delta/x^2$. Solving, $n \triangleq x^2/\ell\delta$. The wavenumber at which this happens is

$$k_m = \frac{m\pi}{\ell} = \frac{n\pi}{x} = \frac{\pi x}{\ell\delta} \qquad (7)$$

or $m = n\,\ell/x = x/\delta$. This determines the onset of the frequency region for which residues of adjacent terms in Eq. (6) have a high probability of changing sign, resulting in a rapid build-up of phase lag.

Fig. 4: Sign of Factors that Determine Sign of Residue in Partial Fracture or Modal Expansion

The build-up of phase lag will continue until the negative residue regions begin to dominate, i.e., until the positive regions are smaller than π/ℓ. This occurs when the length of the negative region $n\pi\delta/x^2$ equals the half period of the residue sign variation π/x. Thus, $n = x/\delta$, which happens when

$$k_m = \frac{m\pi}{\ell} = \frac{n\pi}{x} = \frac{\pi}{\delta}$$

or $m = \ell/\delta$. Of course, this is only one factor in the two dimensional mode shapes in Eq. (6), so that the sharpness, or even the appearance of these "transitions" will be affected by the relative values of the dimensions ℓ_1 and ℓ_2, x_1 and x_2, and δ_1 and δ_2.

IV. CONCLUSIONS

It is evident from the preceding discussion that the trend in the phase function for complex structures can be estimated from simple principles, but it is not at all obvious that the simple trend found here is of any use in constructing inverse filters for machine structures. Our effort is now being directed at determining just how much detail is necessary to keep in the phase function in order to reconstruct useful source signatures. In this context, "useful" means producing a source signal that reveals information about an important operating parameter. It is obvious that such a criterion leaves a lot of room for interpretation, and success in source parameter determination is likely to be very situation dependent.

REFERENCES

1. A. Ordubadi, "Component and Fault Identification in a Machine Structure Using an Acoustic Signal," ScD Thesis, Dept. of Mech. Eng., MIT, May, 1980.

2. R. H. Lyon, "Progressive Phase Trends in Multi-Degree-of-Freedom Systems", To appear in *J. Acoust. Soc. Am.*, April, 1983.

3. R. H. Lyon, *Statistical Energy Analysis of Dynamical Systems: Theory and Application*, MIT Press, 1975.

COMPARISON OF STATISTICAL ENERGY ANALYSIS AND FINITE ELEMENT ANALYSIS VIBRATION PREDICTION WITH EXPERIMENTAL RESULTS

L.K.H. Lu, W.J. Hawkins, D.F. Downard
Westinghouse Electric Corporation, Marine Division
Sunnyvale, California
and
R.G. DeJong
Cambridge Collaborative
Cambridge, Massachusetts

In order to further understand the practical application of the Statistical Energy Analysis, a two section plate like frame structure is analyzed by the Finite Element Method, Statistical Energy Analysis, and experimental techniques. Results are compared, discussed and also used as a benchmark for a newly developed in-house SEA Computer Program.

INTRODUCTION

Modern naval machinery is frequently required to have both high power/weight ratio and quiet performance. To meet these conflicting requirements not only is design work based on past experience necessary, but good analytical and testing tools are also required. For dynamical response calculations at low frequency, large scale finite analyses (FEA) are useful, and are routinely carried out. Very often, model tests are also performed on scaled down or prototype models. At high frequency, these methods do not always provide accurate or appropriate results. In this frequency range an alternative approach, Statistical Energy Analysis (SEA)[1] is attractive. Although Statistical Energy Analysis has been used successfully in room acoustics and aerospace structures, the application of SEA to marine machinery is quite recent. With the guidance and assistance of Cambridge Collaborative, Westinghouse has adapted this technique to marine structural design in order to minimize noise transmission. SEA is also applied to the calculation of average structural response. Initial results have also been quite positive, and some of the earlier work has been reported elsewhere.[2,3] To assist in SEA calculation, a Statistical Energy Analysis for Marine Structures (STEAMS) Computer Program has been developed.

It is well known that maximum finite element mesh size is directly related to the minimum half-wave length of interest; hence, the frequency range that is calculable is limited by available computer core and computational cost. On the other hand, SEA is a statistical "average" approach. At low frequency lack of sufficient modal density can make an average response a poor representation of actual results. Further, at high frequency, average results are often the main item of interest. In the intermediate frequency range, either method should be applicable.

In this paper we report results from a specimen made of two folded plates welded together when analyzed by both SEA and FEA methods. These results are then compared with those obtained by shaker tests. It is not our purpose to explore the theoretical aspect of SEA. The goal of this project is to use a simple test specimen, as shown in Figure 1, to investigate the applicable range of FEA and compare the results with those from the newly developed SEA Program.

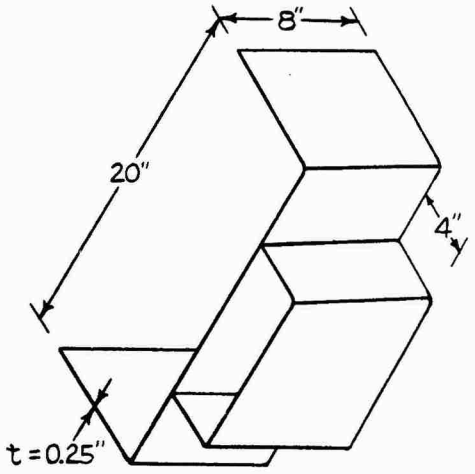

Figure 1. Test Specimen

STATISTICAL ENERGY ANALYSIS MODEL AND COMPUTER PROGRAM

The statistical Energy Analysis (SEA) method is a procedure to calculate vibrational energy balance in a complex system. The subsystems in the SEA model are blocks of "similar modes". Input power (π_{in}), due to mechanical excitation, is calculated by using the known forcing function and estimated input impedance of the subsystem. For each subsystem, the power is not only dissipated by mechanical vibration, but is also transmitted to the neighboring subsystems. The dissipation of power is measured by the loss factor of the subsystem (η_i) and is proportional to the amount of energy stored in that subsystem (E_i) and on the magnitude of the coupling loss factor (η_{ij}). For a system which consists of N modal blocks, the above energy flow relationship can be expressed mathematically as:

$$\begin{vmatrix} \eta_1 + \sum_{j=2}^{N} \eta_{1j} & -\eta_{21} & \cdots & -\eta_{N1} \\ -\eta_{12} & \eta_2 + \sum_{\substack{j=1 \\ j=2}}^{N} \eta_{N2j} & \cdots & -\eta_{N2} \\ \vdots & \ddots & \vdots & \vdots \\ \eta_{1N} & \cdots & \cdots & \eta_N + \sum_{j=1}^{N-1} \eta_{Nj} \end{vmatrix} \begin{vmatrix} E_1 \\ E_2 \\ \vdots \\ E_N \end{vmatrix} = \begin{vmatrix} \pi_{in}^1 / \omega \\ \pi_{in}^2 / \omega \\ \vdots \\ \pi_{in}^N / \omega \end{vmatrix} \qquad (1)$$

The coupling loss factor (η_{ij}) is the parameter governing transmitted power. It has been measured for some structures, although usually it is calculated in terms of known junction impedances. The formulas for coupling loss factors and impedances are tabulized in Reference (3). The loss factor η_i is simply twice the critical damping ratio. It is apparent from Equation (1) that η_i can easily be varied from one subsystem to another. This is very attractive for damping treatment studies.

The resonant velocity and acceleration response of a subsystem are determined by the total energy and the total mass.

$$M_i \langle V_i^2 \rangle = E_i \qquad (2)$$

$$\langle a_i^2 \rangle = \omega^2 \langle V_i^2 \rangle \qquad (3)$$

where $\langle V_i \rangle$, $\langle a_i^2 \rangle$ and M_i are the average mean-square velocity, acceleration and total mass of subsystem number i.

In the SEA calculations by steams computer Program, a structure is divided into many energy blocks and joints. For example, the SEA model of the test specimen consists of 12 energy blocks and 6 joints as shown in Figures 2a and 2b. The modal densities and mechanical impednces of each block are calculated by Subroutines BKSNW and BKIMP, respectively.

Each subsystem may be simulated by beams, plates, or shells in transverse, inplane, shear or any combination of the above wave forms. Coupling loss factors at each joint are computed by the Subroutine CPLF. A maximum of four plates or beams can be considered at a joint. Power input is calculated in the Subroutine PWIMPT. Equation (1) is then assembled in the main program and solved by the simultaneous equation solver SIMEQ. Velocities and accelerations are finally calculated in accordance with Equations (2) and (3). Since computational cost of SEA simulation by STEAMS is usually quite low, parametric studies can easily be carried out. Figure (3) illustrates the flow chart of STEAMS Computer Program.

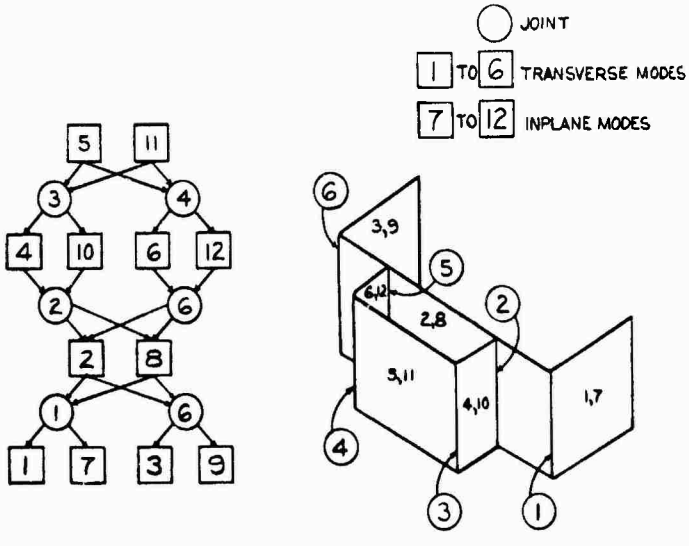

Figure 2. Sea Model

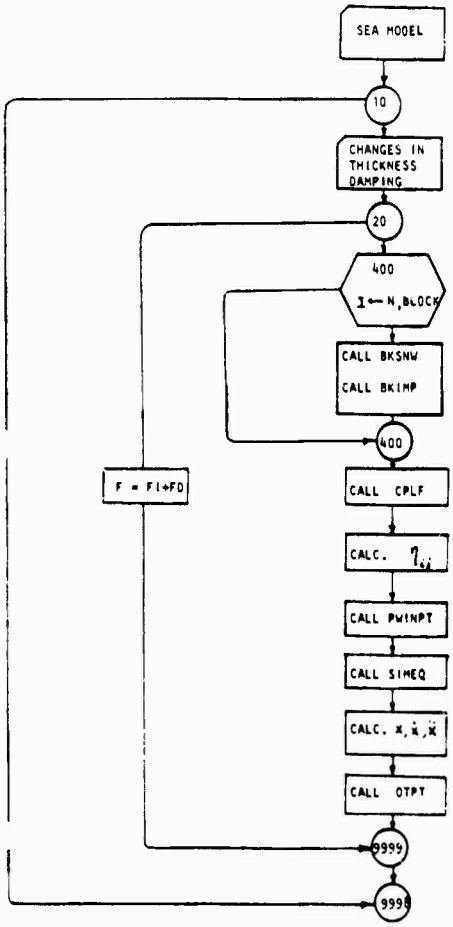

Figure 3. STEAMS Flow Chart

FINITE ELEMENT ANALYSIS AND TEST

The structure was modeled by 96 QUAD4 plate elements with approximately 600 dynamic degrees of freedom. The finite element model is shown in Figure 4. In order to avoid any approximation that might be introduced by dynamic reduction, such as Guyan or generalized dynamic reduction, a full model analysis was performed by NASTRAN Computer Program [4] to extract 144 eigen functions in the frequency range from 0 to 13,000 Hz for further post-processing.

The test specimen was suspended in approximate free-free state and excited with Wilcoxon F4 or F6 shaker attached at the corner of model block number 4. (See Figure 5 for instrumentation arrangement). Periodic-random excitation was used for force input through D.A.C. output.

In the high frequency range (2000 to 15000 Hz), an F6 shaker was used. Acceleration at 4 random locations was measured for each plate and the RMS averaged over 1000 Hz bandwidths. Frequency responses were calculated and then stored on a disk. Anti-aliasing filters were used for both force and acceleration signals.

The above tests were performed using an HP 5451C Analyzer. Tests were conducted on both undamped and damped specimens. For damped tests, EAR C-2003 sheet material was bonded to the inside surface of the plates.

Low frequency (0-1500Hz) frequency response (X/F) measurements were made utilizing Wilcoxon F4 shaker and SMS model 4[5] software. These tests were conducted in conjunction with other detailed modal testing. However, only the frequency response data from those tests were relevant to this paper.

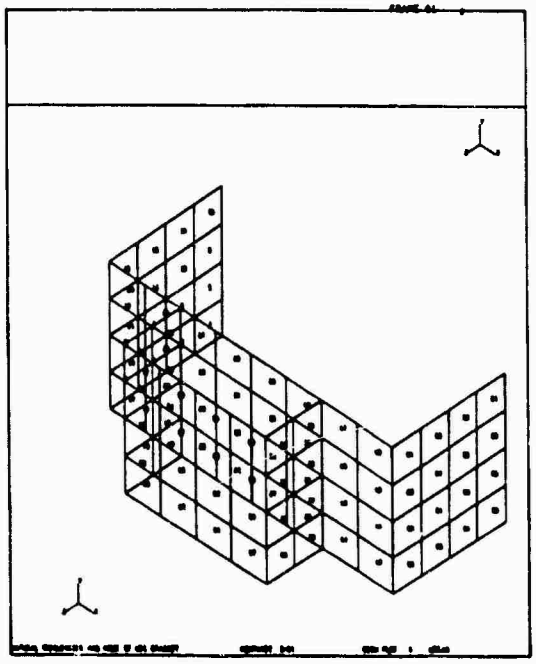

Figure 4. Finite Element Model

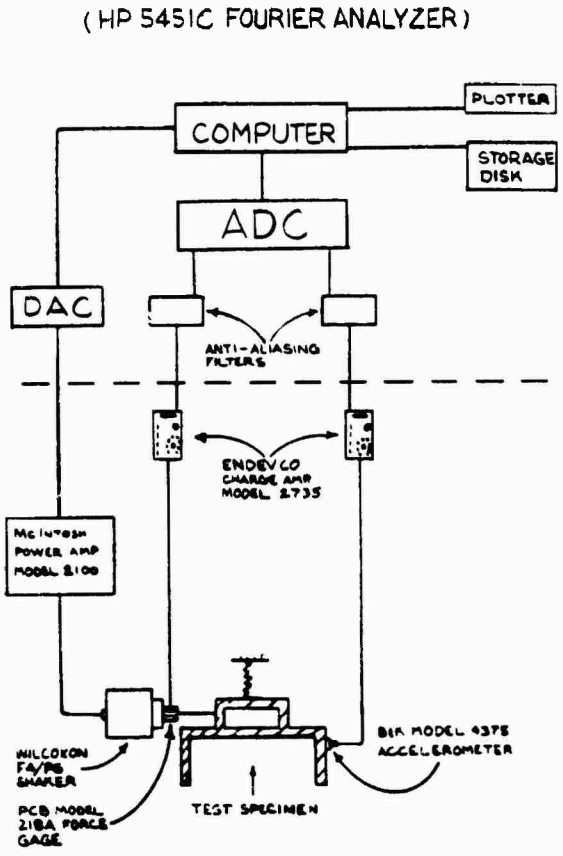

Figure 5. Instrumentation

RESULTS

The frequency response function, $\ddot{x}/Fg$, is synthesized from the NASTRAN output using the following equation.

$$\left(\frac{\ddot{x}_j}{F_s}\right)_{real} + i \left(\frac{\ddot{x}_j}{F_s}\right)_{imag} = \sum_{r=1}^{n} \frac{\psi_j^r \psi_s^r \left[1-\left(\frac{\omega}{\omega_r}\right)^2\right] \omega^2}{k_r \left(\left[1-\left(\frac{\omega}{\omega_r}\right)^2\right]^2 + \left[2\zeta_r \frac{\omega}{\omega_r}\right]^2\right)}$$

$$- \sum_{r=1}^{n} \frac{\psi_j^r \psi_s^r \left[2\zeta_r \frac{\omega}{\omega_r}^2\right] \omega^2}{k_r \left(\left[1-\left(\frac{\omega}{\omega_r}\right)^2\right]^2 + \left[2\zeta_r \frac{\omega}{\omega_r}\right]^2\right)} \qquad (4)$$

Since at high frequency it is mainly the averaged responses that are of interest, the transverse vibration at the middle of each plate is calculated and RMS averaged over a 1,000 Hz frequency bandwidths. The comparison of these averaged results with STEAMS predictions of energy blocks 1 through 6 and with averaged test output are shown in Figure 6. The frequency ranges from 2,000 to 14,000 Hz for both damped and undamped cases. It can be seen that in this frequency range, the STEAMS Computer Program provides better overall predictions than FEA results. Except at the driving point, FEA output shows a sharp decrease in response beyond a certain frequency. For simple plate type of structures, as in this case, this frequency may be related to the finite element mesh size by the following equation.

$$f_{max} = \text{CONST.} \frac{\pi}{S} \cdot no\epsilon \cdot \varkappa \cdot C_L \qquad (5)$$

Where S is the area of the plate, $no\epsilon$ is the number of elements used in the finite element mesh. $\varkappa$ is the radius of gyration of the plate and C_L is the longitudinal wavespeed. The CONST is found to be approximately 0.7 in this example.

For frequency response below 2,000 Hz, FEA yields much better results than STEAMS prediction. For example, the responses at the middle of block 1 are compared in Figure 7. This is due to the average nature of SEA. At low frequency, the modal overlapping becomes small; therefore, the variance starts to increase.[1]

The overall responses from 0 Hz to 14,000 Hz at the top plate (energy block No. 5) are compared in Figure 8. Sharp deviation from test results at low frequency for SEA and at high frequency for FEA are clearly indicated in this Figure.

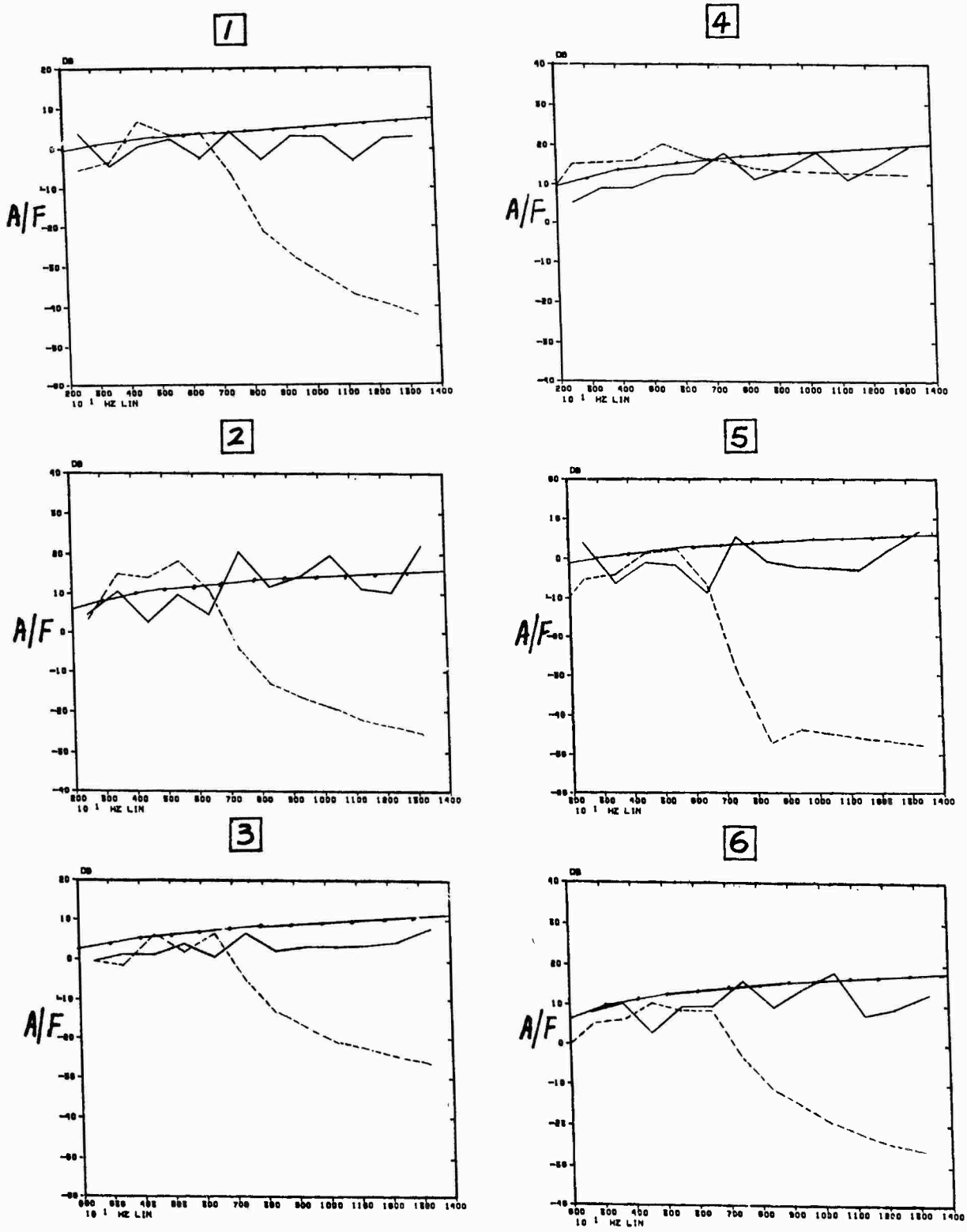

Figure 6A. Comparison of FEA, SEA and Test Results in 2000 to 14000 Hz

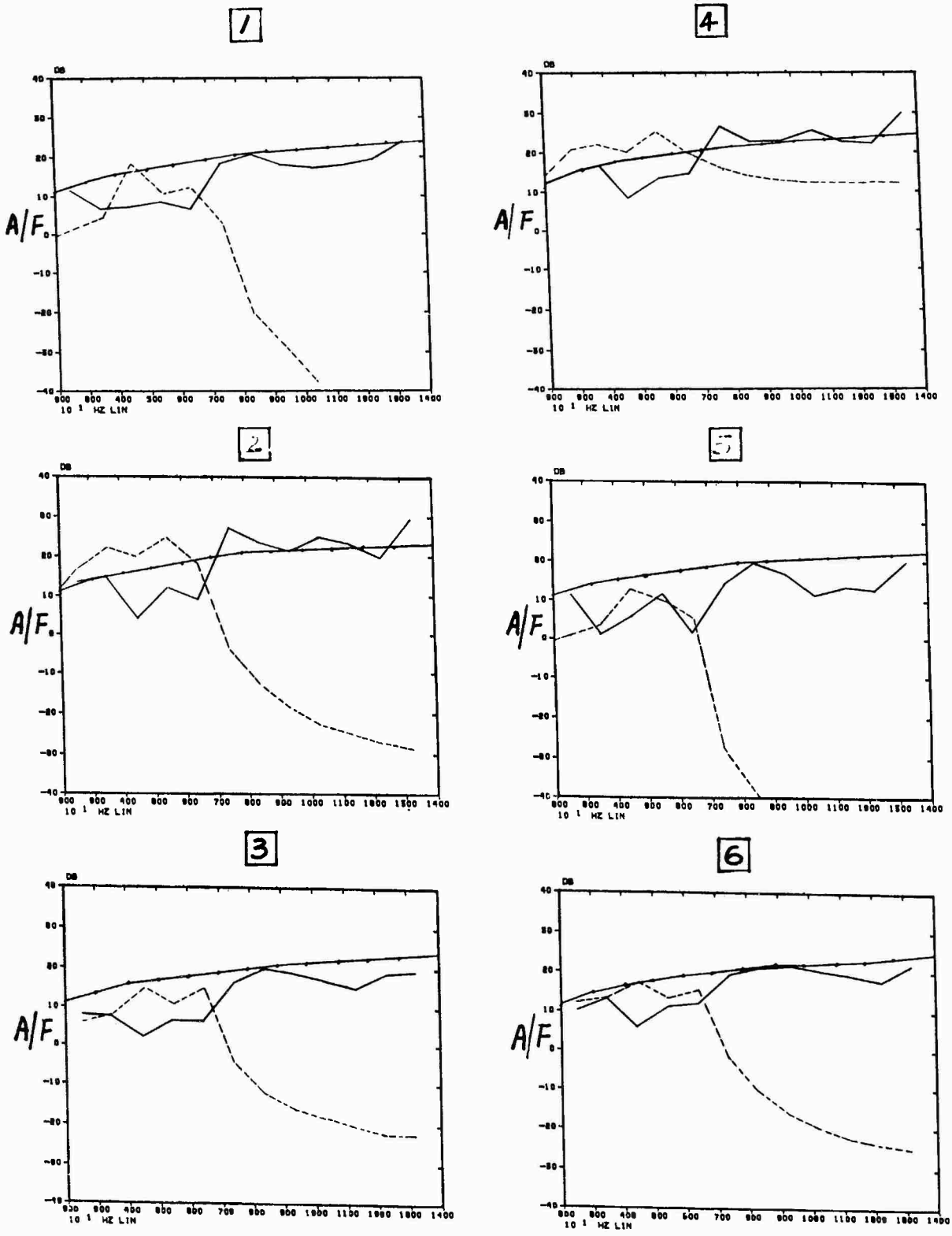

Figure 6B. Comparison of FEA, SEA and Test Results in 2000 to 14000 Hz

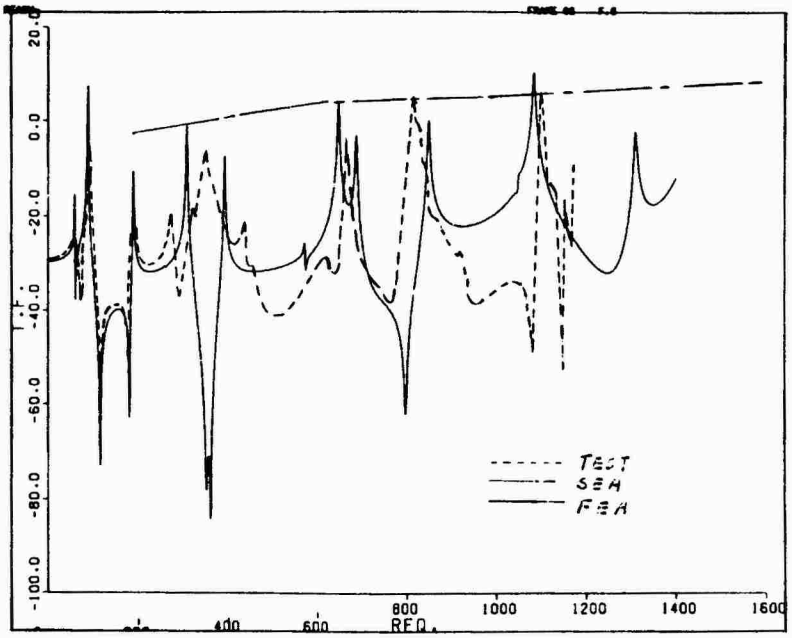

Figure 7. Comparison of FEA, SEA and Test Results at Low Frequency

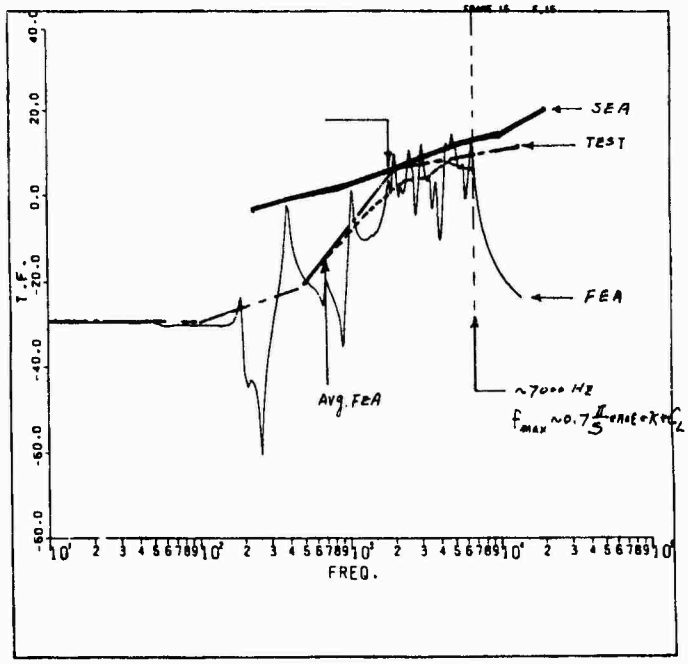

Figure 8. Overall Comparison of SEA, FEA and Test

CONCLUSIONS

1. The above results indicate that SEA calculations by the STEAMS Computer Program provides good predictions in the intermediate and high frequency ranges. Although further refinements could be made.

2. As expected, FEA performs much better than STEAMS in the low frequency ranges. However, the FEA predicts an abrupt drop in response above a certain frequency because of its limitation in the total number of degrees of freedom in a model.

3. It is very important for an analyst to realize the limitation of different tools. Any mis-application of either method may produce erroneous answers.

ACKNOWLEDGEMENTS

The authors would like to thank Mr. P.C. Warner of Westinghouse for his encouragement, support, and discussions throughout the different phases of this project.

REFERENCES

1. R.H. Lyon, Statistical Energy Analysis of Dynamic Systems
The MIT Press, Cambridge, MA 1976

2. L.K.H. Lu and P.C. Warner, "Vibration Analysis of A Large Naval Gear", ASME Paper No. 81-DET-142.

3. R.G. DeJong and J.E. Manning "Statistical Energy Analysis of A Locked Train Design of A Twin Turbine Main Propulsion Reduction Gear" Report to Westinghouse Electric Corp. Cambridge, Collaborative, Cambridge, MA 1982.

4. L. Cremer, M. Heckel, and E.E. Ungar, Structure-Borne Sound, Springer-Veriag, New York, 1973.

5. "MSC/NASTRAN User's Manual", MacNear-Schwender Corp., Los Angeles, CA 1980.

6. "SMS 500 A Model 4.0 Operating Manual", Structural Measurement Systems, Inc., CA., April, 1982.

Discussion

Mr. Shin (Naval Postgraduate School): When you performed the finite element analysis, did you use modal superposition or a direct frequency response analysis?

Mr. Lu: We used the normal modes.

Mr. Shin: Based on the modal analysis, did you check the size of the element to see if it was small enough to capture the high frequency response?

Mr. Lu: Yes. That is why we kept decreasing the size of the finite elements.

Mr. Shin: I think you understand that this is the major problem using the modal superposition. In my experience with NASTRAN, I compare its results with the direct frequency response analysis results before I use it for the actual situation. If I get good agreement, then I project it into the real problem.

Mr. Lu: The reason for this study is to find an optimum finite element size. The frequency resolution improves if I decrease the size of the finite element. But, I cannot afford a finite element that is too small when I analyze a complex structure. Usually the cost of one run on a computer is $5,000

Mr. Feldman (NKF Engineering Associates, Inc.): You drew some conclusions which were based on a relatively simple model. If you had a real complex marine structure, such as machinery and its foundation, would you expect to get the same conclusions?

Mr. Lu: I think our limited experience with marine structures would be nearly the same, using both a statistical energy analysis or a finite element analysis. We have to stop at some upper frequency when we use a finite element analysis because we do not trust the results above that frequency. We do trust the statistical energy analysis results at the higher frequencies, therefore, the conclusion would be nearly the same. The difference is that we can afford to run tests to validate our analyses.